Printing smart sensor and actuator coatings using piezoelectric composites

van Cuong Nguyen

N°d'ordre NNT : **2023ISAL0047**

THESE de DOCTORAT DE L'INSA LYON, membre de l'Université de Lyon

Ecole Doctorale N° ED162 MEGA
MÉCANIQUE, ÉNERGÉTIQUE, GÉNIE CIVIL, ACOUSTIQUE

Spécialité/ discipline de doctorat : Génie électrique

Soutenue publiquement le 07 juillet 2023, par :
Van Cuong NGUYEN

Printing smart sensor and actuator coatings using piezoelectric composites

---

Devant le jury composé de :

DEMOLY Frédéric	Professeur /UTBM-Campus de Sevenans	Rapporteur
BROITMAN Esteban	Docteur, HDR, Senior Researcher /SKF RTD	Rapporteur
GUIFFARD Benoit	Professeur /Université de Nantes	Examinateur
BERNARD Yves	Professeur / Université Paris-Saclay	Examinateur
COTTINET Pierre-Jean	Maître de Conférences, HDR /INSA-LYON	Directeur de thèse
LE Minh Quyen	Maître de Conférences /INSA-LYON	Co-directrice de thèse

Département FEDORA – INSA Lyon - Ecoles Doctorales

SIGLE	ECOLE DOCTORALE	NOM ET COORDONNEES DU RESPONSABLE
CHIMIE	**CHIMIE DE LYON** **https://www.edchimie-lyon.fr** Sec. : Renée EL MELHEM Bât. Blaise PASCAL, 3e étage secretariat@edchimie-lyon.fr	**M. Stéphane DANIELE** C2P2-CPE LYON-UMR 5265 Bâtiment F308, BP 2077 43 Boulevard du 11 novembre 1918 69616 Villeurbanne **directeur@edchimie-lyon.fr**
E.E.A.	**ÉLECTRONIQUE, ÉLECTROTECHNIQUE, AUTOMATIQUE** **https://edeea.universite-lyon.fr** Sec. : Stéphanie CAUVIN Bâtiment Direction INSA Lyon Tél : 04.72.43.71.70 secretariat.edeea@insa-lyon.fr	**M. Philippe DELACHARTRE** INSA LYON Laboratoire CREATIS Bâtiment Blaise Pascal, 7 avenue Jean Capelle 69621 Villeurbanne CEDEX Tél : 04.72.43.88.63 **philippe.delachartre@insa-lyon.fr**
E2M2	**ÉVOLUTION, ÉCOSYSTÈME, MICROBIOLOGIE, MODÉLISATION** **http://e2m2.universite-lyon.fr** Sec. : Bénédicte LANZA Bât. Atrium, UCB Lyon 1 Tél : 04.72.44.83.62 secretariat.e2m2@univ-lyon1.fr	**Mme Sandrine CHARLES** Université Claude Bernard Lyon 1 UFR Biosciences Bâtiment Mendel 43, boulevard du 11 Novembre 1918 69622 Villeurbanne CEDEX **sandrine.charles@univ-lyon1.fr**
EDISS	**INTERDISCIPLINAIRE SCIENCES-SANTÉ** **http://ediss.universite-lyon.fr** Sec. : Bénédicte LANZA Bât. Atrium, UCB Lyon 1 Tél : 04.72.44.83.62 secretariat.ediss@univ-lyon1.fr	**Mme Sylvie RICARD-BLUM** Institut de Chimie et Biochimie Moléculaires et Supramoléculaires (ICBMS) - UMR 5246 CNRS - Université Lyon 1 Bâtiment Raulin - 2ème étage Nord 43 Boulevard du 11 novembre 1918 69622 Villeurbanne Cedex Tél : +33(0)4 72 44 82 32 **sylvie.ricard-blum@univ-lyon1.fr**
INFOMATHS	**INFORMATIQUE ET MATHÉMATIQUES** **http://edinfomaths.universite-lyon.fr** Sec. : Renée EL MELHEM Bât. Blaise PASCAL, 3e étage Tél : 04.72.43.80.46 infomaths@univ-lyon1.fr	**M. Hamamache KHEDDOUCI** Université Claude Bernard Lyon 1 Bât. Nautibus 43, Boulevard du 11 novembre 1918 69 622 Villeurbanne Cedex France Tél : 04.72.44.83.69 **hamamache.kheddouci@univ-lyon1.fr**
Matériaux	**MATÉRIAUX DE LYON** **http://ed34.universite-lyon.fr** Sec. : Yann DE ORDENANA Tél : 04.72.18.62.44 yann.de-ordenana@ec-lyon.fr	**M. Stéphane BENAYOUN** Ecole Centrale de Lyon Laboratoire LTDS 36 avenue Guy de Collongue 69134 Ecully CEDEX Tél : 04.72.18.64.37 **stephane.benayoun@ec-lyon.fr**
MEGA	**MÉCANIQUE, ÉNERGÉTIQUE, GÉNIE CIVIL, ACOUSTIQUE** **http://edmega.universite-lyon.fr** Sec. : Stéphanie CAUVIN Tél : 04.72.43.71.70 Bâtiment Direction INSA Lyon mega@insa-lyon.fr	**M. Jocelyn BONJOUR** INSA Lyon Laboratoire CETHIL Bâtiment Sadi- Carnot9, rue de la Physique 69621 Villeurbanne CEDEX **jocelyn.bonjour@insa-lyon.fr**
ScSo	**ScSo*** **https://edsciencessociales.universite-lyon.fr** Sec. : Mélina FAVETON INSA : J.Y. TOUSSAINT Tél : 04.78.69.77.79 melina.faveton@univ-lyon2.fr	**M. Bruno MILLY** Université Lumière Lyon 2 86 Rue Pasteur 69365 Lyon CEDEX 07 **bruno.milly@univ-lyon2.fr**

*ScSo : Histoire, Géographie, Aménagement, Urbanisme, Archéologie, Science politique, Sociologie, Anthropologie

Acknowledgements

This thesis is the result of three years of research work conducted at the Laboratoire de Génie Electrique et Ferroélectricité of Institut National des Sciences Apppliquées Lyon. This thesis work would not have been accomplished without the support and assistant of the people to whom I wish take this opportunity to express my sincere appreciation.

First of all, I would like to express my profound respect and gratitude to my supervisor, Prof. Pierre-Jean COTTINET, for providing invaluable guidance throughout this research. Discussions with him have always been a learning experience and gave me another point of view for my result. I sincerely thank him for all the confirmation and encouragement he made to relieve my anxiety and motivate to another step.

Second, my deepest gratitude goes to my co-supervisor Dr. Minh Quyen LE, who was always there when I need assistance. She has taught me the methodology to carry out the experiment, data analysis, even presentation and scientific writing with endless patience, training me to be a qualified researcher. I warmly thank her for the suggestions she gave me, whether in the technical, scientific, professional and personal field.

Besides my supervisors, I would like to thank the rest of the jury members: Prof. DEMOLY Frédéric, Dr. BROITMAN Esteban, Prof. GUIFFARD Benoit, Prof. BERNARD Yves, for their detailed reviews, insightful comments and present on my defense.

I am particularly grateful to Ms. Sophie Bernadet from Arc en Ciel Sérigraphie for helping me with screen printing and constantly preparing printed samples for me. Our frequent discussions and cooperation have been productive and substantially accelerated our project, especially during difficult times. My sincere thanks also go to Dr. Jean-Fabien Capsal for introducing the composite fabrication process and providing efficient advice on measurement.

I would like to express my acknowledgments to staffs and colleagues in LGEF laboratory. Dr. Laurence SEVEYRAT, an experienced technician engineer, gave the introduction course in chemical room and guidelines in SEM. I am grateful for the assistance given by Ms. Véronique Perrin, a reliable electronic engineer, for the polarization process. I would like to thank Mr. Frédéric DEFROMERIE, a skillful technician in LGEF, for manufacturing the sensor, the connector. A special thanks goes to Ms. Evelyne Dorieux for helping me deal with the complex administrative stuff.

I would like to extend my thanks to my colleagues and friends, who build a multicultural ambience in the office filled with smiles, rather than only a working place. Thanks to Mr.Leopol Diatezo for helping in doctoral training. Thanks to Dr. Giulia D'Ambrogio for guiding me in fabricating the piezoelectric material and to Mr. Amaury for the metallization. Thanks to Dr. Kritsadi Thetpraphi as the reliable and excellent seniors, who always ready to help me, especially in the 3D printing. Thanks to Mr. Omar Zahaf for helping me with the high voltage characterization. I am grateful for unforgettable and valuable time spent with all other people in LGEF laboratory.

At last but not least, I would like to express my deepest gratitude to my familly for your unconditional love and cares. Thank you so much for always being with me.

Van Cuong NGUYEN

09/05/2023

Résumé

Les matériaux piézoélectriques jouent un rôle crucial dans le développement des matériaux intelligents et des processus de fabrication additive. Ils sont utilisés comme matériaux fonctionnels dans diverses applications, notamment la détection, l'actionnement, la récupération d'énergie et la rétroaction haptique. Les composites piézoélectriques, en particulier, ont été largement étudiés en raison de leur potentiel à améliorer les performances des matériaux piézoélectriques. Ces composites sont formés en incorporant des particules ou des fibres piézoélectriques dans un matériau matrice, ce qui donne des propriétés mécaniques et électriques améliorées. Avec l'avancée des techniques de fabrication additive, les matériaux piézoélectriques peuvent être imprimés en 3D dans des géométries complexes et intégrés à des composants électroniques pour créer des structures intelligentes. La combinaison de matériaux piézoélectriques et de la technologie d'impression 3D a conduit au développement de divers dispositifs, notamment des capteurs, des actionneurs et des systèmes de rétroaction haptique, qui peuvent être personnalisés et fabriqués rapidement.

Les travaux de cette thèse se sont focalisés sur deux applications, à savoir la réalisation de capteurs pour le développement de roulements instrumentés et le développement de réseaux de transducteurs pour les interfaces haptiques. Les deux applications sont basées sur le matériau piézoélectrique composite, qui joue un rôle principal dans le fonctionnement des capteurs ou actionneurs. Des études préliminaires sur les caractéristiques des composites piézoélectriques ont été menées afin d'optimiser les propriétés du matériau et sa compatibilité avec l'impression 3D.

Première application concerne à la réalisation de capteurs pour la surveillance de roulement à bille. Le composite piézoélectrique à base de polymère est directement sérigraphié sur la surface de la structure hôte, qui est assimilée à un substrat en acier instrumenté. En raison de la couche de détection généralement très mince par rapport au substrat sous-jacent, les propriétés mécaniques de l'ensemble du système sont principalement déterminées par les caractéristiques du matériau de type acier. Par conséquent, la méthode développée ici permet d'extraire de manière fiable le comportement piézoélectrique efficace du composite mince grâce à une méthode de flexion à 4 points (4PB). Des caractérisations complètes des propriétés diélectriques et mécaniques, ainsi que des mesures de détection directe par couplage électromécanique sont étudiées sur la conception de la structure faite maison. Des modèles analytiques et éléments finis sont développés pour prédire les propriétés mécaniques du substrat testé ainsi que la sensibilité du capteur sous différentes charges appliquées. Des expériences sont menées sur un montage 4PB, permettant de valider les solutions analytiques et numériques. Un bon accord entre les sorties de capteur prédites par le modèle et les mesures empiriques a été atteint, confirmant la grande fiabilité de l'approche proposée. Tous les résultats ont démontré que le capteur développé est capable de fournir une mesure directe de déformation/contrainte au lieu d'un capteur de jauge de contrainte traditionnel par interpolation, et offre ainsi une méthode efficace pour la surveillance *en ligne* et *in situ* des roulements.

La deuxième application consiste à fabriquer un retour haptique en utilisant un matériau piézoélectrique composite. Des simulations ont été effectuées avec ANSYS pour optimiser le choix du matériau et les dimensions du design. Les expérimentations ont montré la capacité de ce matériau à générer des vibrations pour un retour haptique. Enfin, un démonstrateur de retour haptique a été fabriqué pour permettre aux utilisateurs de ressentir ces sensations. Un circuit électronique a été conçu pour répondre aux spécifications du démonstrateur, et une application Python a été développée pour tester facilement différents types de formes d'onde.

Mots clés : capteur piézoélectrique, piézoélectrique composite, mesure de flexion quatre points, simulation par éléments finis, surveillance de la santé, impression d’écran, retour haptique, actionneur piézoélectrique.

Abstract

Piezoelectric materials play a crucial role in the development of smart materials and additive manufacturing processes. They are used as functional materials in various applications, including sensing, actuation, energy harvesting, and haptic feedback. Piezoelectric composites, in particular, have been widely studied due to their potential to enhance the performance of piezoelectric materials. These composites are formed by incorporating piezoelectric particles or fibers into a matrix material, resulting in improved mechanical and electrical properties. With the advancement of additive manufacturing (AM) techniques, piezoelectric materials can be 3D printed into complex geometries and integrated with electronic components to create smart structures. The combination of piezoelectric materials and 3D printing technology definitively paves the way for next generation of smart multifunctional materials that could be customized and quickly integrated in various sensing and actuating devices.

This thesis focuses on two applications, namely "the development of sensors for instrumented bearings", and "the development of transducer arrays for haptic interfaces". Both applications are based on piezoelectric composite material, which plays a major role in the functioning of the sensors or actuators. Preliminary studies on the characteristics of piezoelectric composites were conducted to optimize the material properties and its compatibility with 3D printing AM.

The first application involves the development of piezoelectric sensors to detect and predict early failure of bearing via direct indicator by monitoring unidirectional (1D) and bidirectional (2D) loads thanks to a smart sensor coating using $BaTiO_3$/PUA polymer-based composite. This a composite ink is directly screen-printed onto the surface of the host structure, which is treated as an instrumented steel substrate. Full characterizations of dielectric and mechanical properties, together with direct sensing measurement are investigated on rectangular-shaped substrate (1D) and cross-shaped substrate (2D) using a 4-point bending (4PB) structure. To ensure the accuracy and stability of measurement as well as the durability of the printed coating, the developed prototype is built according to design rules commonly used in electronic circuit. Analytical and finite element models (FEM) are developed to predict the mechanical properties of the tested substrate as well as the sensor sensitivity under either unidirectional or bidirectional load. Experiments are performed on the 4PB setup to validate the analytical and numerical solutions. All results demonstrate that the developed sensor is capable of providing a direct measurement of deformation/stress instead of a traditional strain gauge sensor with interpolation, and thus provides an effective method for online and in-situ monitoring of bearings. To sum up, high performance of a sensor network coating depends not only on the ultimate characteristics of its own materials, but also on its structural design. Such an issue is nonetheless crucial to achieve reliable condition monitoring of bearing, especially for multidirectional load – a key signature of early failure detection.

The second application involves in the development of piezoelectric actuator for the fabrication of haptic feedback button, demonstrating high potential of such a device for the area of tactile screen. To maximize the perception of user, a haptic system capable of generating a displacement greater than 2 µm at 300 – 700 Hz frequency range is investigated. A FEM (Finite Element Modeling) model via ANSYS multiphysics software was explored to analyze the haptic performance of the wafer structure consisting of a piezoelectric $BaTiO_3$ multilayer coated on a transparent flexible PET substrate. Several parameters dedicated to the geometric and mechanical properties of the wafer, together with those of the electrodes are demonstrated to have significant impact on the actuation ability of the haptic device. The research also involves in experimental characterizations that allow to support the simulation work as well as to validate the reliability of the proposed design. Finally, a demonstrator comprising piezoelectric buttons together with electronic command and conditioning circuits are successfully developed, making a simple way to create multiples sensations to users.

Keyword: piezoelectric sensor/actuator, $BaTiO_3$/PUA composite, four-point bending measurement, finite element simulation, characterizations, health monitoring, screen printing, haptic feedback, design optimization.

Acronyms

1D	unidirectional
2D	bidirectional
3D	three-dimensional
4PB	4-point bending
AC	Alternating current
AM	Additive manufacturing
$BaTiO_3$	Barium Titanate
CAD	Computer-Aid Design
CM	Condition monitoring
CTs	Conductive tracks
DC	Direct current
DL	Dielectric layer
FEM	Finite element method
PCB	Printed circuit board
PE	Polyethylene
PET	Polyethylene terephthalate
PUA	Polyurethane Acrylate
PVC	Polyvinyl chloride
SEM	Scanning electron microscopy
UV	Ultraviolet

General introduction

The development of intelligent materials is currently promoting the integration of functionalities as close as possible to the structure. This research area is closely linked with additive manufacturing (AM) processes, which allow the transition from grafted equipment to fully integrated one. In the near future, multifunctional material AM and their advancements will increasingly be utilized to achieve hybrid mechatronic functions that merge mechanical structure, electronic components, conductive tracks, and functional materials. This topic centers around multifunctional materials combined with 4D printing. Such materials that can convert or adapt to physical stimuli are gradually demonstrating their potential for technological innovation in various application sectors. In addition to possibly replacing traditional transduction processes (sensors and actuators) in certain cases, the new possibilities provided by these materials in terms of multiphysic coupling performance and functionalities are a compelling motivation to address and solve challenges arising from societal issues.

Piezoelectric materials have been and continue to demonstrate their potential as a crucial component in the development of intelligent materials that integrate functionalities closely with the structure. Piezoelectric materials have unique properties that make them ideal for use in intelligent materials development. One of their key features is their ability to convert mechanical energy into electrical energy and vice versa, which makes them highly valuable in applications related to structural control and haptic feedback. Additionally, piezoelectric materials have a high level of sensitivity to mechanical stress, which makes them an excellent choice for sensing applications. Therefore, this thesis work is primarily focused on the development and optimization of piezoelectric materials for printed electronics, with a particular emphasis on their potential applications in the areas of structural control and haptic feedback.

Recently, there has been a growing interest in deploying smart materials as sensing components of condition monitoring (CM) systems. In the field of CM, particularly for ball bearing, structural damage is usually reflected by a change in the system stiffness. Therefore, the use of sensors mounted on the structure to detect structural stiffness changes due to cracks or damage developed at or away from the sensor location is very desirable. However, existing sensing technology (e.g. strain gages, accelerometers, linear voltage displacement transducers) accompanied by interpretation algorithms is not effective for *in situ* monitoring of early damage because of its limited sensitivity, bandwidth, and accessibility to the hidden localized areas, let alone damage initiation and progression. Among the various smart sensor types, piezoelectric materials, due to its high ability to response any stiffness change, offer great promise for researchers to overcome technological locks of the former sensing methods. In a piezoelectric material such as lead zirconate titanate (PZT) or Barium titanate ($BaTiO_3$), an applied uniform load (strain) can generate electric polarization and vice versa. Such an effect is well recognized and has been exploited extensively in a broad field for both sensing and actuation applications. This opens up a broader choice of materials including lead and lead-free ferroelectrics with preferable properties. Considering lead toxicity, there is interest in developing piezoelectric materials that are biocompatible and environmentally friendlier. Several classes of materials are now being reconsidered as potentially attractive alternatives to PZT for special applications. Among them, $BaTiO_3$ is one of the most common used because of its high permittivity, easy process, low cost, and commercial availability.

It is well known that bearing, considered as one of the most critical elements in the rotary machines, has been widely used in various industries, especially in the field of aerospace. It is therefore essential to

determine the early faults conditions from bearings. There are various methods to detect faults in the bearings, such as vibration monitoring, wear debris monitoring, temperature monitoring, soap techniques, non-destructive test, etc. Among them, vibration signal analysis is the most common technique used for checking the condition and finding faults in bearings]. Such a method, however, only provide indirect indicators that require pre-processing stage to convert them into useful representations. The treatment can only be achieved if an adequate model describing the relationship is available. In this thesis, an alternative method to in situ monitor the bearing load is proposed, which enables the early detection and prediction of failure through a direct indicator.

Another application of the piezoelectric composites developed in this thesis is haptic feedback for consumer electronics. The primary function of a screen is to provide an image, which involves many components. Another important function of the screen is tactile feedback, particularly for the virtual keyboard. This is not the case for all manufacturers, but some offer what is called haptic feedback, meaning that when the user touches a key, a vibration feedback confirms that the information has been recorded. This is currently achieved with small vibrating motors. The problem is that these motors take up space, increase weight, consume a lot of energy, and the vibration is not localized.

To solve this problem, companies in the industry such as Arkema or Solvay offer piezoelectric polymer materials, which means that pressure on the materials generates an electrical response, and vice versa: when an electric field is applied, the material deforms, generating a vibration. This vibration can therefore occur only on the letter that was touched, making the haptic feedback more precise. However, for the currently envisaged copolymer ferroelectric materials, one of the obstacles concerns the cost of the materials, as well as a complex manufacturing process due to their intrinsic properties (fluorinated materials). The use of piezoelectric composites appears to be a promising solution due to reasonable material costs and the ability to create multilayer architectures to overcome a moderate piezoelectric coefficient compared to P(VDF-TrFE) type materials. The second part of this thesis aims to explore the feasibility of creating a haptic feedback system using piezoelectric composite materials and to develop a demonstrator for this purpose.

Regarding the evolution process described above, the thesis is split into four related chapters:

In Chapter 1, the background of piezoelectricity is introduced, including the definition and physical explanation of the piezoelectric effect, the general equations derived from it, and a categorical description of piezoelectric materials, with a focus on piezoelectric composites based on $BaTiO_3$. The chapter then explores different techniques for 3D printing piezoelectric materials, followed by a discussion of the potential applications of these composites in structural health monitoring of bearing as well as haptic feedback techniques particularly for tactile screen.

Chapter 2 focuses on the architecture design and fabrication procedures of piezoelectric sensors and actuators, which are utilized for condition monitoring and touchscreen devices, respectively. This chapter provides detailed descriptions of the experimental setups used for the full characterization of these components in terms of their dielectric, conductive, piezoelectric, and mechanical properties. Moreover, the chapter discusses the exploration of ANSYS tool for the simulation and estimation of piezoelectric behaviors. The tool is used to create simple two-dimensional and three-dimensional models that help to predict the performance of the piezoelectric components under various conditions.

Chapter 3 reports on smart sensor coating based piezoelectric composite for bearings' condition monitoring via direct indicators of unidirectional (1D) and bidirectional (2D) loads. First, the chapter begins with an introduction of bearings to provide background knowledge. Second, the results and discussions

related to the performance of the sensor on rectangular-shaped and cross-shaped substrates are presented to evaluate the reliability of piezoelectric composite sensors as well as to validate their design optimization. Last, the chapter offers a review of condition monitoring techniques used for aerospace bearings and concludes by giving recommendations for future research in this field.

Chapter 4 describes the design and development process of a haptic feedback demonstrator using piezoelectric materials. The chapter starts by introducing the concept of haptic feedback and its importance in user experience. Then, it discusses the various parameters that need to be considered in designing an effective haptic feedback system. Next, optimization of the materials and dimensions of the piezoelectric actuators used in the haptic feedback system are investigated through finite element model (FEM) of ANSYS multiphysics software. Last, the results of the experiments conducted to optimize and validate the system are presented and discussed in detail. Based on the optimized design parameters, a haptic feedback demonstrator is successfully developed, which offers an alternative solution to interact with tactile technology and paves the way for next generation of smart multifunctional materials.

Table of Contents

Chapter 1. State of arts

The objective of this chapter is to define the context in which piezoelectric materials are developed, particularly in printed electronics, that allows for an achievement of the different objectives dedicated to this research.

Firstly, we report on the background knowledge of piezoelectricity involving the definition and physical explanations of the piezoelectric effect, together with the corresponding mathematical formulations as well as the categories of these materials. Among them, barium titanate ($BaTiO_3$) is specially investigated in detail because of its interesting physical properties.

Next, we present the development of printed electronics and the different techniques used for printed piezoelectric material. At last, a literature summary on the application of printed piezoelectric composites is carried out and potential applications in structural health monitoring are proposed.

1.1 Background on piezoelectricity

1.1.1. Piezoelectric effect

"Piezo" is derived from the Greek for "to press" [1]. In 1880, Pierre Curie and Jacques Curie discovered that applying pressure to crystals such as quartz, tourmaline, and Rochelle salt generates electrical charges on the surface of these materials [2]. This conversion of mechanical energy into electrical energy is called the *direct piezoelectric effect*. As shown in Figure 1.1 (a), there is a voltage potential across the material. In this way, the piezoelectric effect acts like a miniature battery. Devices that use the direct piezoelectric effect include microphones, pressure sensors, hydrophones, and many other sensing types of devices [3–5]. The piezoelectric effect can be reversed, i.e., referred to as the *inverse piezoelectric effect*. It has been seen in Figure 1.1(b) that the application of an electrical voltage to a piezoelectric material causes the internal generation of a mechanical strain, making it shrinks or expand. Such a phenomenon, firstly predicted by Gabriel Lippman in 1881 via mathematical deduction from fundamental thermodynamic principles, was quickly demonstrated by the Curies throughout experimentation [2].

Many electronic devices today use piezoelectricity such as microphone, acoustic generator (speakers or buzzers, medical ultrasound, sonar transducers, and so on) [3,6,7].

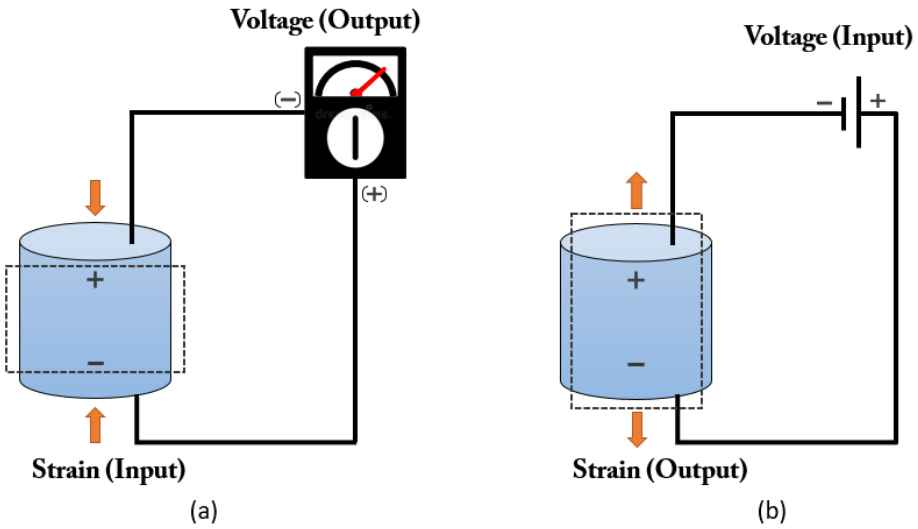

Figure 1.1. (a) Direct piezoelectric effect. (b) Conversed piezoelectric effect.

1.1.2. Piezoelectric equations and coefficients

Piezoelectricity is a property due to the anisotropy of materials and to be able to describe it, the use of the tensor concept under matrix form is essential. Based on the Institute of Electrical and Electronics Engineers (IEEE) standard for piezoelectricity, an orthogonal coordinated system is used to identify the axes as shown in Figure 1.2 [8]. In the piezoelectric material, 1 corresponds to the x-axis representing the stretch direction, 2 relates to the y-axis indicating the transverse direction, and 3 is the z-axis describing the thickness direction. Shear planes 4,5,6 are defined perpendicular to directions 1,2,3. As a result, the electric

polarization and mechanical strain produced by the piezoelectric effect can be described mathematically in the three dimensions.

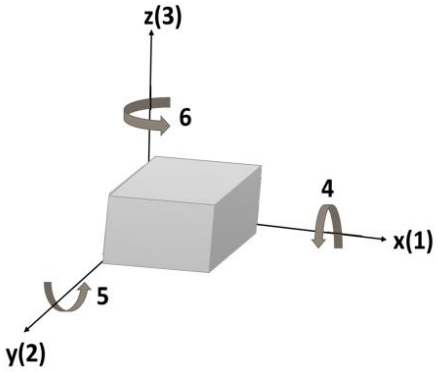

Figure 1.2. Tensor directions to define the constitute equation.

The phenomenon of piezoelectricity results from a coupling between electric quantities (i.e., the electric field E and the electric displacement D) and mechanical quantities (the tensors of constraint T and deformation S). The relations of proportionality which link them, in the case of an isotropic material, can be written in a simplified way:

$$\begin{cases} D = dT \\ S = dE \end{cases} \tag{1.1}$$

We are going to define these quantities as well as the electromechanical coupling coefficient which connects them, expressed here by d.

1.1.1.1 Elastic properties of materials

Elasticity is the ability of a material to deform under stress and then return to its initial state. In 1675, Robert Hooke translated this behavior into a law, in which the material is considered as continuous and homogeneous, and its dimensions are important compared to the deformations it undergoes [9]. The applied force must also be lower than the limit values of the elastic domain. This law expresses the proportional relationship between the stress (represented by the tensor T_{ij}), and the deformation (represented by the tensor S_{kl}). Here the subscripts i, j, k and l vary from 1 to 3 representing the three directions of an orthonormal frame of reference in three-dimensional space (Figure 1.2). The relation is then written as:

$$T_{ij} = c_{ijkl} S_{kl} \tag{1.2}$$

where c_{ijkl} is the elastic stress tensor. Reversing this relation yields the flexibility tensor s_{ijkl} which connects S_{ij} to T_{kl}:

$$S_{ij} = s_{ijkl} T_{kl} \tag{1.3}$$

where T_{ij} and S_{kl} are symmetric tensors of order 2, c_{ijkl} and s_{ijkl} are therefore symmetric tensors of order 4.

1.1.1.2 Dielectric properties of materials

Similarly, the dielectric behavior of a material is explained by the ability of its charges to move under the action of an electric field. The quantities E and D, respectively indicating the electric field and the

displacement of charges. They are connected, in a homogeneous material and with linear behavior, by the relation [10]:

$$D_i = \varepsilon_{ij} E_j \tag{1.4}$$

where ε_{ij} is called dielectric permittivity of the material, with a rank 2 tensor.

Inverting this relationship yields:

$$E_i = \beta_{ij} D_j \tag{1.5}$$

where β_{ij} is the impermeability constant, also rank 2 tensors. In practice, the dielectric permittivity values are normalized by the vacuum permittivity ε_0, equal to $8.85.10^{-12}$ F.m^{-1}. We then speak of relative permittivity ε_r (or dielectric constant).

1.1.1.3 Fundamental relationships of piezoelectricity

The various properties of a piezoelectric material can be described from the four physical quantities explained previously: *D*, *E*, *S* and *T*. The various interactions of this system, without taking into account the influence of the temperature, are detailed on Figure 1.3 [11].

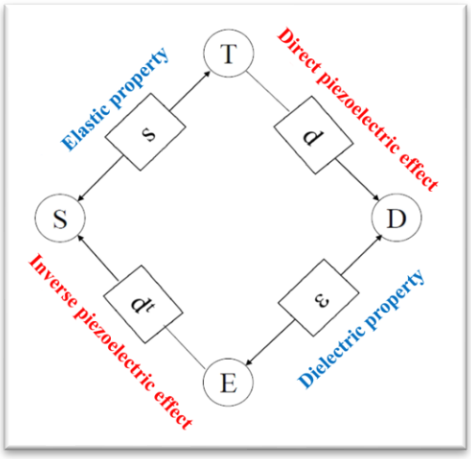

Figure 1.3. Relations between the different physical quantities.

The fundamental relations of piezoelectricity arise from the choice of the thermodynamic function to describe the free energy of the system. Since the piezoelectric coupling of the mechanical and electrical domains is considered in thermodynamics as a quasi-static energy transformation, the free energy can be determined from two appropriate parameters: one chosen from the mechanical domain while the other from the electrical domain. Hence four thermodynamic functions are achieved according to the following expressions [12]:

$$\begin{cases} S = s_E T + d^t E \\ D = dT + \varepsilon_T E \end{cases} \quad \text{Strain-charge} \tag{1.6}$$

$$\begin{cases} T = c_E S - e^t E \\ D = eS + \varepsilon_S E \end{cases} \quad \text{Stress-charge} \tag{1.7}$$

$$\begin{cases} S = s_D T + g^t D \\ E = -gT + \frac{D}{\epsilon_T} \end{cases} \quad \text{Strain-voltage} \tag{1.8}$$

$$\begin{cases} T = c_D S + hD \\ E = -hS + \frac{D}{\varepsilon_S} \end{cases} \quad \text{Stress-voltage} \tag{1.9}$$

The physical parameters E, D, T and S attached to the terms in the different equations correspond to the magnitude considered constant to determine the variable. The relationship between the piezoelectric constants (d, e, g, h) can be derived as:

$$\begin{cases} d = \varepsilon_T g = s_E e \\ e = \varepsilon_S h = c_E d \\ g = \frac{d}{\epsilon_T} = s_D h \\ h = \frac{e}{\varepsilon_S} = c_D g \end{cases} \tag{1.10}$$

Table 1.1 describes the matrix variables (tensors) used in the piezoelectric constitutive equations.

Table 1.1: Variables used in the piezoelectric constitutive equations.

Symbol	Matrix size	Units	Definition
T	6 x 1	$N.m^{-2}$	Stress components (σ_1)
S	6 x 1	-	Strain components (ε_3)
E	3 x 1	$V.m^{-1}$	Electric field components
D	3 x 1	$C.m^{-2}$	Electric charge density displacement components
s	6 x 6	$m^2.N^{-1}$	Compliance coefficients
c	6 x 6	$N.m^{-2}$	Stiffness coefficients
ε	3 x 3	$F.m^{-1}$	Electric permittivity
d	3 x 6	$C.N^{-1}$	Piezoelectric coupling coefficients for Strain-Charge form
e	3 x 6	$C.m^{-2}$	Piezoelectric coupling coefficients for Stress-Charge form
g	3 x 6	$m^2.C^{-1}$	Piezoelectric coupling coefficients for Strain-Voltage form
h	3 x 6	$N.C^{-1}$	Piezoelectric coupling coefficients for Stress-Voltage form

1.1.3. Piezoelectric materials

Before the discussion of different types of piezoelectric materials, it is necessary to distinguish the relationship between dielectric, piezoelectric, pyroelectric, and ferroelectric materials, as indicated in Figure 1.4.

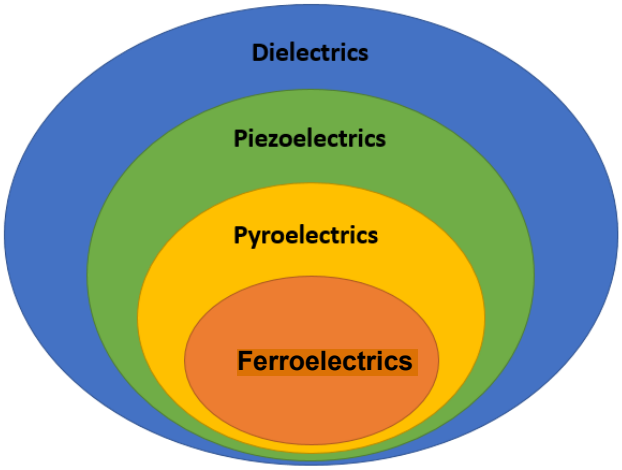

Figure 1.4. Schematic hierarchy of piezoelectric materials [13].

A *dielectric material* is an electrical insulator that can be polarized by an applied electric field [14]. When a dielectric is placed in an electric field, it becomes polarized – positive and negative charges are separated, producing a dipole with dipole moment given by the product of the charges and their separation distance. Among them, the *piezoelectric material* is a group of anisotropic dielectrics that exhibit the ability to generate the electric charge due to the application of stress or strain, or conversely the mechanical deformation due to the applied electric field. *Pyroelectrics* are a sub-class of piezoelectric materials, indicating the variation of polarization as a result of the change in temperature [15]. *Ferroelectric material* is a special case of pyroelectric material. Ferroelectrics have a spontaneous electric polarization which can be reversed by an opposed electric field [16]. Consequently, all ferroelectric materials are also piezoelectric, although not all piezoelectrics are ferroelectrics.

Piezoelectric materials have evolved rapidly since their discovery, i.e., mainly due to their development in various applications. To achieve desired flexibility and high sensing/actuating performance, researchers aim to explore materials that can undergo large deformations (low Young's modulus) with high piezoelectric coefficients.

In general, piezoelectric material can be classified into two classes: natural material, and manmade synthetic materials including single crystals, ceramics, and polymers. The major disadvantage of the natural piezoelectric material is the low sensitivity. Hence, artificial piezoelectric materials have been developed to overcome these limitations so as to improve the piezoelectric properties.

- Nature material

These crystals are anisotropic dielectrics with non-centrosymmetric crystal lattice. Crystal materials like Quartz, Rochelle salt, Topaz, Tourmaline-group minerals, and some organic substances such as silk, wood, enamel, bone, hair, rubber, and dentin come under this category [17]. The main drawback of the natural piezoelectric material is the low piezoelectric constant.

- Single crystal

The piezoelectric effect occurs in single crystals that lack a center of symmetry and thus exhibit the piezoelectric property. There are 32 crystal classes that can be divided into seven categories according to their point groups: cubic, hexagonal, trigonal, tetragonal, orthorhombic, monoclinic, and triclinic. Only 20 of the 32 classes have piezoelectric properties. Among them, 10 classes are polar, exhibiting a spontaneous

polarization without mechanical excitation, and the remaining 10 classes are no polar which only create polarization after subjecting mechanical stress. Quartz, the most popular single crystal piezoelectric material, has wide applications in transducers, high-frequency filters and frequency-controlling oscillators. It has excellent advantages like high mechanical strength of 2-3 GPa, temperature stability and high-voltage sensitivity, but exhibits low piezoelectric properties and dielectric constant [18].

- Ceramics

A ceramic is an inorganic solid material at room temperature. Piezoelectric ceramic is the general designation of ferroelectric ceramics with a piezoelectric effect through the polarization treatment of polycrystals made by mixing oxide (zirconia, lead oxide, titanium oxide, etc.) with high-temperature sintering and solid reaction. Barium titanate ($BaTiO_3$) was firstly synthetized as piezoelectric material after 1945. Piezoelectric ceramics such as lead titanate ($PbTiO_3$) and lead zirconate titanate (PZT) exhibit great potential in manufacturing due to higher piezoelectric constant as opposed to quartz [19]. With good mechanical and stable piezoelectric properties, piezoelectric ceramics have been widely used in sensors, the ultrasonic transducer, micro-displacement device, and other electronic components, etc. as an important force, heat, electricity, light-sensitive functional material. However, most ceramics are brittle, expensive, have a high electric loss and low stability, resulting in limitation in high-frequency systems.

- Polymer

Piezoelectric polymer materials are also referred to as organic lead-free piezoelectric materials. Piezoelectric polymer materials are commonly grouped based on their topology and dipole moment: bulk polymers, polymer composites, and voided charged polymers. In piezoelectric bulk polymers, the piezoelectric properties are determined based on the molecular structure. The most commonly explored piezoelectric polymers are poly(vinylidene fluoride) (PVDF) or its copolymer poly(vinylidene fluoride-*co*-trifluoroethylene) (PVDF-TrFE). PVDF has strong polarity, high d_{33} value (20–28 pC/N), excellent mechanical flexibility, biocompatibility, and low acoustic impedance [20,21]. However, piezoelectric polymer-based materials suffer limitations such as large leakage and low-temperature stability.

1.1.4. Piezoelectric composites based on $BaTiO_3$

Piezoelectric composites belong to the class of smart materials and typically consist of a piezoelectric ceramic filler incorporated in a piezoelectric polymer matrix (Figure 1.5). For other purposes, different type of fillers such as conductive or magnetic powders, could be used to elaborate composites [22,23]. Together with those particulate composites, laminated composites, in which the materials are prepared in a layered assembly for an easier implementation into specific devices.

The piezoelectric response is generally higher in piezoceramics and therefore makes them the most commonly used material. However, piezoceramics are naturally brittle, limiting the strain that it can provide or absorb without being damaged [24]. These materials are susceptible to the growth of fatigue cracks when subjected to high-frequency cyclical loads. On the other hand, there are piezoelectric polymers which are flexible, acoustically well matched to water and able to be produced in large areas and in a variety of shapes. Nevertheless, the low electromechanical coupling and lower dielectric constant limit their applications on an industrial scale. Therefore, composite appears as an alternative to improve properties when compared to single phase materials, being also able to produce comparable piezoelectric output performance [25].

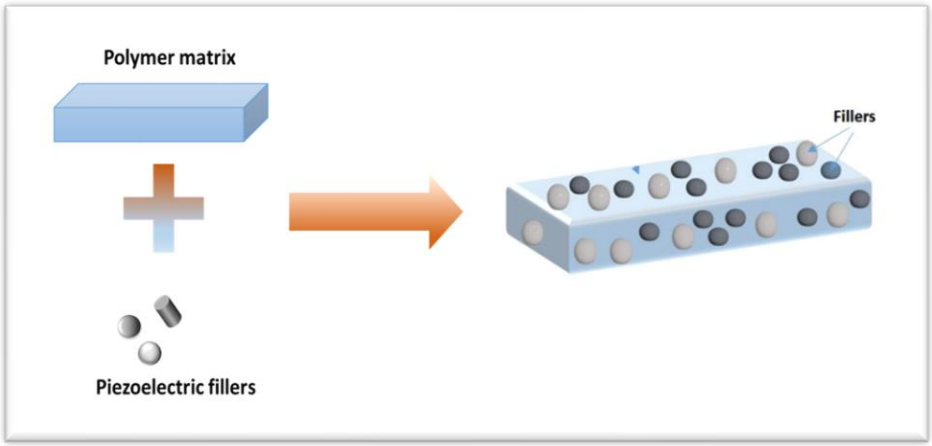

Figure 1.5. Schematic representation of piezoelectric composites.

The selection of polymer and fillers depends on the intentional use of piezoelectric composite. Polymer can be categorized into polar or non-polar, determined by the chain geometry [26]. For nonpolar polymers, under an alternating field, their dipole moments cancel each other which leads to a low polarization. Thus, nonpolar polymers usually have low dielectric constant (less than 3), e.g., polytetrafluoroethylene (PTFE), polyethylene (PE), and polystyrene (PS). By contrast, the dipole moments in polar polymers reinforce each other, resulting a high dielectric constant such as poly (methyl methacrylate) (PMMA), polyvinyl chloride (PVC) [27]. Besides the consideration of dielectric constant, the stiffness, viscosity, transparency, and curing condition should be carefully balanced for the selection of polymer matrix.

In the context of materials for printed electronics, photopolymerizable or UV curable polymers emerge as a good alternative to solvent or melting processing due to the advantages of photopolymerization process, including room curing temperature, curing times of minutes or seconds, reduced VOC (Volatile organic compounds) emissions and space and energy efficiency, among others [28]. To develop the piezoelectric ink, Polyurethane Acrylate (PUA), one of most popular photocurable resins based on the thermoplastic PU, is chosen as polymer matrix. PUA has attracted much attention in ultraviolet (UV) curable coatings attributed to its excellent flexibility, prominent adhesion on substrates, and a variety of adjustable features, ensuring adhesion on the metal surface of the bearing [29,30]. Significant results can be acquired when it is applied in coatings for metals or other electronic products [31]. Photopolymerization or UV curing represents a fast and solvent-free technique to obtain polymer-based composites, being one of the effective methods used in polymerization process. Up to now, just a few studies on UV curable dielectric materials have been reported, mainly focusing on their electrical properties [32,33]. Later, Mendes-Felipe *et al.* provided further characterization on morphological, thermal, mechanical, and dielectric properties of $BaTiO_3$/PUA composites as a function of the particles content and size [34]. However, none of them investigated piezoelectric properties of such materials, which is somehow of high interest in various sensing device applications.

Apart from polymers, fillers can be conductive [35], nonconductive [36], or magnetic [37]. Nonconducting fillers act as insulator, while conductive fillers are chosen to increase the effective electrical conductivity of composites at low concentrations. Besides, properties of composites can be tailored by fillers

shapes, sizes and concentration, which should be verified in the experiment. In this thesis, $BaTiO_3$ (BT) is selected as filler used in piezoelectric composite. BT was the first polycrystalline ceramic material ever discovered that exhibited ferroelectricity. During the 1950s, it was considered as a serious candidate for piezoelectric transducer applications and the basic phenomenological theory for the monodomain, monocrystalline state was developed. However, PZT, which possesses better piezoelectric properties and a higher Curie temperature (T_C), was discovered soon after. This development diminished the interest in BT for piezoelectric applications. It was not until 2009 that Liu and Ren reconsidered the potential of BT-based materials for piezoelectric applications. The outstanding piezoelectric properties found in Ca- and Zr-modified BT resulted in an even greater volume of work related to lead-free piezoelectrics. Consequently, a lead-free piezoelectric capable of replacing PZT in all commercial applications is still far from reality. However, the continuous research and development efforts have led to the commercialization of devices based on lead-free piezoelectrics and several prototypes have been tested [38–41]. Innovations based on lead-free piezoelectrics could position technology startups strategically or could assist manufacturers in diversifying their product portfolios. From a scientific point of view, BT-based materials are a very interesting research platform since their phase diagrams involve phase transitions at relatively low temperature, making them attractive for probing mechanisms of enhanced piezoelectricity. Also, several studies have reported that lead oxide as a component of PZT is toxic and adverse to the environment, so BT is a perfectly suitable alternative.

1.2 3D printing of the piezoelectric materials

Additive manufacturing (AM), or more commonly known as three-dimensional (3D) printing technologies, has been demonstrated as an effective pathway to fabricate functional polymer composites. Geometric flexibility controlled anisotropic properties, and advanced functionality of the printed composites open up opportunities for different applications. The printing of polymers, ceramics, and metals is the most promising research topic for more and more applications. In industries such as automotive and aerospace, 3D printing technology is used to make critical fixture parts [42]. In the application of wireless sensor, this approach enables researchers to produce unique sensors with integrated wireless capabilities. Printing polymers on PCB (printed circuit board) control panel can generate functional electronic components, such as wireless embedded sensors and integrated battery holders [43].

1.2.1. Introduction of printed electronics

Printed electronics is an all-encompassing term for the printing method used to create electronic devices by printing on a variety of substrates. As the demand for wearable devices and thinner electronics grows, printed electrics are being used to create flexible displays, antennas [44,45], sensors [46–48], actuators [49], soft energy devices, and so on [50,51]. The term printed electronics is often related to organic electronics or plastic electronics, in which one or more inks are composed of carbon-based compounds. These other terms refer to the ink material, which can be deposited by solution-based, vacuum-based or other processes. Printed electronics, in contrast, specifies the process, and, subject to the specific requirements of the printing process selected, can utilize any solution-based material. Therefore, with the development of also excellent application of piezoelectric material, it has been an interesting subject in the development of printed electronics.

Printed electronics technology has advanced over time, and inkjet printers can now print electrical circuits cheaply and quickly. In short, printed electronic is one of today's fastest growing technologies, and it is becoming indispensable in a variety of industries such as healthcare, aerospace, media, and transportation [52–54]. The development of printed electronics has made them increasingly popular due to their flexibility, cost-effectiveness, and security features, making them attractive to a variety of industries. Printed circuits have the potential to overcome the technical limitations associated with producing electronics on a large scale, resulting in fewer input materials and lower energy consumption. In addition, it opens up possibilities for previously impossible flexible devices. For instance, companies are using printed electronics to create unique printed signatures to identify banknotes, credit cards, legal documents, and other items [55,56]. Photovoltaics is another industry that is benefiting from these advancements [57]. Due to the lower cost of polymer, printed electronics have the potential to significantly alter solar power projects. Figure 1.6 clearly shows its benefits compared to those of conventional approach.

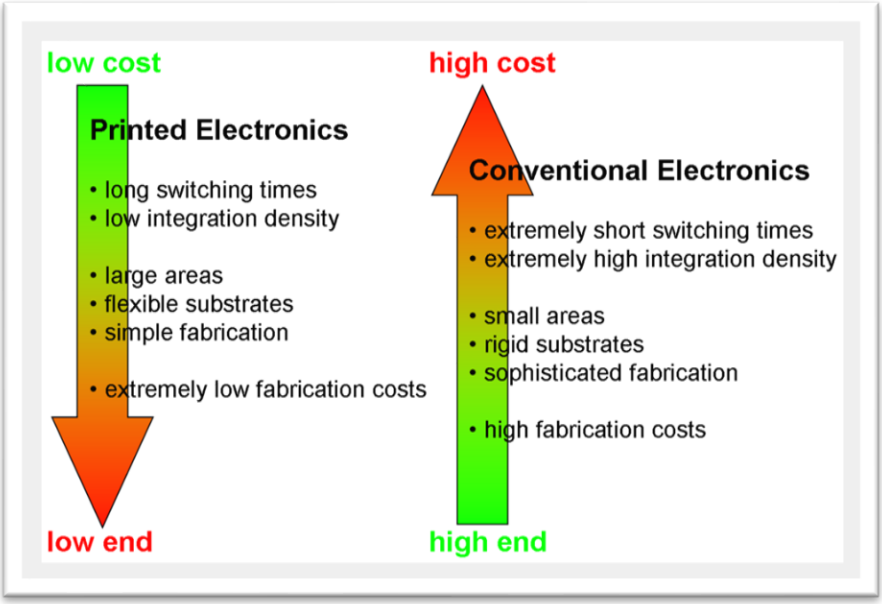

Figure 1.6. Benefits of printed electronics compared with conventional electronics.

1.2.2. Techniques used for printing piezoelectric materials

Piezoelectric material is a promising subject of printed electronics based additive manufacturing (AM). Indeed, it can definitely become an important element in the electrical circuit as a capacitor, sensor, actuator, electrode, etc. The attraction of printing technology for the fabrication of electronics mainly results from the possibility of preparing stacks of micro-structured layers (and thereby thin-film devices) in a much simpler and cost-effective way compared to conventional electronics. Also, the ability to implement new or improved functionalities (e.g., mechanical flexibility) plays an important role. The selection of the printing method is determined by requirements concerning printed layers, ink properties, substrate, as well as economic and technical considerations of the final products.

Printed electronics utilizes high throughput printing techniques, such as roll-to-roll gravure, flexography, inkjet, and screen printing of chemical solution processed electrically functional materials (conductive, resistive, semi-conductive and dielectric inks) for layer-on-layer fabrication of electronic

sensors, devices and circuits. Due to the wide range of printing technologies, the materials must meet certain requirements depending on the type of printing being performed and on the application.

Printed electronics technologies can be divided in contact and non-contact techniques as shown on Figure 1.7:

- contact techniques (screen printing, flexographic printing, gravure printing, etc.), in which the printing plate is in direct contact with the substrate.
- non-contact techniques (extrusion printing, aerosol printing, inkjet printing, etc.), where only the deposition material get in contact with the substrate.

Currently, contact printing technologies are widely used, but they are associated with high material waste and have limitations regarding the resolution and range of materials used such as substrates, inks, and solvents. On the other hand, non-contact printing technologies offer several advantages such as accurate pattern alignment, reduced risk of substrate contamination and damage, and the ability to work with various substrates including rubbers and polymers, which require low processing temperatures. Non-contact printing also simplifies the switching process as it only requires a digital image instead of a physical mask, without any additional costs. However, non-contact printing techniques face difficulties when completing multilayered devices, as they are prone to damage and deformation when exposed to thermal stresses and high-temperature processes.

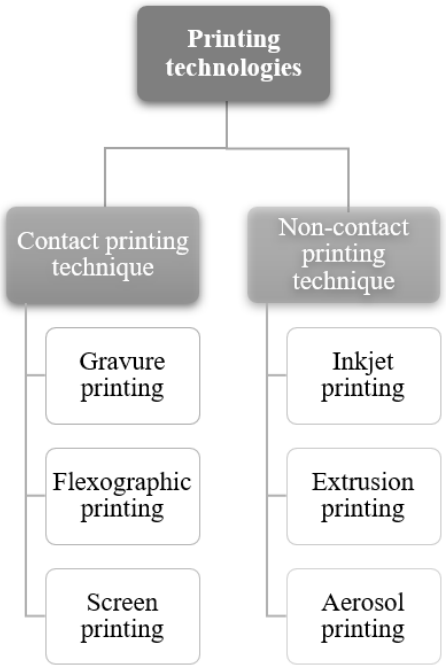

Figure 1.7. Printing technologies classification.

1.2.2.1 Gravure printing

Gravure printing is known for its high print quality, high print speeds, variable film thickness, use of low viscosity materials and simplicity of transferring the material onto the substrate. The gravure cylinder (image carrier), steel doctor blade, rubber impression roller, and ink fountain are the main components of the typical gravure printing process as shown in Figure 1.8 [58]. Chromium and copper coated steel are used in the manufacture of the gravure cylinder. The image carrier is etched electromechanically, chemically or

by laser to form an image area, which is usually made up of small gravure cells. The gravure printing transfers large amounts of material to the print area at high speeds with nominal distortion. As the cylinder rotates, it picks up material into the small cells and transfers it to the substrate with the impression cylinder. Then the doctor blade wipes the excess material remaining off the cylinder. The angle of the doctor blade also plays a key role in the print process. Transferring the material from the cells onto the substrate is assisted by the impression roller.

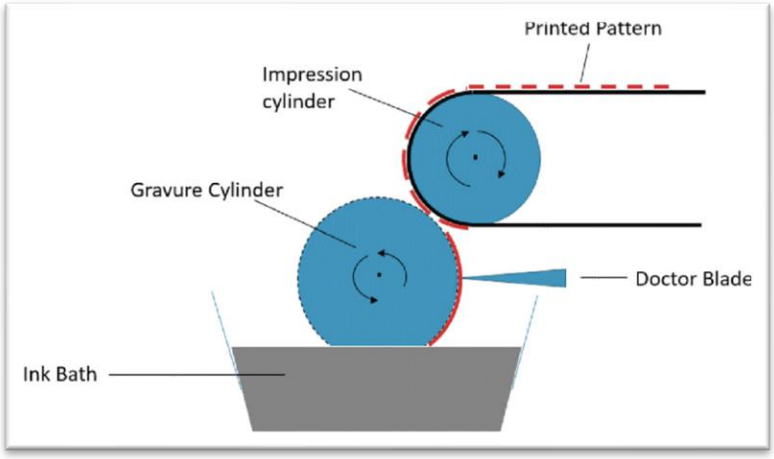

Figure 1.8. Principal schema of gravure printing.

1.2.2.2 Flexographic printing

Flexographic printing is known for depositing a wide range of thicknesses with the same resolution. In the flexographic printing technique, an indirect printing process uses the same nominal resolution plate with anilox rolls of different cell volumes. Impression cylinder, plate cylinder, anilox roller, doctor blade and inking unit are the main parts of the flexographic printing are shown in Figure 1.9 [59]. Proceedings used for the doctor blade and anilox roller is usually stainless steel. The flexible plate is made of either photopolymer or rubber. The image areas of the plate are raised with respect to the surface of the plate. The anilox roller transfers the material from the ink pan to the image areas of the plate cylinder. Transferring the material from the image areas onto the substrate is assisted by the impression cylinder.

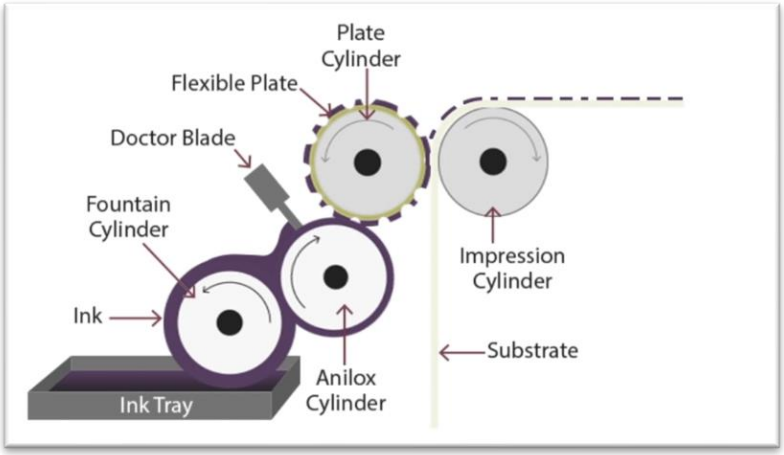

Figure 1.9. Principal schema of flexographic printing

1.2.2.3 Screen printing

Screen printing uses a porous mesh image carrier (screen), which yields thicker material deposits compared to other printing methods. Typical screen-printing setup is composed of a squeegee and screen-printing plate (including screen fabric, stencil, and frame) [60]. The materials used for the screen fabric and stencil vary depending upon the use of solvents and cleaning agents. Polyurethane is the usual material used for the squeegee. As illustrated in Figure 1.10, ink is deposited on top of the screen that is sweep with pressure by the squeegee. The material passes through the screen and transfers onto the substrate, which typically has the form of a single sheet.

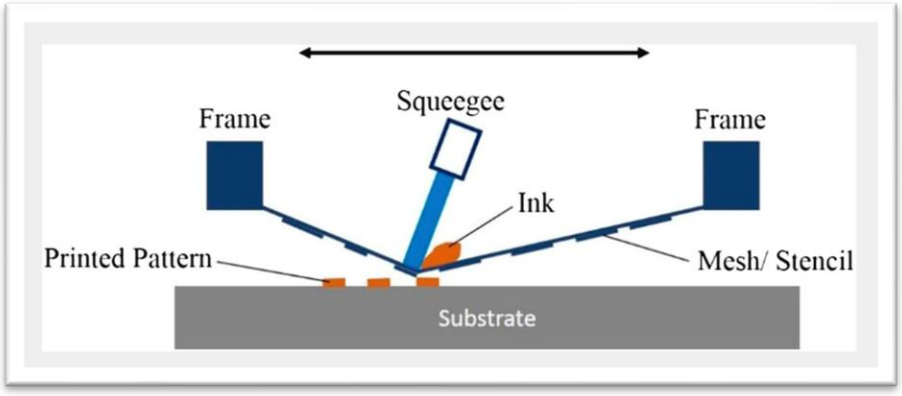

Figure 1.10. Principal schema of Screen printing.

Screen printing is a technology that has been often used for printed electronics. This technique produces large waste of production material (including ink). The biggest limitation is reflected in the level of resolution. Also, the planar system speed is low in comparison to other conventional printing processes [61].

1.2.2.4 Inkjet printing

The main advantage of an inkjet printing process is the no need for a physical mask or image carrier. Instead, inkjet printing uses a direct deposition technique and a virtual digital image carrier. Inkjet printing is known for thin ink deposits and is classified into either continuous inkjet or drop-on-demand inkjet based on the ink transfer method used. Drop-on-demand inkjet is further categorized as thermal inkjet and piezo inkjet printing processes. The deposited solution dried to form a very thin layer and the successive deposition of layers results in a high-resolution printed object. Figure 1.11 shows the principal of the inkjet printing technique [62].

Inkjets are flexible and versatile, but offer low throughput of around 100 m^2/h. It is thus well suited for low viscosity, soluble materials like organic semiconductors [63]. With high-viscosity materials, like organic dielectrics, and dispersed particles, like inorganic metal inks, difficulties due to nozzle clogging occur. Because ink is deposited via droplets, thickness and dispersion homogeneity might be reduced. Using many nozzles simultaneously and pre-structuring the substrate allows improvements in productivity and resolution, respectively. However, in the latter case non-printing methods must be employed for the actual patterning step.

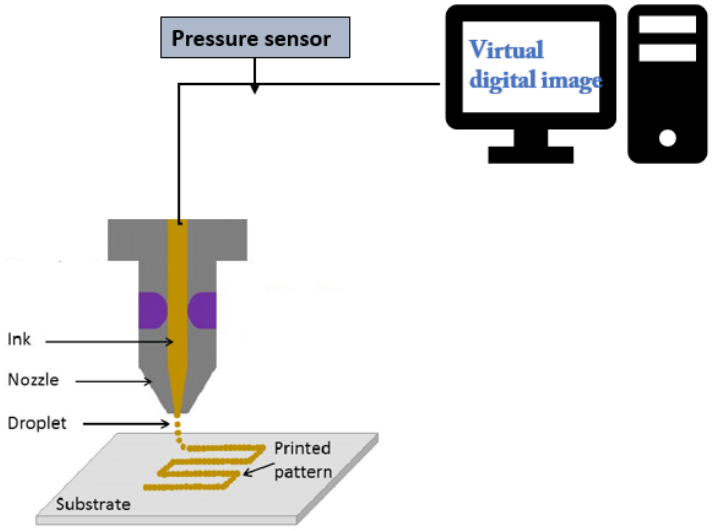

Figure 1.11. Principal schema of inkjet printing.

1.2.2.5 Extrusion printing

In extrusion-based 3D-printing technique (also known as robocasting), a filament of a paste-like material is extruded from a small nozzle moving across a platform [64]. Figure 1.12 illustrates the principal schema of extrusion printing. The object is thus built by printing the required shape layer by layer. Material (typically made of ceramic slurry or polymer paste with high viscosity) is then extruded through a small nozzle as the nozzle's position is controlled, drawing out the shape of each layer of the CAD (computer aid design) model. The material exits the nozzle in a liquid-like state but retains its shape immediately, exploiting the rheological property of shear thinning. Robocasting slurry-based technologies [65–67] enables low cost and accurate manufacturing without use of laser or photopolymerization methods. It is distinct from fused deposition modelling as it does not rely on solidification or drying to retain its shape after extrusion.

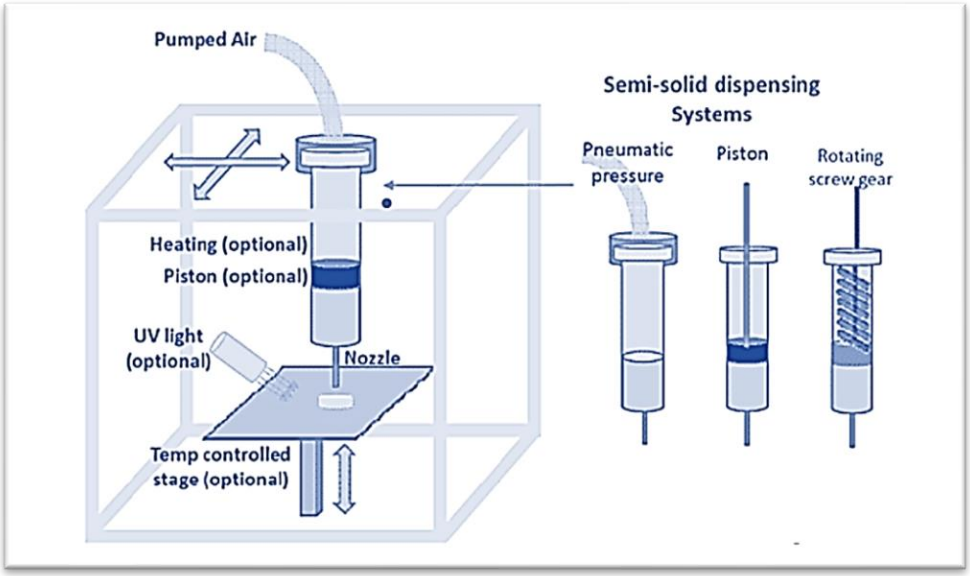

Figure 1.12. Principal schema of extrusion printing.

1.2.2.6 Aerosol Jet printing

Aerosol Jet Printing (also known as Maskless Mesoscale Materials Deposition or M3D) is another material deposition technology for printed electronics. The Aerosol Jet process begins with atomization of an ink, via ultrasonic or pneumatic means, producing droplets on the order of one to two micrometers in diameter. The droplets then flow through a virtual impactor which deflects the droplets having lower momentum away from the stream. This step helps maintain a tight droplet size distribution. The droplets are entrained in a gas stream and delivered to the print head. Here, an annular flow of clean gas is introduced around the aerosol stream to focus the droplets into a tightly collimated beam of material. The combined gas streams exit the print head through a converging nozzle that compresses the aerosol stream to a diameter as small as 10 µm. The jet of droplets exits the print head at high velocity (~50 meters/second) and impinges upon the substrate. Electrical interconnects, passive and active components are formed by moving the print head, equipped with a mechanical stop/start shutter, relative to the substrate [68].

Despite the high velocity, the printing process is gentle; substrate damage does not occur and there is generally minimal splatter or overspray from the droplets. Once patterning is complete, the printed ink typically requires post treatment to attain final electrical and mechanical properties. Post-treatment is driven more by the specific ink and substrate combination than by the printing process. A wide range of materials has been successfully deposited with the Aerosol Jet process, including diluted thick film pastes, conducting polymer inks, thermosetting polymers such as UV-curable epoxies, and solvent-based polymers like polyurethane and polyimide, and biologic materials. The principal schematic of aerosol jet printing is shown in Figure 1.13.

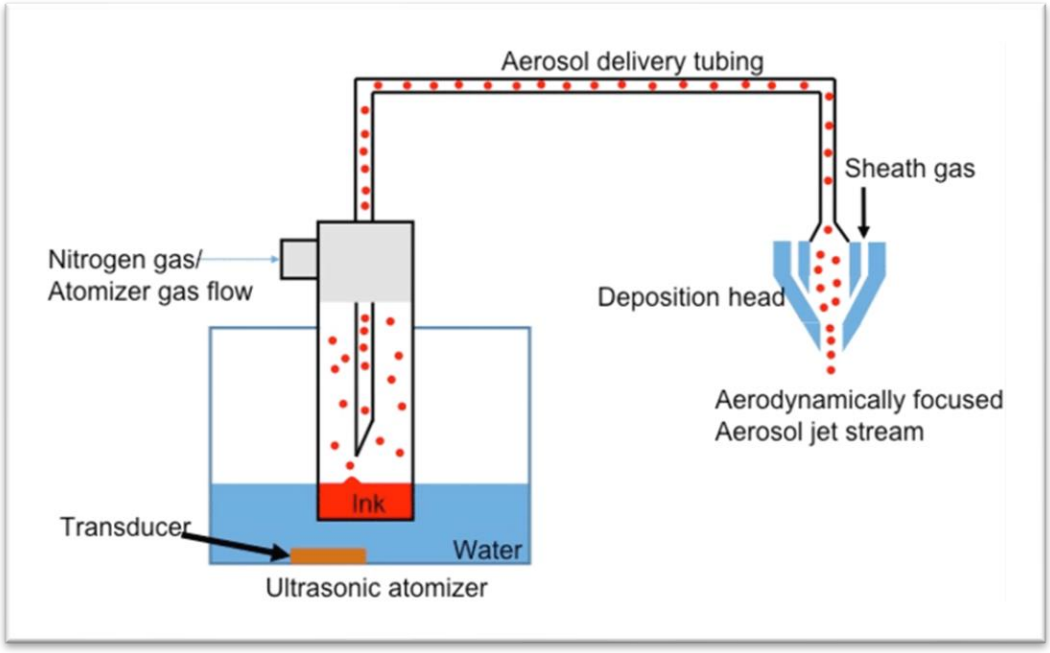

Figure 1.13. Principal schema of aerosol jet printing.

Even though printed electronics promise great advantages, there is a fair amount of effort required during its development. Selecting suitable inks and processes must be considered to maintain overall

compatibility of the printed layers' materials as well as to ensure reliable printed electronic structures. For instance, the relation between the surface energy of the substrate and surface tension of the material is critical. The choice of a suitable substrate is usually driven by cost, material drying/curing parameters, and end-user requirements. Some of the important properties of substrates include but are not limited to thermal and mechanical stability, flexibility, solvent resistance, surface roughness, surface energy, recyclability and resistance to moisture, gas and vapor transition (barrier properties). Polymer, paper, and glass are the typical substrates used in printed electronics. Another important factor to consider in printed electronics is complexity of the material. Viscosity of ink is one of the major factors considered in the print process. For instance, screen printing needs very high viscous material as opposed to inkjet print. So based on different piezoelectric composite, it has different techniques suitable.

1.3 Potential applications of printed piezoelectric composites

1.3.1. General applications

Piezoelectric composite materials are a class of materials that belong to smart and multifunctional materials. The ability to transduce mechanical to electrical signals and vice-versa provide their materials with increasing technological interest for the development of sensors and actuators or energy harvesters in the form of thin, flexible and potentially large area films. This material class combines the excellent properties of ceramic fillers and polymeric matrix, allowing high dielectric constant and piezoelectric coefficient and excellent thermal and mechanical properties, being successfully implemented in areas such as consumer electronics, aerospace and automotive applications or biomedicine.

1.3.1.1 Electronic application

Throughout history, technological advancements have been marked by the use of distinct materials, including stone, bronze, and the iron age. In today's world, the development of multifunctional materials is a key driving force behind technological progress. Piezoelectric materials are one such example, often cited for their versatility in the development of electronic devices. As the demand for sensors and actuators continues to grow in fields such as automotive and aerospace, the importance of piezoelectric materials in technological innovation is becoming increasingly apparent. [69,70]. Piezoelectric actuators are integral to various vehicle components, serving as a means of converting electrical signals into precise physical movements known as strokes. These strokes can be used to finely adjust lenses, mirrors, and other components, or even to trigger a hydraulic valve or act as a small volume pump. Piezoelectric actuators are ideal for applications that prioritize simplicity and reliability, as they require no maintenance and can be operated billions of times without experiencing any wear or deterioration. APC International manufactures a variety of actuators used in automobiles [71,72]. An example of piezoelectric on automotive application, as illustrated in Figure 1.14 (a), is an active vibration damping in helicopters [73].

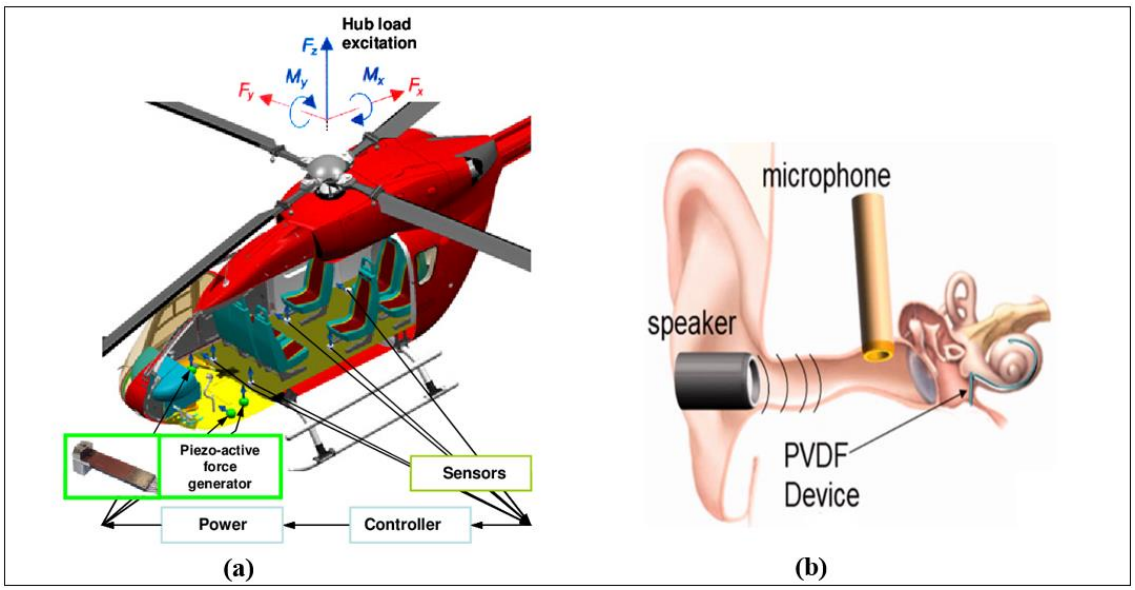

Figure 1.14. (a) Piezo active vibration and noise control in helicopters, (b) Piezoelectric microphones based on PVDF have been developed to detect sound inside the cochlea.

Piezoelectric actuators are utilized in systems to actively dampen vibrations in mechanical structures where vibrations are undesired. The design of vibration damping is aimed at decreasing noise, minimizing fuel consumption, and reducing energy waste. Although the reduction of sound levels in helicopter structures has been the focus of recent attention, this technology can be extended to other areas, including planes, wind turbines, motors, machine tools, laboratory tables (especially optical), and more.

Furthermore, composites composed of PZT embedded in PVDF polymer have been investigated as sensors in application like benders, tire pressure, and knock sensor [74–76]. Protection of spacecraft form radiation used in submarines, seismic and geological research are areas in which piezoelectric materials have been implemented, mainly in acoustic applications. Piezoelectric microphones based on PVDF have been developed to detect sound inside the cochlea, as shown in Figure 1.14 (b) [77]. Piezoelectric Parylene-C (ortho-chloro-p-xylene) polymer was also employed in microphones and actuators applications.

1.3.1.2 Energy harvesting

One way to incorporate piezoelectric transducers into structures is by directly integrating them into the composite layers or bonding them to the external layer. This allows for voltage sensing as a representation of the local strain experienced by the structure or for the generation of local stress, effectively utilizing the transducers as actuators. Moreover, due to the direct piezoelectric effect, which converts mechanical energy into electrical energy, specific energy harvesting circuits can retrieve electrical energy from dynamic mechanical loads during operational conditions for self-powered applications. The use of piezoelectric transduction has garnered attention in the field of electromechanical energy harvesting, where mechanical vibrations are converted into electrical energy [78]. ZnO nanowires, lead zirconate titanite (PZT) nanofibers, barium titanate ($BaTiO_3$) and PVDF are examples of piezoelectric materials that have been used to construct nanogenerators and to effectively power small electronic devices, such as lighting up LEDs [12,79]. Figure 1.15 shows a Vertical Nanowire Integrated Nanogenerator (VNIG) which is an energy harvesting device

capable of converting external kinetic energy into electrical energy via action by a nano-structured piezoelectric material [80].

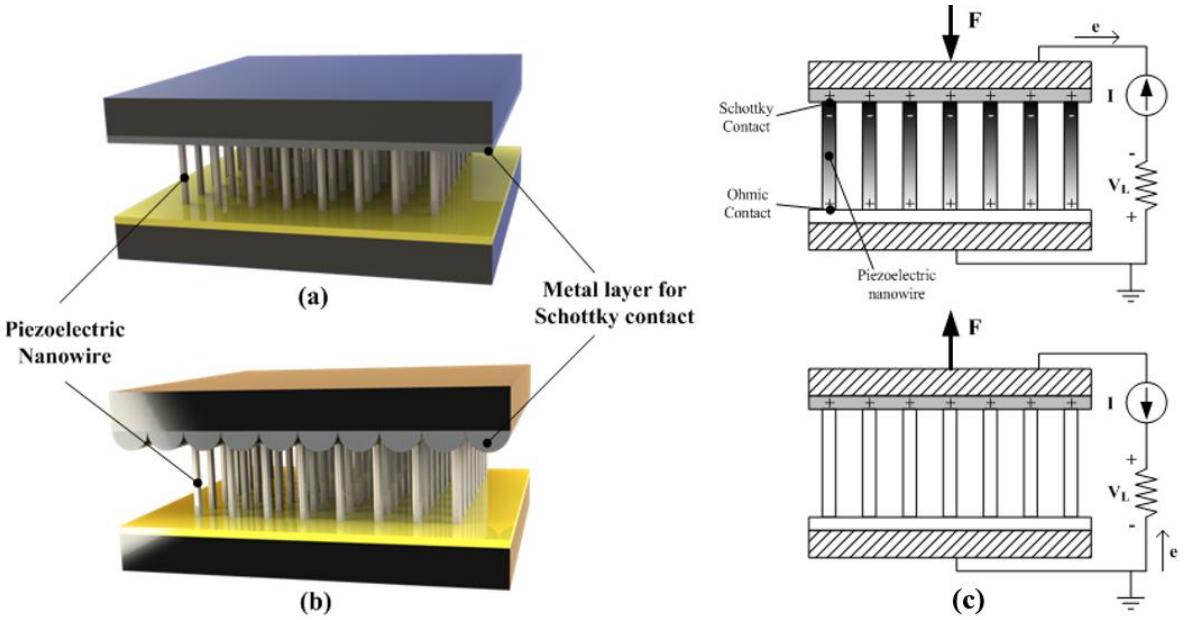

Figure 1.15. Schematic view of typical Vertical nanowire Integrated Nanogenerator: (a) with full contact, and (b) with partial contact, (c) working principle of nanogenerator where an individual nanowire is subjected to the force exerted parallel to the growing direction of nanowire.

Self-charging structures are primarily intended to power small electronic components, such as piezoelectric shoes, electronic skin, and other energy harvesting devices. These devices utilize the vibrations generated by human body activities like walking, running, breathing, and dancing to provide energy for low-power electronic devices [81]. The potential to capture the energy expended during biological processes as a means of powering low-energy electronic devices has also been investigated. The movement of the heart and lungs represents an endless supply of energy throughout one's life [82]. One of the first highlights in this area is related with the use of an implantable physiological power supply using PVDF films.

1.3.1.3 Environmental sensor

The impact of industrialization on the environment has raised serious concerns. The accumulation of pollutants in the air, soil, and water is a threat that requires urgent attention from the scientific community. Water remediation, in particular, is a critical environmental challenge. To address this issue, various approaches such as physical adsorption, biological methods, and chemical oxidation have been implemented on a global scale [83–85].

Piezocatalysis has been combined with photocatalytic oxidation for environmental treatment and purification. Piezoelectric materials generate an electric field that separates free electron-hole pairs, which can react with dissolved oxygen molecules and water to decompose organic pollutants. Extensive research has been conducted on materials such as ZnO, MoS2, and BaTiO3. For example, a MoS2/PDMS film was utilized as the negative layer of a piezocatalyst, while a copper thin layer acted as the positive electrode. Traditional battery technology has several shortcomings, but the triboelectric nanogenerator (TENG) offers an alternative solution. TENG can convert mechanical energy from hydropower and other natural sources

into electricity, enabling the creation of a clean and distributed energy network that benefits various wireless devices [86]. The active edge sites of the piezoelectric component provide a catalytically active surface that generates free radical oxygen, which can decompose pollutants. In addition to its role as a piezocatalyst and energy harvester, the composite can also serve as an active sensor for monitoring the flow of water and detecting its contamination [87].

Monitoring atmospheric conditions with dedicated sensors for organic and inorganic pollutants, potentially toxic elements, and pathogens is crucial for promoting sustainable development. Traditional methods of pollutant monitoring involve chromatographic techniques. However, due to their fast response times and high sensitivity to mass, piezoelectric resonators are increasingly used as chemical sensors for detecting components such as ions, molecules, and their fragments or clusters. [88].

A different type of environmental monitoring, although an application with added value, is the use of PVDF fibers with potential to detect stress and strain in the fluid flow, including oceanic current monitoring [89].

1.3.1.4 Biomedical application

A major focus of biomedical research is to improve quality of life through the development of monitoring devices and measuring equipment. One such device that has been developed for almost two decades is the piezoelectric nanogenerator (PENG). This device serves as an ideal power supply, collecting biomechanical energy from physiological activities such as muscle movement, heartbeat, respiration, and gastric peristalsis, and converting it into electrical signals to detect physiological/pathological indicators, stimulate nerves, pace the heart, aid in tissue repair, and control weight (Figure 1.16) [90].

The development of measuring equipment and health monitoring devices has been a significant effort in the biomedical area to improve the quality of life. Electronic skins, or e-skins, have emerged as a platform for continuous and real-time monitoring of human physiological signals, finding potential in prosthetics, robots, wearable devices, artificial intelligence, medical equipment, and other areas. Piezoelectric materials, such as ZnO, PVDF, and BaTiO3, play a crucial role in this field due to their flexibility, biosafety, and ease of processing [91]. In a study using a composite nanogenerator based on PVDF fibers, it was observed that the device could act as a sensor for real-time monitoring of radial artery pulse and respiratory information. Additionally, PVDF-TiO2 nanofibers demonstrated their potential applications in wearable healthcare monitoring systems and their ability for self-cleaning, as TiO2 can effectively degrade organic pollutants. A device for human motion monitoring was developed based on PVDF nanofibers with tetragonal-phase BaTiO3 NWs and a wireless circuit system. This device allows signals from human movement to be transmitted wirelessly and displayed on a mobile phone over a long distance of 8 m. The results demonstrate the potential of wearable medical electronics in the fields of rehabilitation and sports medicine [92].

Piezoelectric materials, when processed correctly, offer a robust biomaterial that can not only function as monitoring devices for bioelectronic and biomechanical purposes, but also have the ability to closely interact with biological tissues [93]. The field of tissue engineering aims to recreate cellular microenvironments through scaffold systems, both in vitro and in vivo. Piezoelectric materials have the potential to contribute to this field, as they can mimic the electrical and mechanical cues present in tissues. By using piezoelectric materials to produce scaffolds, researchers can create structures that act as actuators, influencing cellular behavior and promoting natural tissue formation [94]. PVDF and its copolymers have already proven their potential in bone, skeletal muscle and neural tissue engineering [95]. Furthermore, it

was confirmed that the incorporation of different fillers, such as cobalt ferrites (Co_2FO_4), magnetite (Fe_3O_4) or Terfenol-D in PVDF matrix or silk fibroin matrix, ensure the natural regeneration of bones. Another study with a copolymer of PVDF, P(VDF-TrFE) revealed that the incorporation of ZnO nanoparticles promote blood vessel formation (angiogenesis) – one of the main problems in tissue engineering approaches. This study also conclude that a composite scaffold favored its integration into the surrounding tissue when compared with non-composite scaffold [96].

There are many applications that piezoelectric composites may bring in the future. In this thesis, we take a focus on two different applications of such materials using screen-printing technique: structural health monitoring for bearing (in collaboration with SKF aerospace), and haptic for smart tactile screen (in collaboration with Volvo).

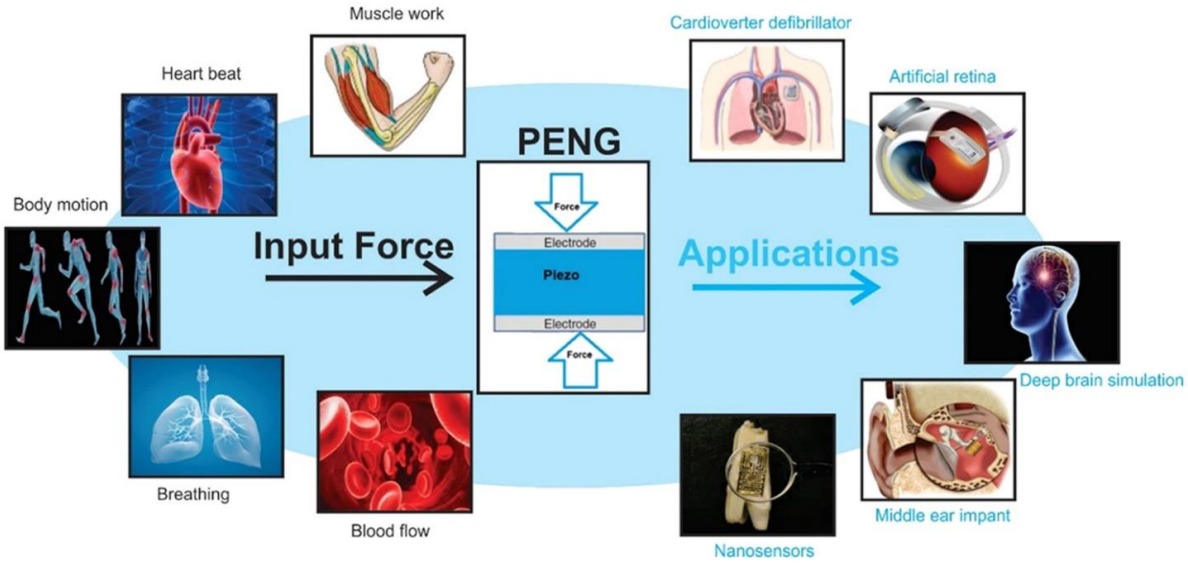

Figure 1.16. Potential application of piezoelectric nanogenerator in the biomedical area.

1.3.2. Structural health monitoring for bearing

Aircraft operators are continually striving to reduce both the amount and the cost of maintenance. While at the same time ensuring the aircraft safety, reliability and integrity are not usually compromised. One solution which has seen a lot of attention is known as condition monitoring, with the aim of developing the ability to detect, diagnose and locate damage, even predicting the remaining useful life of the structure or system [97]. In the field of aerospace, bearings are the key elements that are widely used as low friction joints between rotating components. Since the rotational motion is often a significant function of the overall system (such as wheels or rotor on an aircraft), proper functioning of a bearing over its designed life cycle is of vital importance to ensure product quality, prevent machine damage or even loss of human life. However, because of faulty installation, inappropriate lubrication, overloading, and other unpredictable adverse conditions, premature and sudden failures of individual bearings often occur in real world applications. For improved bearing health and safety monitoring, the research community has been investigating a wide range of topics related to bearing structural design, dynamics, tribology, fault detection, identification, and signal processing techniques. Various sensing and measurement technologies have been developed for improved monitoring of bearing operational parameters. Typical representatives

include acoustic emission meters, fiber optic monitors, and vibration spectrum analyzers [98,99]. To measure bearing vibrations, eddy current-based displacement sensors have been developed that can be mounted through or to the side of a bearing cap to monitor radial or axial shaft motion with respect to the bearing. Other types of bearing vibration sensors make use of velocity, acceleration, temperature, or spectral energy information [41,100]. While these efforts have considerably advanced the state-of-the-art of bearing condition monitoring, few of them have been widely used for practical, on-line applications. The need for an effective, reliable, and on-line bearing fault detection technique is primordial to detect and replace faulty bearings on several aircraft engines. This situation clearly indicates the need for developing an integrated bearing condition monitoring and self-diagnostic technique for on-line, in-process applications. Figure 1.17 shows the basic concept of a smart bearing.

In this research, we propose an alternative method to detect and predict early failure of bearing via direct indicator based on the use of piezoelectric composites (cf. Chapter 3).

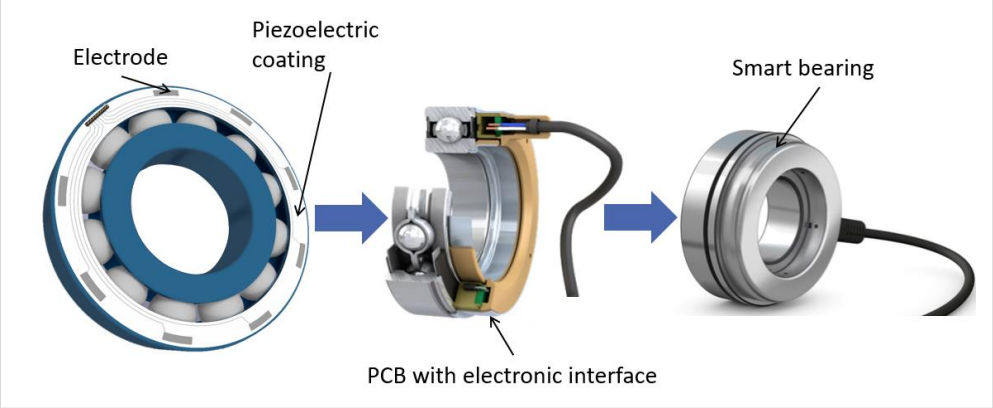

Figure 1.17. Concept of structural health monitoring based on piezoelectric composites.

1.3.3. Haptic for tactile screen

Haptic/Tactile feedback (or haptics) is the use of advanced vibration patterns and waveforms to convey information to a user or operator as illustrate in Figure 1.18. The word *haptic*, from the Greek, means “tactile, pertaining to the sense of touch” [101]. The idea of haptic dates back to the 90s but developed late because the simulation of tactile signals is quite complicated. Computers easily communicate visual and auditory signals but have difficulty with touch. Users can see images, type with the keyboard, hear sounds in the speaker, but cannot feel by touch what is happening inside the device. After much research, the challenge is solved by analyzing the composition of the sensation of “touch” [102]. Recent technological development has led to the invention of different designs of haptic devices, electromechanical devices that mediate communication between the user and the computer and allow users to manipulate objects in a virtual environment while receiving tactile feedback. The main criteria behind providing an interactive interface are to generate kinesthetic feedback and relay information actively from the haptic device. Sensors and feedback control apparatus are of paramount importance in designing and manufacturing a haptic device. In general, haptic technology can be implemented in different applications such as gaming, teleoperation [103], medical surgeries [104,105], augmented reality (AR) [106,107], and virtual reality (VR) devices [108,109]. This paper classifies the application of haptic devices based on the construction and functionality in various

fields, followed by addressing major limitations related to haptics technology and discussing prospects of this technology [102].

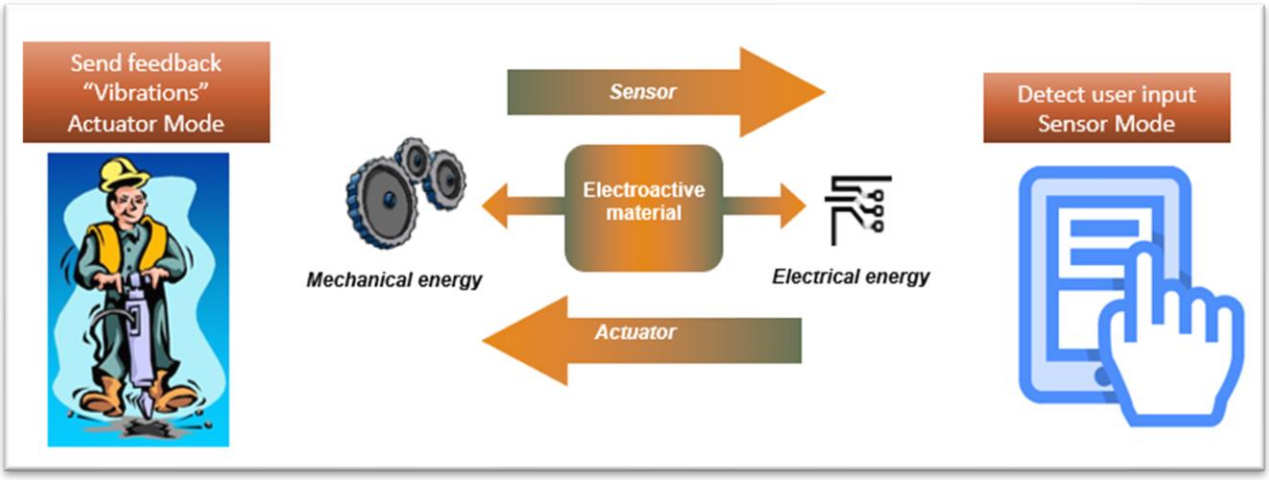

Figure 1.18. Haptic feedback diagram.

The most basic type of touch that the haptic system produces is vibration. The first generation of haptics often used electric vibration motors (like the vibration feature of mobile phones), the drawback of which was to vibrate the entire device. Innovative haptic systems enable location-specific vibrations with more varied frequency, duration, intensity, and tactile effects. Currently, haptic not only reproduces the sensation of touch when one interacts with a real object but includes all situations where the sensation of "touch" is generated. The executioner can be a person, a machine, or both; while the scenario environment can be real, virtual, or a hybrid. For example, human-machine interaction, virtual human-object interaction, remote controlled human-object interaction, or robot interaction.

Nowadays, haptic systems have multiple applications in video games, in medicine, in robotics, in automotive or in our personal computers (see Figure 1.19). In its simplest form, an example of a haptic is a mobile phone with virtual buttons that vibrate when touched by the user [102]. Engineers placed small voltage sensors under the display and designed the display to move slightly when a button is pressed. Vibration, screen movement, and synced sounds make it feel like pressing a real button. To a higher level, haptic allows the user to hold, grasp, pull, push, feel and interact with both virtual and computer-generated objects.

The automotive industry is rapidly adopting haptics in cars for a more intuitive driving experience. With integrated haptic sensors, drivers can control the car and detect directions. They can input data through touch and communicate vital information with their car. Widespread adoption of haptic technology in automobiles includes a touch-sensitive dashboard display that can send vibrating alerts. It eliminates noisy alarms and annoying lights [110]. For example, the steering wheel can vibrate to send an alert to the driver when it is necessary to change lanes, and the seats can send vibrating alerts when the driver is changing lanes slowly or is tired. Drivers can also adjust the temperature and music volume with a wave of their hand. The latest trend in haptic dashboards is capacitive touch technology. It eliminates the need for mechanical buttons and provides greater freedom of control.

In Chapter 4 of this manuscript, the development of printed piezoelectric composite as a haptic feedback system will be investigated, with the aim of demonstrating the great application potential of haptics.

Figure 1.19. Multiple applications of haptic feedback touchscreen.

1.4 Summary

Smart materials, capable of changing their properties as a result of external stimuli like mechanical stress or temperature variation, are manipulated to respond in a controllable and reversible way. Piezoelectric material fits this definition and more than a smart material, it is a revolutionary source for "green energy". The future of such a material is very promising, especially since it is constantly evolving and becoming more efficient and less expensive. The printed piezoelectric composite promises to make a lot of changes in the industry of piezoelectric material. With the development of several techniques in printed electronics, piezoelectric composites are able to be implanted on harsh surfaces with a complex shape.

Among the various types of piezoelectric material, piezoelectric composites based $BaTiO_3$ fillers is chosen for the development of printed ink because of its high permittivity, easy process, low cost, and commercial availability. Several additive manufacturing (AM) including gravure, flexography, inkjet, extrusion, and screen printing have their significant contributions in many scientific areas. In the case of their applications in structural monitoring, each technique has its unique qualifications but not free from limitations that affect the printing process and the final product. For example, inkjet printing is capable of fabricating a complicated structure with high-resolution printing degree, but the whole primary materials used to make the ink should comply with the sensitive requirements and obtain the suitable viscosity to prevent the nozzle blockage [111]. The flexibility and the material availability gave the

opportunity to the extrusion-based 3D printing to be the most used technique in the lab scale, allowing to quickly verify performance of the developed material. This technique has been intensively explored at the LGEF during the thesis of Z. Xiang [112] and K. Thetpraphi [113], as well as during my master [23]. The master report is available in the annex of this manuscript, which is somehow related to the work of my thesis as both dedicated to printing of multifunctional materials for structural health monitoring. Nonetheless, in the thesis, screen printing technique based on industrial process (performed by Arc en Ciel Sérigraphie, ZI LE Forestier, 42630 Regny, France) is used. All architecture of sensor together with design of masks are developed by the LGEF. The following chapters give a detail of this work.

Chapter 2. Fabrication process and characterization methods

Our main objective is to study and characterize the properties of piezoelectric materials in bearing-load monitoring (direct effect as sensor response) and haptic applications (inverse effect as actuator response). To carry out these studies, it is important to determine the methods to approach tasks or problems, and it is necessary to draw the process of the actions required. In this chapter, we start with the design architecture based on several key rules of sensor networks to ensure system efficiency. Then, the choice of materials for the fabrication of piezoelectric composite ink together with the manufacturing steps of screen printing are presented. All experimental characterization tools used in this work are also performed, i.e., followed by a full description of finite element setup built for both sensor and actuator models.

2.1. Architecture design of sensor coating

In aeronautic field, bearings are among the most stressed components of aircrafts and are a frequent source of failure. Providing the best availability of aircrafts is a key driver in aeronautics industry. Monitoring system able to detect signs of failure before they happen, thanks to sensors and diagnosis/prognosis algorithms, is of primary significance for improving aircraft operability [114]. The usual failures that can be encountered are: improper lubrication, corrosion, contamination, etc. In most cases, bearing defects are manifested by a more or less material removal on a mat surface like inner/outer ring, or even rolling elements [115,116]. They generally lead to several mechanical effects in machines, especially an increase in the load applied to the rolling elements. Therefore, in this chapter, characterization methods of bearing-load monitoring based on the use of smart sensor coating is investigated.

First, we focus on the architecture design of the system that could have impact on the sensing performance. The innovative idea involves in the implementation of a piezoelectric coating on the outer ring of the bearing, [117], allowing for a direct monitoring of load applied to the bearing surface and hence enabling early detection of irregularities. Then, fine electrodes are added, and together with the metallic bearing surface, they complete an electrical circuit that allows for the characterizations of the electromechanical response of piezoelectric sensors. Last but not least, a network of conductive tracks (CTs) and electrical connectors are also implemented, accompanied by an integration of a dielectric layer so as to prevent from any undesired parasites. The concept of a smart bearing illustrated in Figure 2.2 points out that the piezoelectric layer covers most of the surface of the outer ring, whose deformation induced by load are monitored via the surrounded electrodes linking to an electrical connector. For a sake of simplicity, characterization tests are performed on piezoelectric layer coated on the flat substrate, which was used to simulate the mechanical system of a bearing outer ring.

2.1.1. Unidirectional (1D) and bidirectional (2D) sensors

First of all, a rectangular-shaped substrate is used to test a unidirectional (1D) sensor device. Figure 2.1 illustrates the architecture design of the entire system, which consists of a steel substrate and three printed layers such as dielectric layer, piezoelectric sensor, and conductive tracks (CTs) together with circular electrodes. The electrodes and CTs are made of LOCTITE ECI 1010 E&C ink (i.e., commercialized by Henkel – France technology), with good adhesion, high electrical conductivity, and viscosity of approximately 9 Pa.s adaptable to printing technology. The 20 µm-thickness and 15mm-diameter electrodes are deposited on the sensor surface while the CTs (with 0.7 mm width and similar thickness) are deposited on the dielectric layer (made of PUA) to prevent any measure perturbation caused by nonnegligible CT's length. If the CTs were directly printed on the sensor layer, it would lead to an increase in the active surface and thus an overestimation in the piezoelectric sensitivity. Experimental test in next Chapter will identify the influence of the CTs on the piezoelectric performance, allowing to confirm whether or not the dielectric layer is necessary.

Logically, the size and the shape of the electrode would not affect the sensing performance of the coating, as the piezoelectric sensitivity (expressed by d_{31} or d_{33} coefficient) is related to the intrinsic dielectric and mechanical properties of composite itself. Actually, the dielectric characteristics strongly depends on the fillers while the mechanical behavior is mainly governed by the polymer matrix. In other words, d_{31} or d_{33} coefficients should be unchanged, regardless of which size and shape of electrode are

chosen. Nonetheless, the size of electrode might have an impact on the precision of experimental characterization. On one hand, too small electrode area (denoted as S_e) results in low capacitance and thus low charge measurements of the sensor. This leads to considerable measure uncertainties, making the output signal more sensible to any perturbations (e.g., noise signal, electrostatic effect of environment). On the other hand, too large S_e could decrease the spatial resolution of the sensor mapping, making it difficult to accurately determine local load application. For sample designed with CTs, the selection of electrode's size must be further considered to comply with the compromise of design. Actually, the electrode area (S_e) should be large enough with respect to the CT's one so as to diminish its negative impact. In contrast, S_e would not be so large to reserve sufficient place for the CT patterns, which becomes critical when the number of CTs increases. Concerning the electrodes' shape, it would not affect significantly the 4-point bending (4PB) test performance. Indeed, within the inner load application, the 4PB configuration impose a homogeneous mechanical strain on the coating electrodes along the length direction of the substrate (c.f. detailed in 2.5.3) [30]. Therefore, the generated electric signal is revealed to be similar among those electrodes, whatever their shape. As a matter of fact, if the electrodes have different shapes but the same surface area, their output charge measurement would be the same, and so are their piezoelectric response.

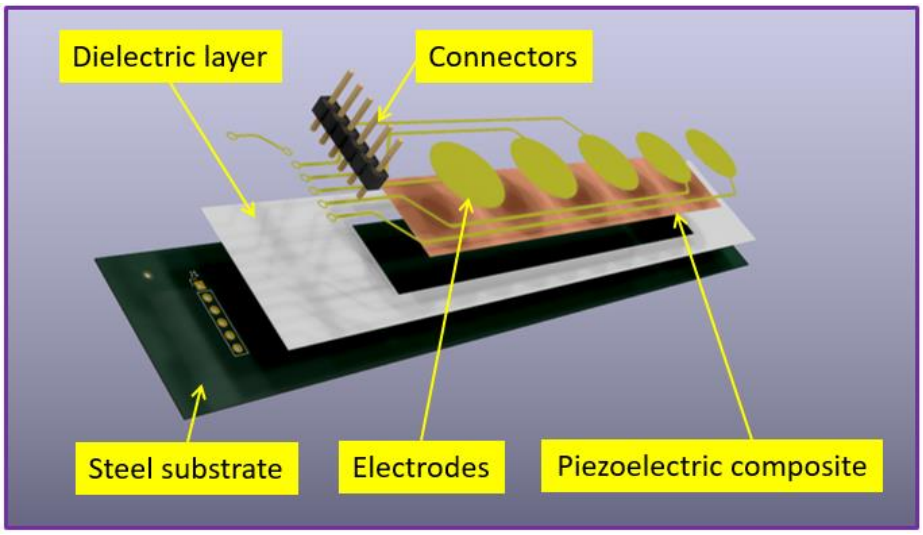

Figure 2.1. Architecture of piezoelectric sensor for condition monitoring of a 1D substrate.

In bearing, there is always a rolling element and it is thus necessary to monitor not only the magnitude of the load but also its directions, for easier maintenance [118]. *Radial load* (also known as transverse force) is perpendicular to the shaft's longitudinal axis, whereas *axial load* (or thrust load) is parallel to this axis. Some bearings can withstand a combination of radial and axial loads applied to the shaft, to some extent [118]. Usually in a bearing system, rolling element is subjected to periodic deformation (local deformation) occurring on the outer ring, in addition to the deformation due to the external force. Thus, during the rotational motion of bearing, maximum deformation occurs when the rolling element is co-axial (in phase) with the sensor (measurement point of charge displacement), while minimum deformation occurs when they are is out of phase. Therefore, it is necessary to evaluate the effects of loading in both directions.

As illustrated in Figure 2.2, a cross-shaped substrate coated with a piezoelectric sensor was also developed in this study to examine the performance of loading in two directions (axial/radial) on the characteristics of the tested sample. The steel cross substrate was used to simulate the mechanical property of a bearing. Three thin layers are also printed on the cross substrate such as dielectric layer, piezoelectric sensor, and conductive tracks (CTs) together with electrodes. But there are some differences on dimension compared to the 1D substrate. The electrodes, designed with a circular (12 mm diameter) or rectangular (12×3 mm^2) shape in a 10 µm thickness, is deposited on the piezoelectric layer. The CTs (with similar thickness, 0.7 mm width) are also printed on the dielectric layer (DL) to prevent any measure perturbation caused by their nonnegligible length. The influence of the CTs as well as the efficiency of the DL are discussed later in Chapter 3.

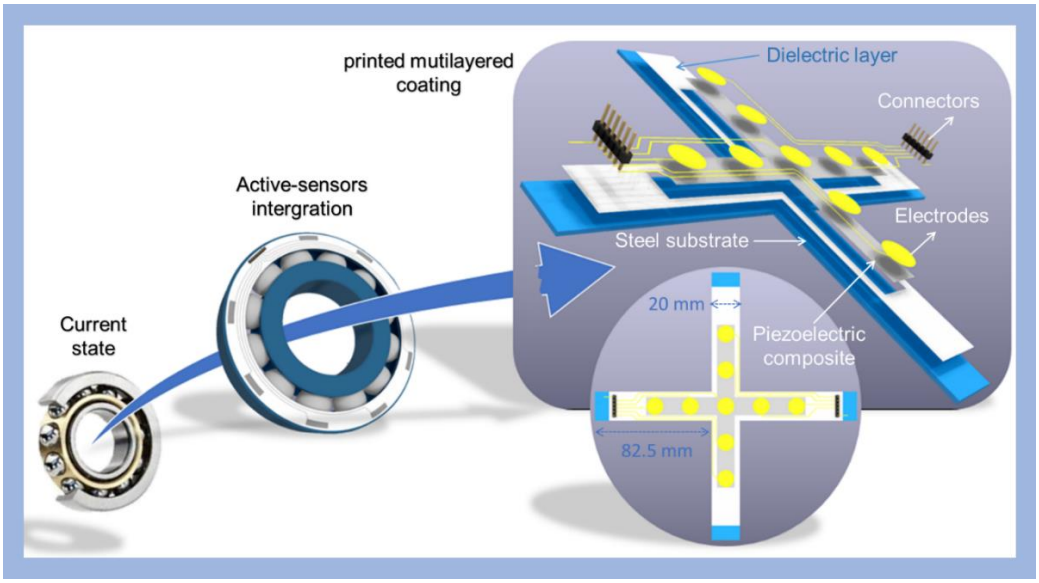

Figure 2.2. From the current state of bearing to a new generation coated with bidirectional printed sensor for condition monitoring.

2.1.2. Rules of sensor network design

Not only affected by mechanical changes, the system also acts as an electrical network where change in electric field is critical for sensor's life and performance. Accordingly, to ensure the accuracy and stability of measurement as well as the durability of the printed components, the developed prototype must meet requirements of basic electronic design rules. The four principal rules, as summarized in Figure 2.3, set specifies certain geometric and connectivity restrictions to ensure sufficient margins to account for variability in AM process, so as to ensure that the sensor device works correctly [119].

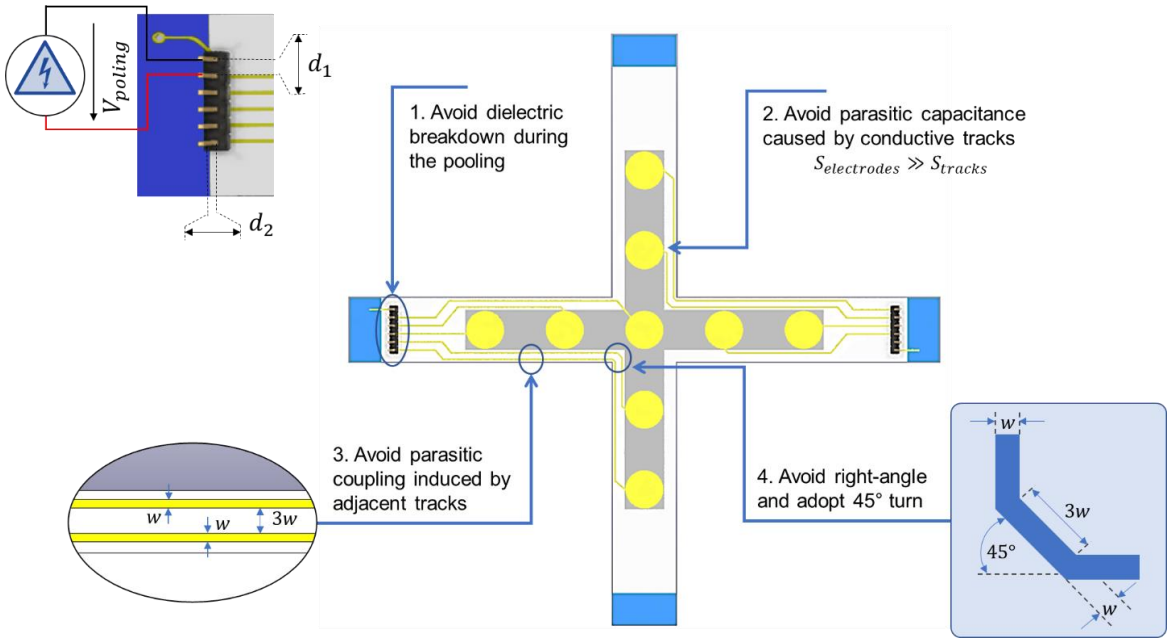

Figure 2.3. Four principal rules of sensor network design.

1) *Could the applied voltage during polarization cause any arcing in the air ?* The first rule, given to avoid dielectric breakdowns during polarization, concerns the space of pin connector (namely *spacing rule*). In our case, the sample is polarized under a poling field of $E_p = 6V/\mu m$ (at 80°C for 20 min). Considering a 20-µm-coating thickness, the applied bias voltage is thus equal to $V_p = 120V$. The permittivity of an ideal dielectric (e.g., air) is revealed to be constant, nonetheless, with a strong enough electric field, all practical dielectrics fail in this respect. The failure is typically abrupt and is noticed as a sharp rise in conductivity, indicating that electrons are successfully ejected from their host molecules. The threshold value of the electric field intensity at which this occurs is known as dielectric strength, and the sudden change in behavior observed with an electric field greater than the threshold value is known as a dielectric breakdown. *Typical dielectric breakdown* of the air is considered to be 3 V/µm. Such a critical value should be avoided at all costs by verifying whether or not the distance between two adjacent pins (denoted d_1), and the one between pin and ground substrate (denoted d_2) are not too small to provoke any breakdown. As the chosen connector has a pitch of 2.54 mm and an enclosure of 0.8 mm (typical parameters of commercialized available connector), the corresponding electric fields are calculated as:

$$d_1 = 2.54\ \text{mm} \rightarrow E_1 = \frac{V_p}{d_1} \approx 0.05\ \text{V/µm}$$
$$d_2 = 0.8\ \text{mm} \rightarrow E_2 = \frac{V_p}{d_2} \approx 0.15\ \text{V/µm} \quad (2.1)$$

These values are obviously far from the critical breakdown occurring in the air (3 V/µm), so the chosen connector entirely meet the requirement of the *spacing rule*.

2) *Does the capacitive effect induced by conductive tracks (CTs) matter the measurement ?* To prevent parasitic capacities that could disturb measurement, the second rule focuses on the relationship between the surface of electrodes and the one of CTs [120] (namely *surface rule*). It is well-known that parasitic capacitance is usually unavoidable existing between the parts of electronic component or circuit simply due to their proximity. When two different voltage electrical conductors (like CTs) are close together, the electric field between them somehow causes a stored electric charge, which is the main origin of parasitic capacitance. To reduce its impact, it is necessary to ensure that the surface of the sensor (i.e., electrode, denoted S_e) is much larger than that of the CTs (denoted S_t). The ratio (r_C) between the sensor's capacitance (denoted C_e) and the track's capacitance (denoted C_t) can be expressed as:

$$r_C = \frac{C_e}{C_t} = \frac{\varepsilon_{composite}}{\varepsilon_{dielectric}} \times \frac{S_e}{S_t} \times \frac{d_t}{d_e} \tag{2.2}$$

where d_t (~ 10 µm) and d_e (~ 20 µm) are the thickness of the track and the electrode, respectively. Even though the permittivity of the dielectric layer (denoted $\varepsilon_{dielectric}$) is much smaller than that of the composite (denoted $\varepsilon_{composite}$) [121], to ensure that $C_{sensor} \gg C_{track}$, each electrode must have significant area as opposed to its own track liking to the connector. In practice, r_C is chosen greater than 10 to minimize the parasite effect. In anyway, the *surface rule* might be fulfilled, even in the case of electrode associated with the longest track.

3) *How to avoid parasitic coupling induced by adjacent tracks* ? The third rule is dedicated to the separation between two adjacent tracks with respect to their own width (*spacing rule*). When two electrical circuits are in the vicinity of one another, a signal propagating in one circuit can induce a signal in another circuit, due to capacitive (electric field) and/or inductive (magnetic field) coupling between them. This phenomenon is referred to as crosstalk. The general rule says that the separation between the tracks should be at least $3w$, where *w* is the width of the track. This practice helps to reduce crosstalk and coupling between adjacent tracks on the same layer [122,123]. For specific application relating to instrumentation of bearing system, compactness is one of primary criteria. Respecting *spacing rule* is a true challenge, especially when the number of sensors and tracks is important. A compromise must be taken in consideration for achieving properly reliable measurement as well as high sensing performance.

4) *How to deal with track's conner ?* The last rule concerns critical position where CT encounters an important bend (namely *angle rule*). While single discontinuities such as sharp corners make minor difference, cumulatively, they have a significant impact. A sharp track corner creates shunt capacitance to the ground plane, which degrades insertion loss and increases the capacitance. This phenomenon results in the change of characteristic impedance that involves reflections of signal, particularly in a high-frequency domain [124,125]. Therefore, track corners should be as round as possible with a radius no tighter than the differential pair separation. If smooth curves are not possible at the corners, a design with cumulative turns of 45° could be acceptable.

2.2. Material selection and ink formulation

Electronic circuits require specific functional characteristics, and this continues to be a challenge for printing techniques. In order to overcome this challenge, two different approaches can be distinguishing: process engineering where the currently existing materials are tailored in terms of shape, geometry and interconnectivity [126–131], or material engineering where new materials with tailored functional characteristic for each application are developed [132–134]. In particular, for ferroelectric materials, the main approach for tailoring electromechanical coupling is to include bulk fillers with large piezoelectric constant into polymeric matrix [135–137]. Polymers offer advantages such as easy processability or good mechanical properties, while ceramic filler provide high piezoelectric features. The most used ferroelectric filler for this purpose is barium titanate, $BaTiO_3$, crystallizing in perovskite structure, as it is a lead-free ceramic with high dielectric and piezoelectric constant (ε), depending on its purity, grain size, temperature or preparation method [138]. In the case of polymers, polymethylmethacrylate [139], polyetheretherketone (PEEK) [140], polystyrene [141], or polyvinylidene fluoride (PVDF) [142] have been used for the developments of those composites.

In the context of materials for printed electronics, photopolymerizable or UV curable polymers emerge as a good alternative to solvent or melting processing due to the advantages of photopolymerization process, including room curing temperature, curing times of minutes or seconds, reduced VOC (Volatile organic compounds) emissions and space and energy efficiency, among others [28]. To develop the piezoelectric ink, Polyurethane Acrylate (PUA), one of most popular photocurable resin based on the thermoplastic PU, is chosen as polymer matrix. PUA has attracted much attention in ultraviolet (UV) curable coatings attributed to its excellent flexibility, prominent adhesion on substrates, and a variety of adjustable features, ensuring adhesion on the metal surface of the bearing [29,30]. Significant results can be acquired when it is applied in coatings for metals or other electronic products [31]. Photopolymerization or UV curing represents a fast and solvent-free technique to obtain polymer-based composites, being one of the effective methods used in polymerization process. Up to now, just a few studies on UV curable dielectric materials have been reported, mainly focusing on their electrical properties [32,33]. Later, Mendes-Felipe *et al.* provided further characterization on morphological, thermal, mechanical, and dielectric properties of $BaTiO_3$/PUA composites as a function of the particles content and size [34]. However, none of them investigated on piezoelectric properties of such materials, which is somehow of high interest in various sensing device applications.

In this study, the piezoelectric ink, developed according to a collaboration between LGEF and VFP Ink Technologies, should fulfill the following specifications:

- Compatible to 3D printing additive manufacturing (AM): easy manipulation (adequate viscosity and dispersion), and good adhesion with the surface of the steel substrate.
- Durable: abilities of withstanding handling, heat, moisture, and other environmental factors.
- Cost effective of materials and printing process.

The ink is formulated based on the functionalization of Barium titanate ($BaTiO_3$) spherical nano-powder, with the aim of preventing agglomerations when suspended in the ink matrix [143,144] . The nano-powder $BaTiO_3$ were purchased from Inframat^{00} Advanced Materials TM (Product # 5622-ON7), with a purity of 99.95 % and a density of 5.85 g.cm^{-3}. As seen in the SEM (Scanning electron microscopy) pictures of Figure 2.4, the particles are quasi-spherical, with an average size of around 600–700 nm. These particle sizes seem

to be the best compromise between material dispersion and performance in electromechanical conversion [145]. Indeed, the composite piezoelectric activity decreases for particles size lower than 300 nm due to the loss of the tetragonal phase [146] .

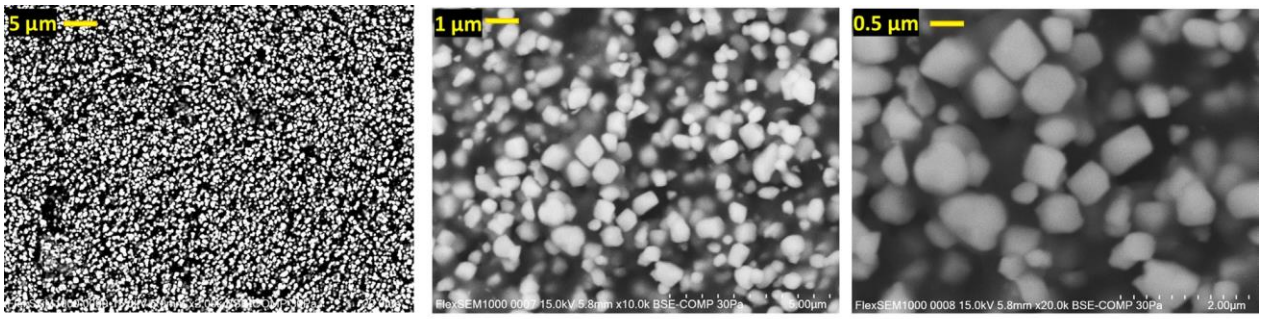

a) b) c)

Figure 2.4: SEM image of $BaTiO_3$/PUA composite with different magnifications: a) x2k; b) x10k; c) x20k.

2.3. Fabrication process based screen-printing technique

2.3.1. Piezoelectric sensors used for condition monitoring (CM) of bearing

To achieve full performance of bearing's CM, the developed sensor must fulfil the following criteria: mechanical flexible, adaptable to different sizes and shapes, cost-effective, easy process, and low environmental impact. In that situation, printing technique becomes a viable option for achieving the deposition of multiple-layered materials in additive manufacturing (AM) that are of various sizes and shapes [49]. Particularly, among the various methods currently in use [23,46,47,145,147], screen printing appears to be a quick, effective, straightforward, durable, and inexpensive process that may be used on an industrial scale [60,61,148]. In our case, the conception of flat substrate with multiple layers of different materials is revealed to be perfectly suitable to AM using screening printing.

Figure 2.5a-d illustrates the fabrication of multilayered piezoelectric sensor coated on a steel substrate. The three layers are screen printed via an industrial process piloted by ACE (Arc en Ciel Sérigraphie). The printing machine is a ¾ automatic ATMA AT600H/E composed of a mesh screen, inks, and a squeegee to transfer a stenciled design onto a flat fabric surface. The printed layer thickness as well as the pattern definition depend on the fabric nature and the mesh. Regarding the prototype design, the printing frame is chosen with 230 meshes and the fabric is made of polyester. Corresponding to each layer, a suitable ink is used, comprising PUA polymer ink (used for the dielectric layer), $BaTiO_3$/PUA composite ink (used for the piezoelectric layer), and silver ink (used for the electrode and conductive tracks). Each layer requires a specific curing process. The best electrical properties of the electrode are met by performing thermal curing of the conductive silver ink in a drying oven (SIEBDRUCK TRO II) between 100 and 150°C. For the dielectric layer, the excellent insulating characteristics require an UV curing at a 500 mJ/cm² power, carried out in a tunnel (SILAIR). To achieve optimal properties such as resin curing, the piezoelectric layer must be also exposed to a UV light (405 nm wavelength), with lower power of 300 mJ/cm² of irradiance, then undergo at room temperature. The proposed printing technique allows to create a very thin film sensor, at the order of 20 µm, leading to an easier polarization process and reduced breakdown probability [149,150].

The final customized product is shown in Figure 2.5e, including five identical piezoelectric sensors numbered from 1 to 5. A 6-pin electrical connector is implemented on the extremity of the dielectric layer, linking to the conductive tracks. The distance between two successive pins is large enough (~ 2.54 mm) to avoid any electrical arc in case of high voltage application.

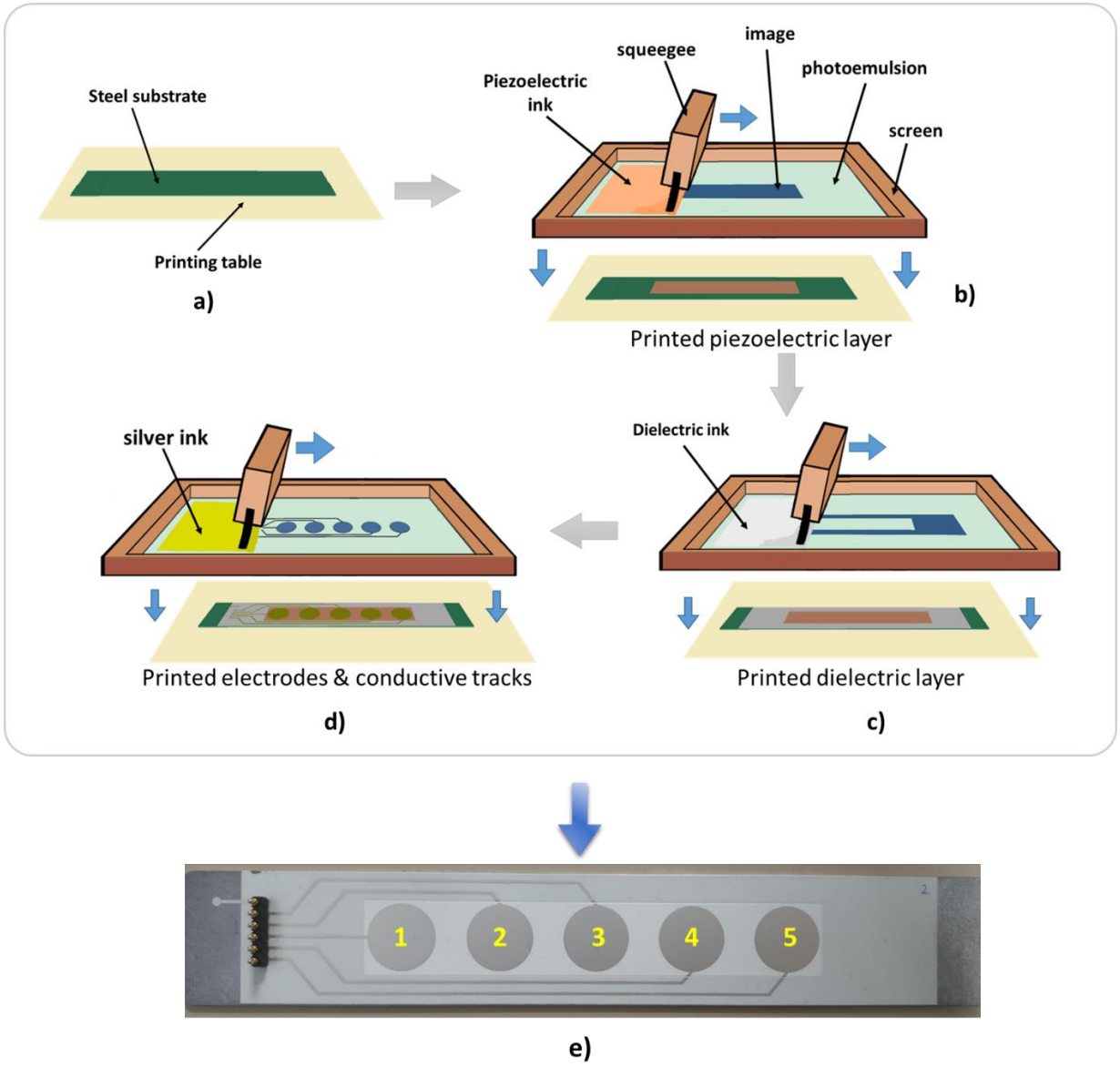

Figure 2.5. Fabrication of piezoelectric sensor via screen printing process: a) setting steel substrate; b) printing piezoelectric layer; c) printing dielectric layer; d) printing electrode and conductive tracks; e) Full printed coating with electrical connectors.

The fabrication of multilayered piezoelectric sensor coated on a 2D cross-shaped steel substrate was shown in Figure 2.6a-d. Highly adaptable to any different shape of substate, the screen-printing process employed in the 2D system is similar to the one used for the fabrication of the 1D substrate. The final bidirectional cross-sensor prototype shown in Figure 2.6e consists of a dielectric layer, a piezoelectric layer on which were deposited nine electrodes (i.e., comprising two on each arm of the cross and one at the center).

Moreover, two electrical connectors implemented on the extremity of the dielectric layer allowed to link to the conductive tracks (CTs) to the electrodes. Regarding an important number of the electrodes embed into a 2D system, the design of CTs is revealed to be challenging. Such a design must fulfill the critical rules descried previously in Subsection 2.1.2 so as to reduce parasitic capacitance throughout measurements.

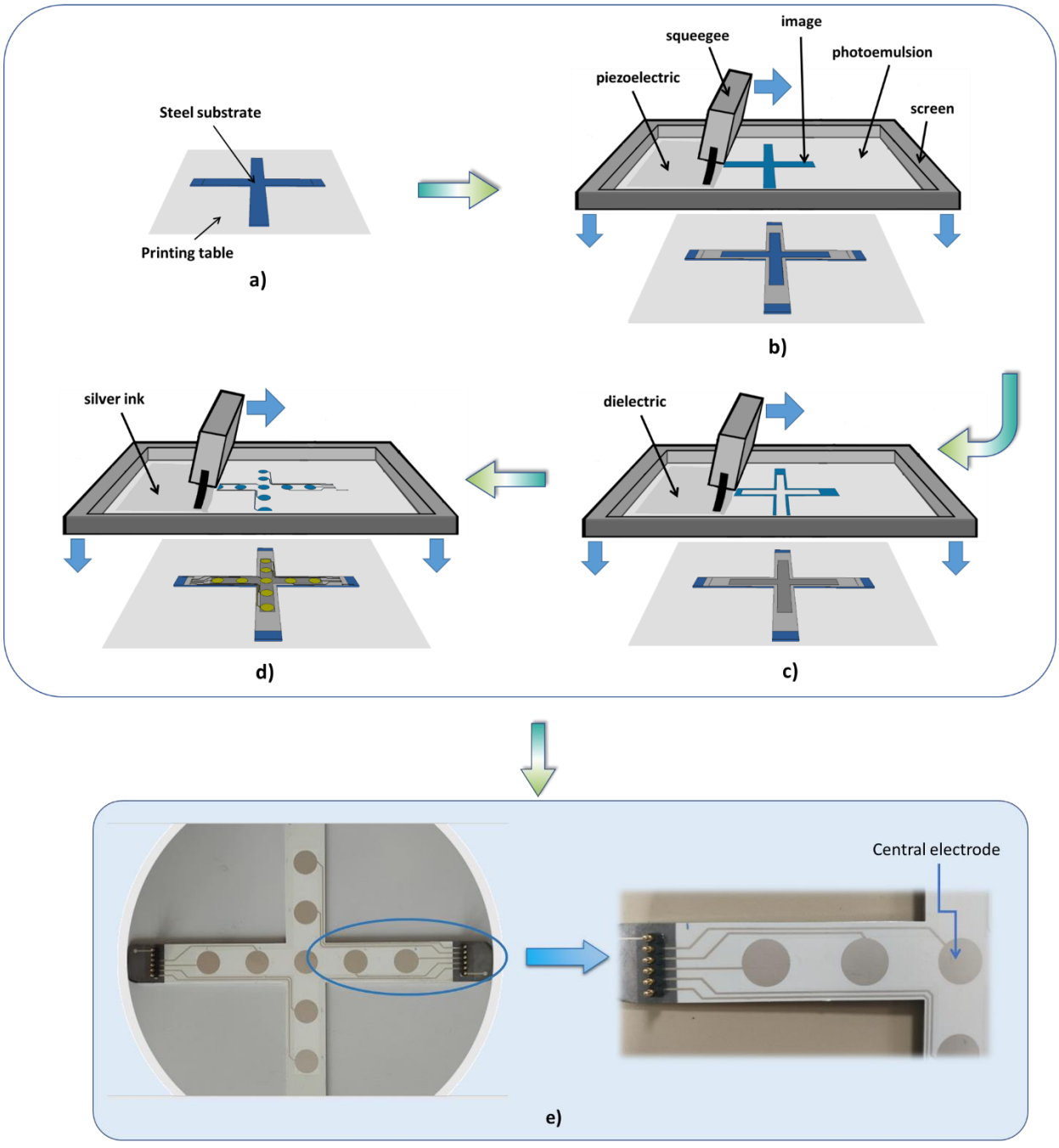

Figure 2.6. Fabrication of two-axis piezoelectric sensor via screen printing process: a) setting steel substrate; b) printing piezoelectric layer; c) printing dielectric layer; d) printing electrode and conductive tracks; e) Full printed coating with electrical connectors.

2.3.2. Piezoelectric actuator used for touchscreen device

Haptics is found in nearly all modern touchscreen devices to increase input/typing accuracy while subsequently improving user satisfaction. Most of haptic technologies used a resistive [151], capacitive [152,153], surface acoustic wave (SAW) [154] or infrared grid [155] to create the sense of touch. To date, piezoelectric materials have been intensively explored among scientific communities [156–158] in the area of tactile touchscreen, but the misunderstanding of their characteristics strongly limits their wide industrial use. This study involves in the development of haptic functions using piezoelectric coatings, together with their full characterizations in both sensor and actuator modes. The piezoelectric ink was printed on a thin and flexible substrate made of Polyethylene terephthalate (called PET) thermoplastic polymer resin. This polymer has advantage of colorless, flexible, low cost, commercialized available, easy process, and good adhesion with lots of inks. Several layers of piezoelectric coating are carried out to produce sufficiently vibration that could be felt by user's fingers. Experiments have pointed out that for achieving a best compromise between the actuation performance and the mechanical flexibility, the thickness of the substrate should be of the same order as the one of the coatings. Here the PET thickness was chosen equal 75 µm, which is supposed to be comparable with the multilayered piezoelectric coating (i.e., 25–30 µm/layer). Experimental and simulation results in Chapter 4 will demonstrate that the actuator coating made with 2 or 3 piezoelectric layers allows to activate enough vibration magnitude (under an appropriate frequency) that could be perceived by human's skin.

Apart from the substrate, the fabrication process based on screen printing of the piezoelectric actuator is similar to that of the piezoelectric sensor descripted above. Figure 2.7 shows an example of a two-layered piezoelectric actuator, which can be modeled as two capacitors connected together in parallel. Contrary to the steel substrate in the case of the sensor coating, the PET substrate is not a conductor thus could not be used as the ground electrode. In order to establish a parallel configuration for two capacitors, it is necessary to print three layers of electrodes. Among these layers, the middle section comprises five electrodes with a diameter of 18mm, which serve as connections to the lower CTs, assuming the role of electrical ground. The circular top and bottom electrodes are interconnected, linking them to the upper CT. Between these electrodes, two piezoelectric layers are incorporated. As a result, the total equivalent capacitance of each sensor is equal to the sum of these two individual capacitors.

a)

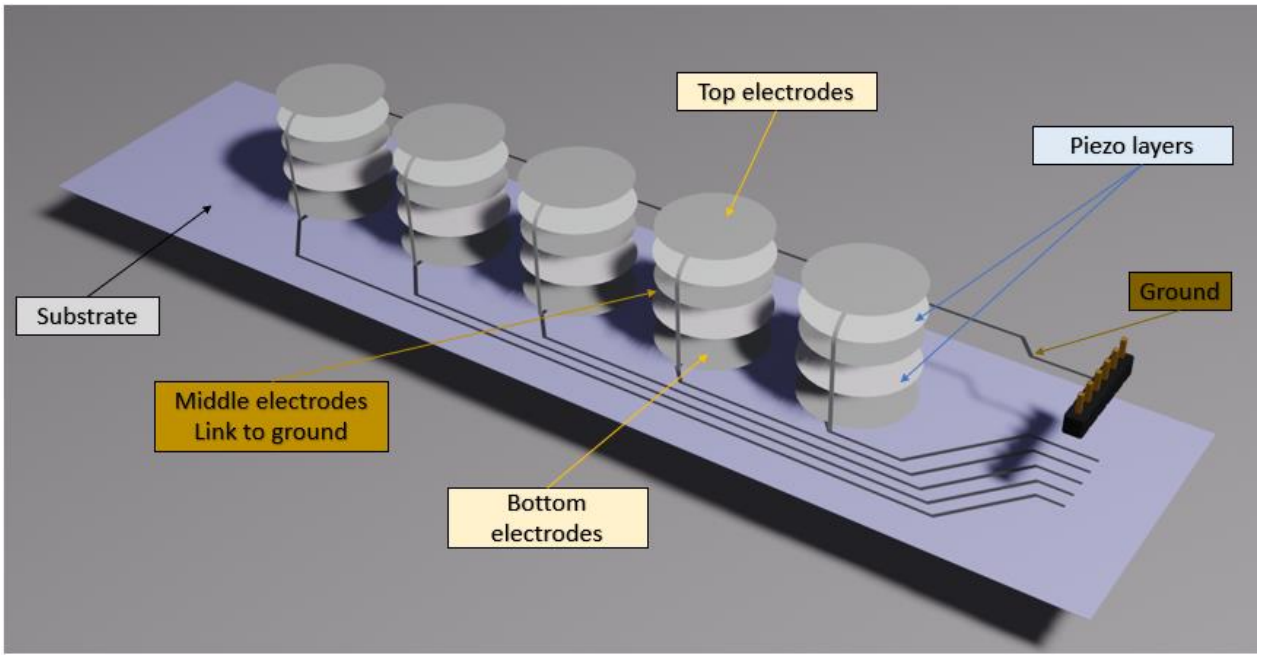

b)

Figure 2.7. a) prototype of piezoelectric actuator coating printed on a flexible PET substrate; b) architecture of two-layers piezoelectric actuator.

2.4. Poling procedure

2.4.1. Test bench principal

Figure 2.8 illustrates the principal of experimental setup for the poling process. The randomly dispersed Pu/$BaTiO_3$ composites were polarized in an oil bath to prevent any voltage breakdown that could happen in the air. To create the electrical contact, the sample was clamped between two copper electrodes to which was applied a DC input voltage. A waveform generator (Agilent 33210A, Keysight Technologies Inc.) is coupled with an amplifier (10/10 B-HS, TREK Inc.) in order to enhance the input signal by a factor of 1000. The electric field (E) was progressively increased until the desired value and kept constant during a few minutes. For a polarization at high temperature, the entire sample holder was placed into an oven (Votsch Industrietechnik TM, VT7004), allowed the control of temperature with high precision. Afterwards, samples are progressively cooled down at room temperature under field. As soon as the field is removed, samples are short-circuited during 5 min to totally evacuated undesired electrostatic charge. To check the success of the polarization procedure, the piezoelectric sensitivity (d_{33}, usually defined as the longitudinal charge coefficient) is measured through a piezometer (Ye2730a – D33 Meter). Error bars, obtained from measurements of different samples poled at the same conditions, have been added on each value of d_{33}.

After the poling process, a formation of dipoles is created, and the ferroelectric composite keeps its remanent polarization even when the voltage is OFF. This effect is a responsibility of piezoelectricity, i.e., a macroscopic phenomenon relating to intrinsic dipole's orientation of particles. An increase in the molecular mobility of the amorph phase of the matrix, i.e., above the glass transition temperature, allows orientation of the electrical dipoles of the particles along the poling field.

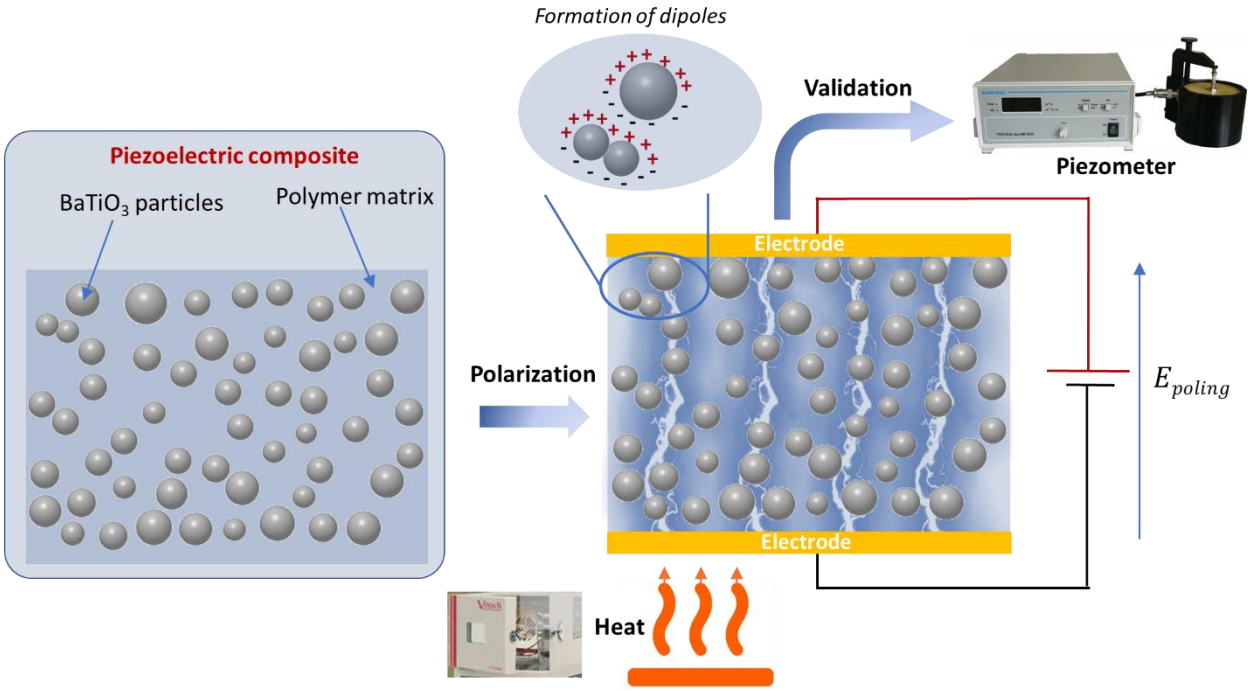

Figure 2.8. Working principal of polarization process.

The following subsection aims to analyze the influence of polarization parameters (magnitude, temperature, time) on the piezoelectric behavior. In this study, the magnitude of the poling field applied to the composite is the same order with respect to the case of the bulk $BaTiO_3$ [159]. This value is revealed to be considerably lower than the one used in classical piezoelectric polymers [160–163], demonstrating great benefit of ferroelectric composite, especially when high voltage application become a serious problem. As the optimum piezoelectric coefficient is reached when the amorphous phase of the polymeric matrix is in the liquid state, optimized polarization is carried out at temperature above the glass transition. Besides, the poling time is also a key factor as the establishment of the local field is governed by macromolecular mobility and interfacial polarization [40].

2.4.2. Influence of polarization conditions on piezoelectric sensitivity

Figure 2.9a illustrates the dependence of the piezoelectric coefficient (d_{33}) as a function of the field level, which is driven for 30 min at constant temperature of 80°C. The applied poling field should be higher than the coercive field, which, for $BaTiO_3$ composites, is approximately 2–3 V/µm [164,165]. It is highlighted that above a magnitude of 4 V/µm, the d_{33} coefficient reaches a saturation regime, which is analogue to the coercive field of the inorganic $BaTiO_3$ ceramic. In such conditions, the local field distributed to the $BaTiO_3$ particles is comparable to the external poling field, to some extent [166]. To ensure good piezoelectric performances, we opt for an electric field of 6 V/µm, which is small enough to not provoke any electrical breakdown of the composite [39].

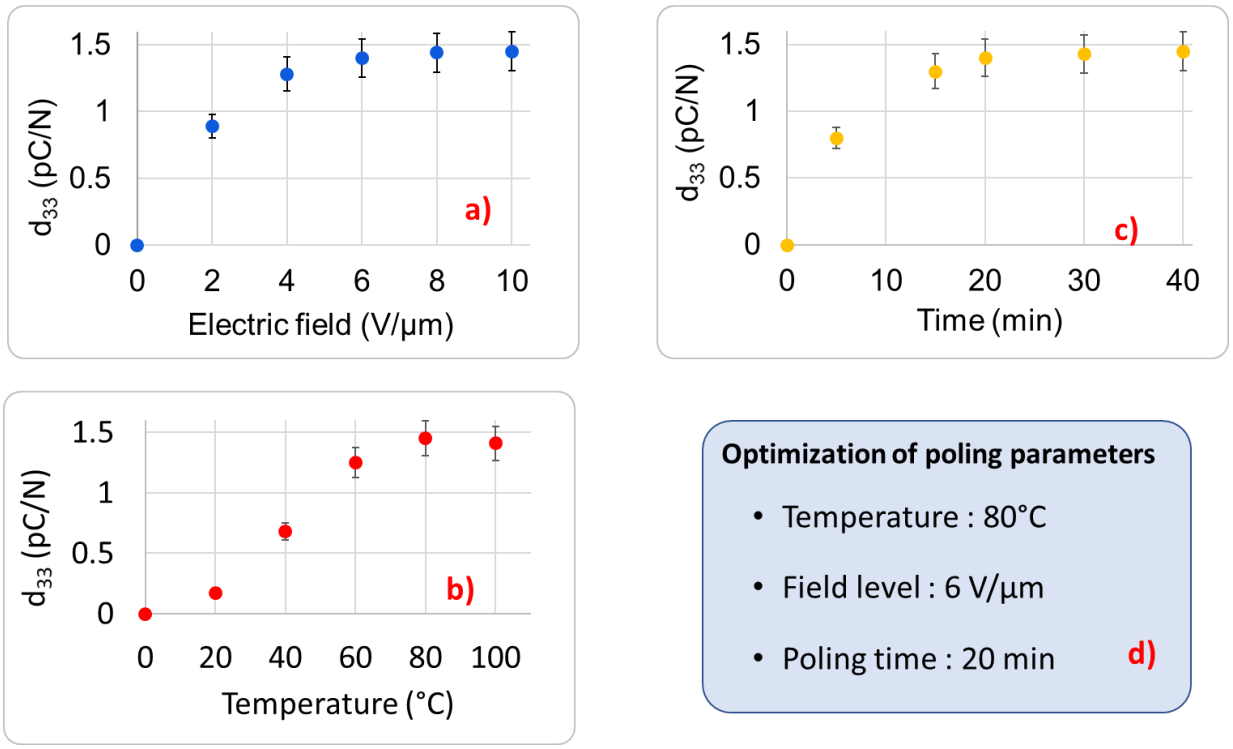

Figure 2.9. Piezoelectric charge coefficient (d_{33}) as a function of: a) Magnitude of electric field; b) temperature; and c) time. d) The best tuning parameters are chosen to optimize the poling process.

Figure 2.9b describes the variation of the piezoelectric coefficient with respect to the poling time, in which the sample are performed at 6 V/µm and 80°C. This temperature has been chosen in the vicinity of the Pu glass transition temperature. The d_{33} coefficient of the composites attain a saturation plateau after a certain poling time (~ 16 minutes), i.e., contrarily to the piezoelectric ceramic whose dipoles orientation is almost instantaneous. Accordingly, the polarization time of composites seems to be governed by the organic phase.

Figure 2.9c shows the evolution of the piezoelectric coefficient with respect to the polarization temperature. Samples were heated up to the set temperature in an oil bath and then polarized under a 6 V/µm electric field for 30 min. The set temperature is limited at 100°C in order not to approach the Curie transition of the inorganic phase. It has been pointed out that there exists a threshold value of d_{33} near 60 °C, above which the maximum steady-state piezoelectric response is achieved. This characteristic is dedicated to the interfacial phenomena of composite, in which $BaTiO_3$ particles are randomly dispersed in the amorphous phase of Pu matrix. Around the glass transition temperature (T_g, around 60°C), molecular mobility involved in the polymeric matrix increases, giving rise to an enhancement in the local field distributed within the particles. This, to some extent, leads to an increase in the piezoelectric coefficient of the composite [40].

The optimization of the poling parameters, at which the composites are conducted to a saturated polarization, might originated from Maxwell-Wagner-Sillars (MWS) interfacial effect. The MWS relaxation is characterized by a consequent increase in the dielectric permittivity of the medium beyond the T_g [40]. As a result, the discrepancy in the permittivity between the particles and the matrix is decreased, leading to higher local field applied to the particles. This local field therefore becomes closer to the coercive field of the composite, which in turn approach to the one of the ceramics (~ 3 V/µm). In that case, poling saturation may occur. Finally, Figure 2.9d summarizes the most appropriated parameters used in poling process.

2.5. Methods of experimental characterization

2.5.1. Broadband spectroscopy

Broadband dielectric spectroscopy of the composites was performed using an impedance-analyzer (Solartron SI-1255 together with an interface 1296) at ambient temperature. The dielectric spectra were acquired using an AC electric field with an amplitude of 1 V_{rms} and a frequency range of 0.1Hz to 1 MHz.

2.5.2. Morphology

In order to evaluate and compare the particles distribution of aligned and random $BaTiO_3$/PUA composites, scanning electron microscopy (SEM) was carried out with a Hitachi Flex SEM 1000II microscope. No conducting layer was coated on the samples because of the low voltage application. The operation was performed under a vacuum of 30 Pa, a working distance of 6 mm, and an accelerating voltage of 15 kV.

2.5.3. *Four-point bending measurement used for sensor testing*

2.5.3.1 Analytical model

For a simple linear substrate, the schematic presentation of the four-point bending (4PB) machine and a photo of the actual experimental setup is respectively shown in Figure 2.10a,b. Usually, the symmetric 4PB testing creates two opposing moments on either side of the beam's centerline, leading a constant bending stress (or strain) between the applied force. As the maximum flexural stress (occurred at the center) is spread over the section of the beam between loading points, the stress concentration of the 4PB test is over a larger region, avoiding premature failure. Due to the small thickness of piezoelectric thin layer in comparison to the substrate, it can be assumed that the sensor layer is exposed to a constant positive strain in parallel to the x-direction that is equal to the strain of the surface layer of the steel substrate [167].

The induced stress at the center (T_{sc}) can be determined by [168,169]:

$$T_{sc} = \frac{Mh}{2\,J} = \frac{3\,Fa}{w\,h^2} \tag{2.3}$$

where F is the load (force); L and b respectively denote the span between the 2 support points and the 2 load points; a is the distance between the support and the load ($a = (L-b)/2$); w and h respectively denote the width and the thickness of the substrate.

According to [170], the deflection at any point between the loading points (denoted x) is given by:

$$d = \frac{Fa\left(a^2+3x^2-3Lx\right)}{Y\,w\,h^3} \tag{2.4}$$

where Y is the Young's modulus of the beam. Consequently, the deflection at the loading point (d_l) and the maximal deflection at the center (d_c) can be calculated as:

$$d_l = \frac{Fa^2(3L-4a)}{Y_s\,w\,h^3} \quad , \quad d_c = \frac{Fa\left(3L^2-4a^2\right)}{4\,Y\,w\,h^3} \tag{2.5}$$

Physically, the product Fa represents the moment of the applied force ($M_z = Fa$) with respect to the z-axis, while the expression $w\,h^3$ is proportional the quadratic moment of area ($I_z = w\,h^3/12$), both are calculated with regard to the z-axis. To the practical point of view, particularly for our tested sample (see Figure 2.5e) the stress is initially induced in the substrate, and the strain is transferred to piezoelectric layer. Therefore, the nature of the substrate will impact the measurements and its Young's modulus (Y_s) is necessary to estimate the strain (S) transferred to piezoelectric sensor. Consequently, the strain at the center (S_c) can be determined using the Hook's law [38]:

$$S_c = \frac{T_{sc}}{Y_s} = \frac{3\,Fa}{Y_s\,w\,h^2} \tag{2.6}$$

For the piezoelectric layer printed above the steel substrate, its well-known electromechanical model can be expressed as [171]:

$$S_1 = Y^{-1}T_1 + d_{31}E_3 \quad , \quad D_3 = d_{31}T_1 + \varepsilon E_3 \tag{2.7}$$

where 1-index and 3-index denote the length and the thickness direction (along x-axis and y-axis), respectively. Y and ε are respectively the Young modulus and the dielectric constant of the material; d_{31} denotes the transversal piezoelectric charge coefficient (d_{31}). S (strain) and T (stress) are the mechanical

parameters whereas *E* (electric field) and *D* (charge displacement) are the electrical parameters. For a sake of simplicity, these four parameters will be used without the index 1 and 3.

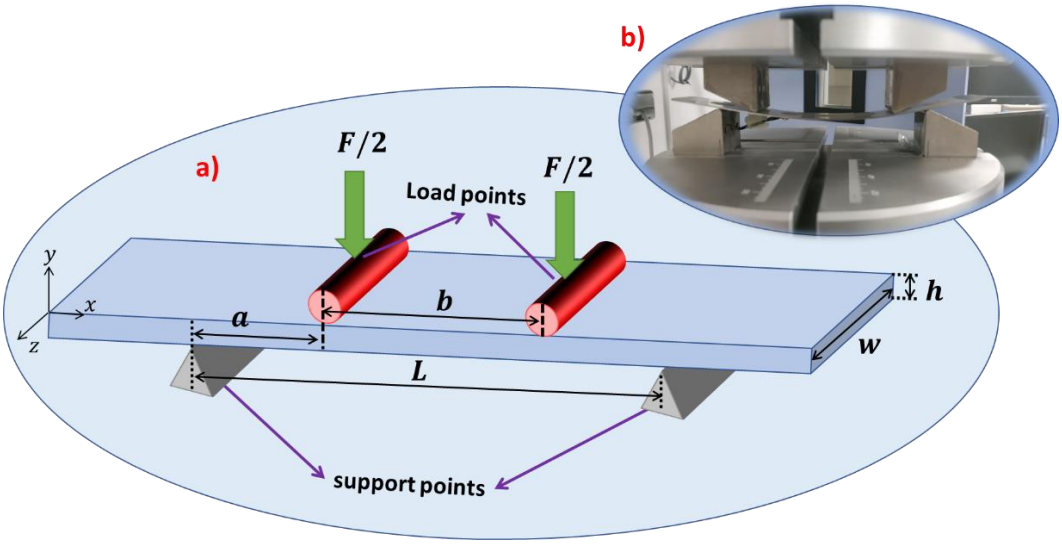

Figure 2.10. Four-point bending principal used in flexural tests: a) schematic representation; b) Zoom-in on the real experimental setup.

In the case of direct piezoelectric effect, the material acts like a sensor (when being subjected to mechanical stress, leading to a generation of an electric charge proportional to that stress). In absent of external applied electric field ($E = 0$), Eq. (2.7) can be simplified as:

$$S = Y^{-1}T \quad , \quad D = d_{31}T \tag{2.8}$$

2.5.3.2 Experimental setup

In practice, a four-point bending (4PB) apparatus is employed to produce uniaxial and uniform stress on the tested substrate, making it possible to facilitate the characterization. The 4PB tests were conducted on steel substrates (with and without piezoelectric sensor) using a SHIMADZU press (AGS-X), as shown in Figure 2.11a. For the single substrate, only mechanical test is performed in order to evaluate the strength of the material and to compare it with the analytical model of Eq. (2.3). On the other hand, for the full specimen (substrate/sensor), piezoelectric characterization tests are carried out under room temperature as well as varying temperature, with the purpose of testing the temperature stability of the piezoelectric composite.

Figure 2.11a shows a typical four-point flexural setup where the loads are symmetrically applied at two points on the top of the specimen. Alternatively, the supports are supplied on the bottom, i.e., possibly located outside or inside the two top fulcrums of force. The desired DC or AC load vertically applied to the bending fixture is quantified via a load sensor (HBM,10N-10kN). The strain gage (RS PRO) is coated on the middle bottom of the specimen, in such a way that it allows to determine the deformation in the length direction. Mechanical characteristics of the substrate can be therefore deduced. Besides, the charge output delivered from the piezoelectric sensor is monitored via a charge amplifier (KISTLER, Type 5015). Finally,

real-time signals are simultaneously acquired and recorded through a Sirius 8XSGT card interfaced with the DEWE software. Post-data treatment was performed with MATLAB and EXCEL.

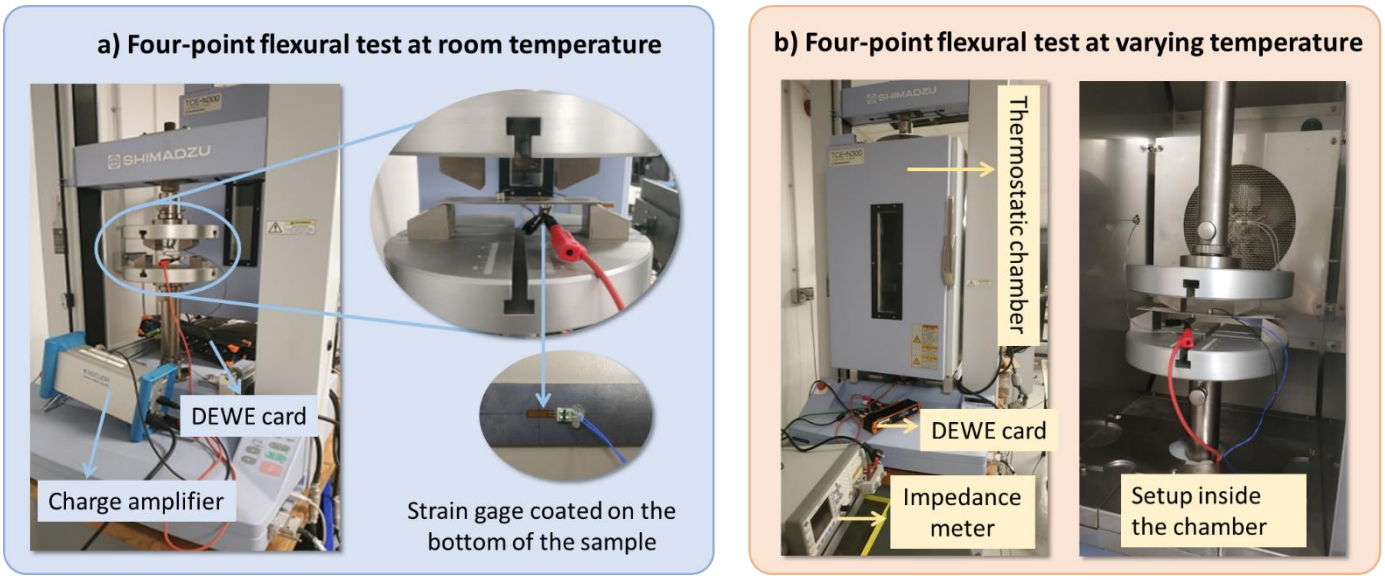

Figure 2.11. Four-point flexure test in different conditions of temperature: a) Room temperature of 20°C; b) varying temperature in the range of [–10°C, 80°C].

Based on the 4PB configuration and regarding the model of Eq. (2.8), the transversal piezoelectric charge coefficient (d_{31}) coefficient of the active element at the center (i.e., electrode 3 in Figure 2.5e) can be calculated as:

$$d_{31} = \frac{D_3}{T_c} = \frac{\frac{Q}{S_{ative}}}{Y\,S_c} \tag{2.9}$$

where S_{active} denote the surface of the gold electrode at the center, respectively; Q denotes the measured electric charge; T_c and S_c are respectively the mechanical stress and strain of the piezoelectric composite at the center. It is worth noting that both the substrate and the sensing piezoelectric layer are subjected to the same induced deformation (S_c), which is empirically measured through the strain gage coated on the middle of the specimen (i.e., position of the electrode 3). This value is then compared to the one predicted by the model of Eq. (2.6). Substituting $d_{33} = \frac{d_{31}}{\nu}$ in Eq. (2.9) yields

$$d_{33} = \frac{\frac{Q}{S_{ative}}}{\nu\,Y\,S_c} \tag{2.10}$$

where d_{33} is the longitudinal piezoelectric charge coefficient and ν is the Poisson coefficient of the piezoelectric material.

In order to investigate the influence of temperature on the piezoelectric response of the sensing layer, the entire 4PB setup is placed inside a controlled temperature environment thanks to a thermostatic chamber (TCR2L type, see Figure 2.11b). Being integrated with a highly precise temperature controller, this device is not only compact, easy use, but also ensures uniform measurement with uncertainty of only ±1.5 °C at

300 mm in height direction. The instrumented substrate is exposed to a large temperature range, increasing from –10ºC to 80ºC, which is revealed to be lower than the Curie temperature of $BaTiO_3$ particles (*i.e.*, around 120°C). For each temperature change, 20 minutes waiting time is required to achieve a stable state. All experimental tests are processed in the same way as those of ambient environment. Considering the thermal dilatation and the Young modulus of the steel substrate is unchanged within the tested temperature range (meaning that S_c is constant), the piezoelectric sensitivity (see Eq. (2.9)) depends on two factors: 1) Q, relating to the dielectric properties; and 2) Y_p, relating to the mechanical properties of the composite.

The relevant question here is to know how and whether-or-not these two factors could be affected by the temperature change. In order to distinguish the temperature influence on these two factors, capacitor measurement of the specimen is carried out using an LCR meter (HP/Agilent 4284A, see Figure 2.11b). Test is conducted under a varying temperature from –10ºC to 80ºC, and an AC voltage of 1Vrms amplitude and 1kHz frequency.

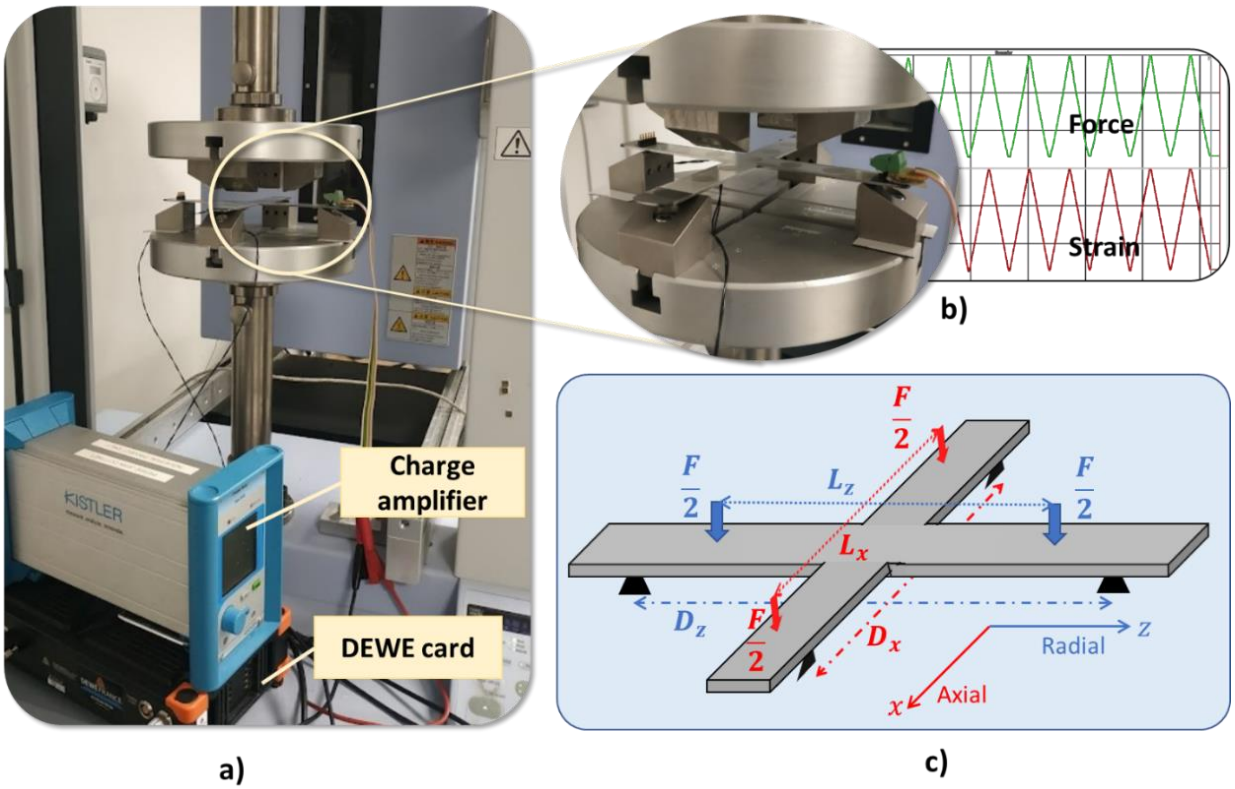

Figure 2.12. Setup of four-point bending (4PB) test using Shimadzu press: a) measurement bench; b) Zoom-in on sample's implementation; c) Test could be performed by adjusting force and distance parameters in *x*- and *z*-axis.

For a cross-shaped substrate, a four-point bending (4PB) apparatus is still used in practice to produce bidirectional and uniform stress on the tested substrate along *x*- and *z*-axis; but in this case, we need more support for top and bottom axes. As shown in Figure 2.12a-b, the biaxial cross sample, being held by four supports underneath, was subjected to four identical forces perpendicular to the tested substrate. Regarding very thin layer of the printed coating (about 20µm) with their excellent adhesion to the substrate surface, the deformation of the coating layer in both directions can be supposed to be similar to the substrate's one. The central electrode (see Figure 2.6e), mostly affected by both directions, is chosen for test measurements.

The other electrodes would have higher response in their preferred direction, which is somehow similar to the case of uniaxial sensor [30]. As a result, studying on the central electrode allows to better highlight the bidirectional effect of the 2D sensor coating. Two strain gages (RS PRO) were thus coated on the middle bottom of the specimen, in such a way that they allow to determine the deformation in both radial (z-axis) and axial (x-axis) directions (cf. Figure 2.12c). Such a deformation does not only depend on the applied force, but also on parameters of distance: D_x and D_z are the supports' span while L_x and L_z are the span between two applied forces, correspondingly to *x*- and *z*-axis. The mechanical characteristics of the substrate could be therefore deduced in different configurations.

2.5.4. Electromechanical setup used for actuator testing

This experimental setup aims to evaluate performance of the piezoelectric material as a haptic touchscreen, by measuring its ability to convert electrical energy into mechanical motion (actuator mode) that would be felt by user. Also, the piezoelectric element is supposed to be tested in the sensor mode when user performs a touch command that could be detected by the piezoelectric device. Consequently, the system activates by vibrating and producing tactile feedback, i.e., the sensation of touch. Figure 2.13 illustrates a typical haptic technology system composed of a touch device with a capacitive button, processor, drive circuit, and an actuator. The input of the haptic technology system might be a touch consisting of a capacitive button that serves as an input to a touch screen device. It detects touch pressure which is then sent to the processor in the form of analog or digital signal. The processor generates a specific waveform according to the touch and finally, piezoelectric actuator creates movements based on the waveform conducted by the processor.

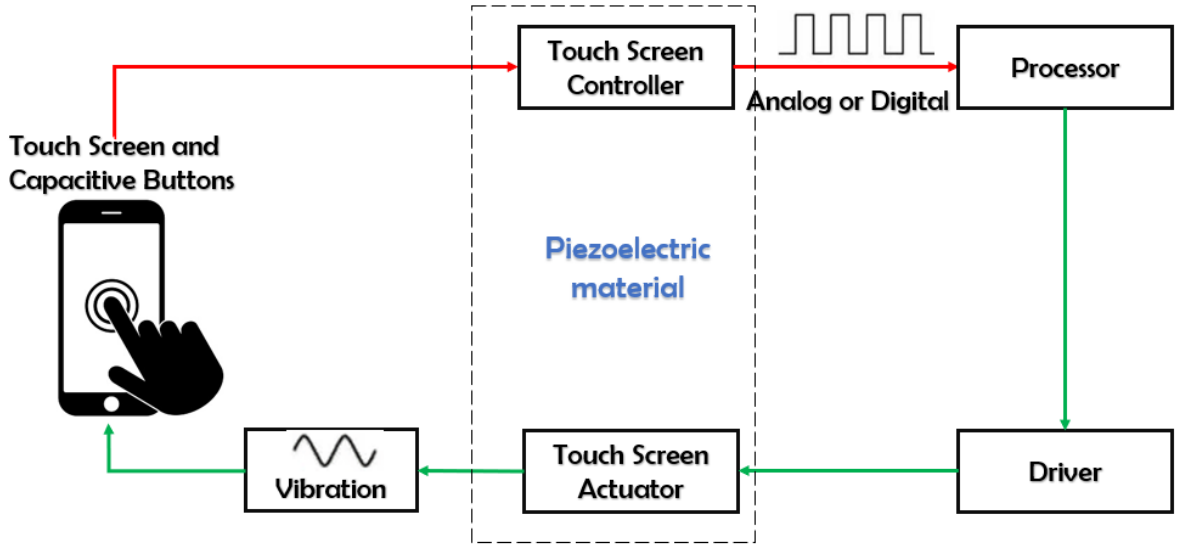

Figure 2.13: Haptic touchscreen system using flexible printed piezocomposite.

The following steps can be used to test a piezoelectric haptic feedback device [172]:

- Preparation: The piezoelectric actuator is mounted in a test setup, including a power supply, measurement instrument, and any necessary fixtures or support structures.
- Mechanical-to-electrical sensing: User applied a mechanical force or displacement to the piezoelectric material that results in the generation of an electrical signal, such as voltage or charge.

This signal is used to trigger the input voltage applied to the piezoelectric element, which in turn induces the feedback motion to the user (corresponding to red arrow shown in Figure 2.13).

- Electrical-to-mechanical actuation: After receiving the trigger mentioned above, an electrical voltage is driven to the piezoelectric element, producing a mechanical motion (such as displacement, strain, or force) that is supposed to be detected by user's fingers (corresponding to green arrow in Figure 2.13).
- Characterization: Analyze the results of the electrical-to-mechanical (actuator) and mechanical-to-electrical (sensor) tests to determine the actuator's response and haptic performance, such as frequency response, linearity, hysteresis, and stability.
- Comparison: Compare the results to the desired specifications and tolerances to determine if the actuator meets the performance criteria of haptic touchscreen device.

2.5.4.1 Electrical-to-mechanical test setup

The test setup for the electrical-to-mechanical actuation is illustrated in Figure 2.14. This setup includes five elements principals: the piezoelectric actuator specimen, a waveform generator (Agilent 33220A), a high voltage amplifier (TREK 10/10B-H-CE-EX), a vibrometer controller (OFV-5000-2G) with a sensor head (OFV-505) [173]. Typically, mechanical vibrations captured by the sensor are amplified and processed through a specified control unit, then converted into an exploitable output signal. The sensor head emits a laser beam pointed to the piezoelectric actuator via a reflective tape glued on its surface (see Figure 2.14 with the zoom on the sample). As a result, the displacement of the sensor is locally measured with a high resolution. A voltage signal, delivered by a sinusoidal waveform generator with tunable amplitude and frequency, was amplified and driven to the piezoelectric specimen, which in turn induced its displacement. The signal delivered from the vibrometer, and the waveform generator can be monitored and recorded using an Oscilloscope (IDS-1054B) or a Sirius 8XSGT card interfaced with the DEWESOFT software application.

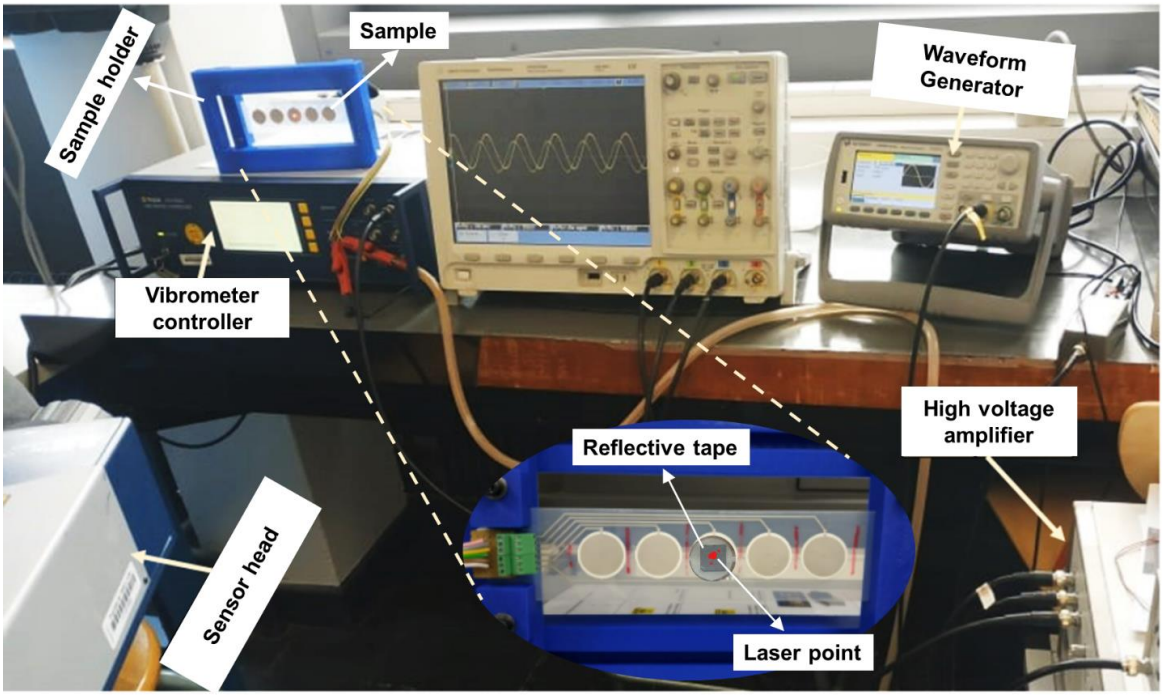

Figure 2.14: Setup opted for the electrical-to-mechanical actuation test without force measurement. Inset in the bottom is a zoom on the sample and its support.

Based on the velocity magnitude (v_{max}) of the piezoelectric specimen measured with the vibrometer, it is possible to infer the maximum displacement (d_{max}) according to the following expression:

$$d_{max} = \int_0^{\frac{T}{4}} v_{max} \sin(\omega t) dt = \frac{v_{max}}{2\pi f} \quad (2.11)$$

where f is the frequency of the induced velocity, which is supposed to be sinusoidal (i.e., similar to the applied voltage) regarding the linear piezoelectric response. As d_{max} is frequency dependence, the selection of an adequate operating frequency is of primary importance to activate enough motion for touchscreen system. Moreover, frequency has also an impact on the human's perception, which is in turn affected by the displacement level of the tactile feedback. After several empirical trials, it has been pointed out that with a displacement of a few micrometers (e.g., 2µm) activated by the piezoelectric thin-film actuator, the set frequency of around hundreds Hz (e.g., 300 Hz) enabled users to clearly perceive vibrations generated to their finger skin.

Knowing the maximum displacement, the maximum deformation (or the strain, denoted as S_{3_max}) along the thickness direction (i.e., 3-axis) of the piezoelectric actuator can be inferred as:

$$S_{3\_max} = \frac{d_{max}}{e} \quad (2.12)$$

where e is the thickness of the piezoelectric element. Under a given electric field (denoted E_3) applied along the 3-axis, the induced strain (S_3) ultimately depends on the property of the piezoelectric material, i.e., the charge coefficient d_{33} according to the following expression:

$$S_3 = d_{33} E_3 \quad (2.13)$$

The above relationship is carried out under a free-load condition. As indicated in Eq (2.12)-(2.13), for a given input voltage, the sample with higher thickness leads to higher displacement, giving rise to enhanced actuation performance. As a matter of fact, several piezoelectric layers were stacked together to create a multilayer tactile structure so as to improve the human's perception.

Figure 2.15 illustrated an experimental setup that allows for the actuation characterization including the measurement of the force applied to the piezoelectric specimen. For a sake of simplicity, the sample was made of only one circular coating (with 18 mm diameter and 28 µm thickness), which was attached inside a round hole (30 mm diameter) situated at the center of a homemade square-shaped support (side length of 85 cm). One side of the piezoelectric sample was bonded with a reflective tape on which pointed by a laser ray issued from the sensor head of the vibrometer. The other side, simulated as a button of a tactile screen, was pressed by an artificial finger (cf. Figure 2.15) that can be slid along the translation support. The customized finger is made of plastic whose elasticity is similar to the one of a human's finger.

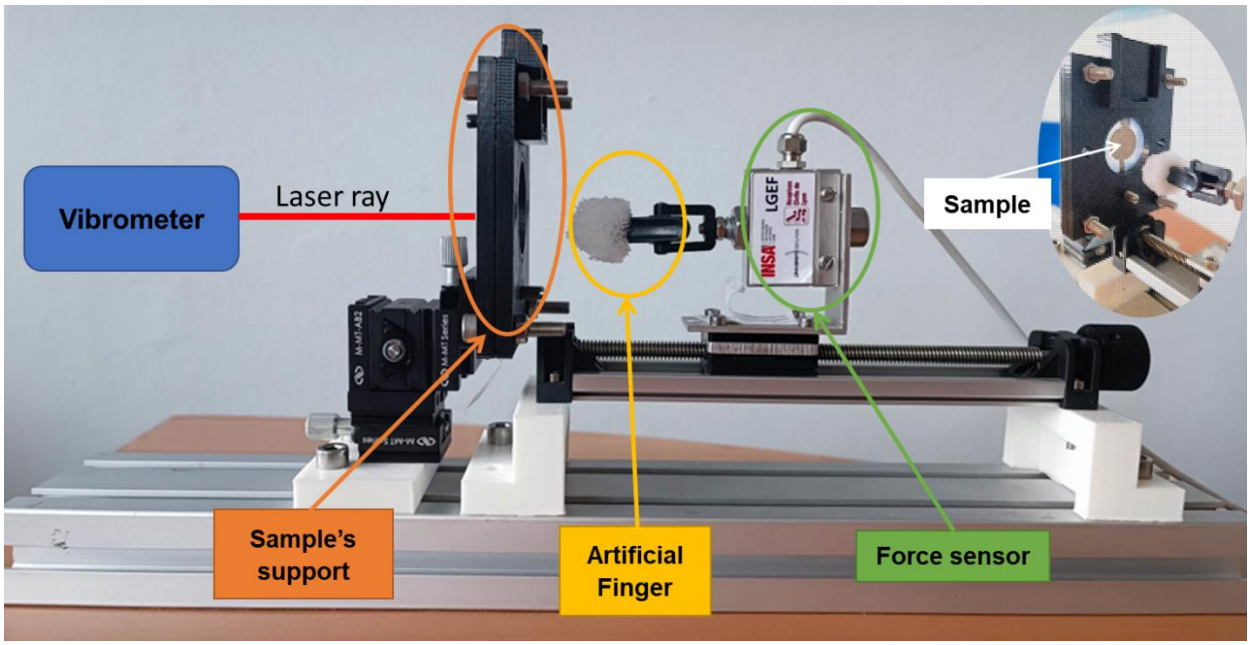

Figure 2.15: Setup opted for the characterization of electrical-to-mechanical actuation with the force measurement. Inset in the top right conner shows the front view of a piezoelectric with its support.

Experiment starts when the artificial finger presses the piezoelectric button capable of withstanding a force of few Newton (i.e., not exceed 5 N). The finger was manually piloted by user along translation direction thanks to a micrometer-screw system, leading to highly precise and smooth movements. A load sensor (DOERLER Mesures LC 102 TC) attached to the finger allows for the determination of the applied force that is supposed to be varied. The force level depends on the displacement of the finger when making a contact with the piezoelectric specimen. As soon as the contact is occurred, the sample is stressed and thus delivers an electrical signal that is detected by an algorithm developed via a Digilent Analog Discovery 2 (sensing effect). An input voltage is activated to apply to the sample, which in turn generates a vibration that can be perceived by the finger (actuating effect). As the sensation of touch via the artificial finger is not obvious, a record of the motion through the vibrometer is carried out to assess the reliability of the haptic device. Based on the determination of the piezoelectric displacement, it is possible to confirm whether or not such a movement could be sensed by the human's finger. For an easier observation, the input voltage is tuned with a constant frequency of 300 Hz and an amplitude of 560V (i.e., equivalent to 20V/µm) to create a deformation stable by the time. Both force and motion signals were simultaneously monitored and recorded using a DEWE card interfaced with a computer via the DEWESOFT.

2.5.4.2 Mechanical-to-electrical test setup

Our objective in sensor mode is to detect user input when the button is pressed, and to determine when and how a haptic response is sent to the user. The force applied when pressing a button is measured using a force-sensing resistor known as "FlexiForce" whose resistance changes when a force is applied [31]. Figure 2.16 illustrates how to measure the force via a Sirius 8XSGT card interfaced with the DEWE software. A calibration of the FlexiForce was carried out that leads to the following relationship between the force (F) and the variable resistor (R_{ca}):

$$F = 67.413\, R_{ca}^{-0.784} \tag{2.14}$$

R_{ca} can be determined based on the measurement of an output voltage (V_s) using a voltage divider circuit (cf. Figure 2.16 where $V_e = 1$ V and $R_1 = 150$ kΩ):

$$R_{ca} = \frac{150\,V_s}{(1-\frac{V_s}{1000})} \tag{2.15}$$

Equations 2.14 and 2.15 were set into the DEWE-Sirius device, allowing to determine the force applied by the finger.

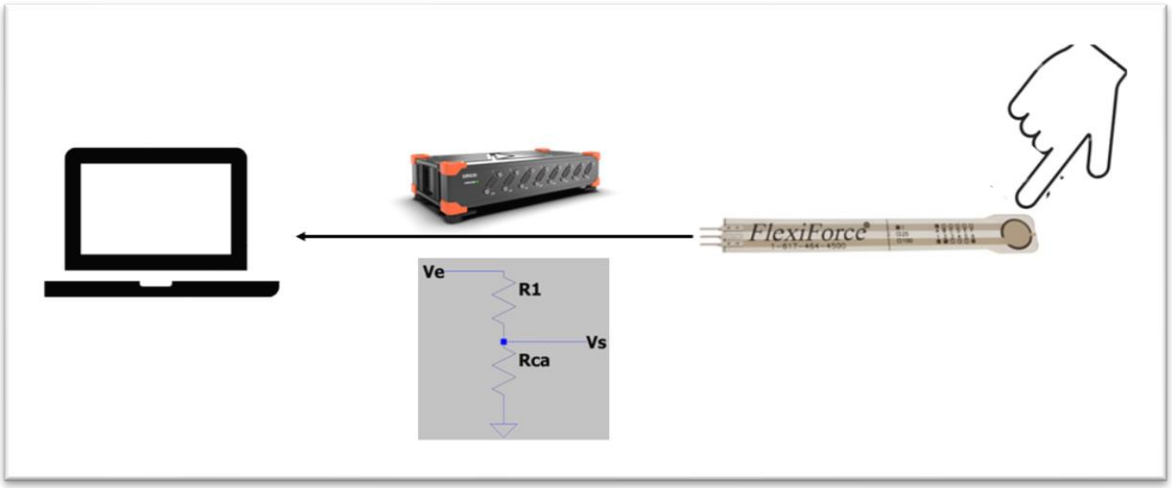

Figure 2.16: Setup used to measure a force when pressing a button.

2.6. Methods of finite element simulation

Finite element (FE) simulation is a numerical method used to model and analyze complex systems and structures in various fields, such as engineering, physics, and biology. It involves dividing a large system into smaller, manageable parts called "elements," and using mathematical equations to simulate how the elements interact and affect each other. FE simulation complements and expands upon traditional physical testing and experimentation in research by allowing for efficient and accurate virtual testing. It offers several advantages over physical testing and experimentation, including cost-effectiveness, time-saving, safe testing, increased accuracy, and improved design optimization. Therefore, to complement and expand upon the physical experimentation and testing, the performance of simulations is also extremely necessary for the research process.

In our research, bearing can indeed be a complex subject to study due to their dynamic nature and interactions with other components. The behavior of bearings can be influenced by a variety of factors such as load, speed, temperature, and lubrication, making it challenging to develop a comprehensive understanding of their behavior. In this case, FE can be a useful tool to simulate the behavior of bearings under different load conditions, allowing researchers to explore and figure out the underlying physical phenomena together with their ultimate relationships. Among several FE tools, ANSYS is a popular simulation software used in a variety of industries and fields. It is a comprehensive simulation platform that offers a wide range of tools and capabilities for modeling and analyzing a variety of physical systems, including structures, fluids, electronics, and electromechanical systems.

2.6.1. Sensor model

To understand the mechanical behavior of the tested substrate as well as the direct piezoelectric effect of the sensor coating, a four-point bending (4PB) setup is modeled using finite element method (FEM) of ANSYS Multiphysics. Figure 2.17a illustrates the 3D geometry model of the unidirectional tested sample while Figure 2.18a presents the 3D geometry model of the tested cross sample. Both comprises four main components including bottom support rollers, steel substrate (beam), piezoelectric layer with five electrodes (circle or rectangular shape), and top blades where is applied by external load. The support spans (D_x and D_z) together with the load distances (L_x or L_z) can be varied. A 4PB model was built with the same dimensions as the real sample.

The properties of the 1D and 2D specimens used in FEM based ANSYS software are shown in Table 2.1, which are relied on the following assumptions, for a sake of simplicity:

- The piezoelectric layer is built by isotropic materials, meaning that electrical and mechanical properties are directional independent.
- The conductive tracks is not involved in the simulation model, and neither the dielectric layer.
- The surface of contact between piezoelectric layer and steel substrate is classified as a bounded contact, which cannot move and rotate between each other (neither sliding nor separating is possible).
- The contact between steel substrate and the supports is classified as fictional contact, meaning that they can slide on the top of each other but cannot be either separated or rotated.
- The center of substrate has only one degree of freedom (Translation in Y direction - direction of load applied).

All piezoelectric composite parameters were determined using empirical measurements. The piezoelectric constants e_{31}, e_{33}, and e_{15} along either *x*- or *z*-axis are computed as a function of Young's modulus (Y) and other piezoelectric constants (d_{33} and d_{31}):

$$\begin{cases} e_{31} = d_{31}(Y_{11}^E + Y_{12}^E) + d_{33}Y_{13}^E \\ e_{33} = 2d_{31}Y_{13}^E + d_{33}Y_{33}^E \\ e_{15} = d_{15}Y_{44}^E \end{cases} \quad (2.16)$$

Noted that the piezoelectric constants e and d represent the sensitivity of the charge detection in response to a mechanical strain and stress, respectively. As the $BaTiO_3$ fillers are randomly dispersed within the PUA matrix, the composite was supposed to be isotropic. Considering no shear load is applied to the specimen (i.e., $d_{15} = 0$), Eq. (2.16) can be thus simplified as:

$$e_{15} = 0 \quad , \quad e_{31} = e_{33} = d_{33}Y(2\nu + 1) \quad (2.17)$$

The above equation allows to estimate the value of the piezoelectric constant implemented on the FEM (see Table 2.1). The bottom of the substrate is electrically grounded. The purpose here is to determine, for each distance of loads and supports, the mechanical strain as well as the potential change induced on the electrodes when the specimen is subjected to an external load.

As shown in Figure 2.18b, the mesh built for the 2D coated substrate model was triangular shape and heterogeneous, with a finer mesh at the electrode-tissue interface where the highest electrical gradients were expected. To obtain the high discretization quality of the modeled system, mesh should be as fine as possible

[174], [175]. The problems encountered when refining the mesh are mainly related to the connection of the structure, but also to the limits imposed by the software or by the computer. As a result, a compromise between the accuracy of the numerical resolution and the calculation time must be considered.

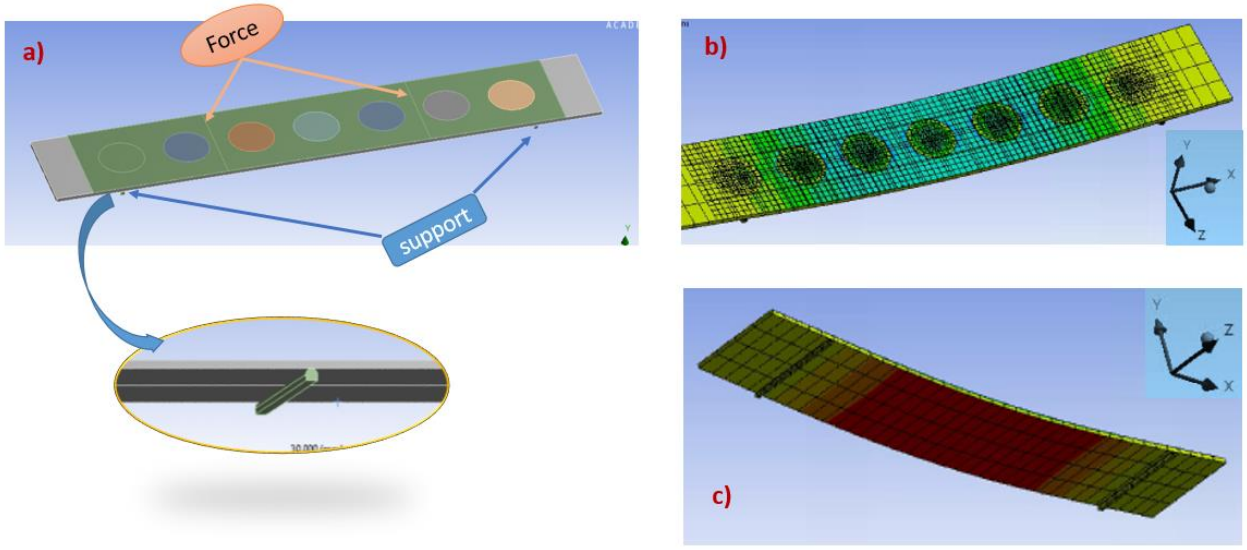

Figure 2.17: FEM of unidirectional coating sensor based ANSYS Multiphysics: a) 4PB configuration; and b)-c) Mesh pattern for physical simulation (top and bottom views, respectively).

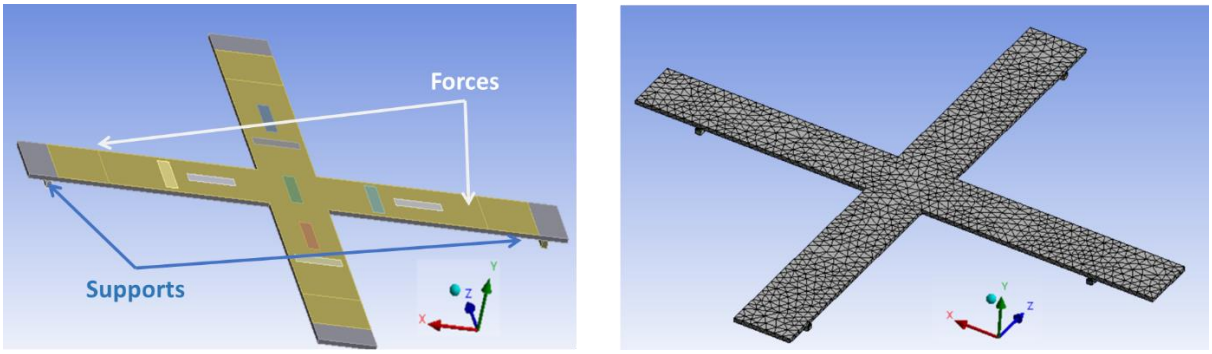

a) b)

Figure 2.18. FEM of the bidirectional coating sensor based ANSYS Multiphysics: a) 4PB configuration; and b) Mesh pattern for physical simulation.

Table 2.1: Parameters of the analytical sensor model.

Material	**Properties**	**Symbol**
1D steel substrate		
Density	ρ	7860 kg/m^3
Poisson's Raito	v	0.33
Young's modulus	Y	210 GPa

Width	w	30 mm
Height	h	1.5 mm
Length	l	185 mm

2D steel substrate		
Density	ρ	7860 kg/m^3
Poisson's Raito	v	0.33
Young's modulus	Y	210 GPa
Width	w	20 mm
Height	h	1.5 mm
Length	l	185 mm

Piezoelectric composite		
Density	ρ'	3000 kg/m^3
Poisson's Raito	v'	0.37
Young's modulus	Y'	7 GPa
Width	w'	20 mm
Height	h'	0.2 mm
Length	l'	160 mm
Relative permittivity	ε'	10.5
Piezoelectric constants	$e_{31} = e_{33}$	0.016 C/m^2
	e_{15}	0 C/m^2

2.6.2. Actuator model

To optimize the design of a piezoelectric actuator, a finite element model (FEM) built on ANSYS simulation software is investigated. As illustrated in Figure 2.19a, a simple geometric design of the piezoelectric actuator consists of a piezocomposite layer sandwiched between the top and the bottom electrodes. They are all together are stacked above a circular PET substrate that is fixed along its circumference. The diameter and the thickness of these layers, indicated in Figure 2.19a, could be modified (detailed in Chapter 4) to optimize efficiency of the actuator. To the practical point of view, electrodes are indispensable to make electrical connections throughout measurement, which is usually needless in simulation model. However, the presence of electrodes does have an impact on the mechanical flexibility, which in turn might affect the actuation performance of piezoelectric devices. To better address this issue, a full piezoelectric model combined with two thin electrodes (~10µm) are considered in the FEM model (see Figure 2.19b). For the best balance between computing time and model accuracy, mesh size of the PET substrate is significantly

larger than that of the piezoelectric layer (cf. Figure 2.19c). The properties of the entire specimen used in FEM are shown in Table 2.2 where the piezoelectric material possesses identical characteristics with respect to the one implemented in the sensor model (see Table 2.1). Moreover, both sensor and actuator models used the same similar assumptions such as anisotropic materials, bounded surface contact between piezoelectric and PET layers, and force application in a one-degree of freedom (cf., Subsection 2.6.1)).

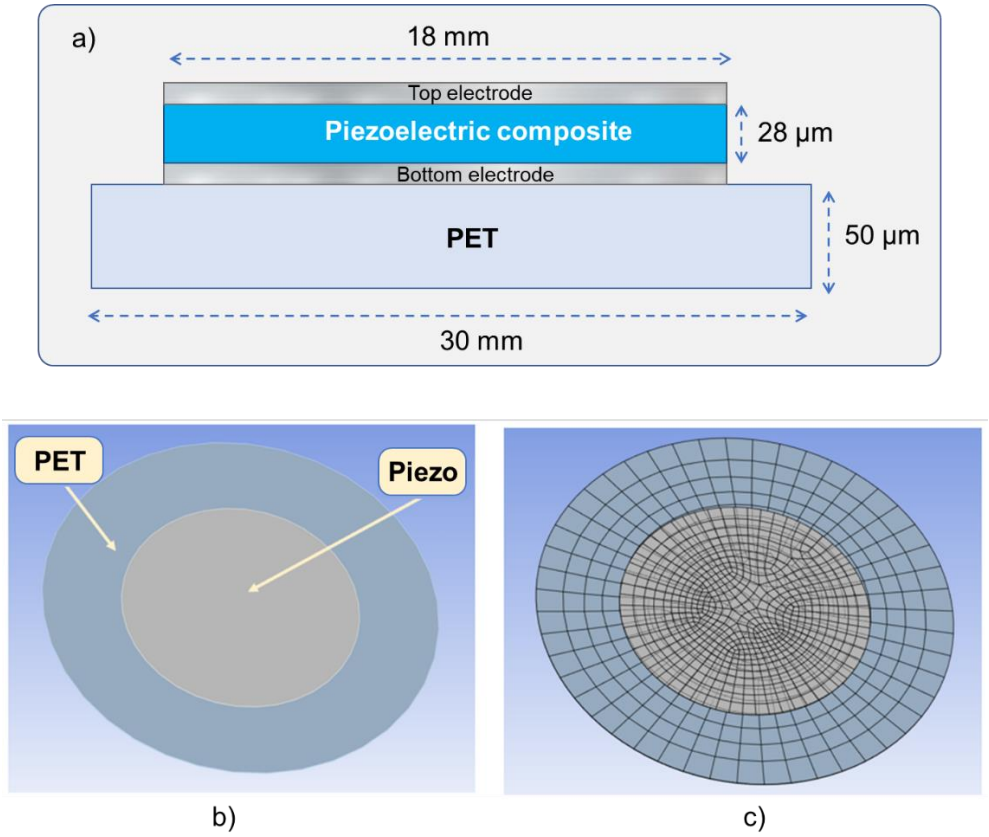

Figure 2.19: a) Geometry of a simple piezoelectric actuator; b) FEM of piezoelectric actuator built on ANSYS software; c) Mesh pattern used in simulation.

Table 2.2: Parameters of the analytical actuator model.

Material	**Properties**	**Symbol**
PET substrate		
Density	ρ	952 kg/m^3
Poisson's Raito	v	0.34
Young's modulus	Y	2.62 GPa
Diameter	d	30 mm
Thickness	t	50 µm
Piezoelectric composite		

Density	ρ'	3000 kg/m^3
Poisson's Raito	v'	0.37
Young's modulus	Y'	7 GPa
Diameter	d'	18 mm
Thickness	t'	28 µm
Relative permittivity	ε'	10.5
Piezoelectric constants	$e_{31} = e_{33}$	0.016 C/m^2
	e_{15}	0 C/m^2

2.7. Summary

Our study is based on two different applications of piezoelectric materials: sensor device for bearing load monitoring, and actuator device for haptic application. To fully achieve performance of each device, the architecture design, the fabrication process as well as the characterization methods have been conducted in different manners, to some extent. For instance, in the sensor system, load of bearing could be monitored in both radical and axial directions by extending the unidirectional (1D) sensor design into the bidirectional one. In the actuator system, however, bidirectional vibration sensed by user is supposed to be unnecessary, explaining why only 1D system has been explored. As the deformation of the piezoelectric element should be sufficiently enough to be detected by user, the idea is to increase a number of the actuator layers so as to boost the resulting strain of the whole haptic system. Furthermore, the target application of the piezoelectric sensor and actuator are different in such a way that the sensing elements were coated on steel rigid substrates (i.e., simulated as ball bearing system) while the actuating elements were deposited on a flexible transparent substrate (i.e., assimilated to touchscreen devices). In any case, the piezoelectric ink together with the fabrication process based on screen-printing AM are identical for both sensor and actuator devices. Finally, numerical model using FEM are conducted to confirm the experimental results. To achieve the best fitting between simulation and measurements, relevant physical parameters used in the ANSYS software of piezoelectric materials are carefully adjusted. Discussions regarding numerical solution together with empirical data will be thoroughly investigated in the next two chapters.

Chapter 3. Smart sensor coating based piezoelectric composite for condition monitoring of bearing

In this chapter, we explore an alternative method to detect and predict early failure of bearing via direct indicator by monitoring unidirectional (1D) and bidirectional (2D) loads thanks to a smart sensor coating. Choosing load as an indicator is relevant, as any change in bearing condition (structural damage) directly affects the load signal [176]. Among various smart sensor types, piezoelectric materials have been chosen because of their ability to respond to any stiffness change [177–179]. Here we thoroughly discuss on characterization results of the printed coatings that allows to assess their sensing performance for the condition monitoring (CM) of bearing. Full characterizations of dielectric and mechanical properties, together with direct sensing measurement are investigated on rectangular-shaped substrate (1D) and cross-shaped substrate (2D) using a 4-point bending (4PB) structure. To ensure the accuracy and stability of measurement as well as the durability of the printed coating, the developed prototype is built according to design rules commonly used in electronic circuit. Finite element model (FEM) are carried out to predict the mechanical property of the tested substrate under either unidirectional or bidirectional load. Regarding the output voltage of piezoelectric sensor, experimental results are revealed to be well corelated to the numerical simulation. It is pointed out that the output signal generated from the sensor (electrode) could be particularly affected due to the capacitive parasite come from the conductive tracks (CTs). Such a phenomenon might be reduced by printing them on the dielectric layer rather than on the piezocomposite layer. The study also investigates on a highly anisotropic shape of electrodes (rectangular instead of circle), indicating that orientation of such electrodes (in axial or radial) does matter the output measurement. To sum up, high performance of a sensor network coating depends not only on the ultimate characteristics of its own materials, but also on its structural design. Such an issue is nonetheless crucial to achieve reliable condition monitoring of bearing, especially for multidirectional load – a key signature of early failure detection.

3.1. Bearing

Bearing is one of the essential elements in almost any rotating machine [180–182]. A bearing is a mechanical component that facilitates the movement of one part of a machine or equipment relative to another. It is designed to reduce friction and provide support for the moving parts by minimizing the contact area between the surfaces in contact. For this reason, most rotating machines are equipped with bearings to support the load and maintain the clearances between the stationary and rotating elements of the machines [183]. Bearings are used in a vast range of applications, from large industrial machinery to small household appliances [5]. They play a crucial role in the smooth and efficient operation of machines as well as equipment, and are considered as essential components in many everyday devices. Bearings, the importance of which can never be overlooked, are according to the Institute of Electrical and Electronics Engineers (IEEE) the most likely elements to fail in an electrical machine [185,186]. Their failure is one of the most common problems that occur with high probability [187], particularly up to 90% in small machines [188].

For improved condition monitoring (CM) of bearing, various sensing and measurement technologies have been involved to provide operational indicators [189–192]. The CM makes it possible to improve knowledge of the structures by better supervising, reducing interventions, and optimizing the materials used. The ultimate goal of the CM involves in the development of autonomous, continuous monitoring systems capable of detecting structure damage in real time to avoid any accidents. The key challenges are in the early detection of damage, allowing optimal maintenance and, as a result, reduced cost.

3.1.1. Bearing geometry

Bearing geometry refers to the design and configuration of the components that make up a bearing. Figure 3.1 shows a typical bearing comprising the following components:

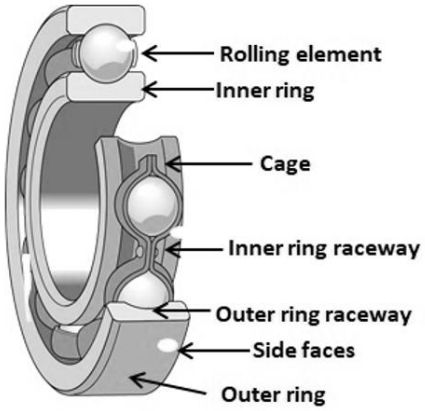

Figure 3.1 : Architecture of a ball bearing.

- Outer ring: This is the outermost part of the bearing that holds the bearing together and helps it to maintain its shape. It also serves as the surface against which the load is applied.
- Inner ring: This is the innermost part of the bearing that holds the rolling elements and helps to guide them. It also serves as the surface against which the rotating shaft is applied.

- Rolling elements: These are the components of the bearing that reduce friction by rolling along the inner and outer rings. Examples of rolling elements include balls, rollers, and needles.
- Cage: Also known as a retainer or separator, the cage is a component that separates and guides the rolling elements, keeping them evenly spaced and preventing them from colliding with each other.
- Seal: Bearings may have seals or shields to keep out contaminants such as dirt and water, and to retain lubricant. Seals may be made of rubber, metal, or plastic.
- Lubricant: Bearings require lubricant to reduce friction and wear between the rolling elements and the inner and outer rings. Common lubricants include oil and grease.
- Mounting features: Bearings may have mounting features such as flanges, threads, or shoulders to facilitate their installation and secure them in place.

These are the basic components of a bearing. The specific design and configuration of a bearing will depend on the application and the type of bearing being used.

3.1.2. Major types of bearing and their uses

The wide variety of applications in which bearings are used has necessitated the design of several bearing architectures depending on the application.

- Ball Bearings: These bearings consist of a row of small metal balls held in a raceway. They are widely used in various applications, including motors, pumps, and fans, where low friction and high speed are required.
- Roller Bearings: These bearings use cylindrical or tapered rollers instead of balls. They can support heavier loads and are commonly used in applications such as conveyor belts, vehicle wheels, and machine tools.
- Thrust Bearings: These bearings are designed to handle axial loads, which means they support forces applied parallel to the shaft's axis. They come in several types, including ball thrust bearings and roller thrust bearings.
- Sleeve Bearings: Also known as plain bearings, these bearings use a simple design with a metal sleeve that slides over a shaft to reduce friction. They are commonly used in applications that require low speed and low noise, such as ceiling fans and household appliances.
- Magnetic Bearings: These bearings use magnetic fields to suspend and rotate a shaft without any physical contact. They are ideal for applications that require high speed, high precision, and low maintenance, such as in turbines and compressors.
- Fluid Bearings: These bearings use a thin layer of fluid to separate two moving parts and reduce friction. They are commonly used in high-speed applications, such as in machine tools and aerospace equipment.
- Tapered Roller Thrust Bearings: These bearings are designed to handle both axial and radial loads. They are commonly used in automotive transmissions and heavy machinery.
- Spherical Roller Bearings: These bearings have a spherical outer ring that allows them to compensate for misalignment and angular movements. They are commonly used in applications such as conveyor belts, construction equipment, and wind turbines.

Figure 3.2 illustrates the main types of bearings. In this research, ball bearings are the subject of the study because they are commonly used in various aerospace applications: ball bearings used in various components of aircraft engines, such as in the main shaft, gearbox, and turbine rotor; in the landing gear of aircraft and also in various components of flight control systems [193].

Figure 3.2: Different types de bearings.

3.1.3. Bearing defects

A theoretical model for calculating bearing life is often provided by manufacturers. However, the contribution of many factors deviates from the normal operating conditions by causing premature deterioration and modifies the predicted operating time. In most cases, bearing defects start with a local loss of material on a dull surface (inner and outer ring, rolling elements). The most common types of bearing defects are:

- Wear: Wear occurs when the rolling elements or raceways of the bearing are subjected to repetitive loading and contact, leading to surface damage and material loss. Wear can result in increased friction, reduced load capacity, and decreased lifespan of the bearing.
- Corrosion: Corrosion occurs when the bearing components are exposed to corrosive environments, such as high humidity or chemical agents, leading to chemical reactions that can cause surface damage and material loss. Corrosion can result in reduced load capacity, increased friction, and premature failure of the bearing.
- Fatigue: Fatigue occurs when the bearing components are subjected to cyclic loading and unloading, leading to the formation of cracks and eventually complete failure of the bearing. Fatigue can result from excessive loads, high speeds, and inadequate lubrication.
- Misalignment: Misalignment occurs when the bearing components are not properly aligned, leading to increased stress, deformation, and damage to the rolling elements and raceways. Misalignment can result in increased friction, reduced load capacity, and premature failure of the bearing.
- Brinelling: Brinelling occurs when the bearing is subjected to excessive static loading, leading to localized plastic deformation of the raceway surface. Brinelling can result in increased friction, reduced load capacity, and decreased lifespan of the bearing.

To prevent bearing defects, it is important to follow proper installation, maintenance, and lubrication practices, and to select the appropriate bearing type and size for the application. Regular inspection and monitoring of the bearing condition can also help to detect defects early and prevent catastrophic failure. There are various methods to detect faults in the bearings, such as vibration monitoring [194,195], wear

debris monitoring [196], temperature monitoring [197], non-destructive test [198,199], and so on. However, some methods are not effective to determine the early faults condition. Among them, vibration signal analysis is the most common technique used for CM of bearings, but only provide indirect indicators that require pre-processing stage to convert them into useful representations. The treatment can only be achieved if an adequate model describing the relationship is available.

Our research explores an alternative method for *in situ* and *online* monitoring of the bearing load using smart piezoelectric sensor coating, making it possible to detect and predict the early failure via direct indicators. For a sake of simplicity, the bearing is assimilated to a steel substrate on which are attached screen printed multilayered sensors [200]. First, a rectangular-shaped substrate was used to characterize the unidirectional (1D) load. Then a more complex structure as a cross-shaped substrate was developed to assimilate the bidireciton (2D) load. Finite element model (FEM) is developed using ANSYS software to figure out the mechanical behavior of the steel substrate in different configurations (1D or 2D with asymmetric/asymmetric feature). Due to the typically thin sensing coating in comparison to the underlying substrate, the mechanical properties of the whole system are mainly determined by the characteristics of the steel-type material. Therefore, the effective piezoelectric behavior of the thin composite could be reliably inferred by using a 4PB setup. Practical tests allows to assess the sensor performance, which might be affected by several factors comprising length of conductive tracks and shape of electrodes. Understanding the role of each factor is of outstanding contribution to improve the structural sensing design so as to match specific requirements of bearing's CM.

3.2. Rectangular-shaped substrate

3.2.1. Simulation results

A four-point bending (4PB) setup is modeled using finite element method (FEM) of ANSYS Multiphysics. As depicted in Figure 3.3a, the 3D geometry comprises three main components including bottom support rollers, steel substrate (beam), and top blades. The support span (L) together with the distance between the load blades (b) can be varied. Regarding their relationship, the top side of the beam can be bended down (when $b > L$), or bended up (when $b < L$) and vice versa for the bottom side. Confirmation can be found in Figure 3.3b,c that illustrates the deformation evolution of the steel substrate across the length. In both cases, it is pointed out that the strain at the surface of the beam between the two inner points (supports or loads) is uniform and uniaxial, i.e. dominated by strain in the x-direction. Accordingly, whatever the configuration, the curvature principally generated in the pure bending area of the beam. Due to the small thickness of piezoelectric thin layer in comparison to the substrate, it can be assumed that the sensor layer is exposed to a constant positive strain in parallel to the x-direction that is equal to the strain of the steel substrate.

To validate the 4PB model implemented in ANSYS, it is necessary to compare the mechanical behavior of the substrate under static force between the simulation and the analytical model developed in Eq. (2.3) of Chapter 2. It has been observed in Figure 3.4 that the mechanical stresses induced from these two approaches are perfectly consistent for a large range of the input force (from 0 to 600 N) in both bending-up ($b < L$) or bending-down ($b > L$) configurations. Furthermore, a linear correlation between the stress and the force are obtained as predicted the analytical expression, confirming high accuracy of the FEM. To some extent, the

simulation enables to get a global and detailed view of the mechanical behavior along the substrate's length, while the analytical model only gives an estimation of the central point where the deflection is supposed to be maximum.

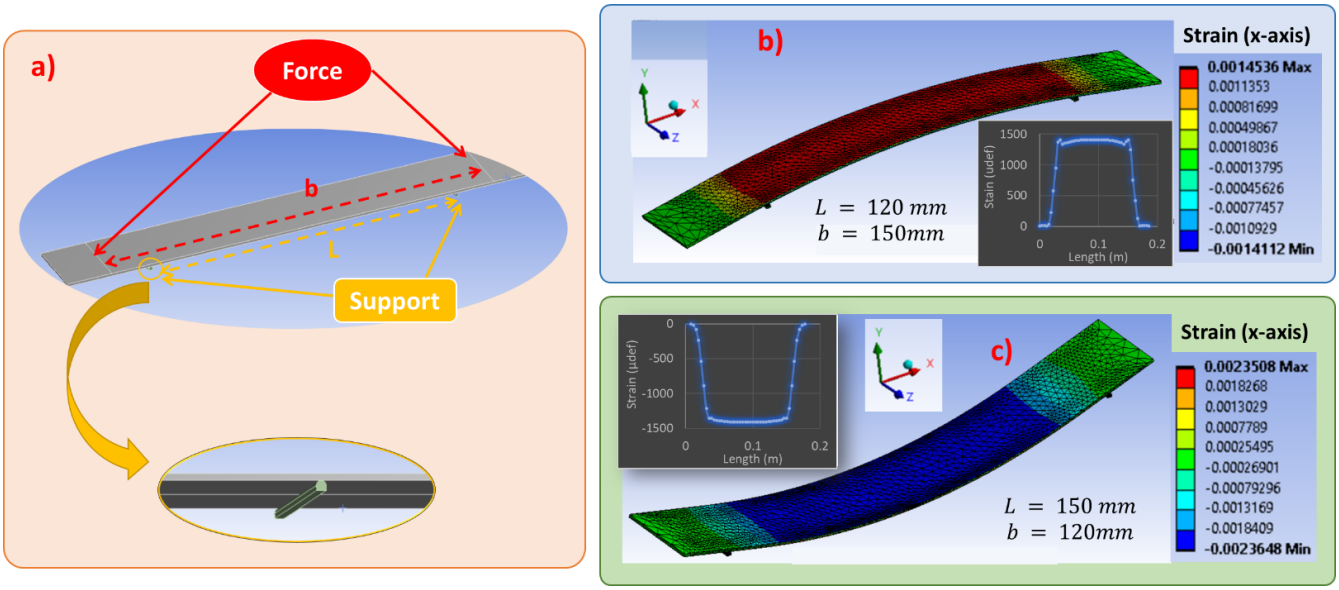

Figure 3.3. Mechanical model using FEM of ASYS: a) Four-point flexure design; x-direction strain across length in two different cases: b) bending down sample with $b > L$; c) bending up sample with $b < L$.

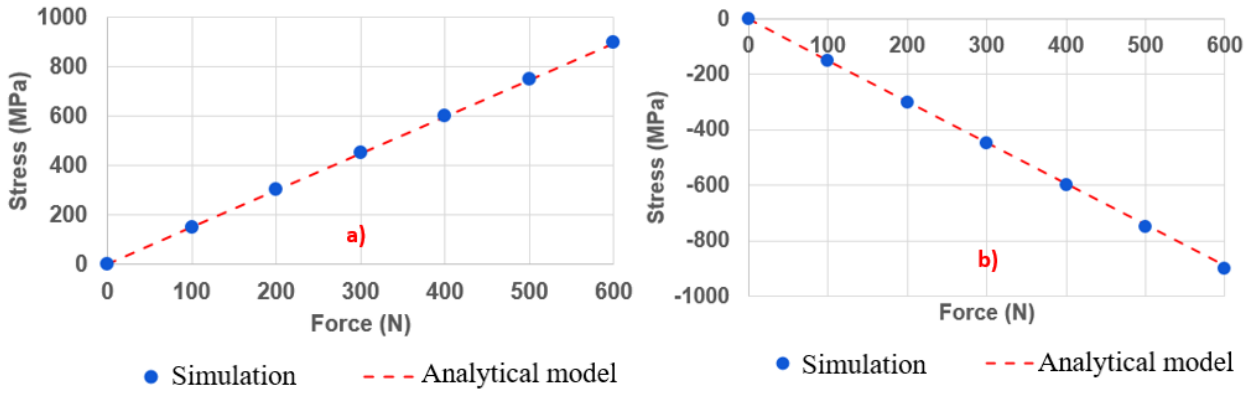

Figure 3.4: Comparison of mechanical properties between analytical model and simulation: a) $b = 120\ mm, L = 150\ mm$; b) $b = 150\ mm, L = 120\ mm$. Dashed lines represent the analytical model according to Eq. (2.3), while dotted symbols display the simulation data.

To investigate the piezoelectric effect of the sensing element, the piezoelectric layer on which attached five electrodes were deposited on the substrate surface (see Figure 3.5a). The purpose here is to determine the potential change appearing on the electrodes when the specimen is subjected to external loading. The support span and load span are respectively set as $L = 150\ mm\ , b = 120\ mm$. During simulation, an upward force from 0N to 300N (with a step increment of 50N) is applied to the beam and the generated output voltage at the center electrode is recorded. Similar practical test is conducted, allowing to obtain the

result of Figure 3.5b. The experimental potential output of the piezoelectric sensor shows very good linearity with the loading level, that well corelates with the theoretical output predictions of piezoelectric materials (Eq. (2.3)). Under 300 N, the measured potential of the sensor is found to be approximately 3.53V, while the corresponding simulation is 3.76V. The experimental outputs are somewhat smaller than the theoretical prediction and such a slight discrepancy may come from several factors such as material properties, measurement setup, and force application method.

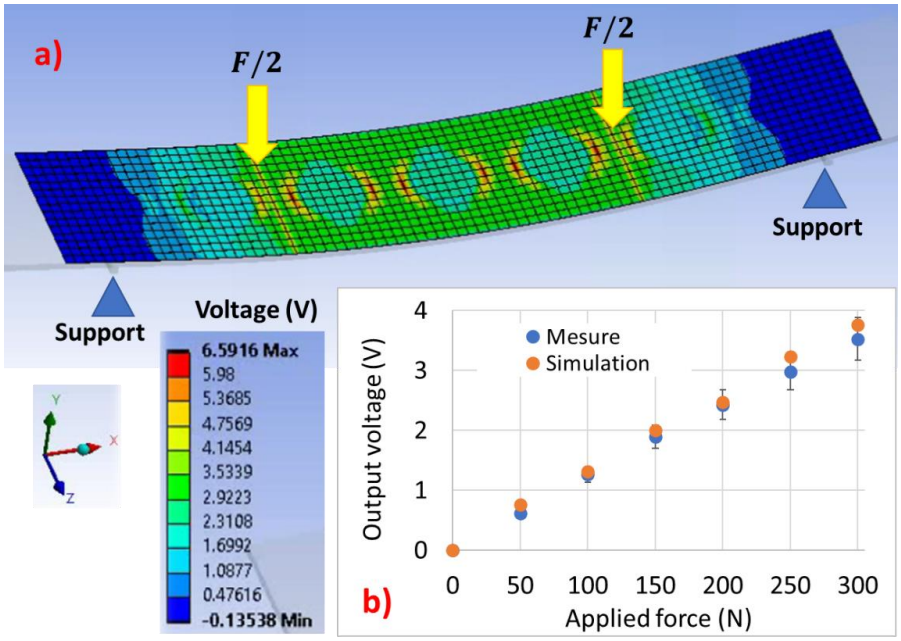

Figure 3.5. Piezoelectric response based FEM : a) voltage distribution on the top surface of $BaTiO_3$ composite sensor.; b) output voltage versus applied force of both simulation and experiement.

3.2.2. Experimental results

3.2.2.1 Broadband spectroscopy

Figure 3.6 illustrates the dielectric behavior of the $BaTiO_3$ composite performed on the 3 electrodes numbered as 1, 2, and 3. The results obtained from the 3 samples are quite similar, to some extent. A small discrepancy between the electrode 1 and the other might come from several sources: 1) measurement uncertainties; 2) non homogeneity of particle's distribution, which is inevitable during process; and 3) non uniformity of the printed layer's thickness, that could affect the calculation of the relative permittivity (ε_r). Actually, ε_r' (the real part of ε_r) is inferred from the measurement of the sample's capacitor (C), according to the following expression:

$$\varepsilon_r' = \frac{e\,C}{A\,\varepsilon_0} \tag{3.1}$$

where ε_0 denotes the permitivity in vacuum, e is the thickness of the piezoelectric layer, and A is the surface of the electrode. The thickness is determined using a simple system (FLORENZA, 24100, Thyez France), where 5 mesured was effectuated on the whole surface to improve accurancy.

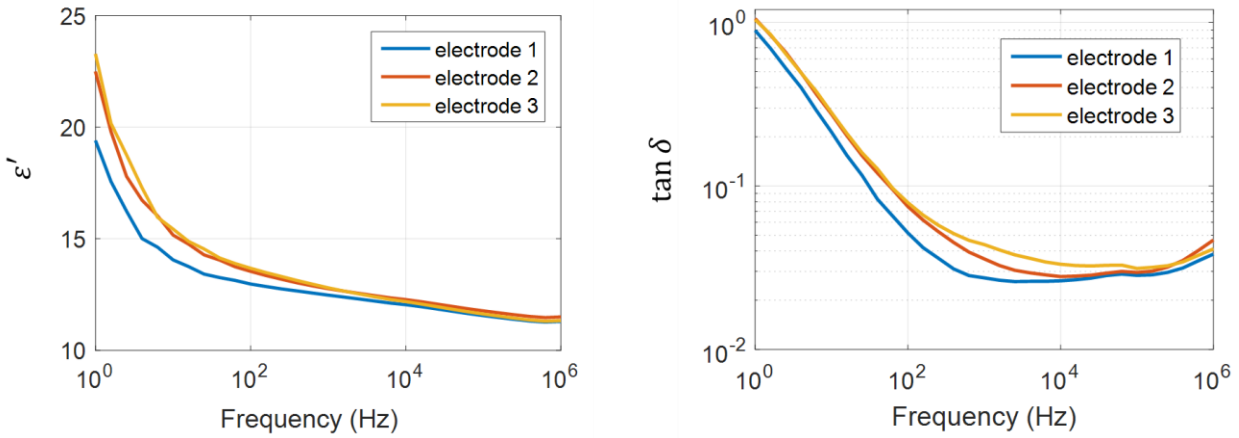

Figure 3.6: Dielectric properties under large frequency range: a) dielectric permitivity; b) dielectric losses.

As seen in Figure 3.6a, for all samples, the decrease relative permittivity (ε_r') with increasing frequency is related to dielectric relaxation of polymer [171,201]. Specifically, this behavior can be explained by the fact that at high frequency, dipoles are not sufficiently rapid to orient themselves, provoking a lag between the oscillating dipole and the applied field dynamics [202,203]. Nonetheless, at low frequency, high ε_r' value is probably originated from the interfacial polarization induced by large discrepancy in the permittivity of $BaTiO_3$ and PUA matrix. Meanwhile, the dielectric loss (tanδ) of the three samples decreases rapidly within low frequency range, which is due to the free charge motion within matrix based on conduction contribution [204–206]. On the other point of view, Aldar *et al*. [207] stated that such a behavior was originated from the basis of space charge polarization, i.e. dedicated to the Debye-type dielectric dispersion. Interestingly, the dielectric loss is lower and more stable within a frequency range of [1 kHz, 100 kHz]. This effect can be related to the dipolar mobility of the polymer matrix that dominates at high frequency [133]. On the other hand, an upward trend occurs at frequency beyond few hundreds of kHz, which is ascribed to the relaxation of dipolar orientational polarization [208–210]. It is reveled in Figure 3.6b that a second peak in the tanδ loss might be observed beyond 1 MHz, i.e., similarly to the one reported in [211]. Generally, dipole relaxation in a dielectric polymer is undesirable for sensor applications because this process is usually accompanied by great variations in permittivity (ε_r') and tanδ.".

3.2.2.2 Mechanical behavior

During experiments, an upward static force increasing from 0N to 400 N is applied to the steel substrate. The resulting deformation at the center (S_c) is recorded from the strain gage while the corresponding stress (T_{sc}) is deduced knowing the Young modulus (Y_s) of the substrate (see Table 2-1).

Figure 3.7a,b highlights the linear relationship between the measured strain and the applied input, regardless which configuration is chosen ($b < L$ or inversely). To some extent, the system exhibits the same mechanical response in either down or up bending, only the sign of the stress and the strain is inversed. This behavior is consistent to the symmetric properties of the 4PB setup. Finally, excellent consistent between experiment and analytical model has been achieved, reflecting high reliability of the model described in subsection 2.5.3 (cf. Chapter 2).

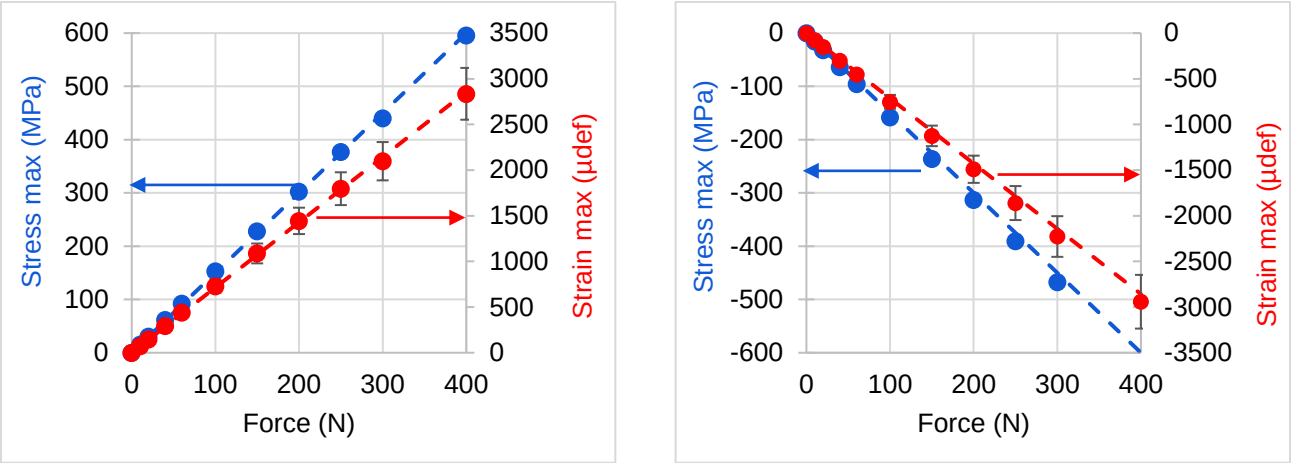

Figure 3.7. Comparison of mechanical properties between analytical model and experimental measure: a) $b = 120\ mm, L = 150\ mm$; b) $b = 150\ mm, L = 150\ mm$. Dashed lines represent the analytical model according to Eqs. (1) and (4), while dotted symbols display experimental data (error bars included).

3.2.2.3 Piezoelectric response

To better assess the piezoelectric performance, dynamic test is carried out under a triangle-waveform load with an amplitude of 175 N and frequency of 0.05 Hz. Figure 3.8a depicts the real-time output charge displacement (D_c) of the $BaTiO_3$ sensor, which is perfectly in phase with the applied load and the measured strain (S_c). This behavior is corelate to the typical characteristics of a piezoelectric material, where the generated electric signal is linear in response to the mechanical solicitation [137,212]. All measurements are carried out at the middle of the specimen, where the deflection is maximal. From the measurement of the strain S_c, it is easy to get the value of the stress ($T_c = Y \times S_c$, regarding Eq. (2.8)) applied on the middle of the sensor layer.

Hysteresis loops of the mechanical and piezoelectric properties are drawn in Figure 3.8b. On one hand, a small hysteresis area of the force-stress curve reflects negligible mechanical losses of the 4PB setup, which are probably due to static friction between the beam and the load points. On the other hand, large hysteresis behavior between the output charge displacement and the applied mechanical stress (D-T loop) confirms the existence of piezoelectric loss occurring during the conversion. It should be noted that for the D-T loop, the product $D \times T$ must be multiplied by a constant parameter (d_{31}/ε) to be equivalent to an energy density, with d_{31} being the charge coefficient and ε being the dielectric constant ($\varepsilon = \varepsilon_r \varepsilon_0$).

Besides the piezoelectric loss, the electromechanical conversion consists of two other loss components: elastic and dielectric losses. In our study, as the deformation of the piezoelectric composite is very small, it is thus reasonable to consider that the mechanical hysteresis loss of the sample is negligible. Nonetheless, the dielectric loss ($\tan\delta$) is more significant especially under low frequency excitation (see Figure 3.6b), which is mainly manifested by the ionic mechanism [132]. Finally, the slope of the output charge displacement versus the stress can be defined as the sensitivity of the piezoelectric sensor (i.e., d_{31} coefficicent), with units of pC/N. Inset of Figure 3.8b reveals that the sensitivity is amplitude independent in the low force range, where d_{31} is almost unchanged whatever the level of the input force. Interestingly, the longitudinal piezoelectric coefficient (d_{33}) can be deduced according to Eq. (2.10), which equal approximately 1.31 pC/N. This value is somehow smaller than the one obtained with the piezometer

(d_{33}~ 1.45 pC/N, see Figure 2.9). By considering the errors produced from each measurement method (i.e., around 10%), these values are coherent and situated within the uncertainty range.

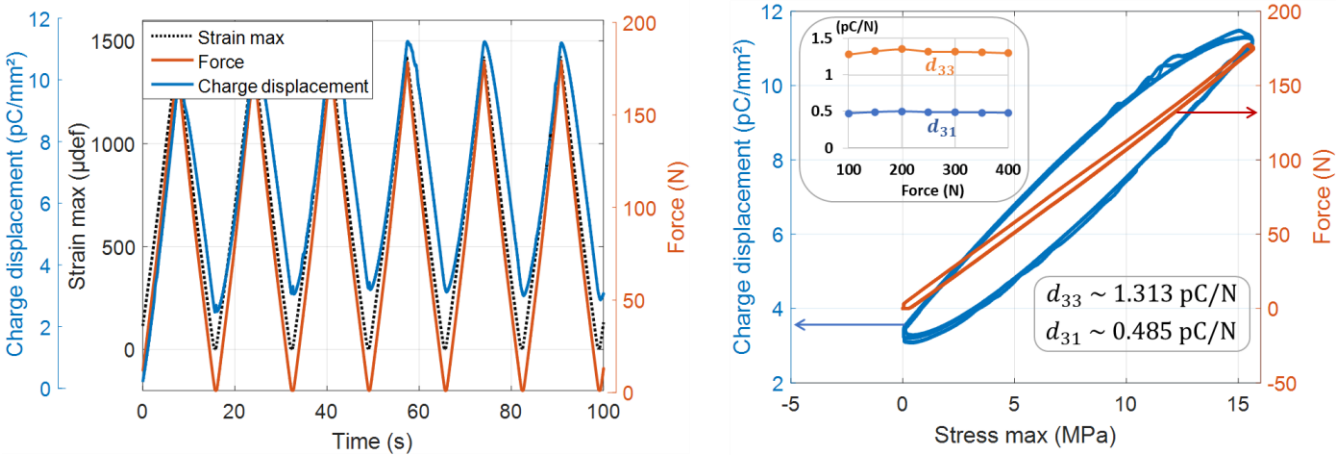

a) b)

Figure 3.8. Electromechanical response: a) Time evolution of strain, force, and charge displacement; b) Hysteresis loop of charge displacement versus strain (blue), and force versus strain (red); inset on the top left side represents the piezoelectric charge coeficicents (d_{33} and d_{31}) âs a function of the applied input force.

To evaluate the influence of the conductive tracks (CT) on the measurement of the piezoelectric response, experimental test is also carried out with another sample containing no CT. Both specimens are exerted by an input load varying from 0 N to 250 N, with an increment of 50 N. Figure 3.9a,b displays the generated charge displacement obtained from two sensors, being subjected to an increasing stress within interval of approximately [0, 20 MPa]. Data are acquired on the 3 electrodes with numbers indicated as shown in Figure 3.9. The results lead to the following conclusion:

- The sensor exhibits greatly linear response, confirming its feasibility in health monitoring for bearing.
- The electrode 1 leads to similar output charge in both two cases, either with or without CT. It is logical as its track length is neglected compared to the one of the electrodes 2 and 3.
- In case of no CT (Figure 3.9a), both electrodes 2 and 3 exhibits the same piezoelectric response. It can be explained by the fact that these electrodes are positioned inside the load points, where the induced strain is unchanged across the length. This value is equivalent to the maximum strain, which is confirmed by simulation result illustrated in Figure 3.3b). On the other hand, a decrease in the mechanical strain of the electrode 1 (i.e., outside the load points) provokes a drop of its output charge displacement.
- When the CT are printed on the sensor surface (Figure 3.9b), the piezoelectric sensitivity (d_{31}) is revealed to be higher in the electrode 3 than electrode 2, so corresponding to 8% discrepancy. Indeed, the higher the CT length, the higher the parasite capacitance being added into the circuit. This induces an overestimation of the sensor sensitivity as opposed to the one without CT, i.e., equivalent to 12% and 5% for the electrodes 3 and 2, respectively. The primary source of deviation probably result from an increase in the resultant capacitance, which in turn leads to slight error in the charge measurement.
- For the electrode 1, a decrease of the out charge with respect to the one of the other electrodes confirms a decrease in its strain, occurred outer the load points. As the charge displacement is plotted as a function

of the maximum stress, the piezoelectric sensitivity can be yielded from the D-T curve of the electrodes 2 or 3 only, but not the electrode 1.

- Assuming that the composite layer is perfectly uniform and the $BaTiO_3$ particles are homogeneously distributed within the polymer matrix. As a matter of fact, a decrease in the output charge displacement should be equivalent to a decrease in the induced strain, leading to unchanged piezoelectric sensitivity for the whole sensor surface, whatever its position. Discrepancy may come from measure uncertainties.

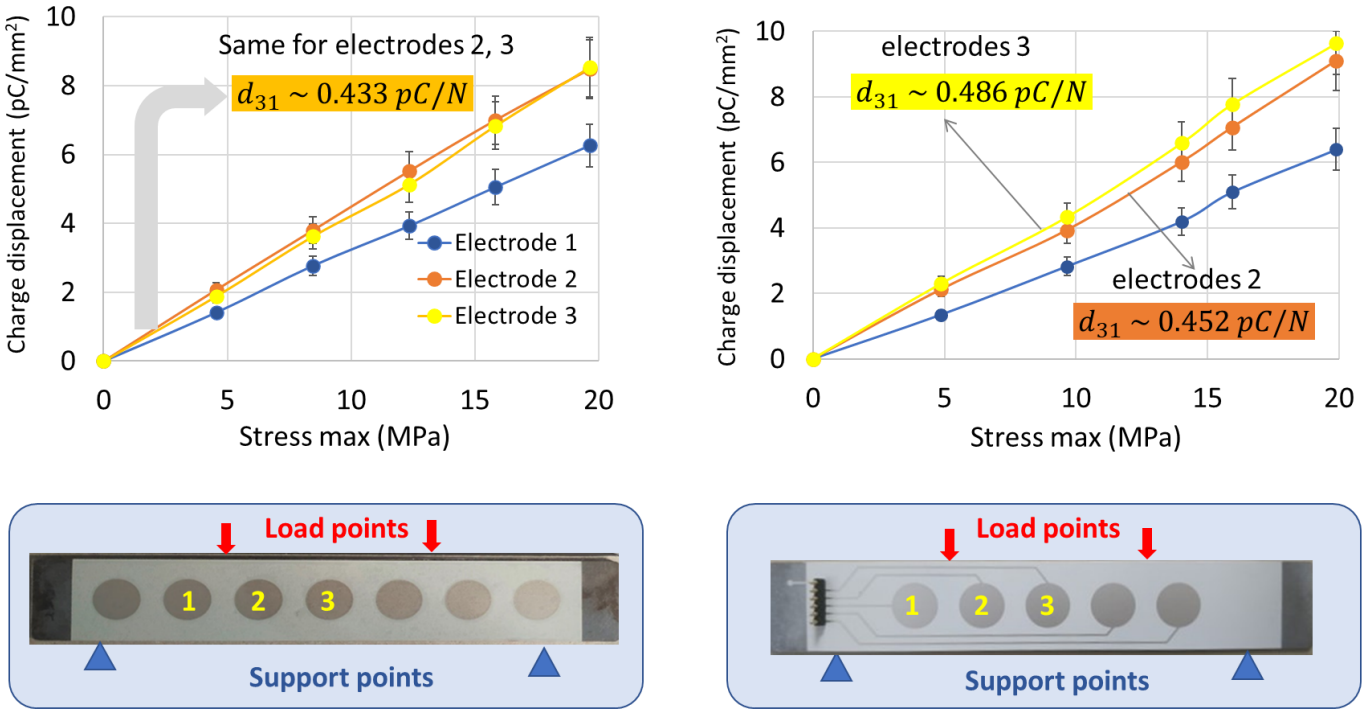

a) b)

Figure 3.9. Charge displacement versus stress of sample: a) without printed conductive tracks; and b) with printed conductive tracks.

The above results clearly highlighted the influence of CT on the piezoelectric characterization. However, discrepancy between CT and non-CT samples is quite small in the value of d31, even for the electrode 3. Considering the measure uncertainties of around 10–20 %, discrepancy caused by CT can be neglected. In other words, insulation treatment is not required to correct the CT effect, leading to simplified printing process. Based on the balance between improvement in measurement precision and simplification in printing steps, it is not worth introducing the dielectric layer.

When the CT are printed on a dielectric layer, we obtain similar result as in the case of sample without CT (Figure 3.9a). No different response between electrodes 2 and 3. However, small discrepancy of d_{31} still exists, which is undoubtedly originated from measure uncertainties between samples.

3.2.2.4 Temperature effect

To evaluate the temperature independence on the piezoelectric response of the printed sensor. The specimen was subjected to a dynamic force of 120 N amplitude and 0.05 Hz frequency. Figure 3.10a illustrates the charge displacement (D) under temperature range from – 20°C to 100°C. As seen, D is

somewhat fluctuated around 0°C, more stable from 10°C to 50°C, and decrease beyond 60°C. To better explain this phenomenon, temperature analysis of the relative permittivity (ε_r') together with the elastic modulus (Y) are carried out, as shown in Figure 3.10b,c. According to Eq. (2.8), the charge displacement D depends on the mechanical stress ($T = YS$) , as well as the piezoelectric coefficient d_{31} that related to dielectric constant (ε_r') of the sensor.

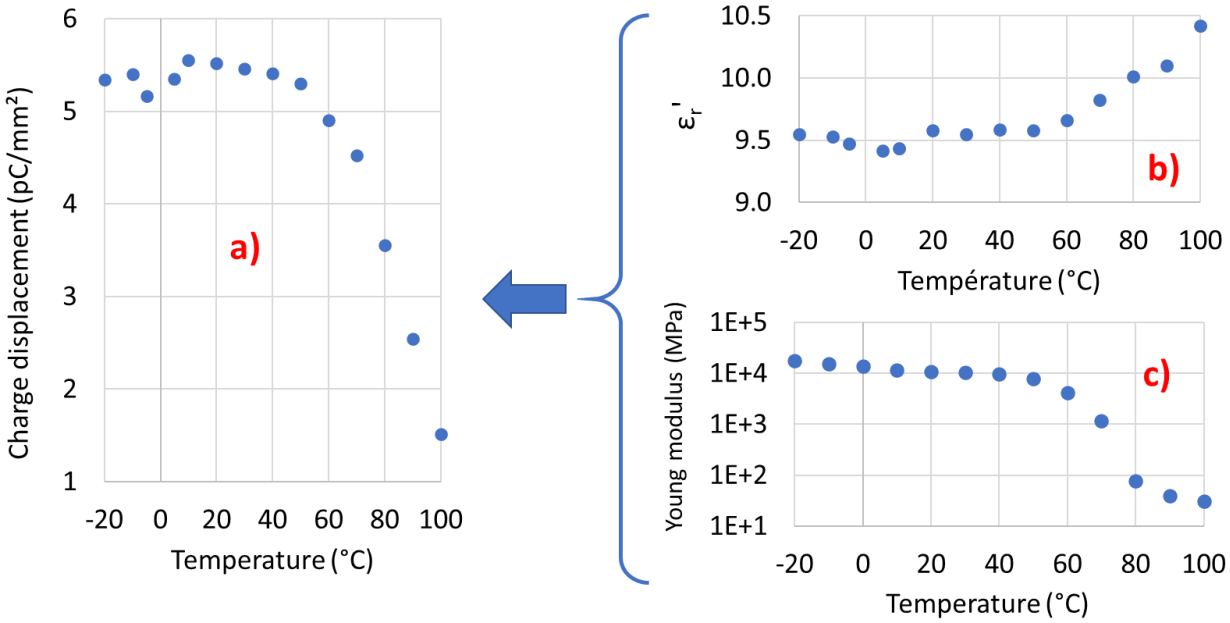

Figure 3.10. Teperature-dependent piezoelectric response: a) evolution of charge displacement relating to b) dielectric permitivity and c) Young modulus of composite.

Based on the results of Figure 3.10, it is possible to conclude that:

- Around 0°C, slight fluctuation of the charge displacement is similar to the relative permittivity. Actually, a phase transition occurs in BaTiO3 around that temperature range, provoking a variation of its dielectric property. It should be noted that such a variation is more obvious in the particle than in the composite, especially when the volume fraction of the particles is small (i.e. ~ 20%).
- The stability of the charge displacement from 10°C to 50°C are consistent with the steady behavior of the relative permittivity and the Young modulus within this temperature range.
- A huge drop in the charge displacement occurs at higher temperature, which mainly comes from the elastic behavior of the polymer. As reported on [213,214], the Young modulus of PUA considerably decreases when being passing the glass transition point (denoted as T_g, close to 60°C). Wilson *et al.* gave an explanation to this phenomenon, i.e., due to an increase in the molecular weight between network junction points (crosslinks) [215]. As the molecular weight between crosslinks increases, the elastic modulus above T_g decreases. This is consistent with theories relating rubber modulus to crosslink density [216].
- The dielectric permittivity somewhat increases with the increasing temperature from 60°C to 100°C. This behavior would stem from two principal causes:
    1) The segmental mobility of polymer with temperature: The higher the temperature, the greater the freedom of the dipole molecular movement. This leads to increase dielectric constant.

2) The dielectric response of the particles is temperature dependent: Above the glass transition, the dielectric permittivity of $BaTiO_3$ powders increase and reach the maximum at temperature that is close to the Curie point (T_g) [217–219].

- From 60°C, a decrease in the Young modulus is dominant with respect to a small increase of the dielectric permittivity (only 10%). As a result, the elastic property of the polymer is the principal contribution that drastically affects the piezoelectric response.

3.3. Cross-shaped substrate

In this study, we extend the 4PB approach to monitor bidirectional load (i.e., axial and radial). As a result, the sensors need to be mounted on a specific structure capable of detecting any mechanical change along two orthogonal axes [220]. A solution relying on the use of a cross-shaped subtract is investigated to testify the sensor ability in response to the bidirectional stress. This could provide valuable insights into the behavior of materials under different loading conditions.

3.3.1. Mechanical behavior based on simulation results

To assess the mechanical strain of the cross substrate in axial (x-axis) and radial (z-axis) directions, 4PB method based on FEM is investigated. All tests are performed under a constant total load of 250 N (i.e., denoted as $2F$), which is equally divided for applying to the four arms. By tuning the distance parameters between the supports (D_x and D_z) as well as the applied load (L_x and L_z), it is possible to distinguish three following configurations:

- Unidirectional load (Figure 3.11a): The mechanical load is applied in one direction only (e.g., axial) where $L_z = D_z = 0$, meaning that neither support nor load is involved in the z-direction.
- Symmetric bidirectional load (Figure 3.12a): The mechanical load is uniformly applied in both radial (z-axis) and axial (x-axis) directions where $L_x = L_z$ and $D_x = D_z$.
- Asymmetric bidirectional load (Figure 3.13d): The mechanical load is applied in the axial, radial directions but not uniform ($L_x \neq L_z$ and/or $D_x \neq D_z$). Three setting are shown in Figure 3.13a-c for a better comparison and for an easier assessment on the influence of each parameter.

For a sake of simplicity, the support span is set to be superior to the load span, meaning that $D_x > L_x$ and $D_z > L_z$. Inverting the sense of these inequalities makes the strain invert its sign, but not its magnitude. Evolution of the mechanical strains along the two axes (denoted S_x and S_z) is illustrated in Figure 3.11b, Figure 3.12b, and Figure 3.13a-c, i.e., correspondingly for each configuration. Pertinent concluding remarks are summarized in Table 3.1.

Table 3.1: Mechanical behavior of the cross substrate under three different configurations of 4PB test.

General observations for all configurations	• The induced strain is drastically dropped at the center (defined as intersecting area of the cross sample), as distribution of load in both directions results in decrease stress and thus strain. • Inversely at the two sides (out of the intersection), the strain is higher as load is contributed to one direction only. • The strain manifests a symmetric behavior with respect to the center, which agrees with the symmetric property of the 4PB method and the cross shape. • Three configurations make both S_x and S_z vary, but the total strain ($S_x + S_z$) is unchanged and only depends on the load level. • For a given load, the total strain of the 2D cross shape is similar to that of the 1D beam shape [30].
Unidirectional load applied along x-axis (Figure 3.11b)	• Strain along *x*-axis (S_x) attains a plateau at the two sides, which somehow corelates to the constant behavior of the beam substrate within the two points applied by inner loads [30]. • As the intersecting area is stressed in both directions, the strain along z-axis (S_z) is also varied at the center, but with much smaller amplitude and inversed sign ($S_z < 0$ while $S_x > 0$). • S_z is negligible at the two sides, as they are out of the intersection that is subjected to free load.
Symmetric bidirectional load (Figure 3.12b)	• As expected, S_x and S_z are perfectly identical. • At the intersecting area, stress is equally distributed along *x*- and *z*-axis, leading to smaller S_x compared to the unidirectional case. • Maximum stress is found at the area applied by load. • The distance parameters (L_x, L_z, D_x, D_z) strongly affect the allure of the stress/strain: L_x and L_z defines the width of the maximum peaks while D_x and D_z delimit the length of the zone where appearing the deformation (meaning that out of this zone no strain is induced).
Asymmetric bidirectional load (Figure 3.13a-c)	Similar to the last three observations as in the case of "Symmetric bidirectional load", moreover: • S_x and S_z are not the same. • The tuning is more flexible, which is based on 4 distance parameters instead of 2 (Figure 3.13c). • Modification of parameter in one direction could lead to change in the other direction: comparison between Figure 3.12b and Figure 3.13a (or Figure 3.13b) where L_z (or D_z) is modified allows to conclude that allure of S_z and S_x all changes. • For a given value of *D*, higher value of *L* gives raise to larger constant plateau on the side area, but smaller peak (Figure 3.13a). • For a given value of *L*, higher value of *D* leads a decrease in the peak level and the plateau width (Figure 3.13b).

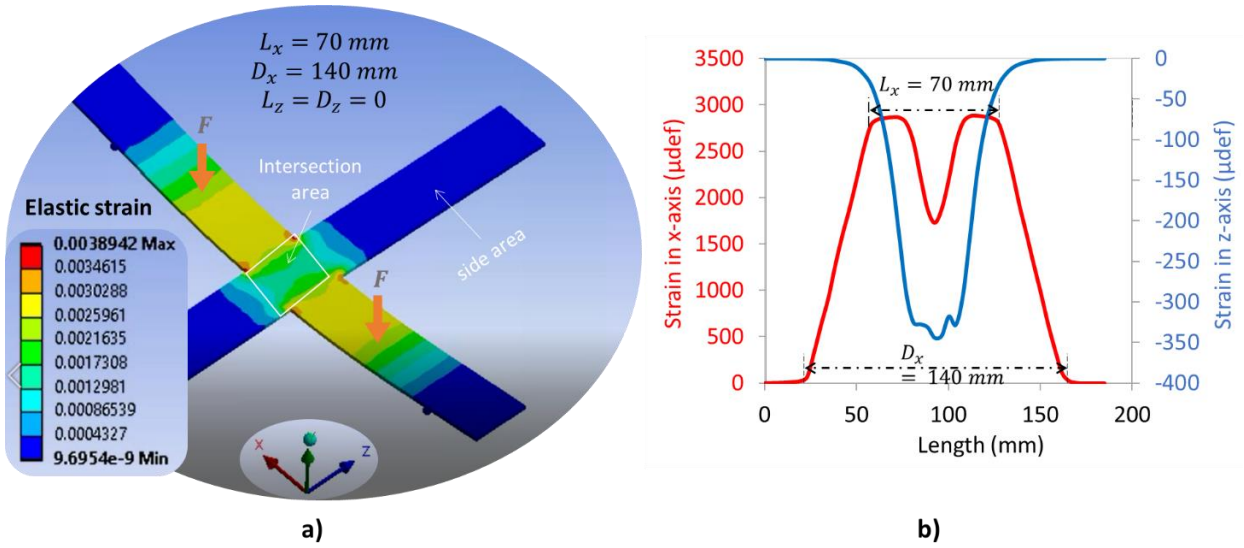

Figure 3.11. Unidirectional model using FEM: a) Four-point flexure design with load applied on x-axis only; b) Strain in both x- and z-axis versus their own length.

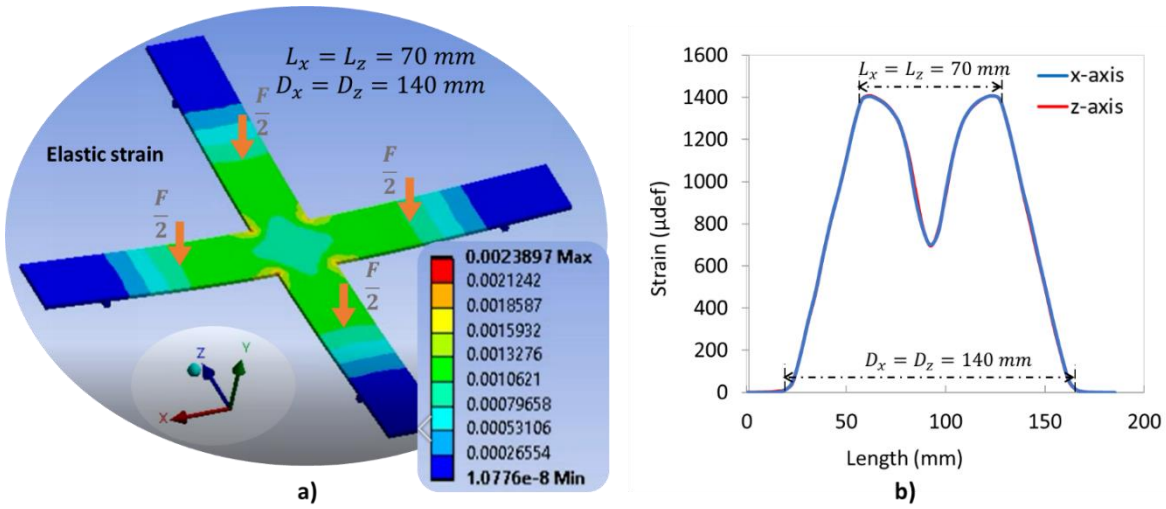

Figure 3.12. Symmetric bidirectional symmetrical model using FEM: a) Four-point flexure design with load applied on x- and z-axis ($L_x = L_z$ and $D_x = D_z$); b) Strain in both x-axis and z-axis versus their own length.

To assess the piezoelectric performance, a total upward load from 0 N to 250 N (with a step increment of 50 N) is applied to the cross substrate, and the generated output voltage at the center electrode is recorded (Figure 3.14a). Similar practical test is conducted, allowing to compare the voltage values measured from the bending test and those obtained by the simulation. As confirmed in Figure 3.14b, the experimental potential output of the piezoelectric sensor shows very good linearity with the loading level, that well corelates with the numerical output predictions of piezoelectric materials [30]. Under 250 N, the measured potential of the sensor is found to be approximately 1.4 V, while the corresponding simulation is 1.5 V. The experimental outputs are somewhat smaller than the model estimation, and such a slight discrepancy may come from several factors such as material properties, measurement setup, and force application method.

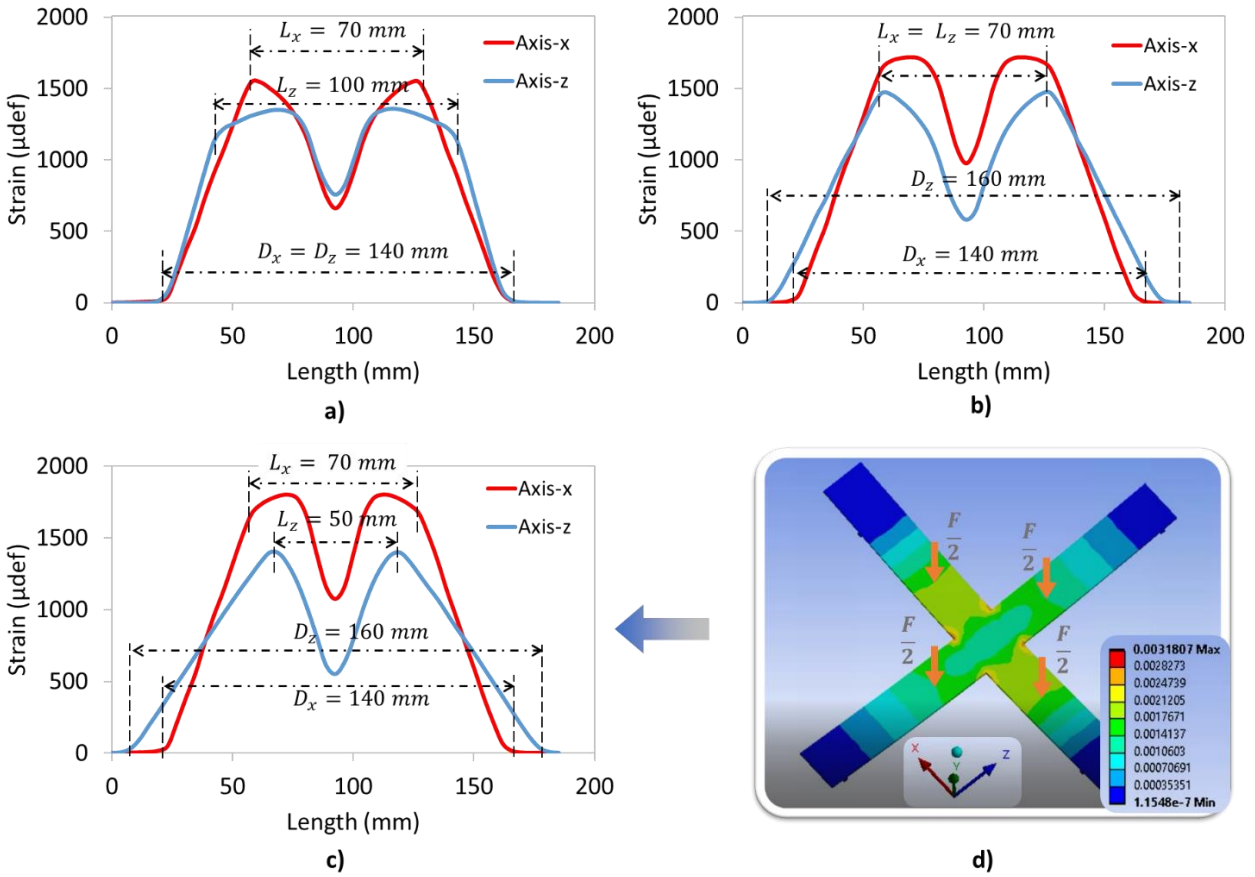

Figure 3.13. Asymmetric bidirectional model using FEM: Strain in both x-axis and z-axis versus their own length with a) $L_x \neq L_z$ and $D_x = D_z$; b) $L_x = L_z$ and $D_x \neq D_z$; c) $L_x \neq L_z$ & $D_x \neq D_z$ where numerical image is shown on d).

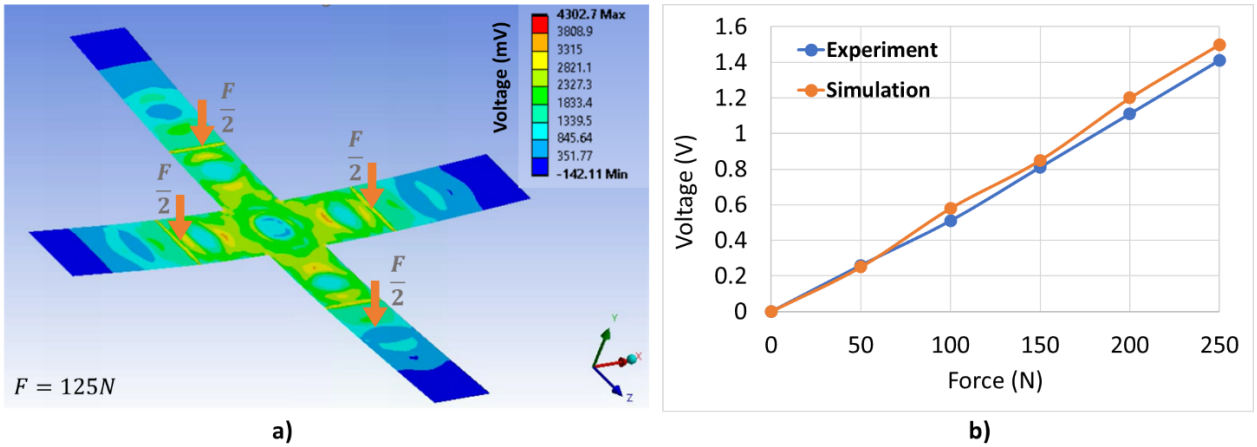

Figure 3.14. Comparison of the output voltage between experiment and simulation.

3.3.2. Bidirectional effect based on experimental results

3.3.2.1. Linearity of piezoelectric response

This study aims to assess the linearity of the piezoelectric behavior in response to a given mechanical stress, which strongly depends on the three configurations previously introduced in Subsection 3.3.1. Mechanical behavior based on simulation results unidirectional load, symmetric and asymmetric bidirectional load.

Figure 3.15 depicts the piezoelectric charge displacement of the central electrode in response to the total strain, which is the sum of the axial and radial strain values. The input load is controlled by a triangular and periodic waveform whose amplitude varied from 0 to 250 N, with an increment of 50 N. For all configurations, excellent linearity of the piezoelectric response has been achieved, reflecting high sensing performance of the printed coating in a detection of either unidirectional or bidirectional load. Interestingly, the uni-axis gives raise to higher total strain than the multi-axis, resulting in a little higher charge displacement. This observation somehow corelates to the simulation reported above where the strain of the center is revealed to be drastically dropped in both directions. Such an effect, nonetheless, does not much affect the piezoelectric charge coefficient estimated from the slope of the characteristics curve shown in Figure 3.15. Concerning the bidirectional load, both symmetric and asymmetric setting parameters lead to the same measures in the total strain and the charge displacement. Finally, all these results confirm high robustness of the 4PB method as well as stable piezoelectric response of the sensor coating prototype, whatever the level and the direction of the input load are driven.

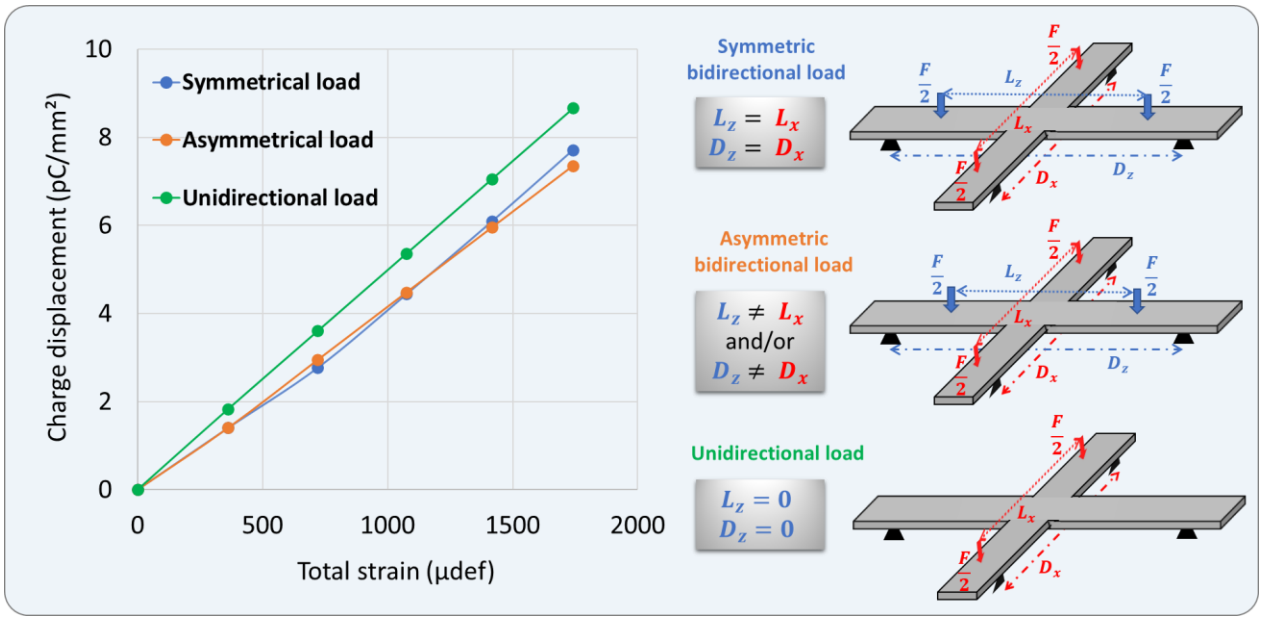

Figure 3.15. Charge displacement measured at the center electrode as a function of its total strain under three configurations of 4PB: unidirectional load, and bidirectional load with symmetry or asymmetry.

3.3.2.2. Impact of the conductive tracks and the dielectric layer

With the aim of evaluating the effect of conductive tracks (CTs) on the piezoelectric sensing performance, test measurements are performed on the peripheric electrode that leads to the farthest distance

from the electrical connector (see Figure 3.16). For other electrode with shorter CTs, the effect of CTs would be smaller; but an efficient treatment to somehow eliminate the impact of these tracks is still considered to ensure the correct signals of the sensors. Due to that reason, a simple solution based on integration of a dielectric layer on which are coated the CTs is getting involved. For a better comparison, three designs are performed as described in Figure 3.16:

- No tracks no dielectric (namely NTND): Only circle electrodes are stacked on the piezoelectric layer, no conductive track neither dielectric layer is needed. This design is considered as the simplest one that leads to the best accuracy in empirical measurement. That why it is preferred to be employed on lab-scale characterizations. In industrial scale, however, CTs are needed to perform online monitoring via the sensing device printed on the bearing surface. After being implemented, the sensor coating might not be dismantled out of the bearing system.
- With tracks with dielectric (namely WTWD): CTs are coated on the DL to minimize their effect with respect to the active area defined by the electrodes, which are in turn coated on the dielectric layer. This architecture is built in a full configuration composed of four layers, which is intentionally designed to be integrated on the bearing system.
- With tracks no dielectric (namely WTND): Sample with CTs and electrodes all printed on the piezoelectric layer, as no dielectric layer is implemented. This design allows to figure out whether or not the CTs have an impact on the sensor measurement.

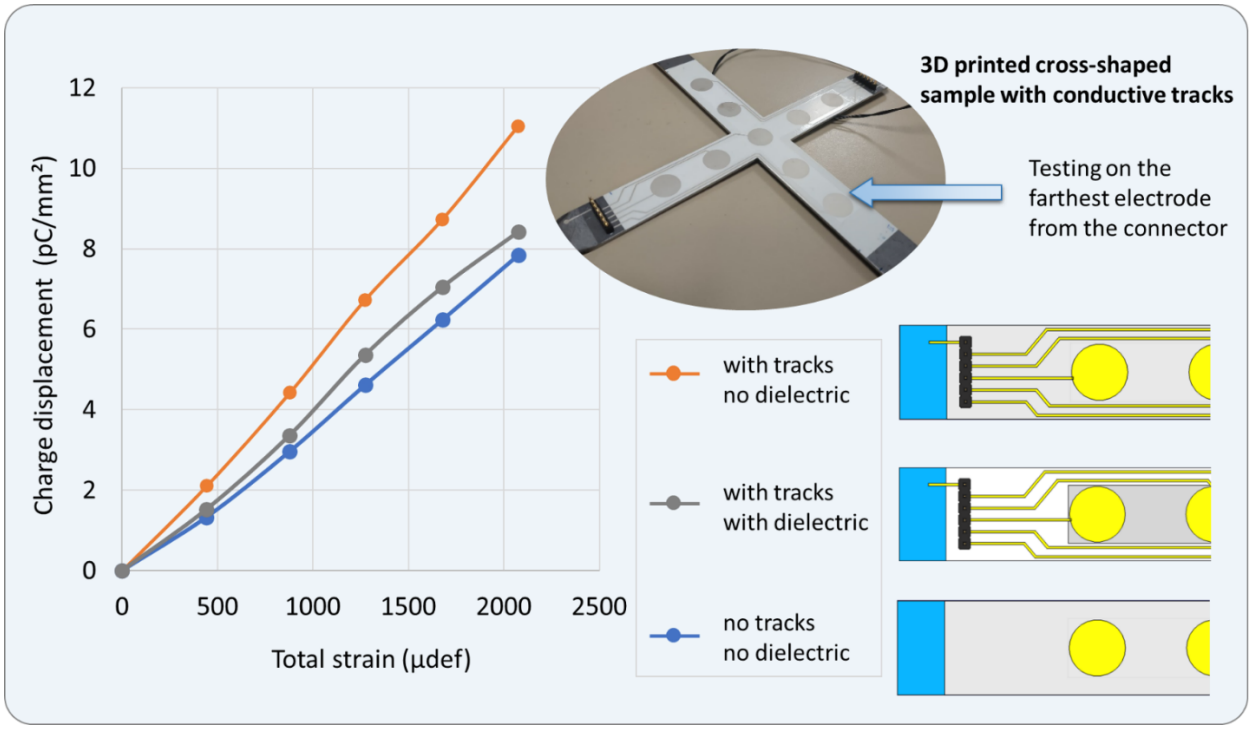

Figure 3.16. Piezoelectric response of three tested samples with or without conductive tracks (CTs) and dielectric layer. Measurements were performed on peripherical electrode that has the longest CT.

Regardless the load level (varying from 0 to 250N), all samples result in the same total strain, confirming that both CT and DL do not much affect the mechanical properties of the sensor coating. Interestingly, the two samples with CTs have higher charge displacement than the NTND sample (blue curve), demonstrating that CTs do disturb the electrical measure of the sensor. Although the diameter of the tracks is revealed to be small enough (0.7 mm width), their length is nonetheless considerable, particularly when they pass over

the most deformed regions of the sample. As it can be seen, the WTND sample gives rise to an increase of 40 % in the piezoelectric sensitivity (i.e., reflected by the slope of the orange curve displayed in Figure 3.16) as opposed to the NTND counterpart (blue curve). Figure 3.16 indicates great contribution of the dielectric layer (DL) in correcting the sensor output signal troubled by significant-length tracks. Indeed, a presence of DL in the WTWD design (gray curve) has successfully compensated the CTs impact. A discrepancy of 9 % only was observed with respect to the referenced sample without tracks (NTND), contrarily to 40 % as in the case of without dielectric layer (WTND). Actually, the fact of introducing the DL did not allow to totally overcome the CTs' impact on the charge measurement, which might be come from small dielectric losses of the DL itself. However, regarding the measure uncertainties (of around 10%), 9% discrepancy between the WTWD and NTND samples seems to be a satisfying result, confirming that implementation of DL is of primary importance in a real device.

3.3.2.3. Influence of electrodes' shape

The previous experiments were carried out on samples printed with circle electrodes whose shape was revealed to be directional independent. In other words, the mechanical strain measurement of these circle sensors is similar in both axial and radial directions, and so is the charge displacement. To highlight the effect of sensor's shape on the output signal, electrodes were designed as an anisotropic rectangular shape ($12 \times 3\ \mathrm{mm}^2$) with sufficiently high aspect ratio (factor 4 between the two sides). Full printed coating composed of nine rectangular sensors are displayed in Figure 3.17a, where sensors' length can be put along either axial or radial direction. With the aim of separating the effect of conductive tracks (CTs), practical tests were performed on the simple design with neither CT nor electrical contact. Consequently, the out signals of the sensors are acquired through two "permanent magnet" connectors attached on the electrode and the steel substrate, which is conductive enough to be considered as an electric ground. The selected magnets are revealed to be good conductors so as to ensure excellent continuity of the whole circuit.

The electrodes are numbered from 1 to 9 as depicted in Figure 3.17b. For a sake of simplicity, experiment was only set in the unidirectional configuration, e.g., in radial axis as described Figure 3.18a. It can be observed that the induced strain (computed from numerical model) drastically drops at the center and seems to be constant at the two sides. This explains why the piezoelectric response of the electrode 3 (blue curve) is lower than the one acquired from other side sensors along the radial direction (i.e., electrodes 4, 5, 6, and 7 shown in Figure 3.18b). Interestingly, for a given applied load, these side electrodes attain identical output electrical charge (and thus the piezoelectric sensitivity); even though they are not oriented in a similar direction. Concretely, electrodes 5 and 6 are placed along the axial direction while electrodes 4 and 7 in the radial one. As a consequence, the orientation (and thus the shape) of the sensor does not influence the measurement, if it is located on the area induced by a constant deformation. Inversely for the sensor 3 whose strain strongly varies at the electrode's surface; its electrical signal might be affected by its orientation and shape. It is therefore interesting to perform the response of the sensor 3 in axial direction as well. Rotating the cross sample by an angle of 90° allows to achieve this configuration, and the result is displayed in Figure 3.18b (red curve). Based on the comparison of the charge generated on the central sensor along two directions (red and blue curves), several relevant points are pointed out as below:

- Orientation of the sensor 3 does matter to the charge measure, which is manifested by discrepancy between radial and axial direction.

- Radial direction of the sensor 3 (equivalent to its width axis) leads to higher output signal than axial direction (equivalent to its length axis), because of significant strain variation occurring at the cross's center.
- Mechanical strain, strongly affects the determination of the sensor sensitivity, must be estimated for the whole area covered by the electrode.
- In reality, the deformation on the bearing might not be always uniform, the shape and orientation of the electrode should be carefully considered.

Figure 3.17. Cross-shaped sensor network coated with rectangular electrodes: a) Full printed coating with CTs and DL; b) Simple coating without CTs and DL.

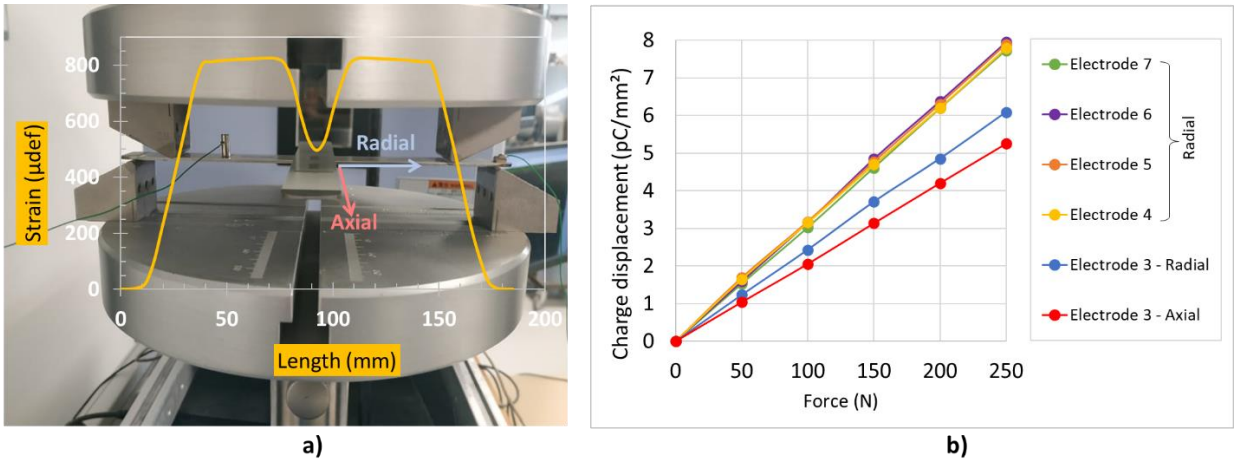

Figure 3.18. 4PB unidirectional test of cross substrate coated with rectangular sensors: a) Mechanical strain measured at the center electrode; b) Evolution of the charge displacement in response to the mechanical load applied to different electrodes. For the center electrode, measure was carried out on both axial and radial directions.

Noted that the output electrical charge of the other side sensors (i.e. electrodes 1, 2, 8, 9) in the radial direction is assumed to be negligible as no load applied on their substrate. This behavior is also confirmed by numerical simulation described in Figure 3.11a. Thus, the curve of these sensors were not displayed in Figure 3.18b. Thanks to the symmetry of the cross shape, the response of electrodes 1, 2, 8, 9 in axial direction would be similar to the one of electrodes 4,5,6,7 in radial direction. To sum up, side sensors can be used to monitor unidirectional load, and their output signal is the same for cross substrate and beam substrate [30]. Central sensor gives out a response in both axial and radial loads, so could be used as bidirectional sensing device. To the material point of view, all these sensors have the same physical characteristics, but depending how they are implemented with respect to the host structure, they could induce different output behaviors. Last but not least, understanding the sensor's characteristics is not sufficient; enhancing its design and implementation is of primary importance as well to fully achieve the sensor's potential.

3.4. Condition monitoring of aerospace bearing

3.4.1. Smart coating design

Aircraft operators are continually striving to reduce both the amount and the cost of maintenance. While at the same time ensuring the aircraft safety, reliability and integrity are not usually compromised. One solution which has seen a lot of attention is known as condition monitoring, with the aim of developing the ability to detect, diagnose and locate damage, even predicting the remaining useful life of the structure or system [221]. In the field of aerospace, bearings are the key elements that widely used as low friction joints between rotating components. Since the rotational motion is often a significant function of the overall system (such as wheels or rotor on an aircraft), proper functioning of a bearing over its designed life cycle is of vital importance to ensure product quality, prevent machine damage or even loss of human life [222]. However, because of faulty installation, inappropriate lubrication, overloading, and other unpredictable adverse conditions, premature and sudden failures of individual bearings often occur in real world applications. For improved bearing health and safety monitoring, the research community has been investigating a wide range of topics related to bearing structural design, dynamics, tribology, fault detection, identification, and signal processing techniques [223,224]. Various sensing and measurement technologies have been developed for improved monitoring of bearing operational parameters. Typical representatives include acoustic emission meters, fiber optic monitors, and vibration spectrum analyzers [116,225]. To measure bearing vibrations, eddy current-based displacement sensors have been developed that can be mounted through or to the side of a bearing cap to monitor radial or axial shaft motion with respect to the bearing [226]. Other types of bearing vibration sensors make use of velocity, acceleration, temperature, or spectral energy information [227,228]. While these efforts have considerably advanced the state-of-the-art of bearing condition monitoring, few of them have been widely used for practical, on-line applications. The need for an effective, reliable, and on-line bearing fault detection technique is primordial to detect and replace faulty bearings on several aircraft engines [229]. This situation clearly indicates the need for developing an integrated bearing condition monitoring and self-diagnostic technique for on-line, in-process applications.

Figure 3.19 illustrates a future perspective of smart sensor coating used for condition monitoring of bearing. The printing process of the piezoelectric ink on outer ring (Figure 3.19a) is revealed to be similar

to what has been done on the steel substrate. Bearing could be instrumented with thin-film coating sectorized by 8 electrodes with dimension of $L \times W = 2 \times 8\ mm^2$ and 10 µm thickness (Figure 3.19b). Regarding the important curvature of bearing, the area of each electrode is designed small enough to be considered as a flat surface whose configuration is close to the. As a matter of fact, it can be supposed that the force applied on each electrode is almost constant, leading to homogenous deformation induced in each sensing element. This specific design makes it possible to accurately determine the local force exerted on the rolling balls in axial and radial directions. Monitoring charge measurements of all sectorized piezoelectric sensors allows to determine a complete load mapping of the whole bearing system. Due to specified geometry of the outer ring, rectangular electrodes were preferred instead of circle ones. Electrical connector together with conductive tracks stacked on a dielectric layer are also included to facilitate measurements as well as to achieve full smart coating with minimization of undesired effect. Different sizes of housing system were used to fit with several dimension of bearing. Typically the bearings used in the laboratory have 15 mm of thickness, 110 mm and 45 mm of outer-ring and inner-ring diameters, respectively. The real bearing used in a motor of aircraft is usually bigger. Future development focuses on implementation of the developed active sensor bearing on a dedicated test bench, together with assessment of the design performance in a real condition (Figure 3.19c).

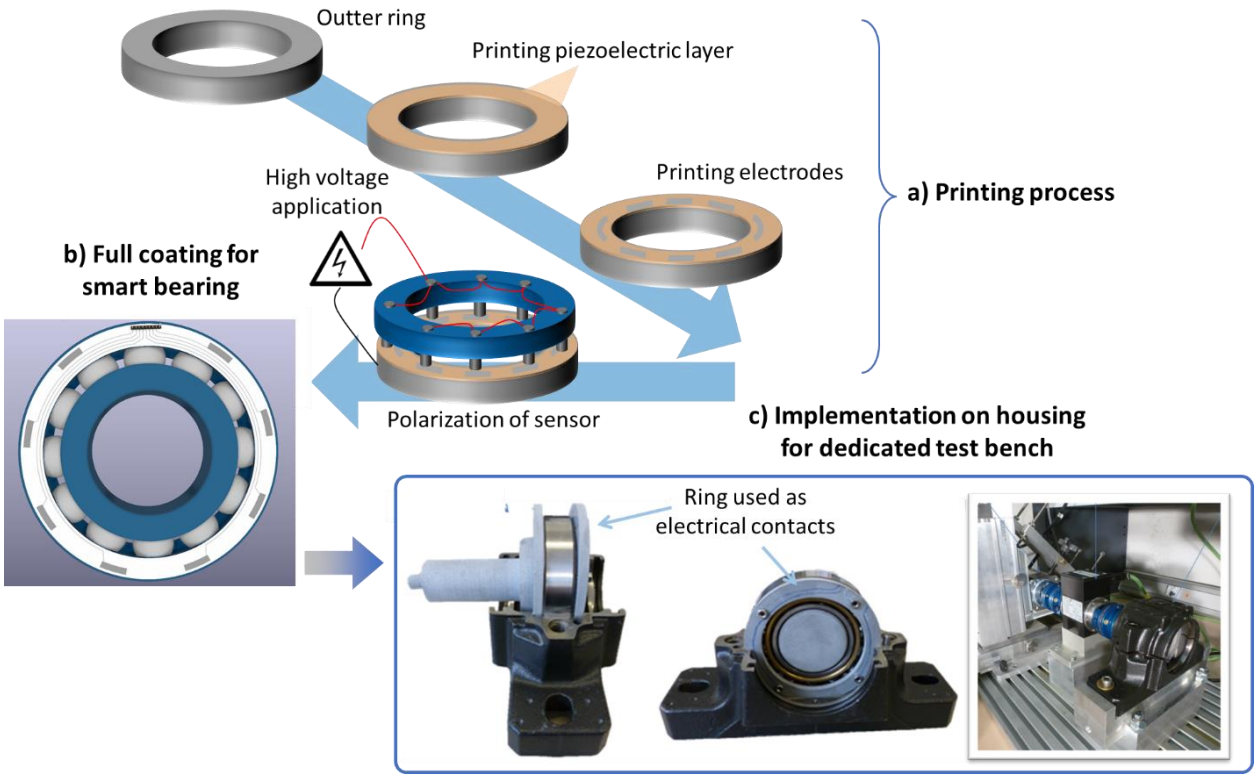

Figure 3.19. Future development on smart sensor coating for condition monitoring of applied load: a) Printing process, b) Full design of smart bearing; c) Implementation on housing for dedicated test bench.

3.4.2. Preliminary results – A comparison with strain gage

Figure 3.20a-b respectively illustrated the bearings instrumented with a commercially available strain gage and piezoelectric sensors sectorized by 8 electrodes of 2 µm thickness, i.e., designed by our team. For a sake of simplicity, data acquisition is merely performed on one sensing piezoelectric element. The dimension of each electrode is small enough ($W \times L = 2 \times 5\ mm^2$) to be considered as a flat surface. In this preliminary test, a static load of 10kN was applied to the bearing by means of a hydraulic press, in the axial direction only. The inner ring of the bearing was driven via a synchronous electric motor (AKM33H, Kollmorgen) with a rotational speed of 2000 rpm. As observed in Figure 3.20, allure of the electric charge delivered through the piezoelectric coating is somehow correlate to the measured strain of the commercial gage that is in response to the same mechanical excitation. Some discrepancies has been observed, which can be explained by two following reasons.

First, the position of the two sensing elements on the bearing is not identical, as illustrated in Figure 3.20c. The position of the strain gage was in the path of the mechanical stress, while the piezoelectric composite was chosen to be integrated on the bearing outer ring. Consequently, these two sensors do not capture exactly the same information of deformation, and the level of mechanical stress sensed by the piezoelectric coating is much lower with respect to the strain gage. Figure 3.20c clearly confirms this observation, where the load distribution (i.e., proportional to the deformation) is substantially higher in the mechanical path than on the outer ring. However, to implement a strain gage, a groove has been machined to locally increase the level of mechanical stress seen by the sensitive element. Such an approach is not applicable with an important number of sensors, since it is intrusive for the bearing structure that would lead to a complete redesign and significant human/material costs. This is one of the major technological locks regarding the principle of force measurement using resistive sensors, which exhibit very poor response when not being accessed closely to the mechanical source. The results in Figure 3.20a,b revealed that the piezoelectric technology, to some extent, possesses higher sensitivity and easier integration. As it is not necessary to implement the piezoelectric coating directly in the path of the applied load induced by the passage of the balls, several sensing elements can be printed on the outer ring to create a mapping sensor for condition monitoring of the whole bearing structure.

Second, contrarily to the piezoelectric active element, the strain gage is passive and thus needs a conditioning circuit to convert a resistance variation to an output voltage. The output signal is relatively sensible to noise because of the poor signal-to-noise ratio. Accordingly, the signal induced from the strain gage has been filtered to remove high-frequency noises, resulting in signal distortion due to harmonics alteration. The signal is acquired on a quarter bridge configuration where the output voltage (Δu) is proportional to the strain (S):.

$$\Delta u = \frac{V_{cc}}{4} \times GF \times S \tag{3.2}$$

where V_{cc} and GF denote the supplied voltage and the gage factor, respectively. The GF of the chosen commercial strain sensor is quite small (i.e., equal to 2), leading to very low Δu signal. In practice, an amplitude of 2-µdef deformation results in a voltage variation of 5 µV only. Such an amplitude is drastically low compared to the output directly acquired from the piezoelectric coating (i.e., around 2–3 mV). Better sensitivity of the strain gage can be enhanced by selecting a higher GF, but sensor is less linear and more sensitive to the temperature variation.

The above preliminary result confirms the reliability of the proposed approach for load-sensing bearings. Further studies are planned to improve the experimental setup that can generate radial loads applied to the ball bearing. This stage is of high important to be able to validate the testing procedure in a real-world operation of the aerospace system.

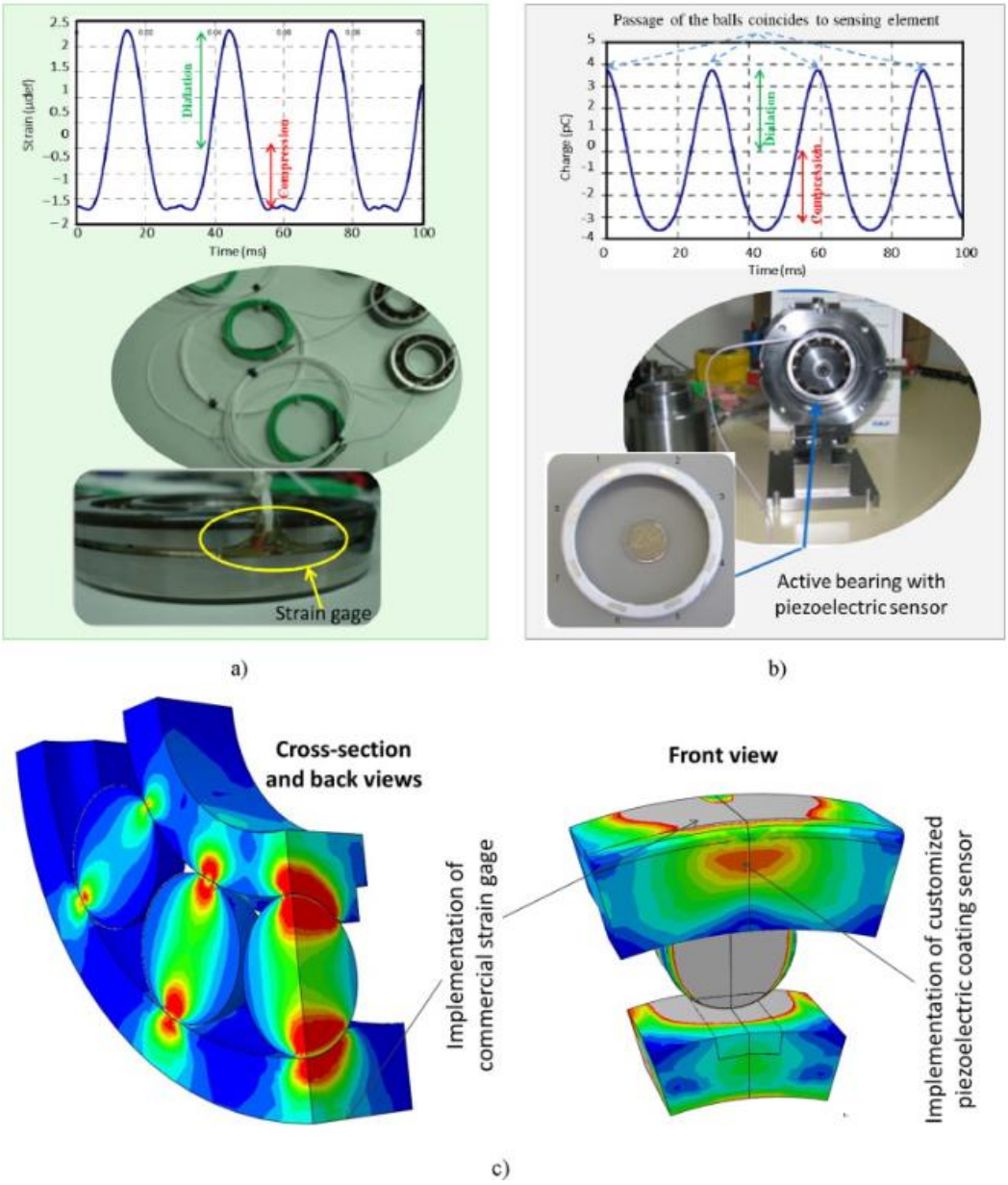

Figure 3.20: Typical response of a) strain gage, and b) piezoelectric sensor throughout a passage of ball bearing. c) Load distribution on the bearing's ring and balls using FEM: for a better visualization, scale color are not the same in the two image's views – grey color is considered as the maximum load.

3.5. Summary

Based on the results presented in this chapter, it can be concluded that the piezoelectric sensor is a promising technique for bearing condition monitoring applications. The substrate was instrumented by a customized piezoelectric sensor, enabling to deliver linear electrical signal in response to mechanical solicitations. A four-point bending experiment has been conducted to test the performance of the screen-printed sensor, with a sensitivity (d_{33}) of approximately 1.31 pC/N in comparison to 1.35 pC/N estimated through the finite element simulation. The empirical results, which perfectly agreed with the theoretical predictions, demonstrated a feasibility of directly measuring the substrate's deformation through electromechanical coupling of piezoelectricity. It has been revealed that the developed sensors exhibited good repeatability and constant sensitivity. The simulation values were found to be in good agreement with the experimental results, which confirmed the validity of the model hypothesis and the reliability of the results.

Moreover, the investigation of different aspects of the experiment provided valuable insights into the behavior of the piezoelectric sensor. The analysis of the sensor response as a function of temperature showed that the commercial ink containing polyurethane acrylate (PUA) polymer is not stable at high temperature. Actually, this polymer has low glass transition point (around 60 °C), leading to a drastically drop in the elastic modulus around that critical point. As a matter of fact, the temperature dependence of the composite can be further enhanced by choosing another matrix. For instance, sensor based PDMS polymer is stable at temperature closed to the Curie point of BaTiO3 (i.e., around 120 °C)[230].

The bidirectional effect was also found to have a significant impact on the behavior of the sensor, and it should be considered when designing and interpreting the results of the experiment. Finally, the influence of the electrode shape was examined, and it emphasizes that understanding the sensor's characteristics is not sufficient; enhancing its design and implementation is of primary importance as well to fully achieve the sensor's potential.

Overall, the results presented in this chapter demonstrated the potential of the piezoelectric sensor for CM of bearing and highlighted the importance of considering various factors that can affect the sensing performance. These findings would be used to improve the design and implementation of piezoelectric sensors for various applications in the future.

Chapter 4. Haptic feedback using piezoelectric materials

This research, i.e., given by the collaboration between the LGEF and the Volvo, focusses on the development of a piezoelectric actuator capable of generating a sensation to user who manipulates it. The objective here is to explore the possibility of developing a haptic tactile interface that might be replaced mechanical buttons in truck's cabins. A FEM (Finite Element Modeling) model via ANSYS multiphysics software was investigated to analyze the haptic performance of the wafer structure consisting of a piezoelectric BaTiO3 multilayer coated on a transparent flexible substrate. Several parameters dedicated to the geometric and mechanical properties of the wafer, together with those of the electrodes are demonstrated to have significant impact on the actuation ability of the haptic device. The research also involves in experimental characterizations that allow to support the simulation work as well as to validate the reliability of the proposed approach. Finally, a demonstrator comprising piezoelectric buttons together with electronic command and conditioning circuits are successfully developed, making a simple way to create multiples sensations to users.

4.1. Description of haptic feedback

Nowadays, human interaction with technology mainly focus on the visual and auditory aspects of perception as they are considered as the most prominent senses that humans rely on for interpreting the world around them [231,232]. However, the complete human experience isn't limited to these two, but formed from five basic senses (sight, hearing, touch, smell, taste) [233]. While the incorporation of smell and taste into technology interfaces is still in the early stages of development, the sense of touch is becoming an increasingly important component of human interaction with technology [234]. Every day we interact with a ton of electronic devices, some of them we carry around (like laptops or mobile phones) with others being wearable (like smart watches, wristbands, clothing). By introducing proper implementation, modern gadgets enable us not only to see or hear, but literally feel and experience virtual environments and interactions more realistically [235]. That is exactly where the haptic technology comes into play.

4.1.1. Definition, process and classification

Simply put, haptic feedback (haptics) is a technology, which allows one to receive tactile information through their sensations, by applying forces, vibrations, or touches [235]. For example, when typing on a smartphone keyboard, user might feel a slight vibration to confirm that a key has been pressed [236]. Similarly, when playing video games, user feels like he/she are actually in the game thanks to vibrations generated from the controller [237].

These examples are haptic technology at its most basic level of tactile response. But haptic feedback goes a tad further where communication is concerned. Haptic feedback can be used for communication purposes, particularly in situations where verbal or visual communication is difficult or impossible. For instance, haptic feedback can be used to provide tactile cues for individuals who are visually impaired or deaf, allowing them to better understand their surroundings or receive notifications [238]. Haptic technology can also be used in situations where it is important to communicate information discreetly, such as in medical settings where doctors need to communicate with each other during a surgical procedure without disturbing the patient [239]. Additionally, haptic feedback can be involved to provide remote touch sensations, allowing individuals to communicate touch sensations to each other even if they are not physically in the same location. Overall, haptic feedback has the potential to greatly enhance our ability to communicate with each other, particularly in situations where traditional forms of communication are limited.

Haptic feedback relies on two systems to engage the haptic sense – one on the human side and one on the machine side. Each requires an input, a translation, and an output, as shown in Figure 4.1. The human side includes the haptic sensors in the skin and the neural pathways that transmit information to the brain. The machine side includes the sensors that detect the user's touch, the algorithms that interpret the input, and the actuators that generate the haptic feedback [240].

The process of haptic feedback involves several steps. First, the user interacts with a haptic-enabled device, such as a touchscreen, by applying pressure or making contact with the surface. This generates an input signal that is detected by the machine's sensors. The signal is then translated by the machine's algorithms into a haptic response, such as a vibration or force. This response is then outputted by the machine's actuators, which generate the physical sensation that the user feels. The user's haptic sensors in

the skin detect the physical sensation and transmit information to the brain, which interprets the sensation as a particular texture, shape, or force. This completes the feedback loop, where the user's action generates an input signal that is translated and outputted by the machine, and then detected and interpreted by the user's haptic sensors and brain.

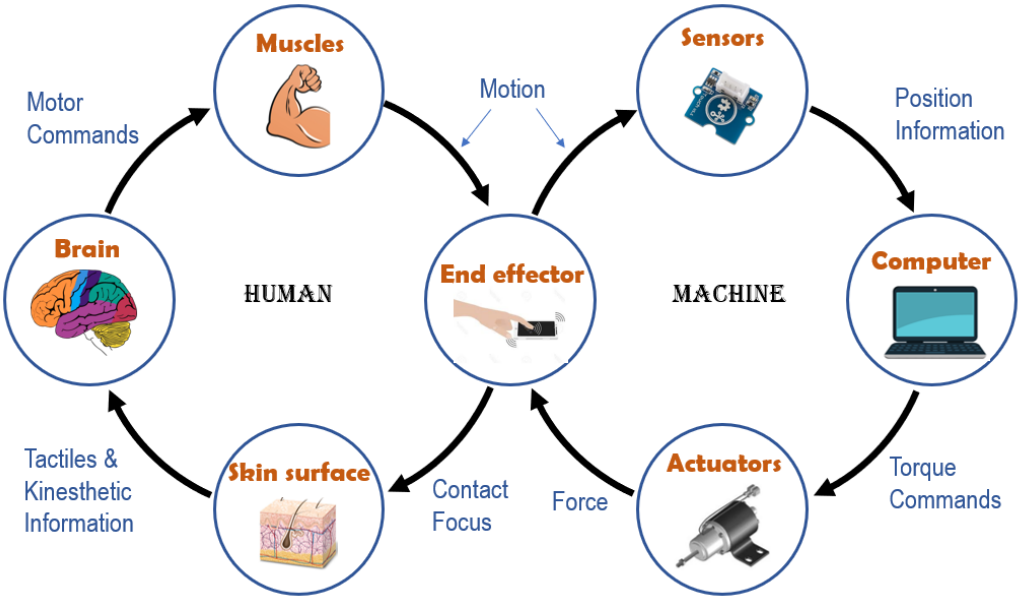

Figure 4.1: A diagram illustrating a process of haptic feedback [240].

Haptic defines a family of technologies that work similarly. But each haptic technology communicates in different ways. Here are some of the most common haptic technologies in use [241]:

- Force Feedback: Force feedback provides resistance or pressure to users through physical feedback, simulating the feeling of pushing, pulling, or manipulating an object. It is the kind of haptic technology that appeared first (starts in the late 1960s). Therefore, it is the most studied and well-implemented in different applications so far. This type of haptic technology is commonly used in gaming controllers and other devices that require precise control [242].
- Vibrotactile Feedback: This type of haptic technology provides physical feedback to users through vibrations or pressure, which can simulate the sensation of touch. Vibrotactile feedback is by far the most common type of haptic. This can be accomplished through the use of motors, actuators, or other types of mechanisms that produce tactile sensations.
- Thermal Feedback: Thermal feedback uses changes in temperature to provide tactile feedback to users, simulating sensations such as warmth, coldness, or heat. This type of haptic technology is commonly used in medical devices and virtual reality systems [243].
- Electrotactile Feedback: This type of haptic technology uses electrical currents to stimulate the skin and provide tactile feedback to users. It can create sensations such as vibrations, tingling, and pressure, and can be used in applications such as virtual reality and medical prosthetics. It can also be useful for users with visual or auditory impairments, providing an alternative way to receive information through tactile notifications and alerts [244].
- Ultrasound Tactile Feedback: Ultrasound tactile feedback is a haptic technology that creates touch sensations through high frequency sound waves. It can simulate touch and texture and is used in haptic displays, touchscreens, and virtual reality. Its contactless nature makes it useful for medical and hygiene-sensitive environments, as well as in low-light or noisy environments where other feedback may not be effective [245].

The objective of our project is exploring the possibility of developing a haptic interface to replace mechanical buttons thanks to piezoelectric materials, so vibrotactile feedback is the technology used in our target application. In order to build an effective haptic feedback demonstrator, it is important to have a good understanding of how humans perceive touch, the sensitivity of human skin, and the limitations of human sense of touch. Indeed, our skin is only able to detect a certain range of frequencies and amplitudes, and this range can vary depending on the location on the body [246]. Additionally, different types of receptors in the skin are sensitive to different types of stimuli, such as pressure, temperature, and vibration. By understanding these factors, we can design haptic feedback systems that are optimized for specific applications and provide a more realistic and immersive user experience.

4.1.2. Sensory receptor

4.1.2.1 Biological receptors

To perceive the world around us we are equipped with five senses: Hearing, smelling, sight and touch. This vocabulary works in our daily life, however for a more technical approach we use other terms such as: Thermal, chemical, optical, pain and mechanical sensors [247].

- *Thermal sensor* for registering the change of temperature especially within the skin.
- *Chemical sensors* for reacting to odorous or gustatory substances.
- *Optical sensors* for reacting to the impact of photons within the cones and rods in the retina.
- *Pain sensors*, also named nociceptors, identify chemical and physical tissue damage.
- *Mechanical sensors* for detecting mechanical tensions and strains within the skin or muscles.

The nervous system of our body helps to establish a connection between our brains and our receptors. For example, when your hand touches an object, the mechanoreceptors in the skin are activated, and they start a chain of events by signaling to the nearest neuron that they touched something. This neuron then transmits this message to the next neuron which gets passed on to the next neuron and on it goes until the message is sent to the brain. Now the brain can process what your hand touched and send messages back to your hand via this same pathway to let the hand know if the brain wants more information about the object, it is touching or if the hand should stop touching it [248].

4.1.2.2 Cutaneous receptor

A cutaneous receptor is the type of sensory receptor found in the skin (the dermis or epidermis) (see Figure 4.2). They are a part of the somatosensory system. Cutaneous receptors include mechanoreceptors (pressure or distortion), nociceptors (pain), and thermoreceptors (temperature) [249]. When talking about haptics we are interested in mechanical receptors – mechanoreceptors. Our skin has four types of mechanoreceptors:

- *Ruffini corpuscle* is sensitive to skin stretching and contributes to the kinesthetic sense.
- *Meissner's corpuscle* is sensitive to shape and textural changes.
- *Pacinian corpuscle* is primarily responsible for sensitivity to vibration.
- *Merkel disc* provides information on pressure, position, and deep static touch features such as shapes and edges.

Figure 4.2 shows the four skin mechanoreceptors as well as their location in a finger. It is possible to excite one type of receptor, e.g., Pacinian receptors for creating a sensation in a large area while Meissner's corpuscle receptors for producing a more localized sensation.

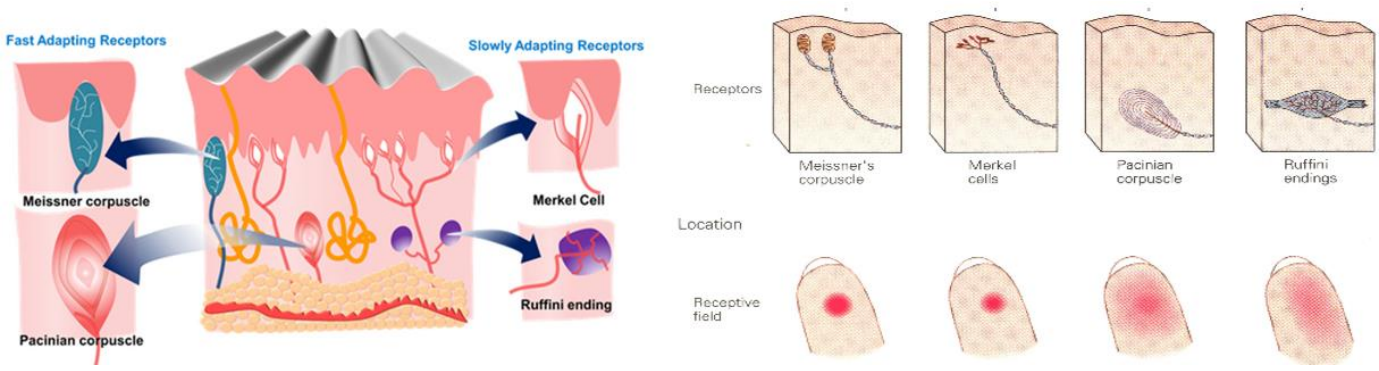

Figure 4.2: Skin receptors & location

Some researchers have tried to describe the *absolute perception threshold* [250], when humans start to perceive an interaction in their skin. Haptic perception depends on factors like force, the positioning of the body part, displacement, and frequency. The works from Hugony, Talbot and other researchers have established the direction to understand haptic perception [251]. Based on the previous works, Handwerker performed *haptic perception threshold* curve characterizing by the penetration depth as a function of the frequency. Generally, the perception curve is a combination of the four tactile sensor types but the RA-Meissner's and Pacinian receptors have more influence in perception. As demonstrated in Figure 4.3, the perception is strongly frequency dependence where the maximum sensitivity are identified at 350 Hz (i.e., corresponding to a minimum penetration depth). Therefore, to maximize the perception of user, a haptic system capable of generating a displacement of 2 µm at 300 – 700 Hz frequency range is investigated. It is worth noting that the characteristics shown in Figure 4.3 is validated with large transmission areas ($> 1cm^2$) of the input force such as in the case of a large button or a tactile screen. This matter might be considered in the design of the haptic button that will be addressed in next section.

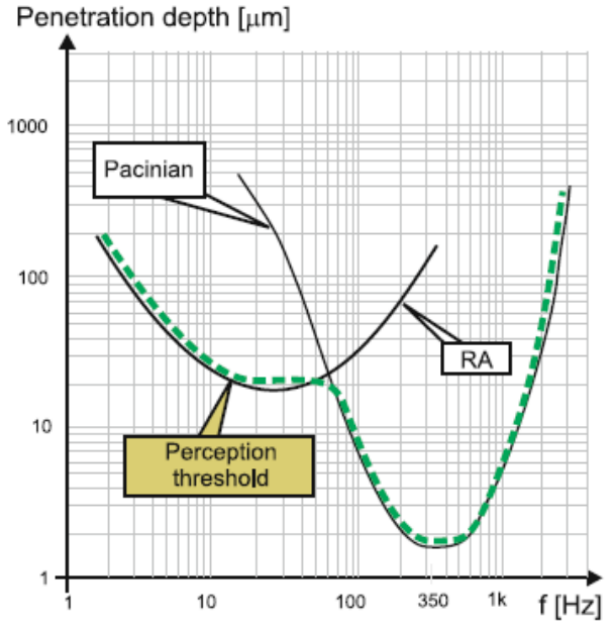

Figure 4.3: Absolute perception threshold characterized by penetration depth as a function of the frequency [250].

4.1.3. Stiffnesses and force of a button press

To improve the user experience, stiffness is a crucial factor to consider when designing a haptic device, as it refers to the degree of resistance an object has to deform under a given input force [252]. The material stiffness of the button must be considered because the initial touch of a material gives information about its haptic properties. Humans are capable of immediately discriminating, whether touching a metallic plate, a wood surface, or a plastic support. Our fingertips can identify, not only the vibration level, but also the texture of an object. If the button is not stiffer enough, the user might break it or be afraid of pushing it. On the other hand, if the button is stiffer, it is hard for the material to be deformed to create vibrations. Usually, the stiffness is characterized by the Young's modulus of the material (denoted Y), and it is defined as the ratio of stress (force per unit area) to strain (proportional deformation) along an axis or line within the material. Y also known as the modulus of elasticity, is a material property that describes how resistant a solid material is to elastic deformation when a force is applied to it [253].

To build effective tactile feedback, it is also important to study the force applied to a button and how it changes over time. Actually, this force is not constant and greatly affected by several factors like the dimension of the button, the shape and size of the user's finger, the speed of the press, and the surface on which the button is mounted. Nam and Shin developed a methodology to measure the force-touch applied on smartphones via an application, with which the user press some grey squares on the screen multiple times [254]. Tests were performed on 22 subjects and the force variation for each normal touch was recorded as displayed in Figure 4.4. It can be observed that the force varied quickly during the first 110 ms with a significant increase and attains a maximum value of 4 N. After that, all subjects decrease their force and latch the button after approximately 200ms.

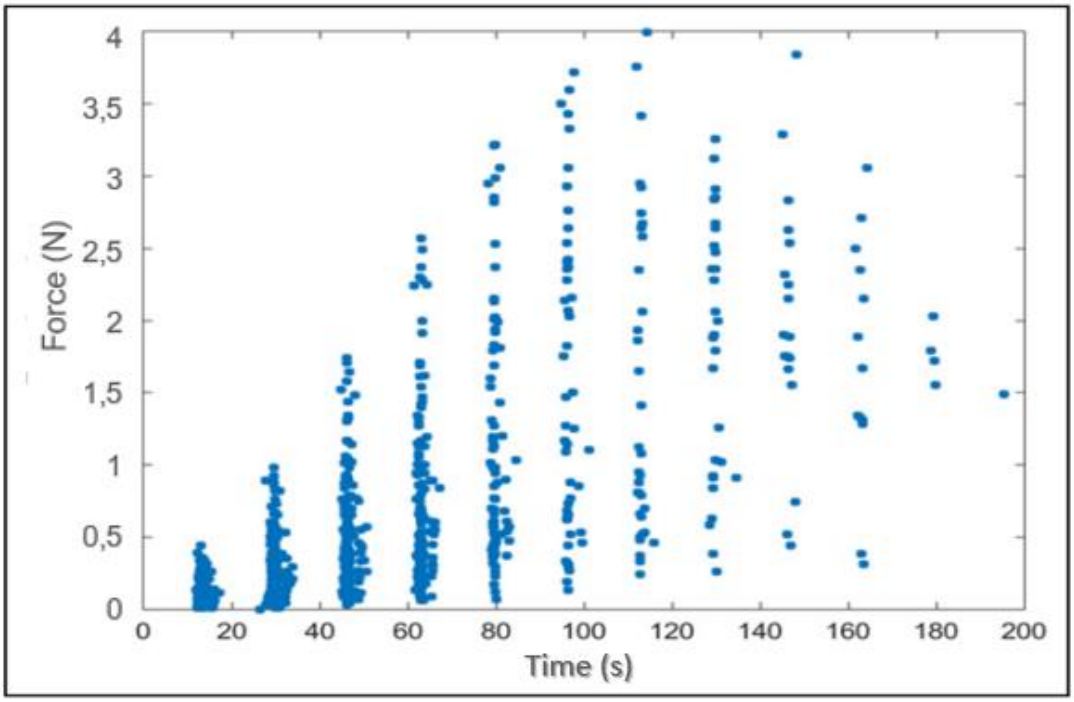

Figure 4.4: Force variation in time of normal touch on screen.

Based on the above results, the specifications of the haptic device can be determined as follows:

- Piezoelectric actuator:
  - Minimum displacement of 2 µm for within a frequency range of 300–700 Hz,
  - Withstanding a maximum pressing force of 5 N (i.e., defined by our partner Volvo).
  - Circular shape with 30 mm of diameter.
- Demonstrator design:
  - User input must turn on a led.
  - When pressing a button, user must receive vibrations as feedback.
  - If there are multiple buttons, only the pressed button must be detected to avoid crosstalk.

4.2. Design optimization

The haptic button is designed as a small piezoelectric wafer made of piezoelectric $BaTiO_3$ composite, sandwiched between two silver electrodes, and a substrate layer of a flexible material-based Polyethylene terephthalate (PET). More details have been described in Subsection 2.6.2 of Chapter 2. When the button is pressed, the force applied to the piezoelectric wafer generates a voltage (sensor mode) detected by a specific program developed by our team. This detection allows for the activation of a high voltage applied to the wafer, which in turn generates a dynamic mechanical strain exerted on the button (actuator mode) [255]. This deformation creates a vibrotactile feedback sensation that can be felt by the user, similar to the feeling of pressing a mechanical button.

4.2.1. Influence of radius ratio

Optimizing the radius dimension of a wafer actuator (consisting of the piezoelectric layer coated on a structural membrane as displayed the inset in Figure 4.5) is of primary importance, as it can significantly affect the performance and efficiency of the actuator. Poncet *et al.* investigated the effect of radius dimension on the performance of a piezoelectric wafer actuator based on a static finite element model (FEM) [256]. In this work, the piezoelectric EAP actuators have been manufactured out of polymer substrates as polyethylene naphtalate (PEN). The piezoelectric stack consists of a 4.7 µm PVDF–TrFE film sandwiched between 800 nm-thick PEDOT–PSS bottom and top electrodes. The optimum ratio between the radius of the piezoelectric polymer and that of the membrane was determined to maximize the membrane displacement along the thickness axis, leading to the best haptic performance. The membrane displacement was simulated under a given DC actuation voltage, while the ratio between the actuator radius and the membrane outer radius was varied from 20 to 100 %. As seen in Figure 4.5, the ratio equal to 60% offers the greatest amplitude displacement regardless of the considered outer membrane radius and the substrate thickness. This result will be considered in the design rule used for our further device development, in which the haptic button consists of a 30 mm-diameter PET substrate. Therefore, the piezoelectric diameter is supposed to be equal 18 mm so that to achieve the best actuator performance.

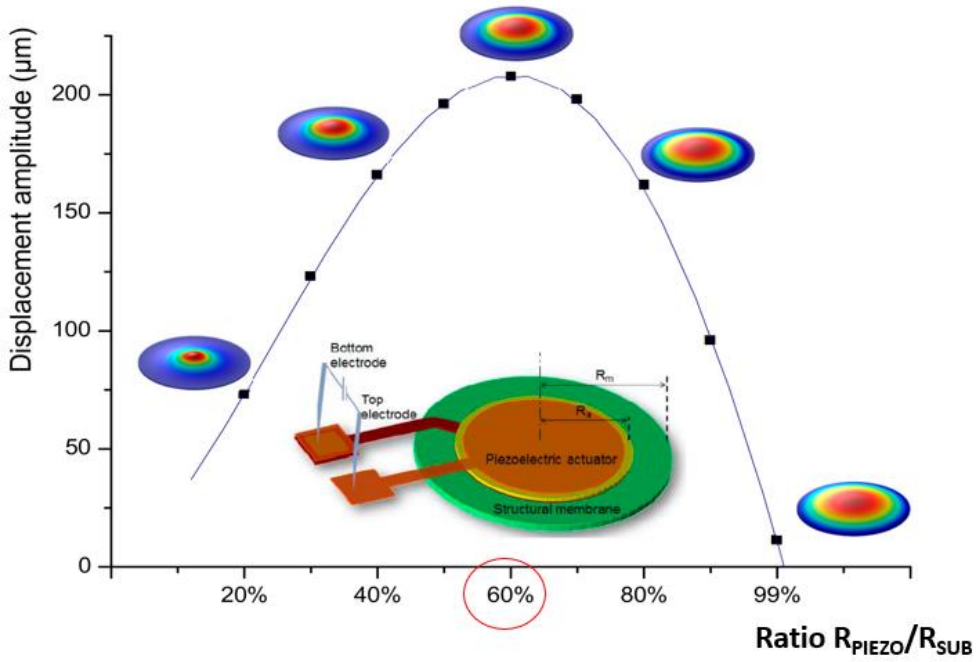

Figure 4.5: Optimization of the radius ratio to obtain maximal displacement for a circular actuator [256].

4.2.2. Influence of thickness ratio

Thickness optimization is crucial in the design of piezoelectric devices as it directly affects the haptic feedback performance. A finite element model (FEM) built on ANSYS simulation software is used to understand the influence of ratio between the active composite thickness (denoted t_{piezo}) and the PET substrate's one (denoted t_{sub}) on the displacement of the button. To simplify the model and reduce the computational time, the two thin electrodes are discarded from the model. The FEMs thus only consist of a PET substrate, and a $BaTiO_3$ composite with two different thickness of 28 µm or 56 µm. Those with 28 µm correspond to single-layered piezo-actuators (as the thickness of each layer is typically around 25-30 µm), while those with 56 µm are dedicated to two-layered ones. Indeed, additive manufacturing (AM) based screen printing makes it easy to create multilayered structures, by just repeating the process as in the case of the single layer. On the other hand, reducing the thickness smaller than 25-30 µm is difficult since it requires additional processing steps such as etching or polishing The thickness of the PET model is varied in such a way that the thickness ratio t_{sub}/t_{piezo} is within the interval [0.5 ; 4]. To assess the actuation ability, each sample is excited by a constant electric field (denoted E) of $10\ \mathrm{V/\mu m}$ or $50\ \mathrm{V/\mu m}$.

Figure 4.6 shows how the displacement and the wafer changes as a function of the thickness ratio. For a given input electric field, lower thickness ratio gives rise to higher displacement, so improving the haptic perception. A ratio of 0.5 results in the best actuation performance, but would weaken the structure (too thin substrate) and reduce the durability of the device [257]. Therefore, it is important to consider both the haptic performance and the structural strength when optimizing the thickness of the piezoelectric layer. To the practical point of view, a ratio of 1.5 is reveled to be an appropriate choice to achieve the best compromise between performance, durability, and user comfort. For instance, the single-layered piezoelectric button is designed with $t_{piezo} = 28$ µm and $t_{sub} = 50$ µm (standard size of PET that is available in the market)

allows to get optimized thickness ratio. In the case of two-layered samples (56µm thick), the displacement is boosted almost double as opposed to the single-layered ones, which is coherent due to their double thickness. Indeed, in the multilayered structure, each piezoelectric layer behaves as a capacitor and they are all parallelly connected together and thus powered under the same electric field. Considering that these capacitors are identical in terms of piezoelectric sensitivity (the same d_{33} coefficient), it can be assumed that all of them result in the same deformation (S) as in the case of the one-layered sample. Hence, the displacement of the whole multilayered structure is boosted as much as the number of the layers (i.e., proportional to the thickness). Last but not least, the multilayer architecture allows to improve the actuation performance without changing the input voltage level. Inversely to the single-layered one, much higher voltage is needed to achieve such an actuation ability, provoking increase probability of electrical breakdown of the device [132].

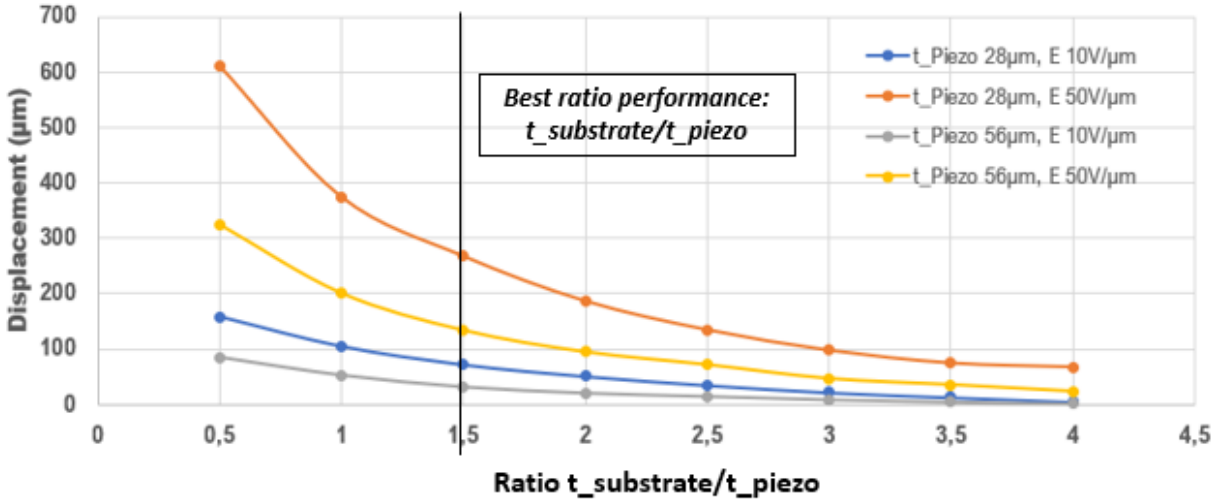

Figure 4.6: Optimization of the thickness ratio to obtain maximal displacement for a circular actuator.

4.2.3. Influence of Young's Modulus

This study aims to assess how the stiffness of the PET substrate influences on the actuation behavior of the piezoelectric button. Usually, a rigid material will create a button capable of withstanding the force of a fingertip but in exchange some performances might be deteriorated. A trade-off between the stiffness and haptic perception needs to be considered in the design of a piezoelectric haptic button whose stiffness could be improved based on two solutions [258]:

- Modification of the PET substrate thickness (t_{sub}): This is an easy solution but it might not modify the thickness ratio of the structure, which was chosen equal to 1.5 according to Subsection 4.2.3.
- Option 2: Use another substrate material with a different Young Modulus (denoted Y)**.** Materials with a higher Y are stiffer and more resistant to deformation under load, while those with a lower Y are more flexible so easier to be deformed.

Here we assess the influence of the mechanical properties of the substrate on the actuation ability of the piezoelectric wafer. A "fictional material" available from ANSYS library was chosen to simulate the substrate properties. The mass density and the poison coefficient were respectively set as 952 Kg/m^3 and 0.34, whereas the Young's modulus (Y) varied within 0.5–10 GPa. The thickness of the substrate remains

constant at 50 µm. Figure 4.7 illustrates the maximum displacement of the wafer as a function of *Y* under two different levels of the input electric field. Whatever the electric field, higher *Y* induces a decrease in the displacement. PET with its low Young's modulus of 2.6 GPa leads to sufficient displacement (e.g., ~ 50 µm under low input electric field of 10V/µm) to perform satisfactory haptic performance. The stiffness of the button could be adjusted by somewhat modify the thickness of the PET, to some extent. Accordingly, this study confirms good mechanical characteristics of the PET to fulfill the requirement in terms of haptic performance and device stiffness.

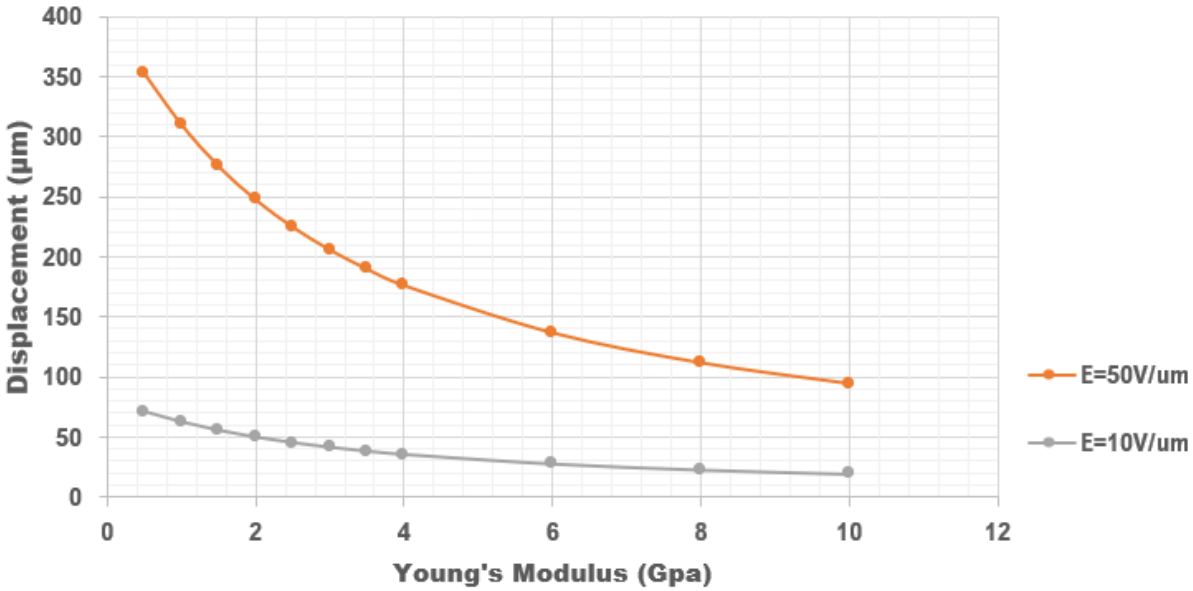

Figure 4.7: Influence of the Young's Modulus on the displacement of the actuator excited by different electric field of 50 V/µm and 10 V/µm.

4.2.4. Influence of electrodes

In the previous FEMs, the electrodes are not considered to reduce the computational time of simulation, also to overcome their effect with respect to the other factors needed to be studied. They are responsible for applying the electric field across the piezoelectric layer, which generates the mechanical deformation and resulting haptic feedback. In the practical point of view, the presence of electrodes is mandatory, and as a result, its impact on the haptic performance of the actuator device should be carefully addressed [119]. In general, the electrodes should be as thin as possible to minimize their influence on the mechanical properties of the device. However, they must be also a good conductor, and durable to withstand an important number of the deformation cycles. Common materials used for electrodes in piezoelectric devices include gold, platinum, aluminum, and silver [259]. In our case, silver was chosen due to its excellent electrical conductivity, good adhesion properties, and adaptable to 3D printing additive manufacturing (AM).

To better emphasize the influence of the electrodes, two different FEMs (with and without electrode) was created via ANSYS. Both models consisted of the PET substrate and the $BaTiO_3$ piezoelectric layer with identical characteristics. "Harmonic Response" block function [260] was used to observe the maximum

displacement as a function of the frequency within a range of 10 – 700 Hz. As revealed in Figure 4.8a-b, the full piezoelectric wafer (with electrode) results in a decrease in the displacement by approximately 25-30% as opposed to the simplified one (without electrode). This can be explained due to the fact that the electrodes, with their non-negligible thickness (around 5–10 µm), are stiffer than the piezoelectric material and thus limit its ability to deform. In other words, the electrodes create a mechanical constraint on the piezoelectric layer, making its motion reduced when input voltage is applied. It is interesting to note that the resonance frequency for first mode of both full and simplified models does not seem to be changed (~ 180Hz).

In spite of the decrease in the actuation ability, the full piezoelectric wafer still achieves good displacement for frequencies below 300 Hz. As demonstrated previously in the section of this chapter, the tactile perception of a fingertip is supposed to be optimal beyond 300 Hz, more precisely within the interval of 300 – 700 Hz . Unfortunately, the displacement may not reach the desired value of 2 µm (i.e., the minimum threshold for the user to feel something) in such an interval, especially with electroded wafer. Reducing the electrode thickness could make the displacement improved, but too thin electrodes might be fragile and easily deteriorated vis-à-vis considerable cycles of mechanical solicitation. An alternative solution involves in the development of multilayered piezoelectric actuator. Indeed, when multiple piezoelectric layers are stacked together, they can generate a larger displacement due to the increase in the total electric charge across the thickness of the piezoelectric layers. This phenomenon is known as the "stacking effect" [261]. The stacking effect can be further enhanced by arranging the polarity of the piezoelectric layers in a certain pattern. For example, if the piezoelectric layers are arranged with alternating polarities, the overall displacement of the button can be increased. This is known as the "poling pattern" or "polarization pattern" [261]. However, adding more piezoelectric layers can also increase the stiffness of the button, which may affect the haptic performance. Therefore, it is important to find a balance between the number of layers and the desired displacement. It will be pointed out that, in the following simulation results, two stacked piezoelectric layers are enough to achieve the desired displacement.

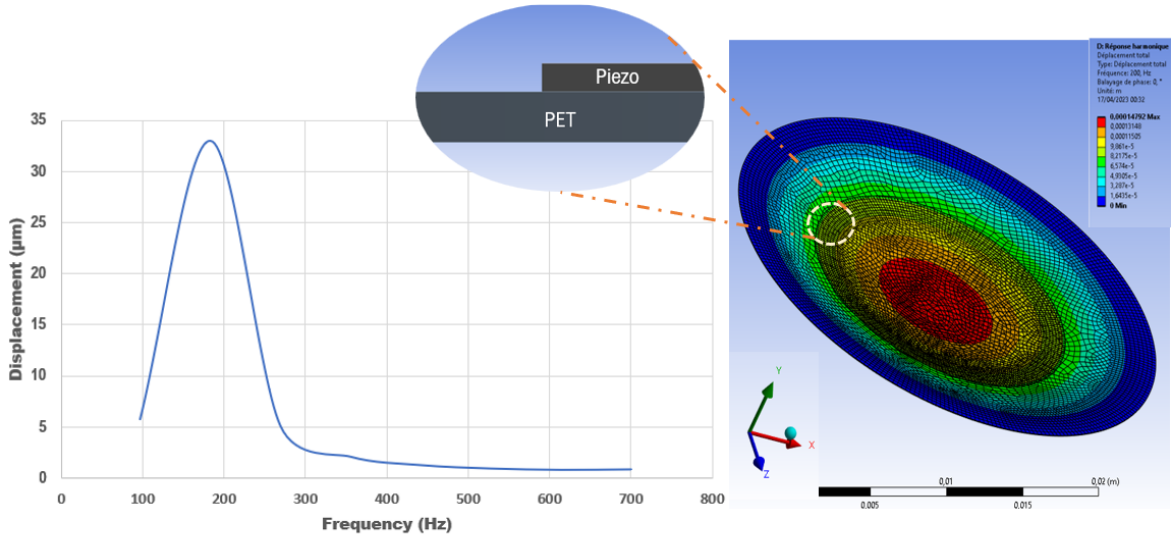

a)

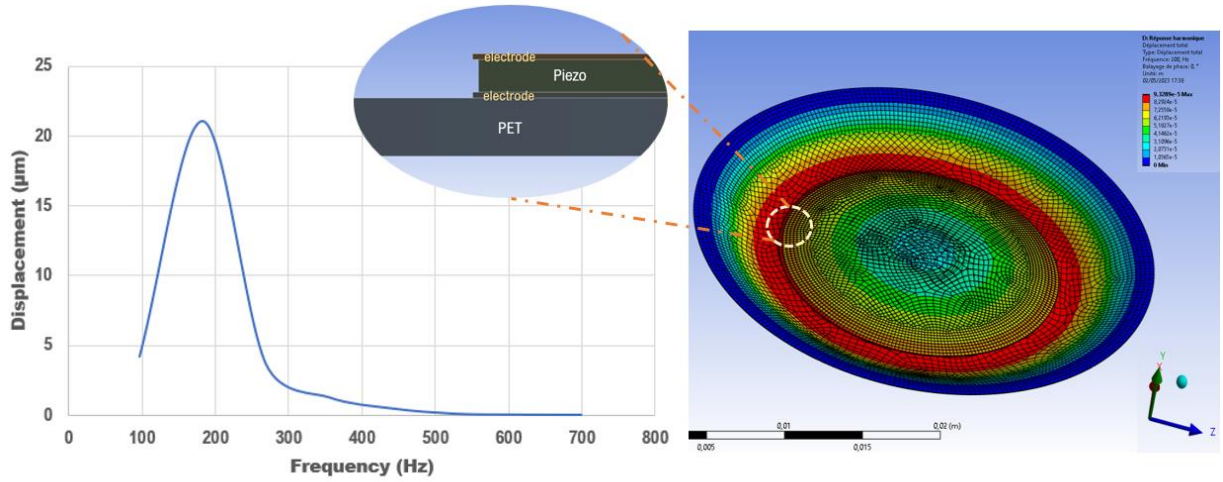

b)

Figure 4.8: Frequency response of the displacement based FE model of a single-layered piezoelectric specimen: a) without electrode; b) with electrode.

Two-layered piezoelectric model was built via ANSYS, in which the contact between the two layers is assumed to be bonded. In other words, there is no slipping liaison between them and they behave as a single entity. The piezoelectric layers are arranged with alternating polarities, meaning that the surfaces in contact of two adjacent piezoelectric layers have opposite polarities. If the top layer has a positive polarity, then the layer beneath it will have a negative polarity. This arrangement creates an electric field that is opposite in direction between adjacent layers, resulting in an increase in the overall displacement of the button when a voltage is applied. This is because the electric field generated by the top layer is reinforced by the electric field generated by the layer beneath it, resulting in a larger net displacement of the button.

Figure 4.9 shows the frequency response of the two-layered piezoelectric haptic button that is compared with the one-layered counterpart. It can be seen that increasing the number of layers can indeed increase the displacement value, especially around the resonance frequency. Such an increase may not be as much as expected (less than double) but it makes the button capable of reaching the desired limit displacement of 2 µm. Noted that Figure 9 displays the results of the one-layered and two-layered samples without electrode. Those with the electrodes achieve similar enhancement, with somewhat smaller displacement within the bandwidth of 300 – 700 Hz. However, in any case, a displacement of the two-layered sample attains the desired value, ensuring good quality of haptic perception. This result allows to validate the architecture of the two-layered piezoelectric button, which will be implemented in our experimental prototype in the next parts.

In this section of design optimization, we conducted simulations to optimize the structure of a piezoelectric wafer and established the wafer dimensions with a substrate thickness of 50 µm. After testing the first version of the device, it has been found that while the wafer could withstand the stress applied by a fingertip, it felt fragile as if touching a piece of paper, which made us hesitant to press the button due to fear of breaking it. Here we propose a solution to increase the stiffness of the button by modifying the thickness

of the PET substrate from 50µm to 75µm. Figure 4.10 illustrates the improved design of a two-layered piezoelectric button, which will be employed in the experimental prototype for the next part.

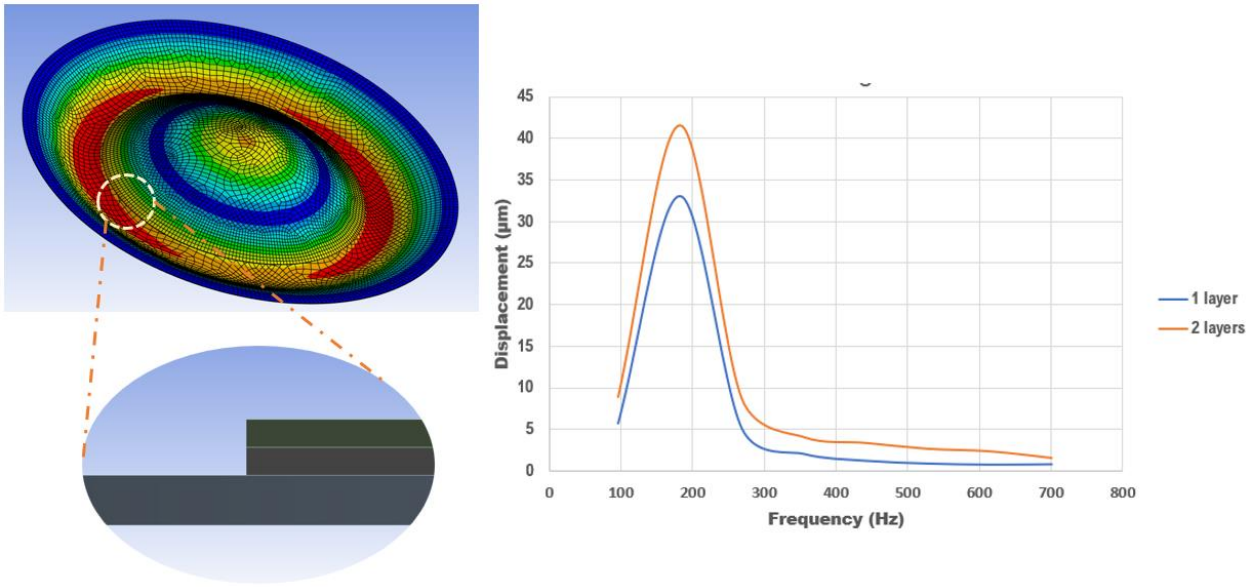

Figure 4.9: Influence of multilayer model (without electrode): a) FE model of a two-layered piezoelectric specimen; b) frequency response of the displacement of single- and two-layered samples.

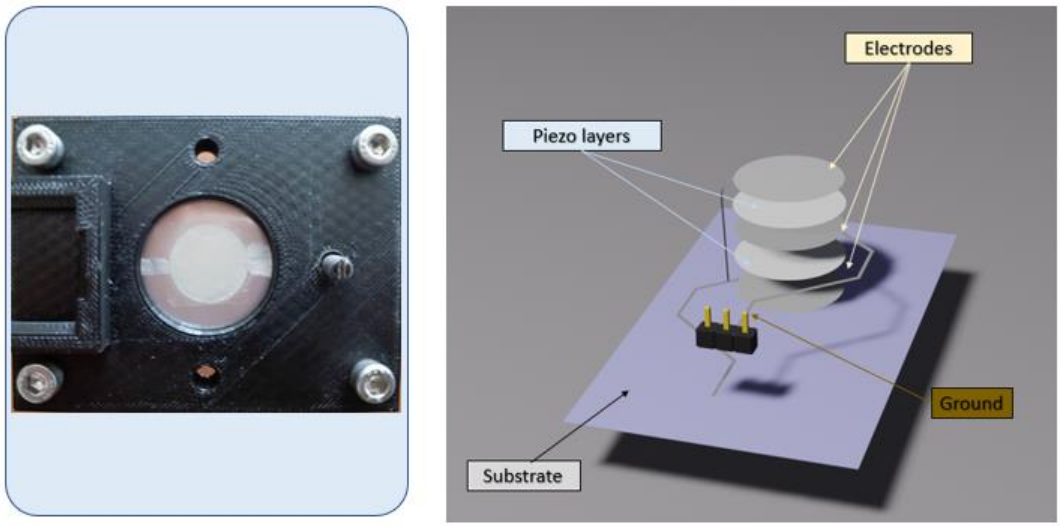

Figure 4.10: Wafer structure complete: a) installation on a sample's support; b) conception complete with 2-layer piezoelectric.

4.3. Experimental results

4.3.1. Displacement spectrum without load

This experimental setup (described previously in Subsection 2.5.4) was conducted with the aims of validating the above simulation results as well as measuring the actual displacement of the piezoelectric specimen when subjected to an electric field of 10V/µm. In particular, it is essential to verify whether or not the device could generate a feedback displacement with amplitude superior to 2µm, i.e., defined as the minimum threshold that can be perceived by a fingertip. For a given frequency of the applied voltage, the velocity of the piezoelectric specimen is acquired (denoted Vl), and the maximum displacement (denoted d_{max}, also defined as the amplitude of displacement) can be inferred as:

$$d_{max} = \int_0^{\frac{T}{4}} Vl_{max}\, sin(\omega t) \; = \frac{Vl_{max}}{2\pi f} \tag{4.1}$$

Figure 4.11 displays the experimental and simulation curves of the displacement spectrum, which lead to the resonance frequency (denoted f_r) respectively equals 470 Hz and 180 Hz. It is possible to find *n resonant mode* based on the flowing analytical model:

$$f_r = \frac{\lambda_n^2\, t}{2\,\pi\, r^2} \sqrt{\frac{E}{12\,\rho\,(1-\nu^2)}} \tag{4.2}$$

- E: Young's modules (Pa)
- ν: Poisson's ratio.
- ρ: Density (kg.m^{-3})
- t: Thickness (m)
- r: Outer radius of the substrate (m)
- λ_n: Eigenvalue at the n resonant mode (dimensionless). For the first mode $\lambda_1 = 3.2$

Based on the theoretical model of Equation (4.2), the first resonance frequency (f_{r1}) was found equal to 50 Hz. Experiment led to significant discrepancy of f_{r1} with respect to the numerical and analytical models. This fact could be attributed to several factors such as:

- In the simulation, the outer radius of the wafer was considered to be constant as the wafer was supposed to be fixed (i.e., static condition). Inversely to reality, the wafer could move slightly when pressed by a fingertip. In other words, measurements were conducted in a quasi-static environment, which is not similar to the case of the simulation.
- Discrepancy between the Young's modulus of materials ($BaTiO_3$ composite and PET substrate) specified in ANSYS and the real ones.
- In practice, the wafer may not be centered exactly on the support, producing some small changes in its geometry and thus shifting the resonance frequency, to some extent.
- The imperfections in the fabrication process leads to variations in the thickness and properties of the different layers.

In spite of discrepancy in the resonance frequency, the experimental and numerical curves leads to a displacement beyond the haptic detection threshold (2µm) within a bandwidth of 300 – 700 Hz. This means that if the user puts his/her finger on the wafer without applying pressure ($F \approx 0$ N), he/she could detect

some kind of vibrations. To improve the user perception, the level of these vibration could be changed by simply adjusting the applied electric field.

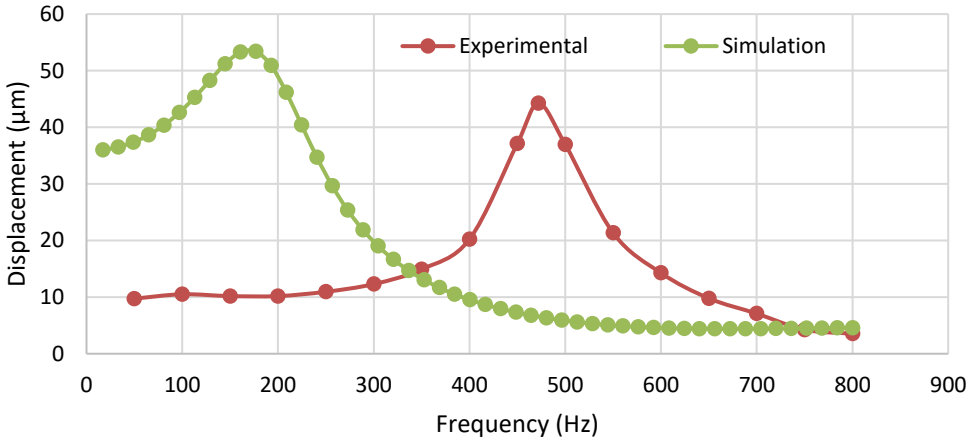

Figure 4.11: Displacement spectrum (without load) determined based on experiment and simulation.

4.3.2. Actuator mode: Displacement and force relationship

This subsection aims to figure out the displacement behavior as a function of the input force pressed by a customized artificial finger. Although the target application requires the developed button capable of withstanding a pressing force not greater than 5 N, experiences were carried out by varying the force in a larger range of 0 – 11 N. After detecting the force exerted by the finger through a generation of an electrical signal (sensor mode), actuator mode is activated. During such a configuration, a constant electric field with adjustable amplitude of 10 – 60 V/µm at a fixed frequency of 300 Hz was applied to the piezoelectric wafer, which in turn induced the mechanical vibrations perceived by the finger skin. The purpose here is to find out adequate levels of the applied electric field (denoted E) to conduct the displacement of the button beyond the lower detection threshold (~ 2 µm) of the human perception.

As illustrated in Figure 4.12 a-b, the displacement was computed from the velocity signal captured by the laser vibrometer. The details of the experimental setup have been addressed in Subsection 2.5.4. To facilitate assessment of the actuation performance, post-treated data based on the maximum value of the displacement (cf. Equation 4.1) was employed instead of real-time data, which allows to discard the influence of undesired electrical noises. As seen in Figure 4.12 c-e, a MATLAB algorithm was developed to compute the maximum displacement (d_{max}) relying on the identification of the local maximum values that were then interpolated to obtain a smooth envelop. The example of the data treatment shown in Figure 4.12 was dedicated to the wafer subjected to an electric field of 60 V/µm.

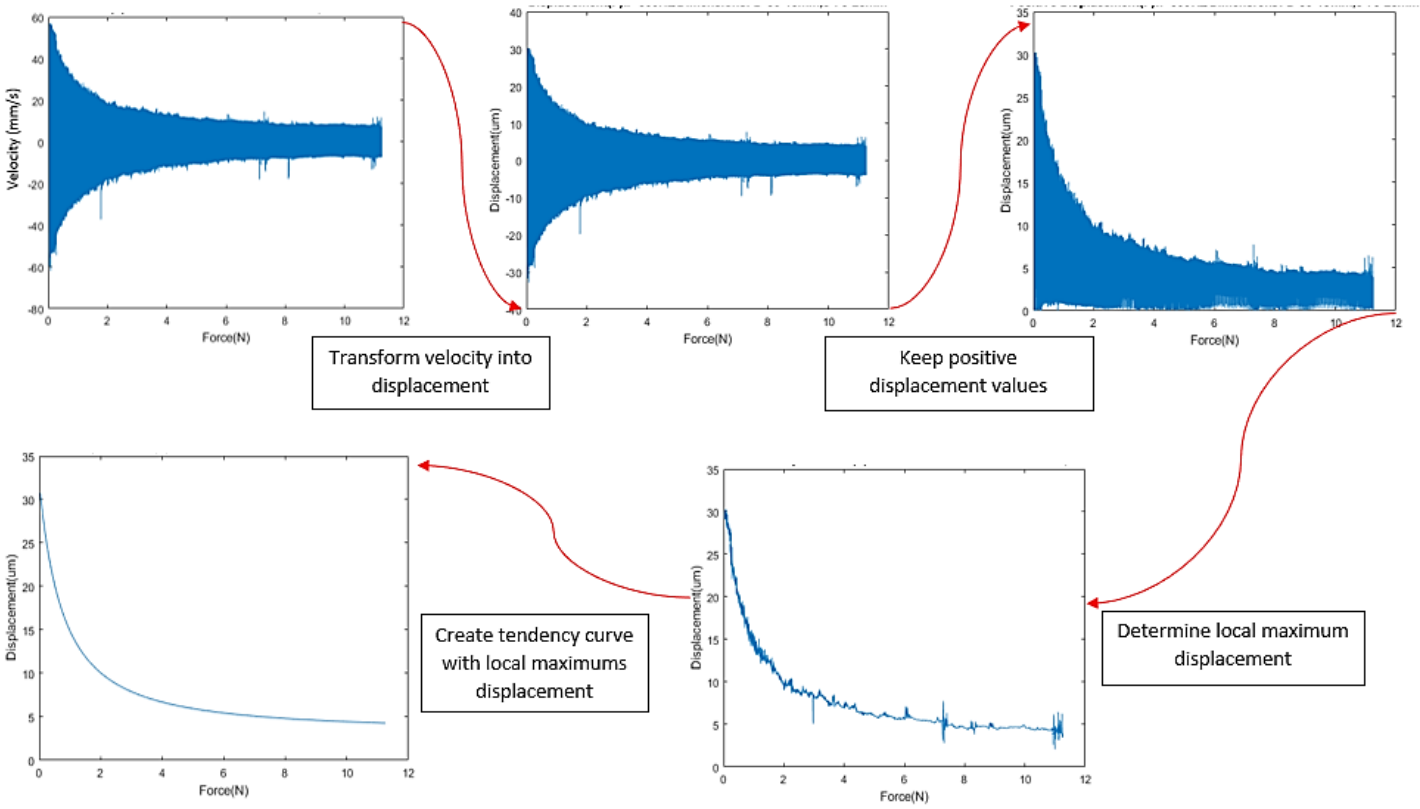

Figure 4.12: Steps to calculate the maximum envelop of the displacement as a function of the input force pressed by an artificial finger: a) raw data of velocity measure; b) displacement computed from the velocity; c) displacement remined with positive values only; d) using "local maximum function" to determine the local maximum of the displacement; and e) maximum envelop of the displacement based on interpolation method. Actuation test was performed under an applied electric field of 60 V/µm at a frequency of 300 Hz.

Figure 4.13 resumed all the results of the treatment with the electric field (E) varied from 10 to 60 V/µm. Whatever the level of E, d_{max} induced by the piezoelectric button drastically drops even with an apparition of a small force (from 0 N to 2 N). Above 2 N, however, d_{max} gradually decreases with an increase in the input force. In the case $E \geq 30\ V/\mu m$, d_{max} is revealed to be beyond the haptic detection threshold in the full range of the force (0 – 11 N). Regarding the specifications imposed by Volvo, the pressing force shall not exceed 5 N, thus a lower value of E as 20 V/µm is supposed to be enough to fulfill the requirements. Such a value is clearly an adequate choice to get the best compromise between haptic performance and breakdown probability of the piezoelectric composite, which could be dramatically deteriorated with high electric field application.

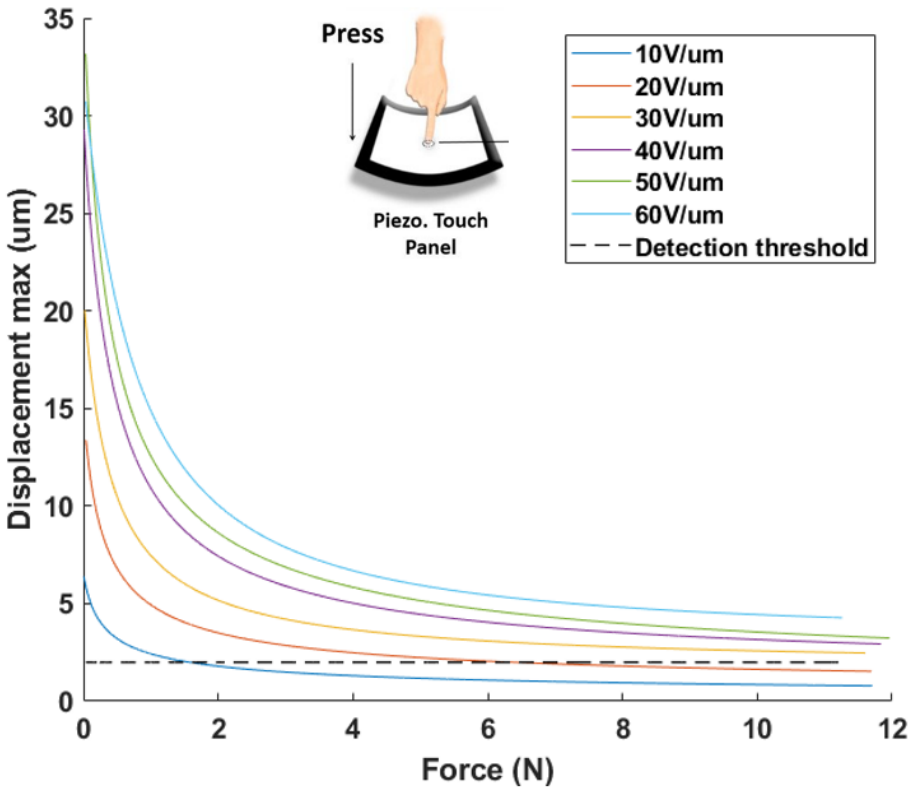

Figure 4.13: Displacement-versus-load of the piezoelectric specimen when subjected to different level of electric field.

4.3.3. Sensor mode: Activation of haptic response

Our objective in sensor mode is to detect user input when the button is pressed, and to determine when and how a haptic response is sent to the user. This stage, characterizing the transition from sensor mode to actuator mode, is thus of crucial importance. To begin, we classified the ways of pressing a button based on the duration of the press (quick, medium, and long that correspond to a duration of 0.2 s, 0.5 s, and 1 s, respectively). The test setup for sensor mode is shown in Figure 2.16 in Section 2.5.4.

Figure 4.14 displays the time evolution of the force measurement based on the three types of press performed by two subjects. Although multiple presses were recorded for each subject, only one of them was shown. This allows to demonstrate the curve's shape by keeping the maximum force and press duration consistent. As observed, the force increases quickly from 0 N to the maximum value (denoted F_{max}), then decreases at a similar rate. As observed, the value of F_{max} strongly depends on the press duration as well as the subject. Logically, the longer the duration, the higher the force value. Whatever the type of press, the forces' allure driven by both subjects is somehow close to a quadratic function (or a 2nd degree polynomial), in which only one peak is present. After several trials, it can be revealed that the medium and short durations of around 0.2 – 0.5 s correspond to natural gesture of a finger when pressing a tactile button. In these cases, the pressing force are shown not greater than 3 N, confirming the reliability of the specifications, in which F_{max} shall not exceed 5 N. Regarding the long duration of 1s, the force can rise up more than 10 N. This explains why in the previous study relating to actuator mode (Subsection 4.3.2), the range of the input force

was extended to 11 N. Indeed, the long press could be existed in reality, but only occasional for some specific purposes of user. Accordingly, this type of press, in most cases, does not faithfully describe the natural movement of a touch screen.

Figure 4.15 illustrates the piezoelectric response corresponding to different types of button presses. Here we particularly take a focus on the medium presses, as they are supposed to be the most commonly used in everyday scenarios. To achieve this, the voltage level at which the button press is considered a "mean press" needs to be determined. After analyzing the data of Figure 4.15b, the detection point of 0.5 V was selected. This value was found to be much higher than the electrical noise level that could cause false detections. The detection point could be set at 0.3V to detect quick presses as well, but this would make the button somehow more sensitive to mechanical vibrations as well as electrical noise, resulting in unwanted haptic responses. Finally, determining the voltage detection level for a mean press makes the design of a haptic feedback system more reliable, allowing for an accurate detection of the user input with less sensitive to noises and vibrations.

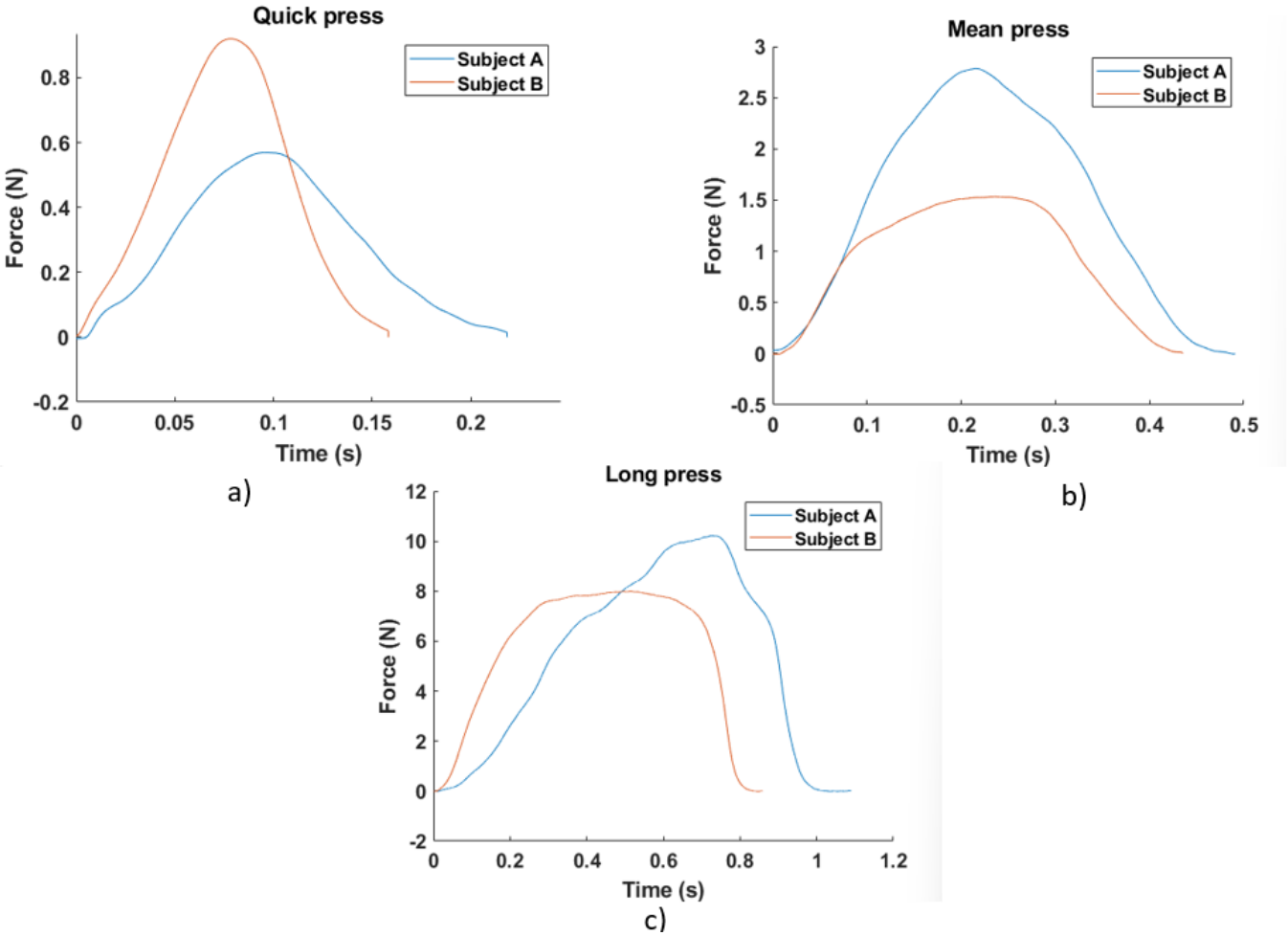

Figure 4.14: Time evolution of the pressing force under three configurations: a) quick press; b) medium press; and c) long press.

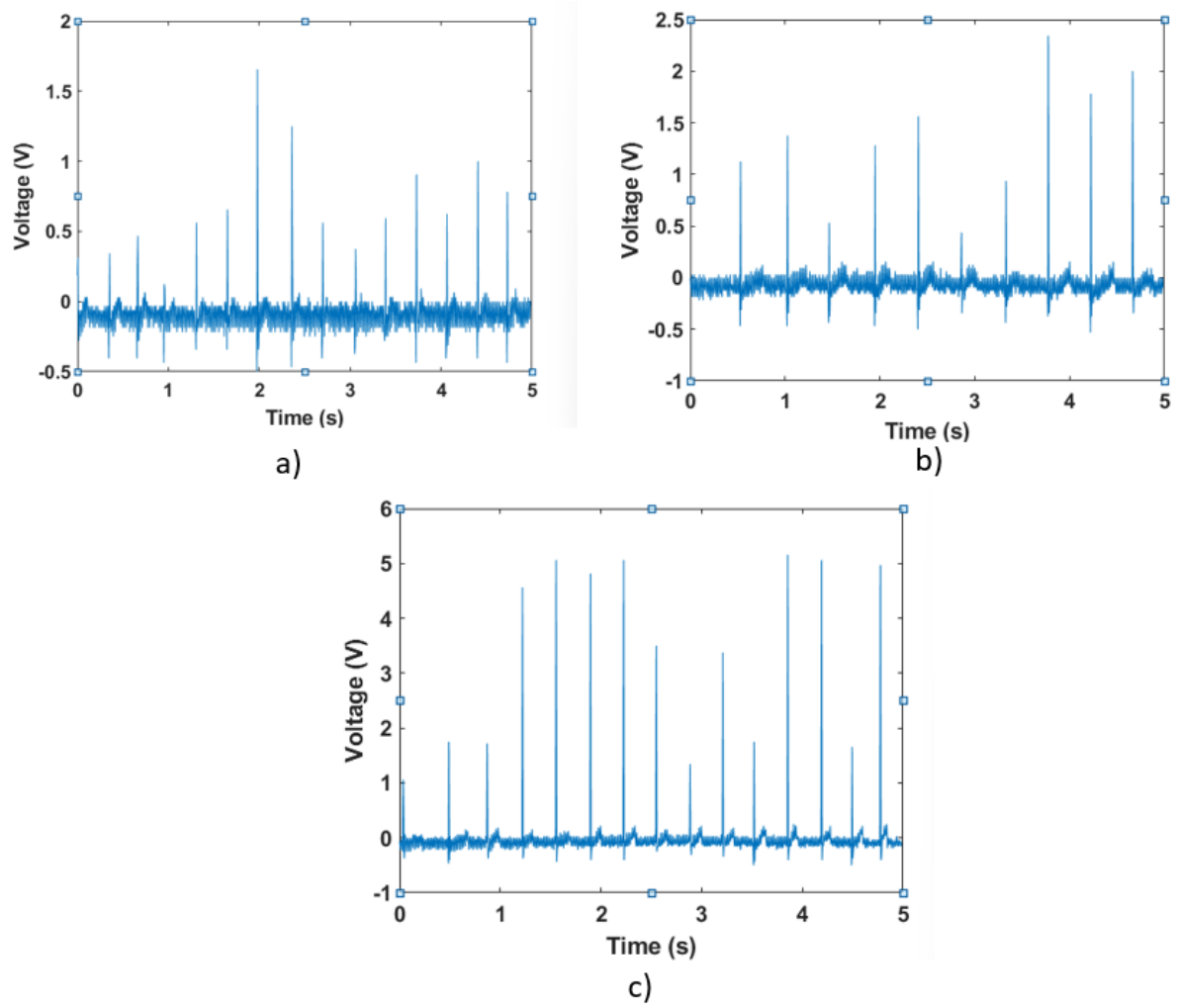

Figure 4.15: Piezoelectric response under three configurations: a) quick press; b) medium press; and c) long press.

4.4. Electrical schema: Haptic button

In this project, we use Analog Discovery 2 (abbreviated as AD2) to develop a prototype of the haptic button circuitry, test its performance, and optimize its design. The AD2, a powerful tool for prototyping and testing electronic circuits, is a portable USB-powered device that includes a variety of instruments such as an oscilloscope, waveform generator, logic analyzer, and power supplies [262]. The AD2allows us to easily measure and analyze the signals generated by the haptic button circuitry, which is critical for ensuring its proper functioning.

The haptic button's electronic circuit is a crucial component in ensuring its proper functionality. One of its key features is the *"Analogic protection"* mechanism, which protects the input pins of the AD2 from damage. This is essential as any damage of the input pins can affect the accuracy of the measurements and ultimately lead to the malfunction of the entire system [263].

Another essential component of the circuit is the *"Command circuit"*, which is responsible for amplifying the signal to a maximum voltage of 400 V. This amplified signal is used to activate the haptic response, which is a crucial part of the haptic button's functionality.

In order to test and refine the circuit, a prototype using a protoboard was first developed. This allowed to test the various components of the circuit and make any necessary modifications before performing on to the final product based on printed circuit board (PCB) design. Each button in the circuit has an independent "Analogic protection" and "Command circuit" to ensure that it operates independently of the others. Additionally, the circuit includes some resistance to manipulate LEDs, which can be used to provide visual feedback to the user. Ultimately, the AD2 is responsible for controlling every aspect of the circuit, ensuring that the haptic button operates smoothly and accurately. Overall, the electronic circuit is a crucial component in ensuring the proper functionality of the haptic button and requires careful design and testing to ensure optimal performance.

The haptic button starts working in *sensor mode*. The AD2 reads the voltage generated by the button after the *analog protection* and waits for a value higher than the voltage detection to activate the haptic response. When the *actuator mode* is activated, the AD2 generates a signal (sinusoidal, triangular, or square) that is amplified using a 400V amplifier from *Piezomaster*. The *command circuit* closes the static relay to send the haptic response to the piezoelectric component. At the same time the *analog protection* does its job by protecting the signal seen by the oscilloscope. Figure 4.16 shows an overview of the electric circuit for one haptic button. Explanation of the functionality for the *command circuit* as well as the *analog protection* will be addressed in the following subsections.

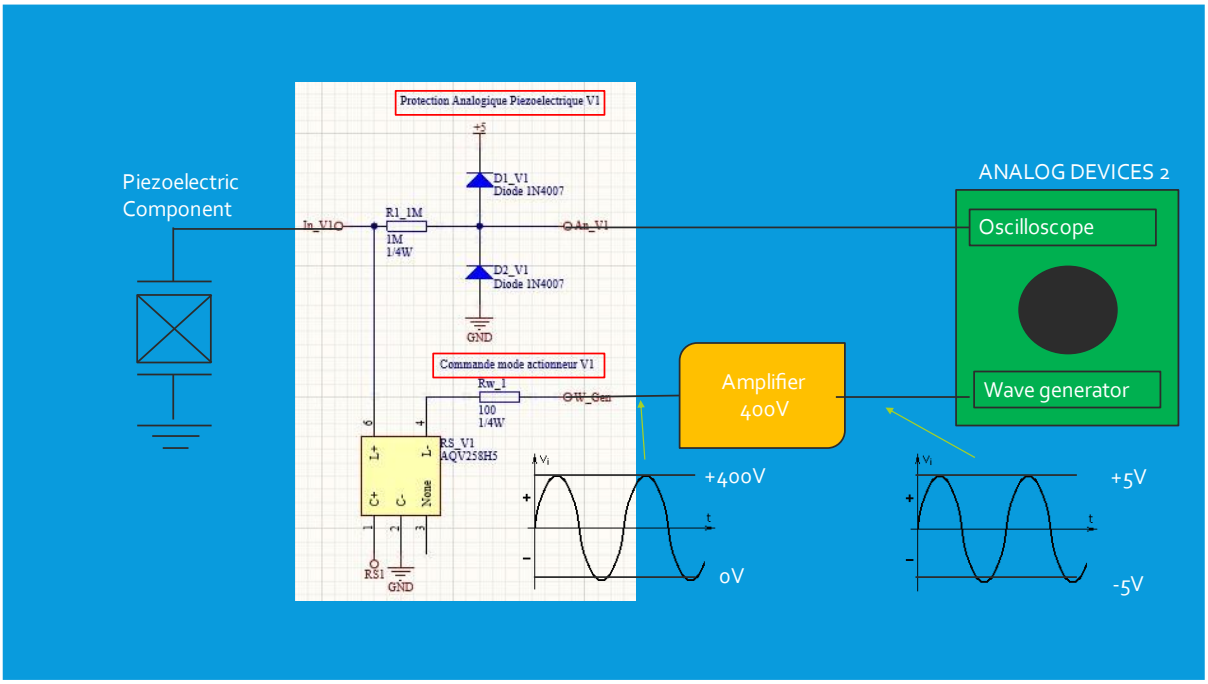

Figure 4.16: Simplified electric circuit for haptic button.

4.4.1. Analogic protection

The *analog protection* purpose is to avoid damaging the input pins of the AD2 by limiting the higher voltages and redirecting the current. In actuator mode, an output voltage of 400V, directly applied to the piezoelectric button, must be limited when seen by oscilloscope. The solution was to create a transient

voltage suppressor diode (TVS) [264] as schematically drawn in Figure 4.17. This protection circuit, using two diodes to prevent the electronic circuits from transients and overvoltage threats, is functioned as follows:

- $V_{osc} \geq 5V$: Diode D_1_V_1 let the current flow and V_{osc} is set to 5V.
- $V_{osc} \leq 0V$: Diode D_2_V_1 let the current flow and V_{osc} is set to 0V.
- $5V > V_{osc} > 0V$: Both diodes block the current, the voltage seen by V_{osc} is no limited to either 5 V or 0 V.

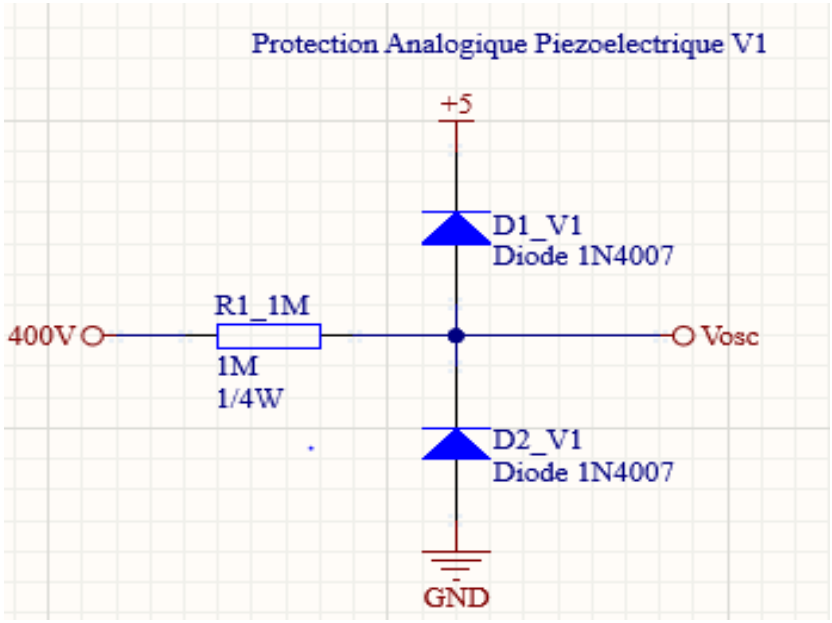

Figure 4.17: Analogic protection for a button

In actuator mode, the oscilloscope only displays 2 values (5V or 0V) as we work with values higher of 5V and inferior to 0V. A resistance of 1MΩ was placed before the TVS to limit the maximum current to 0.4 mA. In sensor mode, the piezoelectric response varies up to 5V maximum. The piezoelectric response does not change since the signal does not exceed the limits imposed by the diodes. In this case the resistance creates a voltage drop in the piezoelectric response, but the signal seen by the oscilloscope does not much change because of low current in the system (high impedance of piezoelectric sample).

4.4.2. Command circuit

The command circuit helps to separate the amplifier from the piezoelectric with a switch using a static relay as illustrated in Figure 4.18 (no moving part, ref. AQV258H5) [265]. The amplifier is directly connected to the switch operated by the AD2, which decides when to send the haptic response to the piezoelectric button. The control inputs are connected internally to an LED, which shines across an air gap to light sensors. The light sensor is connected to the transistors which open or close, supplying the relay load with power. When the transistor is closed, current can flow freely through the relay, the load is thus connected to the power supply. Otherwise it is disconnected in the case when the transistor is open that makes the current blocked. The pairing of the LED with light sensors is called an optocoupler and is a common technique to link two parts of a circuit without a direct electrical connection.

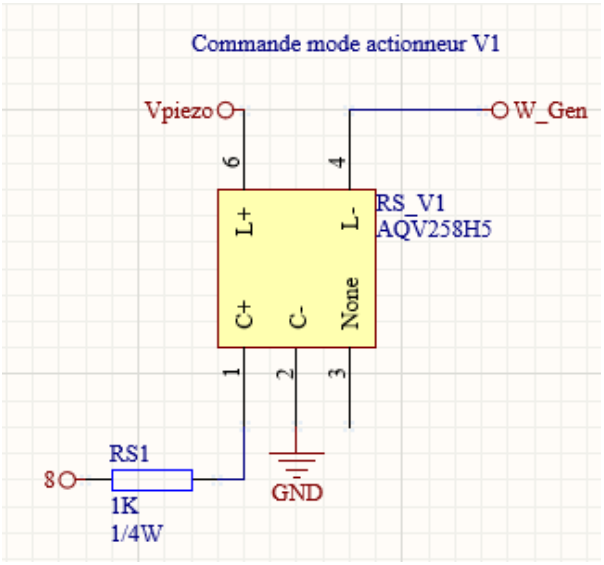

Figure 4.18: Command circuit for a piezoelectric button

4.4.3. Electrical diagram

Figure 4.19 displays the complete setup of the haptic button circuit, which comprises of four main components:

- a generator connected to an amplification unit to increase the output voltage to 400V.
- analogic protection circuit and command circuit, which are responsible for protecting the input pins of the AD2 and commanding the amplified signal.
- AD2, which has an Analog Devices connector for communication with the rest of the circuit.
- piezoelectric haptic button that is connected to the AD2.

This complete setup enables the generation of a variety of haptic sensations with the help of a user-friendly GUI (a Graphical User Interface) controlled by a Python program.

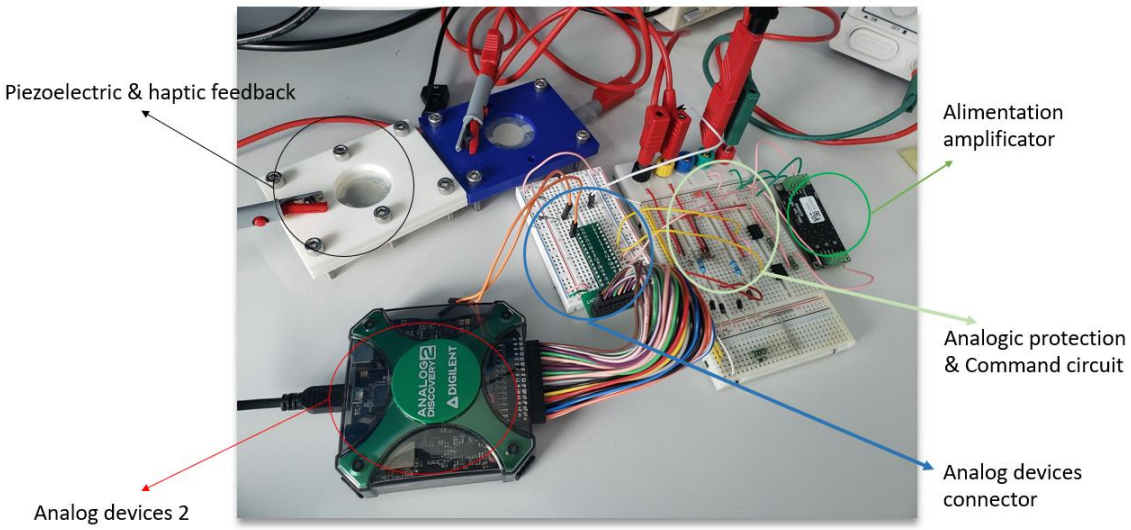

Figure 4.19: Tested electrical circuit for piezoelectric button.

4.5. Developpement of haptic demonstrator

The main goal of this chapter involved in the development of a haptic button demonstrator that could produce multiple sensations for people to experience. Our aim was to design an interactive device that was visually appealing and easy to use. The demonstrator comprises of two haptic buttons that can be programmed to generate a distinct sensation. Since the prototype was set to have one waveform generator and one amplifier, only one button can be activated at a time in actuator mode.

When a button is pressed, the corresponding piezoelectric button starts vibrating, and two LEDs light up. After the haptic response ends, there is a short delay, which can be configured, before the piezoelectric voltage returns to zero. A yellow LED indicates when it is possible to press a button again. A Python program controls all the electronics and allows the user to change the waveform for each button through a Graphical User Interface (GUI) [266]. The haptic button demonstrator not only provides an opportunity for users to experience different sensations but also allows for customization and control of the stimuli. The GUI interface is a user-friendly way to modify the waveform and adjust the parameters of the haptic response. This feature enables the user to tailor the haptic feedback to their liking and experiment with different combinations to produce unique sensations.

Finally, the haptic demonstrator device has been successfully developed as presented in Figure 4.20, which consists of the piezoelectric button and support, printed circuit board (PCB), 400V amplifier PiezoMaster and the Analog Device 2 (AD2). In the following, we provide further details about hardware and software of the device.

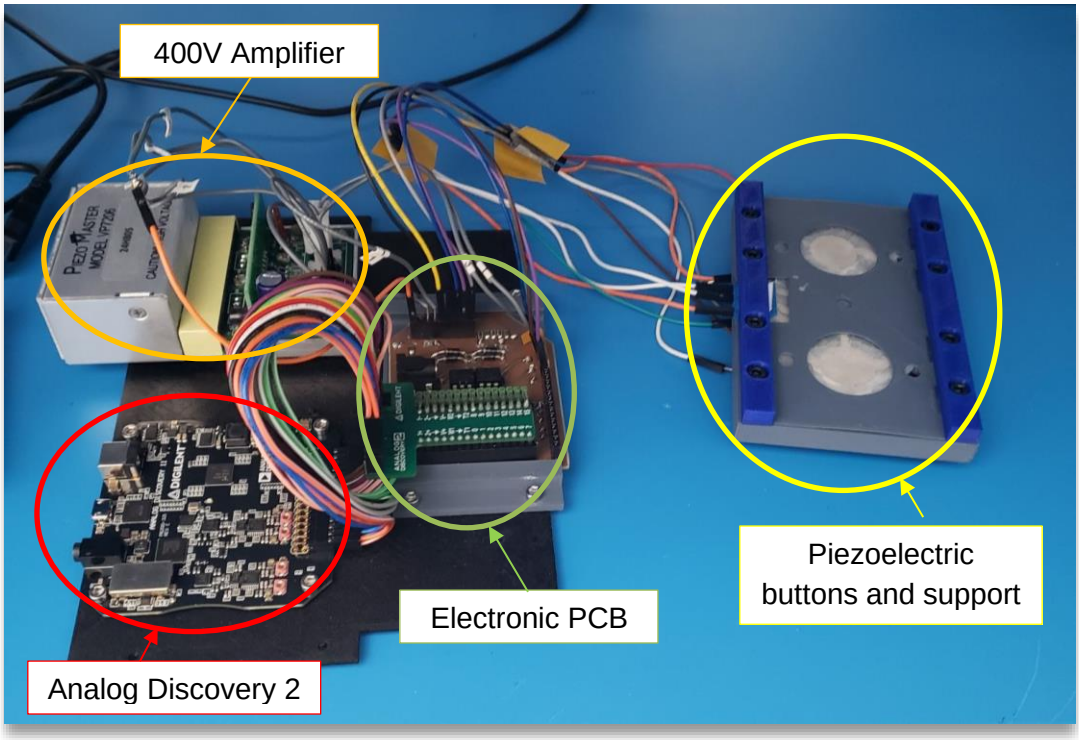

Figure 4.20: Prototype of haptic device.

4.5.1. Hardware description

The support design of one haptic button shown in Figure 4.10 has been extended to the design with two buttons as shown in Figure 4.21a. The electrode has a diameter of 18mm (Figure 4.21b) and the conductive tracks were designed by following the rules defined in Chapter 2. Based on the position of the electrodes, a 3D model for the support structure was built in two separate parts that can be clamped together. The support structure has two 30mm-dimater circle holes to accommodate the haptic buttons and two small holes for placing the LEDs. The connection was set at the same position as the piezoelectric design to ensure proper functioning of the circuit.

The haptic demonstrator circuit comprises the piezoelectric wafer together with the *analog protection* and *command circuits* for one button. To make the circuit more efficient and compact, a printed circuit board (PCB) housing all the electronics was performed via Altium Designer software, which enables to create a precise and professional layout [267]. The final prototype is depicted in Figure 4.22, where the components arrange neatly on the PCB, ensuring a more organized and efficient design.

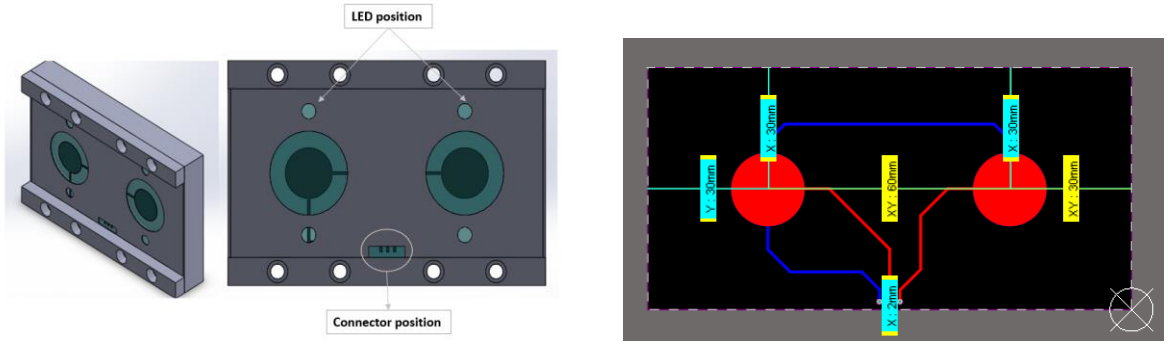

a) b)

Figure 4.21: Design of a haptic demonstrator: a) two haptic button implemented in a single support; b) electrode dimension.

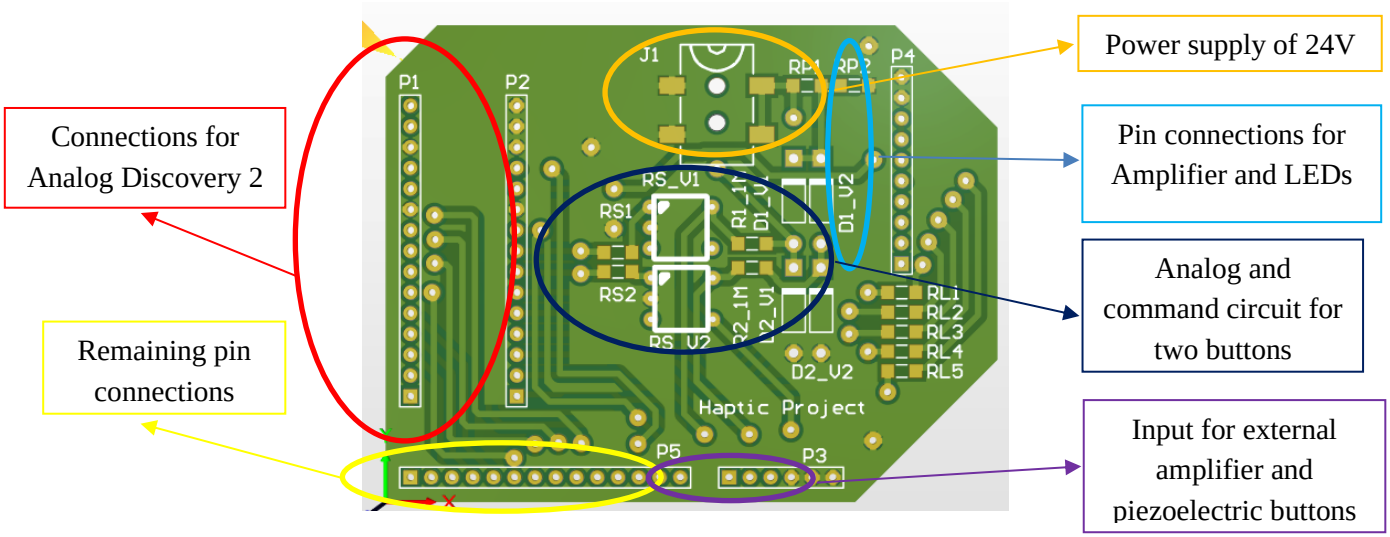

Figure 4.22: PCB design of haptic device based piezoelectric wafer.

4.5.2. Software description

The AD2 creates custom waveform, reads voltage with the oscilloscope, controls static relays using digital outputs. This is possible because this device has a lot of tools at our disposal. However, it needs an external computer to analyze and correctly control the haptic demonstrator. To control the AD2 and other products, *Diligent* created a custom integrated development environment (IDE) named *WaveForms*. This last IDE has a graphical user interface to manipulate all tools in the AD2 like the oscilloscope, logic analyzer, waveform generator, power supply, impedance analyzer, spectrum analyzer, data logger, etc. To fulfil further specific needs, *Waveforms* offer the possibility to control devices using JavaScript with an internal documentation library, called *WaveForms SDK* [268]. For the haptic control, SDK with Python codes are used to create a project in Visual Studio 2019 [269].

Figure 4.23a describes a flowchart of the developed program used to activate the vibrotactile feedback after a button is pressed. The program includes setting up and declaring values that need for the AD2. The functional part of the code is located at the end of the program, where a while loop constantly reads the voltage input from the oscilloscope. Once a valid voltage surpasses the detection point, the "generateWave" function is called to activate the waveform generator for the specified button using the user-selected waveform. After the haptic response is sent, the generator turns off and the program resumes reading the piezoelectric voltage. This entire process constitutes the "functional code" of the program.

The Python code performs two separate tasks simultaneously. The first task is the functional code described above, which reads the voltage and generates haptic responses based on the user's input. The second task is a graphical user interface (GUI) application displayed in Figure 4.23b, which aims to modify the waveform applied to each button in real-time. A waveform is defined as a combination of various attributes like amplitude, type of wave, duration, frequency, etc., in the waveform class.

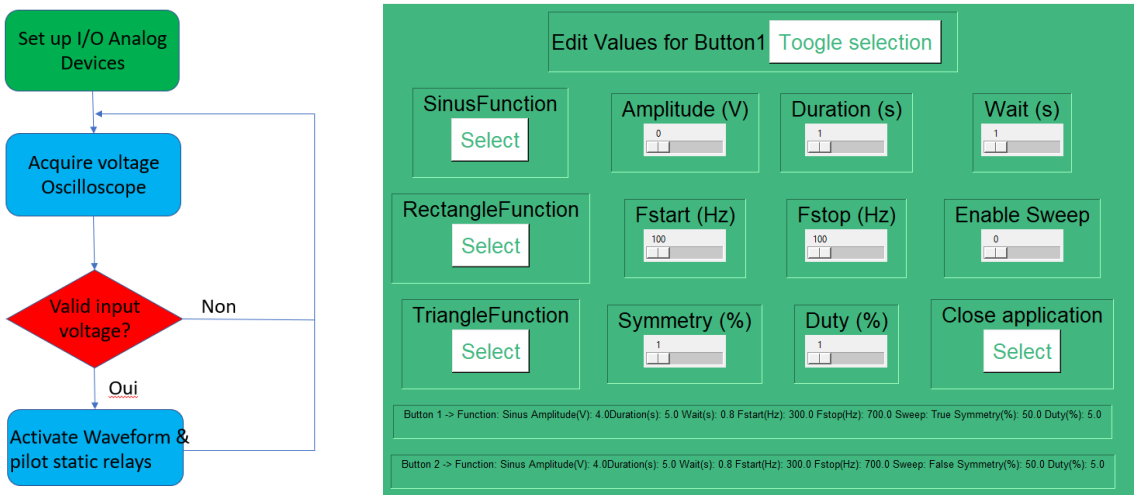

a) b)

Figure 4.23. Software development: a) Flowchart of the program for an activation of the haptic feedback; b) graphical User Interface (GUI) application.

4.5.3. Validation of haptic device

The haptic demonstrator provides three types of signals: sinusoidal, square, and triangular. According to the theory, vibrations around 300Hz are supposed to obtain the best perception, although those within the range of 100 – 700Hz could be detected by the device. During the testing phase, it has been observed that for some signals, it is possible to hear sounds coming from the piezoelectric buttons, while for others, it was easier to perceive the vibrations. In order to classify the perception and comfort as a function of the input waveform signal, two categories are investigated including sensibility and audio/sound:

- Sensibility: Could I perceive the vibrations?
- Audio/sound: How loud are the sounds coming from the button?

We conducted multiple trials on signals with a frequency of 300 Hz, and then performed a sweep within the frequency range of 300 – 700Hz. Tests were carried out on 10 subjects who have to response to the above questions by expressing their feeling in perception and sound that found in the classification table. The results obtained from the tests are compiled in Table 4.1, which are relied on the average response of the 10 subjects. In experience, the sinusoidal signal with a sweep was the most enjoyable sensation because a majority of subjects could feel the vibrations very clearly without any unwanted noises. The square wave was also a good signal, but the triangular wave was not effective as vibrations were difficult to be detected and a lot of uncomfortable noises. It seems that the performances in the haptic quality and audio sound are somehow related. For instance, in the triangular wave, the haptic perception is poor, which might be due to the fact that an important mechanical energy is transformed into acoustical energy, leading to small vibration and undesired sound. This behavior, to some extent, is inverse in the case with the sine wave.

It is worth noting that there is a non-negligible dispersion of the 10 subjects when tested the haptic demonstrator. Actually, people had different preferences for the types of signals they enjoyed. Some individuals (~ 20 %) perceived the square wave vibrations better than the sinusoidal ones. Additionally, some participants (~ 30 %) did not prefer the sweep option and instead preferred signals around 300 Hz. It was clear that there was not a particular type of signal that was preferred by everyone, as people had varying preferences for haptic signals. The variability of the result shown is Table 4.1 was not performed in this study, as the number of the subjects was not sufficient to get convincing statistical analyses. In future work, more subjects (~ 20 – 30) should be involved, together with other relevant numerical indicators that are of primary importance for assessing the performance of the haptic device.

Table 4.1: Response of haptic demonstrator for different waveform/frequency

Waveform/ frequency	Human sensibility	Audio - Sound
Sine / 300 Hz	+ +	- - -
Sine Sweep / 300 – 700Hz	+ + +	-
Square / 300 Hz	~	+
Square Sweep / 300 – 700 Hz	+	+ + +

Triangle / 300 Hz	- -	+ +
Triangle / 300 – 700Hz	-	+ + +

Classification

Symbol	- - -	- -	-	~	+	+ +	+ + +
Sensibility	Nothing	Bad	Disappointed	Average	Nice	Good	Excellent
Sound	Quiet	Low	Soft	Ambient	Noisy	Loud	STOP

4.6. Summary

This chapter demonstrated high potential of the piezoelectric materials in the development of haptic button for tactile screen. These materials exhibit excellent ability to function as sensor for detecting user input, and as actuator for sending haptic responses. Moreover, they are adaptable to 3D printing additive manufacturing and can be coated in thin film layers, allowing for an easy integration in the touch screen. Design optimization based on FEM via ANSYS was carried out, allowing to find out that several factors relating to the geometric parameters (i.e., radio and thickness ratios) of the piezoelectric wafer, the substrate stiffness, the electrode's property could have significant impacts on the haptic performance. Experimental characterization allows to validate the numerical solutions as well as the reliability of the actuation device. It has been revealed that, besides the materials' properties, the haptic perception also strongly depends on the characteristics of the feedback signal, which is determined by the frequency, the displacement amplitude, and the type of waveform. As demonstrated, most users could feel good perception generated from the haptic button under a bandwidth of 300–700 Hz, and a minimum movement of 2 µm. Better comfort was obtained with sinus and square waves, rather than triangle wave with an apparition of undesired audio noises.

Last but not least, according to the requirement of Volvo, the haptic demonstrator has been successfully developed that allowed users to experience their sensations. An electronic circuit was fabricated according to the target specifications, and a Python application was developed to easily manipulate various types of waveforms. As different people can have different sensations with respect to the waveform they receive, practical tests should be carried out on a numerous of subjects so as to better validate the quality of the piezoelectric device. Finally, the haptic demonstrator developed in this study offers an easy solution to interact with tactile technology, paving the way for next generation of smart multifunctional materials.

General Conclusion

The thesis reported on the development and optimization of piezoelectric materials for printed electronics, in connection with applications related to condition monitoring of ball bearing and haptic feedback for touchscreen.

First, the study involved the development of multilayered sensor coatings via the 3D screen-printing technique, which relies on standard design rules of the electronic sensor network. To avoid parasitic capacitances of the printed sensor circuit, the conductive tracks (CTs) were deposited on a dielectric layer while the electrodes were coated on the piezocomposite layer (made of $BaTiO_3$ ferroelectric fillers randomly dispersed within Polyurethane Acrylate (PUA) thermoplastic). For a better achievement of reliable measurements, other geometric constraints of CTs were also investigated. A measurement setup was conducted, leading to comprehensive electromechanical characterizations of piezoelectric thin-film structures used for the condition monitoring (CM) of bearings. The bearing was assimilated to a cross-shaped steel substrate, which was instrumented by customized piezocomposite sensors capable of delivering linear electrical signals in response to an application of bidirectional load (axial and radial). The experimental setup, including two four-point bending (4PB) sample holders, allowed to drive the bidirectional strain to the sensor, which in turn implied an output signal by measuring the induced charges. Regarding the strain distribution in the sensing layer computed by a finite element model (FEM), it has been revealed that the center of the cross substrate resulted in a significant drop as opposed to the two sides. This effect can be explained by the fact that the input load was somehow distributed in both axial and radial directions. Consequently, a piezoelectric sensor implemented on the intersecting area of the cross sample is capable of detecting load in both directions. As the strain induced on that area was not homogenous, the orientation and shape of the electrode coated on it could affect the sensor output signal, to some extent. Finally, there are several parameters relating to the structural design of smart sensor coatings that might have an impact on sensing performance. Understanding the ultimate role of each parameter is of crucial importance to achieve reliable condition monitoring of bearings. To sum up, the investigation explored in this work is proof of an innovative concept in multidirectional load-sensing bearings, which will be conducted in a real-world operation to validate its reliability for the aeronautic field. To boost the piezoelectric sensitivity, an improvement in the process via dielectrophoresis structuration of the material is envisaged in future work. Other alternatives intend to increase the filler's concentration with the use of highly anisotropic fillers (e.g., rod or wire shape) to enhance the printed coating performance.

Second, this thesis presents the development of haptic feedback using piezoelectric material as actuator cable of generating vibration sensation to user. The process began with the creation of FEM to simulate and optimize different parameters implemented in haptic button model. To achieve the desired vibration effect on the skin, the haptic system must be able to drive a displacement of at least 2 µm at a frequency range of 300 – 700Hz. By setting the radius ratio of the piezoelectric layer and substrate layer at 60%, the maximum displacement is achieved. The thickness of these layers was chosen to balance between good displacement and stiffness, ensuring that they are not easily broken. Additionally, even though the electrodes are very

thin, the presence of electrodes can have a significant influence on the performance of piezoelectric haptic feedback devices. In the context of the described work, the goal was to develop a haptic button with a displacement limit of 2 µm. To achieve this, an additional layer of piezoelectric material was added to the button architecture to increase its haptic properties. The results of experimental testing confirmed the effectiveness of this approach, although there was some discrepancy between the predicted theoretical results and the actual experimental measurements.

To further optimize the design, a haptic demonstrator was fabricated and an electronic circuit was developed to meet the specifications of the demonstrator. A Python application was also created to enable easy testing of different types of waveforms. Testing on the demonstrator showed clear haptic feedback on the finger, although it was noted that different people had varying preferences for the type of signal they enjoyed. Some individuals perceived square wave vibrations better than sinusoidal ones, and some preferred signals around 300Hz instead of the sweep option. These results highlight the importance of considering individual user preferences when designing haptic feedback mechanisms. By optimizing the design to accommodate a range of preferences, it is possible to create more effective and user-friendly haptic interfaces.

In conclusion, piezoelectric composites and printed electronics have significant potential for various applications, such as structural control and haptic feedback. The development of multilayered sensor coatings using screen printing techniques has led to reliable measurements for condition monitoring of bearings. Last but not least, the investigation of multidirectional load-sensing bearings is an innovative concept that has the potential to be applied in the aeronautic field. In the development of haptic feedback, the use of piezoelectric materials has also shown promise in achieving desired vibration effects on the skin. Although some discrepancies between predicted theoretical results and actual experimental measurements were observed, the effectiveness of this approach was confirmed through practical tests performed on several subjects who clearly felt the vibration feedback generated from the haptic demonstrator developed by our team. In this device, an electronic circuit was successfully fabricated according to the target specifications imposed by Volvo, and a Python application was developed to easily manipulate various types of waveforms. As different people can have different sensations with respect to the waveform they receive, further practical tests should be carried out on a more important number of subjects so as to better assess the quality of the piezoelectric device.

Future work can include the improvement of the piezoelectric sensitivity through the use of dielectrophoresis structuration of the material or the use of highly anisotropic fillers. Furthermore, it is important to consider individual user preferences when designing haptic feedback mechanisms to create more effective and user-friendly haptic interfaces. Overall, the potential of piezoelectric composites and printed electronics is vast, and continued research in this field could lead to innovative solutions for a wide range of applications, including in the fields of structural control, haptic feedback, and beyond.

References

[1] G.W. Taylor, Piezoelectricity, New York, 1985.

[2] S. KATZIR, THE DISCOVERY OF THE PIEZOELECTRIC EFFECT, in: S. KATZIR (Ed.), THE BEGINNINGS OF PIEZOELECTRICITY: A Study in Mundane Physics, Springer Netherlands, Dordrecht, 2006: pp. 15–64. https://doi.org/10.1007/978-1-4020-4670-4_2.

[3] A.L. Williams, Piezoelectric Microphones, Journal of the Society of Motion Picture Engineers. 23 (1934) 196–209. https://doi.org/10.5594/J05439.

[4] Y. Yang, H. Pan, G. Xie, Y. Jiang, C. Chen, Y. Su, Y. Wang, H. Tai, Flexible piezoelectric pressure sensor based on polydopamine-modified BaTiO3/PVDF composite film for human motion monitoring, Sensors and Actuators A: Physical. 301 (2020) 111789. https://doi.org/10.1016/j.sna.2019.111789.

[5] S. Shi, W. Geng, K. Bi, J. He, X. Hou, J. Mu, F. Li, X. Chou, Design and fabrication of a novel MEMS piezoelectric hydrophone, Sensors and Actuators A: Physical. 313 (2020) 112203. https://doi.org/10.1016/j.sna.2020.112203.

[6] P. Baumann, Piezoelectric Buzzer, in: P. Baumann (Ed.), Selected Sensor Circuits: From Data Sheet to Simulation, Springer Fachmedien, Wiesbaden, 2023: pp. 183–220. https://doi.org/10.1007/978-3-658-38212-4_8.

[7] A. Manbachi, R.S.C. Cobbold, Development and Application of Piezoelectric Materials for Ultrasound Generation and Detection, Ultrasound. 19 (2011) 187–196. https://doi.org/10.1258/ult.2011.011027.

[8] 176-1987 IEEE Standard on Piezoelectricity., n.d.

[9] J. Rychlewski, On Hooke's law, Journal of Applied Mathematics and Mechanics. 48 (1984) 303–314. https://doi.org/10.1016/0021-8928(84)90137-0.

[10] M. Akram, A. Javed, T.Z. Rizvi, Dielectric properties of industrial polymer composite materials, Turkish Journal of Physics. 29 (2005) 355–362. https://doi.org/10.22401/jnus.13.1.10.

[11] A. Arnau, D. Soares, Fundamentals of piezoelectricity, Piezoelectric Transducers and Applications. (2008) 1–38. https://doi.org/10.1007/978-3-540-77508-9_1.

[12] Z. Wang, X. Pan, Y. He, Y. Hu, H. Gu, Y. Wang, Piezoelectric Nanowires in Energy Harvesting Applications, Advances in Materials Science and Engineering. 2015 (2015). https://doi.org/10.1155/2015/165631.

[13] H. Khanbareh, Expanding the Functionality of Piezo-Particulate Composites, (2016). https://doi.org/10.4233/UUID:AAB2497D-6EEC-4956-8C15-8F5FDEDC94F3.

[14] Dielectric Material - an overview | ScienceDirect Topics, (n.d.). https://www.sciencedirect.com/topics/materials-science/dielectric-material (accessed January 13, 2023).

[15] Pyroelectricity - an overview | ScienceDirect Topics, (n.d.). https://www.sciencedirect.com/topics/materials-science/pyroelectricity (accessed January 13, 2023).

[16] Y. Xu, Ferroelectric Materials and Their Applications, Elsevier, 2013.

[17] K. Uchino, Piezoelectric ceramics for transducers, Ultrasonic Transducers: Materials and Design for Sensors, Actuators and Medical Applications. (2012) 70–116. https://doi.org/10.1533/9780857096302.1.70.

[18] Y. Saigusa, Chapter 5 - Quartz-Based Piezoelectric Materials, in: K. Uchino (Ed.), Advanced Piezoelectric Materials (Second Edition), Woodhead Publishing, 2017: pp. 197–233. https://doi.org/10.1016/B978-0-08-102135-4.00005-9.

[19] H. Jaffe, Piezoelectric Ceramics, Journal of the American Ceramic Society. 41 (1958) 494–498. https://doi.org/10.1111/j.1151-2916.1958.tb12903.x.

[20] A. Eddiai, M. Meddad, R. Farhan, M. Mazroui, M. Rguiti, D. Guyomar, Using PVDF piezoelectric polymers to maximize power harvested by mechanical structure, Superlattices and Microstructures. 127 (2019) 20–26. https://doi.org/10.1016/j.spmi.2018.03.044.

[21] H. Lee, R. Cooper, K. Wang, H. Liang, Nano-Scale Characterization of a Piezoelectric Polymer (Polyvinylidene Difluoride, PVDF), Sensors. 8 (2008) 7359–7368. https://doi.org/10.3390/s8117359.

[22] Z. Xiang, B. Ducharne, N. Della Schiava, J.-F. Capsal, P.-J. Cottinet, G. Coativy, P. Lermusiaux, M.Q. Le, Induction heating-based low-frequency alternating magnetic field: High potential of ferromagnetic composites for medical applications, Materials & Design. 174 (2019) 107804. https://doi.org/10.1016/j.matdes.2019.107804.

[23] V.-C. Nguyen, M.-Q. Le, J.-F. Mogniotte, J.-F. Capsal, P.-J. Cottinet, Extrusion-Based 3D Printing of Stretchable Electronic Coating for Condition Monitoring of Suction Cups, Micromachines. 13 (2022) 1606. https://doi.org/10.3390/mi13101606.

[24] T.-Y. Zhang, M. Zhao, P. Tong, Fracture of Piezoelectric Ceramics, Advances in Applied Mechanics - ADVAN APPL MECH. 38 (2002) 147–289. https://doi.org/10.1016/S0065-2156(02)80104-1.

[25] Advances in Piezoelectric Polymer Composites for Energy Harvesting Applications: A Systematic Review - Mishra - 2019 - Macromolecular Materials and Engineering - Wiley Online Library, (n.d.). https://onlinelibrary.wiley.com/doi/abs/10.1002/mame.201800463 (accessed January 13, 2023).

[26] Polar Polymer - an overview | ScienceDirect Topics, (n.d.). https://www.sciencedirect.com/topics/engineering/polar-polymer (accessed January 13, 2023).

[27] C. DeArmitt, R. Rothon, Particulate Fillers, Selection, and Use in Polymer Composites, in: S. Palsule (Ed.), Polymers and Polymeric Composites: A Reference Series, Springer, Berlin, Heidelberg, 2016: pp. 1–26. https://doi.org/10.1007/978-3-642-37179-0_1-2.

[28] C. Mendes-Felipe, J. Oliveira, I. Etxebarria, J.L. Vilas-Vilela, S. Lanceros-Mendez, State-of-the-Art and Future Challenges of UV Curable Polymer-Based Smart Materials for Printing Technologies, Advanced Materials Technologies. 4 (2019) 1800618. https://doi.org/10.1002/admt.201800618.

[29] W. Yin, X. Zeng, H. Li, Y. Hou, Q. Gao, Synthesis, photopolymerization kinetics, and thermal properties of UV-curable waterborne hyperbranched polyurethane acrylate dispersions, J Coat Technol Res. 8 (2011) 577. https://doi.org/10.1007/s11998-011-9338-x.

[30] V.-C. Nguyen, M.-Q. Le, A. Fimbel, S. Bernadet, Y. Hebrard, J.-F. Mogniotte, J.-F. Capsal, P.-J. Cottinet, Printing smart coating of piezoelectric composite for application in condition monitoring of bearings, Materials & Design. 215 (2022) 110529. https://doi.org/10.1016/j.matdes.2022.110529.

[31] J. Fu, L. Wang, H. Yu, M. Haroon, F. Haq, W. Shi, B. Wu, L. Wang, Research progress of UV-curable polyurethane acrylate-based hardening coatings, Progress in Organic Coatings. 131 (2019) 82–99. https://doi.org/10.1016/j.porgcoat.2019.01.061.

[32] M. Lombardi, A. Guerriero, G. Kortaberria, I. Mondragon, M. Sangermano, L. Montanaro, Effect of the ceramic filler features on the properties of photopolymerized BaTiO3-acrylic composites, Polymer Composites. 32 (2011) 1304–1312. https://doi.org/10.1002/pc.21154.

[33] S. Won Kim, H. Rak Choi, C. Su Han, D. Bin Kim, J. Won Kim, Y. Soo Cho, Dielectric and current–voltage characteristics of flexible Ag/BaTiO 3 nanocomposite films processed at near room temperature, RSC Advances. 7 (2017) 56038–56043. https://doi.org/10.1039/C7RA11640C.

[34] C. Mendes-Felipe, T. Rodrigues-Marinho, J.L. Vilas, S. Lanceros-Mendez, UV curable nanocomposites with tailored dielectric response, Polymer. 196 (2020) 122498. https://doi.org/10.1016/j.polymer.2020.122498.

[35] H. Gong, Y. Zhang, J. Quan, S. Che, Preparation and properties of cement based piezoelectric composites modified by CNTs, Current Applied Physics. 11 (2011) 653–656. https://doi.org/10.1016/J.CAP.2010.10.021.

[36] A.K. Roy, Z. Ahmad, A. Prasad, K. Prasad, Concentration dependent dielectric properties of Barium Titanate / Polyvenylidene Fluoride (PVDF) and, Advances in Materials Research. 1 (2012) 285–297.

[37] A.S. Tatarenko, V. Gheevarughese, G. Srinivasan, O. V. Antonenkov, M.I. Bichurin, Microwave magnetoelectric effects in ferrite—piezoelectric composites and dual electric and magnetic field tunable filters, Journal of Electroceramics 2007 24:1. 24 (2007) 5–9. https://doi.org/10.1007/S10832-007-9382-1.

[38] G. D'Ambrogio, O. Zahhaf, M. Bordet, M.Q. Le, N. Della Schiava, R. Liang, P.-J. Cottinet, J.-F. Capsal, Structuring BaTiO3 /PDMS nanocomposite via dielectrophoresis for fractional flow reserve measurement, Advanced Engineering Materials. adem.202100341 (2021). https://doi.org/10.1002/adem.202100341.

[39] C. Carbone, M. Benwadih, G. D'Ambrogio, M.-Q. Le, J.-F. Capsal, P.-J. Cottinet, Influence of Matrix and Surfactant on Piezoelectric and Dielectric Properties of Screen-Printed BaTiO3/PVDF Composites, Polymers. 13 (2021) 2166. https://doi.org/10.3390/polym13132166.

[40] J.-F. Capsal, E. Dantras, L. Laffont, J. Dandurand, C. Lacabanne, Nanotexture influence of BaTiO3 particles on piezoelectric behaviour of PA 11/BaTiO3 nanocomposites, Journal of Non-Crystalline Solids. 356 (2010) 629–634. https://doi.org/10.1016/j.jnoncrysol.2009.06.050.

[41] V.-C. Nguyen, M.-Q. Le, A. Fimbel, S. Bernadet, Y. Hebrard, J.-F. Mogniotte, J.-F. Capsal, P.-J. Cottinet, Printing smart coating of piezoelectric composite for application in condition monitoring of bearings, Materials & Design. 215 (2022) 110529. https://doi.org/10.1016/j.matdes.2022.110529.

[42] S. Singamneni, Y. LV, A. Hewitt, R. Chalk, W. Thomas, D. Jordison, Additive Manufacturing for the Aircraft Industry: A Review, Journal of Aeronautics & Aerospace Engineering. 08 (2019). https://doi.org/10.35248/2168-9792.19.8.215.

[43] M.F. Farooqui, M.A. Karimi, K.N. Salama, A. Shamim, 3D-Printed Disposable Wireless Sensors with Integrated Microelectronics for Large Area Environmental Monitoring, Advanced Materials Technologies. 2 (2017) 1–9. https://doi.org/10.1002/admt.201700051.

[44] G. Xiao, P. Aflaki, S. Lang, Z. Zhang, Y. Tao, C. Py, P. Lu, C. Martin, S. Change, Printed UHF RFID Reader Antennas for Potential Retail Applications, IEEE Journal of Radio Frequency Identification. 2 (2018) 31–37. https://doi.org/10.1109/JRFID.2018.2823640.

[45] K. Church, E. MacDonald, P. Clark, R. Taylor, D. Paul, K. Stone, M. Wilhelm, F. Medina, J. Lyke, R. Wicker, Printed electronic processes for flexible hybrid circuits and antennas, in: 2009 Flexible Electronics & Displays Conference and Exhibition, 2009: pp. 1–7. https://doi.org/10.1109/FEDC.2009.5069282.

[46] Q. Liu, M.Q. Le, C. Richard, R. Liang, P.-J. Cottinet, J.-F. Capsal, Enhanced pseudo-piezoelectric dynamic force sensors based on inkjet-printed electrostrictive terpolymer, Organic Electronics. 67 (2019) 259–271. https://doi.org/10.1016/j.orgel.2019.01.028.

[47] J. DeGraff, R. Liang, M.Q. Le, J.-F. Capsal, F. Ganet, P.-J. Cottinet, Printable low-cost and flexible carbon nanotube buckypaper motion sensors, Materials & Design. 133 (2017) 47–53. https://doi.org/10.1016/j.matdes.2017.07.048.

[48] M.Q. Le, F. Ganet, D. Audigier, J.-F. Capsal, P.-J. Cottinet, Printing of microstructure strain sensor for structural health monitoring, Appl. Phys. A. 123 (2017) 354. https://doi.org/10.1007/s00339-017-0970-x.

[49] K. Thetpraphi, W. Kanlayakan, S. Chaipo, G. Moretto, J. Kuhn, D. Audigier, M.Q. Le, P.-J. Cottinet, L. Petit, J.-F. Capsal, 3D-Printed Electroactive Polymer Force-Actuator for Large and High Precise Optical Mirror Applications, Additive Manufacturing. (2021) 102199. https://doi.org/10.1016/j.addma.2021.102199.

[50] Y. Khan, A. Thielens, S. Muin, J. Ting, C. Baumbauer, A.C. Arias, A New Frontier of Printed Electronics: Flexible Hybrid Electronics, Advanced Materials. 32 (2020) 1905279. https://doi.org/10.1002/adma.201905279.

[51] B. Lu, H. Lan, H. Liu, Additive manufacturing frontier: 3D printing electronics, OEA. 1 (2018) 170004–170004. https://doi.org/10.29026/oea.2018.170004.

[52] S. Khan, S. Ali, A. Bermak, Recent Developments in Printing Flexible and Wearable Sensing Electronics for Healthcare Applications, Sensors. 19 (2019) 1230. https://doi.org/10.3390/s19051230.

[53] E.M. Heckman, C.M. Bartsch, E.B. Kreit, R.S. Aga, F. Ouchen, Printed Electronics for Aerospace Applications, in: M.E. Kinsella (Ed.), Women in Aerospace Materials: Advancements and Perspectives of Emerging Technologies, Springer International Publishing, Cham, 2020: pp. 93–104. https://doi.org/10.1007/978-3-030-40779-7_7.

[54] Z. Cui, Printed Electronics: Materials, Technologies and Applications, John Wiley & Sons, 2016.

[55] Printing Ultra-Thin Circuits Into Banknotes Could Give Electronic Security to Paper Currency, Popular Science. (2010). https://www.popsci.com/technology/article/2010-12/stamping-ultra-thin-circuits-banknotes-could-make-even-paper-currency-electronic/ (accessed January 13, 2023).
[56] How printed electronics enable one-time passcode cards, Issuu. (n.d.). https://issuu.com/petersonpublications/docs/cq111_web/s/11194557 (accessed January 13, 2023).
[57] Design and optimization of a printed circuit board for a photovoltaic and thermal linear solar concentrator, (n.d.). https://ieeexplore.ieee.org/abstract/document/5278860/ (accessed January 13, 2023).
[58] Gravure Printing - an overview | ScienceDirect Topics, (n.d.). https://www.sciencedirect.com/topics/engineering/gravure-printing (accessed January 13, 2023).
[59] X. Liu, J.T. Guthrie, A review of flexographic printing plate development, Surface Coatings International Part B: Coatings Transactions. 86 (2003) 91–99. https://doi.org/10.1007/BF02699619.
[60] Screen Printing: How It Works, Benefits & Applications | Ynvisible, (n.d.). https://www.ynvisible.com/news-inspiration/what-is-screen-printing (accessed October 6, 2022).
[61] Advantages and Disadvantages of Screen Printing – NYFIFTH BLOG, (n.d.). https://www.nyfifth.com/blog/2017/09/27/advantages-and-disadvantages-of-screen-printing/ (accessed October 6, 2022).
[62] A. Moya, G. Gabriel, R. Villa, F. Javier del Campo, Inkjet-printed electrochemical sensors, Current Opinion in Electrochemistry. 3 (2017) 29–39. https://doi.org/10.1016/j.coelec.2017.05.003.
[63] Wearable Electronics and Smart Textiles: A Critical Review, Studylib.Net. (n.d.). https://studylib.net/doc/18391355/wearable-electronics-and-smart-textiles--a-critical-review (accessed January 13, 2023).
[64] E. Feilden, E.G.-T. Blanca, F. Giuliani, E. Saiz, L. Vandeperre, Robocasting of structural ceramic parts with hydrogel inks, Journal of the European Ceramic Society. 36 (2016) 2525–2533. https://doi.org/10.1016/j.jeurceramsoc.2016.03.001.
[65] A. Zocca, G. Franchin, H. Elsayed, E. Gioffredi, E. Bernardo, P. Colombo, Direct Ink Writing of a Preceramic Polymer and Fillers to Produce Hardystonite (Ca2ZnSi2O7) Bioceramic Scaffolds, Journal of the American Ceramic Society. 99 (2016) 1960–1967. https://doi.org/10.1111/jace.14213.
[66] L. Rueschhoff, W. Costakis, M. Michie, J. Youngblood, R. Trice, Additive Manufacturing of Dense Ceramic Parts via Direct Ink Writing of Aqueous Alumina Suspensions, International Journal of Applied Ceramic Technology. 13 (2016) 821–830. https://doi.org/10.1111/ijac.12557.
[67] T. An, K.-T. Hwang, J.-H. Kim, J. Kim, Extrusion-based 3D direct ink writing of NiZn-ferrite structures with viscoelastic ceramic suspension, Ceramics International. 46 (2020) 6469–6476. https://doi.org/10.1016/j.ceramint.2019.11.127.
[68] S. Agarwala, G. Guo Liang, W.Y. Yeong, Optimizing Aerosol Jet Printing Process of Silver Ink for Printed Electronics, in: 2017.
[69] Multimodal piezoelectric wind energy harvester for aerospace applications - Sheeraz - 2022 - International Journal of Energy Research - Wiley Online Library, (n.d.). https://onlinelibrary.wiley.com/doi/abs/10.1002/er.8089 (accessed January 13, 2023).
[70] X. Jiang, K. Kim, S. Zhang, J. Johnson, G. Salazar, High-Temperature Piezoelectric Sensing, Sensors. 14 (2014) 144–169. https://doi.org/10.3390/s140100144.
[71] Piezo Devices For Automotives | APC International, (n.d.). https://www.americanpiezo.com/markets/automotive.html (accessed January 13, 2023).
[72] H. Kulkarni, K. Zohaib, A. Khusru, K. Shravan Aiyappa, Application of piezoelectric technology in automotive systems, Materials Today: Proceedings. 5 (2018) 21299–21304. https://doi.org/10.1016/j.matpr.2018.06.532.
[73] P. Jaenker, V. Kloeppel, P. Konstanzer, R. Maier, PIEZO ACTIVE VIBRATION AND NOISE CONTROL IN HELICOPTERS, (n.d.).

[74] K.M. Newbury, D.J. Leo, Electromechanical Modeling and Characterization of Ionic Polymer Benders, Journal of Intelligent Material Systems and Structures. 13 (2002) 51–60. https://doi.org/10.1177/1045389X02013001978.

[75] Y. Hu, C. Xu, Y. Zhang, L. Lin, R.L. Snyder, Z.L. Wang, A nanogenerator for energy harvesting from a rotating tire and its application as a self-powered pressure/speed sensor, Advanced Materials. 23 (2011) 4068–4071. https://doi.org/10.1002/adma.201102067.

[76] Development of a low-cost piezo film-based knock sensor - E Pipitone, L D'Acquisto, 2003, (n.d.). https://journals.sagepub.com/doi/abs/10.1243/0954407036069208?journalCode=pidb (accessed January 13, 2023).

[77] PVDF-Based Piezoelectric Microphone for Sound Detection Inside the Cochlea: Toward Totally Implantable Cochlear Implants - Steve Park, Xiying Guan, Youngwan Kim, Francis (Pete) X. Creighton, Eric Wei, Ioannis(John) Kymissis, Hideko Heidi Nakajima, Elizabeth S. Olson, 2018, (n.d.). https://journals.sagepub.com/doi/full/10.1177/2331216518774450 (accessed January 13, 2023).

[78] M.Q. Le, J.-F. Capsal, M. Lallart, Y. Hebrard, A. Van Der Ham, N. Reffe, L. Geynet, P.-J. Cottinet, Review on energy harvesting for structural health monitoring in aeronautical applications, Progress in Aerospace Sciences. 79 (2015) 147–157. https://doi.org/10.1016/j.paerosci.2015.10.001.

[79] Smart street lights using piezoelectric materials | IEEE Conference Publication | IEEE Xplore, (n.d.). https://ieeexplore.ieee.org/abstract/document/7522506 (accessed January 13, 2023).

[80] R. Hinchet, S. Lee, G. Ardila, L. Montès, M. Mouis, Z.L. Wang, Performance optimization of vertical nanowire-based piezoelectric nanogenerators, Advanced Functional Materials. 24 (2014) 971–977. https://doi.org/10.1002/adfm.201302157.

[81] N. Chapman, B. Chavero, Piezoelectric Energy Harvesting with 3D-Printed Light-Up Shoe, (n.d.).

[82] Conformal piezoelectric energy harvesting and storage from motions of the heart, lung, and diaphragm | PNAS, (n.d.). https://www.pnas.org/doi/abs/10.1073/pnas.1317233111 (accessed January 13, 2023).

[83] H. Magsi, Industrialization, Environment and Pollution, THE DIPLOMATIC INSIGHT. 7 (2014) 24–26.

[84] S. Chawla, H. Uppal, M. Yadav, N. Bahadur, N. Singh, Zinc peroxide nanomaterial as an adsorbent for removal of Congo red dye from waste water, Ecotoxicology and Environmental Safety. 135 (2017) 68–74. https://doi.org/10.1016/j.ecoenv.2016.09.017.

[85] C. Cao, X. Xie, Y. Zeng, S. Shi, G. Wang, L. Yang, C.Z. Wang, S. Lin, Highly efficient and stable p-type ZnO nanowires with piezotronic effect for photoelectrochemical water splitting, Nano Energy. 61 (2019) 550–558. https://doi.org/10.1016/j.nanoen.2019.04.098.

[86] S. Sriphan, N. Vittayakorn, Hybrid piezoelectric-triboelectric nanogenerators for flexible electronics: Recent advances and perspectives, Journal of Science: Advanced Materials and Devices. 7 (2022) 100461. https://doi.org/10.1016/j.jsamd.2022.100461.

[87] J.-H. Lin, Y.-H. Tsao, M.-H. Wu, T.-M. Chou, Z.-H. Lin, J.M. Wu, Single- and few-layers MoS2 nanocomposite as piezo-catalyst in dark and self-powered active sensor, Nano Energy. 31 (2017) 575–581. https://doi.org/10.1016/j.nanoen.2016.12.013.

[88] T.A. Kuchmenko, L.B. Lvova, A Perspective on Recent Advances in Piezoelectric Chemical Sensors for Environmental Monitoring and Foodstuffs Analysis, Chemosensors. 7 (2019) 39. https://doi.org/10.3390/chemosensors7030039.

[89] S. Egusa, Z. Wang, N. Chocat, Z.M. Ruff, A.M. Stolyarov, D. Shemuly, F. Sorin, P.T. Rakich, J.D. Joannopoulos, Y. Fink, Multimaterial piezoelectric fibres, Nature Mater. 9 (2010) 643–648. https://doi.org/10.1038/nmat2792.

[90] A. Rayegani, M. Saberian, Z. delshad, J. Liang, M. Sadiq, A. Matin Nazar, S.A.H. Mohsan, M. Khan, Recent Advances in Self-Powered Wearable Sensors Based on Piezoelectric and Triboelectric Nanogenerators, Biosensors. 13 (2022). https://doi.org/10.3390/bios13010037.

[91] X. Chen, Y. Song, Z. Su, H. Chen, X. Cheng, J. Zhang, M. Han, H. Zhang, Flexible fiber-based hybrid nanogenerator for biomechanical energy harvesting and physiological monitoring, Nano Energy. 38 (2017) 43–50. https://doi.org/10.1016/j.nanoen.2017.05.047.

[92] W. Guo, C. Tan, K. Shi, J. Li, X.-X. Wang, B. Sun, X. Huang, Y.-Z. Long, P. Jiang, Wireless piezoelectric devices based on electrospun PVDF/BaTiO3 NW nanocomposite fibers for human motion monitoring, Nanoscale. 10 (2018) 17751–17760. https://doi.org/10.1039/C8NR05292A.

[93] Piezoelectric Biomaterials for Sensors and Actuators - Chorsi - 2019 - Advanced Materials - Wiley Online Library, (n.d.). https://onlinelibrary.wiley.com/doi/abs/10.1002/adma.201802084 (accessed January 13, 2023).

[94] C. Ribeiro, V. Sencadas, D.M. Correia, S. Lanceros-Méndez, Piezoelectric polymers as biomaterials for tissue engineering applications, Colloids and Surfaces B: Biointerfaces. 136 (2015) 46–55. https://doi.org/10.1016/j.colsurfb.2015.08.043.

[95] C. Ribeiro, V. Correia, P. Martins, F.M. Gama, S. Lanceros-Mendez, Proving the suitability of magnetoelectric stimuli for tissue engineering applications, Colloids and Surfaces B: Biointerfaces. 140 (2016) 430–436. https://doi.org/10.1016/j.colsurfb.2015.12.055.

[96] R. Augustine, P. Dan, A. Sosnik, N. Kalarikkal, N. Tran, B. Vincent, S. Thomas, P. Menu, D. Rouxel, Electrospun poly(vinylidene fluoride-trifluoroethylene)/zinc oxide nanocomposite tissue engineering scaffolds with enhanced cell adhesion and blood vessel formation, Nano Res. 10 (2017) 3358–3376. https://doi.org/10.1007/s12274-017-1549-8.

[97] A knowledge driven approach to aerospace condition monitoring - ScienceDirect, (n.d.). https://www.sciencedirect.com/science/article/pii/S0950705111000748 (accessed January 13, 2023).

[98] M.V. KiranKumar, M. Lokesha, S. Kumar, A. Kumar, Review on Condition Monitoring of Bearings using vibration analysis techniques., IOP Conf. Ser.: Mater. Sci. Eng. 376 (2018) 012110. https://doi.org/10.1088/1757-899X/376/1/012110.

[99] J.-D. Kim, I.-H. Choi, Development of a tool failure detection system using multi-sensors, International Journal of Machine Tools and Manufacture. 36 (1996) 861–870. https://doi.org/10.1016/0890-6955(96)00115-0.

[100] Contactless Monitoring of Ball Bearing Temperature | IEEE Conference Publication | IEEE Xplore, (n.d.). https://ieeexplore.ieee.org/abstract/document/1604416 (accessed January 13, 2023).

[101] What is Haptic Feedback? Types, devices and use | Teslasuit Blog, Teslasuit. (2022). https://teslasuit.io/blog/haptic_feedback/ (accessed January 13, 2023).

[102] S. Kim, G. Lee, Haptic feedback design for a virtual button along force-displacement curves, in: 2013: pp. 91–96. https://doi.org/10.1145/2501988.2502041.

[103] A. Bolopion, S. Régnier, A Review of Haptic Feedback Teleoperation Systems for Micromanipulation and Microassembly, IEEE Transactions on Automation Science and Engineering. 10 (2013) 496–502. https://doi.org/10.1109/TASE.2013.2245122.

[104] F. Ganet, M.-Q. Le, J.F. Capsal, J.F. Gérard, S. Pruvost, J. Duchet, S. Livi, P. Lermusiaux, A. Millon, P.-J. Cottinet, Haptic feedback using an all-organic electroactive polymer composite, Sensors and Actuators B: Chemical. 220 (2015) 1120–1130. https://doi.org/10.1016/j.snb.2015.06.071.

[105] O.A.J. van der Meijden, M.P. Schijven, The value of haptic feedback in conventional and robot-assisted minimal invasive surgery and virtual reality training: a current review, Surg Endosc. 23 (2009) 1180–1190. https://doi.org/10.1007/s00464-008-0298-x.

[106] T.-H. Yang, J.R. Kim, H. Jin, H. Gil, J.-H. Koo, H.J. Kim, Recent Advances and Opportunities of Active Materials for Haptic Technologies in Virtual and Augmented Reality, Advanced Functional Materials. 31 (2021) 2008831. https://doi.org/10.1002/adfm.202008831.

[107] C. Bermejo, P. Hui, A Survey on Haptic Technologies for Mobile Augmented Reality, ACM Comput. Surv. 54 (2021) 184:1-184:35. https://doi.org/10.1145/3465396.

[108] G.S. Ruthenbeck, K.J. Reynolds, Virtual reality for medical training: the state-of-the-art, J Simulation. 9 (2015) 16–26. https://doi.org/10.1057/jos.2014.14.

[109] C. Wee, K.M. Yap, W.N. Lim, Haptic Interfaces for Virtual Reality: Challenges and Research Directions, IEEE Access. 9 (2021) 112145–112162. https://doi.org/10.1109/ACCESS.2021.3103598.
[110] Y. Gaffary, A. Lécuyer, The Use of Haptic and Tactile Information in the Car to Improve Driving Safety: A Review of Current Technologies, Frontiers in ICT. 5 (2018). https://www.frontiersin.org/articles/10.3389/fict.2018.00005 (accessed January 13, 2023).
[111] M.S. Algahtani, A.A. Mohammed, J. Ahmad, Extrusion-Based 3D Printing for Pharmaceuticals: Contemporary Research and Applications, Current Pharmaceutical Design. 24 (n.d.) 4991–5008.
[112] Z. Xiang, Enhancing low-frequency induction heating effect of ferromagnetic composites : Toward medical applications, These de doctorat, Lyon, 2021. https://www.theses.fr/2021LYSEI022 (accessed January 6, 2023).
[113] K. Thetpraphi, Development of electroactive polymer actuators for next generation mirror : Live-Mirror, These de doctorat, Lyon, 2020. https://www.theses.fr/2020LYSEI058 (accessed January 6, 2023).
[114] W. Chen, R. Mills, R.S. Dwyer-Joyce, Direct load monitoring of rolling bearing contacts using ultrasonic time of flight, Proceedings of the Royal Society A: Mathematical, Physical and Engineering Sciences. 471 (2015) 20150103. https://doi.org/10.1098/rspa.2015.0103.
[115] D. Payne, What Causes Bearing Failures and Preventative Measures You Need to Know, (n.d.). https://www.bdsbearing.com/blog/bearing-failures (accessed October 3, 2022).
[116] P. Gupta, M.K. Pradhan, Fault detection analysis in rolling element bearing: A review, Materials Today: Proceedings. 4 (2017) 2085–2094. https://doi.org/10.1016/j.matpr.2017.02.054.
[117] L.I. Guo-Chao-1, B. Wei-2, L.I. Yong-Cai-3, G. a. O. Li-Xin-1, Z. Jian-4, Simulation and Dynamic Analysis of Outer Ring Fault on Rolling Bearings Using Explicit Finite Element Method, China Mechanical Engineering. 23 (2012) 2825.
[118] I. Huseyin Filiz, G. Gorur, Analysis of preloaded bearings under combined axial and radial loading, International Journal of Machine Tools and Manufacture. 34 (1994) 1–11. https://doi.org/10.1016/0890-6955(94)90035-3.
[119] V.-C. Nguyen, M.-Q. Le, S. Bernadet, Y. Hebrard, J.-F. Mogniotte, J.-F. Capsal, P.-J. Cottinet, Design Rules of Bidirectional Smart Sensor Coating for Condition Monitoring of Bearings, Polymers. 15 (2023) 826. https://doi.org/10.3390/polym15040826.
[120] T. Automation, What is the Parasitic Capacitance Effect?, Tempo. (2020). https://www.tempoautomation.com/blog/what-is-the-parasitic-capacitance-effect/ (accessed October 6, 2022).
[121] D.A. van den Ende, S.E. van Kempen, X. Wu, W.A. Groen, C.A. Randall, S. van der Zwaag, Dielectrophoretically structured piezoelectric composites with high aspect ratio piezoelectric particles inclusions, Journal of Applied Physics. 111 (2012) 124107. https://doi.org/10.1063/1.4729814.
[122] F.D. Mbairi, W.P. Siebert, H. Hesselbom, High-Frequency Transmission Lines Crosstalk Reduction Using Spacing Rules, IEEE Transactions on Components and Packaging Technologies. 31 (2008) 601–610. https://doi.org/10.1109/TCAPT.2008.2001163.
[123] EDN, M. RANGU, Getting EMC design right – First time, Part 7: Crosstalk, EDN. (2014). https://www.edn.com/getting-emc-design-right-first-time-part-7-crosstalk/ (accessed October 6, 2022).
[124] O. Media, Addressing EMC Preemptively in Ethernet Connected Devices, Embedded Computing Design. (n.d.). https://embeddedcomputing.com/application/networking-5g/addressing-emc-preemptively-in-ethernet-connected-devices (accessed December 15, 2022).
[125] H. Zhang, S. Krooswyk, J. Ou, High Speed Digital Design: Design of High Speed Interconnects and Signaling, in: Elsevier Inc., 2015: pp. 1–257.
[126] V. Correia, K.Y. Mitra, H. Castro, J.G. Rocha, E. Sowade, R.R. Baumann, S. Lanceros-Mendez, Design and fabrication of multilayer inkjet-printed passive components for printed electronics circuit development, Journal of Manufacturing Processes. 31 (2018) 364–371. https://doi.org/10.1016/j.jmapro.2017.11.016.
[127] X. Zhang, J. Villafuerte, V. Consonni, E. Sarigiannidou, J.-F. Capsal, A. Bruhat, D. Grinberg, L. Petit, P.-J. Cottinet, M.-Q. Le, Optimization Strategies Used for Boosting Piezoelectric Response of Biosensor Based on Flexible Micro-ZnO Composites, Biosensors. 12 (2022) 245. https://doi.org/10.3390/bios12040245.

[128] G. D'Ambrogio, O. Zahhaf, M.-Q. Le, M. Bordet, P. Lermusiaux, N. Della Schiava, R. Liang, P.-J. Cottinet, J.-F. Capsal, Piezoelectric biosensor for smart cardiovascular grafts based on NaNbO3 fibers/PDMS structured composite, Materials & Design. 223 (2022) 111195. https://doi.org/10.1016/j.matdes.2022.111195.

[129] K. Thetpraphi, M.Q. Le, A. Houachtia, P.-J. Cottinet, L. Petit, D. Audigier, J. Kuhn, G. Moretto, J.-F. Capsal, Surface Correction Control Based on Plasticized Multilayer P(VDF-TrFE-CFE) Actuator—Live Mirror, Advanced Optical Materials. 7 (2019) 1900210. https://doi.org/10.1002/adom.201900210.

[130] Z. Xiang, M.Q. Le, P.-J. Cottinet, P. Griffiths, G.P. Baeza, J.-F. Capsal, P. Lermusiaux, N. Della Schiava, B. Ducharne, Development of anisotropic ferromagnetic composites for low-frequency induction heating technology in medical applications, Materials Today Chemistry. 19 (2021) 100395. https://doi.org/10.1016/j.mtchem.2020.100395.

[131] O. Zahhaf, G. D'Ambrogio, A. Giunta, M.-Q. Le, G. Rival, P.-J. Cottinet, J.-F. Capsal, Molten-State Dielectrophoretic Alignment of EVA/BaTiO3 Thermoplastic Composites: Enhancement of Piezo-Smart Sensor for Medical Application, International Journal of Molecular Sciences. 23 (2022) 15745. https://doi.org/10.3390/ijms232415745.

[132] F. Pedroli, A. Marrani, M.-Q. Le, C. Froidefond, P.-J. Cottinet, J.-F. Capsal, Processing optimization: A way to improve the ionic conductivity and dielectric loss of electroactive polymers, Journal of Polymer Science Part B: Polymer Physics. 56 (2018) 1164–1173. https://doi.org/10.1002/polb.24636.

[133] N. Della Schiava, M.-Q. Le, J. Galineau, F. Domingues Dos Santos, P.-J. Cottinet, J.-F. Capsal, Influence of Plasticizers on the Electromechanical Behavior of a P(VDF-TrFE-CTFE) Terpolymer: Toward a High Performance of Electrostrictive Blends, J. Polym. Sci. Part B: Polym. Phys. 55 (2017) 355–369. https://doi.org/10.1002/polb.24280.

[134] J.-F. Capsal, J. Galineau, M.-Q. Le, F. Domingues Dos Santos, P.-J. Cottinet, Enhanced electrostriction based on plasticized relaxor ferroelectric P(VDF-TrFE-CFE/CTFE) blends, Journal of Polymer Science Part B: Polymer Physics. 53 (2015) 1368–1379. https://doi.org/10.1002/polb.23776.

[135] J. Oliveira, V. Correia, H. Castro, P. Martins, S. Lanceros-Mendez, Polymer-based smart materials by printing technologies: Improving application and integration, Additive Manufacturing. 21 (2018) 269–283. https://doi.org/10.1016/j.addma.2018.03.012.

[136] G. D'Ambrogio, O. Zahhaf, M.-Q. Le, J.-F. Capsal, P.-J. Cottinet, Dielectrophoresis Structurization of PZT/PDMS Micro-Composite for Elastronic Function: Towards Dielectric and Piezoelectric Enhancement, Materials. 14 (2021) 4071. https://doi.org/10.3390/ma14154071.

[137] X. Zhang, M.-Q. Le, O. Zahhaf, J.-F. Capsal, P.-J. Cottinet, L. Petit, Enhancing dielectric and piezoelectric properties of micro-ZnO/PDMS composite-based dielectrophoresis, Materials & Design. 192 (2020) 108783. https://doi.org/10.1016/j.matdes.2020.108783.

[138] P. Barber, S. Balasubramanian, Y. Anguchamy, S. Gong, A. Wibowo, H. Gao, H.J. Ploehn, H.-C. Zur Loye, Polymer Composite and Nanocomposite Dielectric Materials for Pulse Power Energy Storage, Materials. 2 (2009) 1697–1733. https://doi.org/10.3390/ma2041697.

[139] H.C. Pant, M.K. Patra, A. Verma, S.R. Vadera, N. Kumar, Study of the dielectric properties of barium titanate–polymer composites, Acta Materialia. 54 (2006) 3163–3169. https://doi.org/10.1016/j.actamat.2006.02.031.

[140] R.K. Goyal, V.V. Madav, P.R. Pakankar, S.P. Butee, Fabrication and Properties of Novel Polyetheretherketone/Barium Titanate Composites with Low Dielectric Loss, J. Electron. Mater. 40 (2011) 2240. https://doi.org/10.1007/s11664-011-1743-5.

[141] Z. Yang, H. Peng, W. Wang, T. Liu, Crystallization behavior of poly(ε-caprolactone)/layered double hydroxide nanocomposites, Journal of Applied Polymer Science. 116 (2010) 2658–2667. https://doi.org/10.1002/app.31787.

[142] S.F. Mendes, C.M. Costa, C. Caparros, V. Sencadas, S. Lanceros-Méndez, Effect of filler size and concentration on the structure and properties of poly(vinylidene fluoride)/BaTiO3 nanocomposites, J Mater Sci. 47 (2012) 1378–1388. https://doi.org/10.1007/s10853-011-5916-7.

[143] S. Dalle Vacche, F. Oliveira, Y. Leterrier, V. Michaud, D. Damjanovic, J.-A.E. Månson, Effect of silane coupling agent on the morphology, structure, and properties of poly(vinylidene fluoride–trifluoroethylene)/BaTiO3 composites, J Mater Sci. 49 (2014) 4552–4564. https://doi.org/10.1007/s10853-014-8155-x.

[144] T. Siponkoski, M. Nelo, J. Peräntie, J. Juuti, H. Jantunen, BaTiO3–P(VDF-TrFE) composite ink properties for printed decoupling capacitors, Composites Part B: Engineering. 70 (2015) 201–205. https://doi.org/10.1016/j.compositesb.2014.11.017.

[145] D. Grinberg, S. Siddique, M.-Q. Le, R. Liang, J.-F. Capsal, P.-J. Cottinet, 4D Printing based piezoelectric composite for medical applications, Journal of Polymer Science Part B: Polymer Physics. 57 (2019) 109–115. https://doi.org/10.1002/polb.24763.

[146] J.-F. Capsal, C. David, E. Dantras, C. Lacabanne, Piezoelectric sensing coating for real time impact detection and location on aircraft structures, Smart Mater. Struct. 21 (2012) 055021. https://doi.org/10.1088/0964-1726/21/5/055021.

[147] Z. Xiang, V.-C. Nguyen, B. Ducharne, N.D. Schiava, J.-F. Capsal, P.-J. Cottinet, M.-Q. Le, 3D Printing of Flexible Composites via Magnetophoresis: Toward Medical Application Based on Low-Frequency Induction Heating Effect, Macromolecular Materials and Engineering. n/a (2021) 1–13. https://doi.org/10.1002/mame.202100211.

[148] C. Carbone, M. Benwadih, G. D'Ambrogio, M.-Q. Le, J.-F. Capsal, P.-J. Cottinet, Influence of Matrix and Surfactant on Piezoelectric and Dielectric Properties of Screen-Printed BaTiO3/PVDF Composites, Polymers. 13 (2021) 2166. https://doi.org/10.3390/polym13132166.

[149] E.Y. Wu, R.-P. Vollertsen, On the Weibull shape factor of intrinsic breakdown of dielectric films and its accurate experimental determination. Part I: theory, methodology, experimental techniques, IEEE Transactions on Electron Devices. 49 (2002) 2131–2140. https://doi.org/10.1109/TED.2002.805612.

[150] F. Pedroli, A. Flocchini, A. Marrani, M.-Q. Le, O. Sanseau, P.-J. Cottinet, J.-F. Capsal, Boosted energy-storage efficiency by controlling conduction loss of multilayered polymeric capacitors, Materials & Design. 192 (2020) 108712. https://doi.org/10.1016/j.matdes.2020.108712.

[151] H. Phung, P.T. Hoang, H. Jung, T.D. Nguyen, C.T. Nguyen, H.R. Choi, Haptic Display Responsive to Touch Driven by Soft Actuator and Soft Sensor, IEEE/ASME Transactions on Mechatronics. 26 (2021) 2495–2505. https://doi.org/10.1109/TMECH.2020.3041225.

[152] E. Vezzoli, T. Sednaoui, M. Amberg, F. Giraud, B. Lemaire-Semail, Texture Rendering Strategies with a High Fidelity - Capacitive Visual-Haptic Friction Control Device, in: F. Bello, H. Kajimoto, Y. Visell (Eds.), Haptics: Perception, Devices, Control, and Applications, Springer International Publishing, Cham, 2016: pp. 251–260. https://doi.org/10.1007/978-3-319-42321-0_23.

[153] S.P. Parikh, J.M. Esposito, Negative Feedback for Small Capacitive Touchscreen Interfaces: A Usability Study for Data Entry Tasks, IEEE Transactions on Haptics. 5 (2012) 39–47. https://doi.org/10.1109/TOH.2011.71.

[154] A. Akther, J.O. Castro, S.A.M. Shaegh, A.R. Rezk, L.Y. Yeo, Miniaturised acoustofluidic tactile haptic actuator, Soft Matter. 15 (2019) 4146–4152. https://doi.org/10.1039/C9SM00479C.

[155] S.E. Emgin, A. Aghakhani, T.M. Sezgin, C. Basdogan, HapTable: An Interactive Tabletop Providing Online Haptic Feedback for Touch Gestures, IEEE Transactions on Visualization and Computer Graphics. 25 (2019) 2749–2762. https://doi.org/10.1109/TVCG.2018.2855154.

[156] G.C. Schmidt, J.M. Werner, T. Weissbach, J. Strutwolf, R. Eland, W.-G. Drossel, A.C. Hübler, Printed Multilayer Piezoelectric Transducers on Paper for Haptic Feedback and Dual Touch-Sound Sensation, Sensors. 22 (2022) 3796. https://doi.org/10.3390/s22103796.

[157] B. Baylan, U. Aridogan, C. Basdogan, Finite Element Modeling of a Vibrating Touch Screen Actuated by Piezo Patches for Haptic Feedback, in: P. Isokoski, J. Springare (Eds.), Haptics: Perception, Devices, Mobility, and Communication, Springer, Berlin, Heidelberg, 2012: pp. 47–57. https://doi.org/10.1007/978-3-642-31401-8_5.

[158] V. Tikka, P. Laitinen, Designing Haptic Feedback for Touch Display: Experimental Study of Perceived Intensity and Integration of Haptic and Audio, in: D. McGookin, S. Brewster (Eds.), Haptic and Audio Interaction Design, Springer, Berlin, Heidelberg, 2006: pp. 36–44. https://doi.org/10.1007/11821731_4.

[159] T.A. Perls, T.J. Diesel, W.I. Dobrov, Primary Pyroelectricity in Barium Titanate Ceramics, Journal of Applied Physics. 29 (1958) 1297–1302. https://doi.org/10.1063/1.1723430.

[160] G. Teyssedre, A. Bernes, C. Lacabanne, DSC and TSC study of a VDF/TrFE copolymer, Thermochimica Acta. 226 (1993) 65–75. https://doi.org/10.1016/0040-6031(93)80207-Q.

[161] G.A. Samara, F. Bauer, The effects of pressure on the β molecular relaxation and phase transitions of the ferroelectric copolymer P(VDF0.7TrFe0.3), Ferroelectrics. 135 (1992) 385–399. https://doi.org/10.1080/00150199208230040.

[162] B. Chu, X. Zhou, B. Neese, Q.M. Zhang, F. Bauer, Relaxor Ferroelectric Polymer–Poly(vinylidene fluoride-trifluoroethylene-chlorofluoroethylene) Terpolymer High Electric Energy Density and Field Dependent Dielectric Response, Ferroelectrics. 331 (2006) 35–42. https://doi.org/10.1080/00150190600732926.

[163] S.C. Mathur, J.I. Scheinbeim, B.A. Newman, Piezoelectric properties and ferroelectric hysteresis effects in uniaxially stretched nylon-11 films, Journal of Applied Physics. 56 (1984) 2419–2425. https://doi.org/10.1063/1.334294.

[164] J. Fu, Y. Hou, M. Zheng, Q. Wei, M. Zhu, H. Yan, Improving Dielectric Properties of PVDF Composites by Employing Surface Modified Strong Polarized BaTiO3 Particles Derived by Molten Salt Method, ACS Appl. Mater. Interfaces. 7 (2015) 24480–24491. https://doi.org/10.1021/acsami.5b05344.

[165] R. Li, Z. Zhao, Z. Chen, J. Pei, Novel BaTiO3/PVDF composites with enhanced electrical properties modified by calcined BaTiO3 ceramic powders, Materials Express. 7 (2017) 536–540. https://doi.org/10.1166/mex.2017.1393.

[166] T. Furukawa, K. Ishida, E. Fukada, Piezoelectric properties in the composite systems of polymers and PZT ceramics, Journal of Applied Physics. 50 (1979) 4904–4912. https://doi.org/10.1063/1.325592.

[167] K. Prume, P. Muralt, F. Calame, T. Schmitz-Kempen, S. Tiedke, Piezoelectric thin films: evaluation of electrical and electromechanical characteristics for MEMS devices, IEEE Transactions on Ultrasonics, Ferroelectrics, and Frequency Control. 54 (2007) 8–14. https://doi.org/10.1109/TUFFC.2007.206.

[168] J. Richter, M.B. Arnoldus, O. Hansen, E.V. Thomsen, Four point bending setup for characterization of semiconductor piezoresistance, Rev Sci Instrum. 79 (2008) 044703. https://doi.org/10.1063/1.2908428.

[169] E. Lund, T.G. Finstad, Design and construction of a four-point bending based set-up for measurement of piezoresistance in semiconductors, Review of Scientific Instruments. 75 (2004) 4960–4966. https://doi.org/10.1063/1.1808917.

[170] B.J. Goodno, J. Gere, Statics and Mechanics of Materials, Cengage Learning, 2018.

[171] N. Della Schiava, K. Thetpraphi, M.-Q. Le, P. Lermusiaux, A. Millon, J.-F. Capsal, P.-J. Cottinet, Enhanced Figures of Merit for a High-Performing Actuator in Electrostrictive Materials, Polymers. 10 (2018) 263. https://doi.org/10.3390/polym10030263.

[172] J. Holterman, P. Groen, An introduction to piezoelectric materials and applications, Stichting Applied Piezo, Apeldoorn, 2013.

[173] Function generator, Wikipedia. (2022). https://en.wikipedia.org/w/index.php?title=Function_generator&oldid=1127358980 (accessed February 6, 2023).

[174] A.H. Ganie, A.A. Memon, M.A. Memon, A.M. Al-Bugami, K. Bhatti, I. Khan, Numerical analysis of laminar flow and heat transfer through a rectangular channel containing perforated plate at different angles, Energy Reports. 8 (2022) 539–550. https://doi.org/10.1016/j.egyr.2021.11.232.

[175] S. Zandi, P. Saxena, M. Razaghi, N.E. Gorji, Simulation of CZTSSe Thin-Film Solar Cells in COMSOL: Three-Dimensional Optical, Electrical, and Thermal Models, IEEE J. Photovoltaics. 10 (2020) 1503–1507. https://doi.org/10.1109/JPHOTOV.2020.2999881.

[176] D. Petersen, C. Howard, Z. Prime, Varying stiffness and load distributions in defective ball bearings: Analytical formulation and application to defect size estimation, Journal of Sound and Vibration. 337 (2015) 284–300. https://doi.org/10.1016/j.jsv.2014.10.004.

[177] A. j Croxford, P. d Wilcox, B. w Drinkwater, G. Konstantinidis, Strategies for guided-wave structural health monitoring, Proceedings of the Royal Society A: Mathematical, Physical and Engineering Sciences. 463 (2007) 2961–2981. https://doi.org/10.1098/rspa.2007.0048.

[178] D.L. Mascarenas, M.D. Todd, G. Park, C.R. Farrar, Development of an impedance-based wireless sensor node for structural health monitoring, Smart Mater. Struct. 16 (2007) 2137–2145. https://doi.org/10.1088/0964-1726/16/6/016.

[179] A.H. Alavi, H. Hasni, N. Lajnef, K. Chatti, F. Faridazar, An intelligent structural damage detection approach based on self-powered wireless sensor data, Automation in Construction. 62 (2016) 24–44. https://doi.org/10.1016/j.autcon.2015.10.001.

[180] Model based fault diagnosis of a rotor–bearing system for misalignment and unbalance under steady-state condition | Elsevier Enhanced Reader, (n.d.). https://doi.org/10.1016/j.jsv.2009.07.014.

[181] Application of correlation matching for automatic bearing fault diagnosis | Elsevier Enhanced Reader, (n.d.). https://doi.org/10.1016/j.jsv.2012.07.022.

[182] K.A. Loparo, M.L. Adams, W. Lin, M.F. Abdel-Magied, N. Afshari, Fault detection and diagnosis of rotating machinery, IEEE Transactions on Industrial Electronics. 47 (2000) 1005–1014. https://doi.org/10.1109/41.873208.

[183] B.J. Hamrock, W.J. Anderson, Rolling-Element Bearings, (1983). https://ntrs.nasa.gov/citations/19830018943 (accessed March 7, 2023).

[184] The Applications of Bearings II: This is how bearings are used for machines in industry / Bearing Trivia / Koyo Bearings(JTEKT), (n.d.). https://koyo.jtekt.co.jp/en/2019/11/column01-06.html (accessed March 7, 2023).

[185] An experimental based assessment of the deviation of the bearing characteristic frequencies | QUT ePrints, (n.d.). https://eprints.qut.edu.au/74408/ (accessed March 7, 2023).

[186] O.V. Thorsen, M. Dalva, A survey of faults on induction motors in offshore oil industry, petrochemical industry, gas terminals, and oil refineries, IEEE Transactions on Industry Applications. 31 (1995) 1186–1196. https://doi.org/10.1109/28.464536.

[187] L. Renforth, Paul.S. Hamer, D. Clark, S. Goodfellow, R. Tower, Continuous, remote on-line partial discharge (OLPD) monitoring of HV EX/ATEX motors in the oil and gas industry, in: Industry Applications Society 60th Annual Petroleum and Chemical Industry Conference, 2013: pp. 1–8. https://doi.org/10.1109/PCICon.2013.6666017.

[188] C. Bianchini, F. Immovilli, M. Cocconcelli, R. Rubini, A. Bellini, Fault Detection of Linear Bearings in Brushless AC Linear Motors by Vibration Analysis, IEEE Transactions on Industrial Electronics. 58 (2011) 1684–1694. https://doi.org/10.1109/TIE.2010.2098354.

[189] P. Wei, Z. Dai, L. Zheng, M. Li, Fault diagnosis of the rolling bearing with optical fiber Bragg grating vibration sensor, in: Optical Measurement Technology and Instrumentation, SPIE, 2016: pp. 652–659. https://doi.org/10.1117/12.2247039.

[190] Y. Jin, R.S. Gao, R.O. Warrington, Microcomputer-based real-time bearing monitor, in: 1993 IEEE Instrumentation and Measurement Technology Conference, 1993: pp. 709–714. https://doi.org/10.1109/IMTC.1993.382551.

[191] P.J. DEMPSEY, J.M. CERTO, W. MORALES, Current Status of Hybrid Bearing Damage Detection, Tribology Transactions. 48 (2005) 370–376. https://doi.org/10.1080/05698190591008568.

[192] G. D'Ambrogio, O. Zahhaf, Y. Hebrard, M.Q. Le, P.-J. Cottinet, J.-F. Capsal, Micro-Structuration of Piezoelectric Composites Using Dielectrophoresis: Toward Application in Condition Monitoring of Bearings, Advanced Engineering Materials. 23 (2021) 2000773. https://doi.org/10.1002/adem.202000773.

[193] Aerospace ball bearings, (n.d.). https://www.ahrinternational.com/ahr_aerospace_ball_bearings.htm (accessed March 7, 2023).
[194] S. Poddar, N. Tandon, Detection of particle contamination in journal bearing using acoustic emission and vibration monitoring techniques, Tribology International. 134 (2019) 154–164. https://doi.org/10.1016/j.triboint.2019.01.050.
[195] C. Malla, I. Panigrahi, Review of Condition Monitoring of Rolling Element Bearing Using Vibration Analysis and Other Techniques, J. Vib. Eng. Technol. 7 (2019) 407–414. https://doi.org/10.1007/s42417-019-00119-y.
[196] R. Ranjan, S.K. Ghosh, M. Kumar, Fault diagnosis of journal bearing in a hydropower plant using wear debris, vibration and temperature analysis: A case study, Proceedings of the Institution of Mechanical Engineers, Part E: Journal of Process Mechanical Engineering. 234 (2020) 235–242. https://doi.org/10.1177/0954408920910290.
[197] T. Touret, C. Changenet, F. Ville, M. Lalmi, S. Becquerelle, On the use of temperature for online condition monitoring of geared systems – A review, Mechanical Systems and Signal Processing. 101 (2018) 197–210. https://doi.org/10.1016/j.ymssp.2017.07.044.
[198] H. Zhang, C. Zhang, C. Wang, F. Xie, A survey of non-destructive techniques used for inspection of bearing steel balls, Measurement. 159 (2020) 107773. https://doi.org/10.1016/j.measurement.2020.107773.
[199] L.V. Fricke, S.E. Thürer, C. Kahra, S. Bährisch, S. Herbst, F. Nürnberger, B.-A. Behrens, H.J. Maier, C. Klose, S. Barton, Non-destructive Evaluation of Workpiece Properties along the Hybrid Bearing Bushing Process Chain, J. of Materi Eng and Perform. (2022). https://doi.org/10.1007/s11665-022-07598-3.
[200] N.N. Gandhi, Load Estimation and Uncertainty Analysis Based on Strain Measurement With Application to Load Sensing Bearing, Master's Thesis, Delft University of Technology, 2016. https://repository.tudelft.nl/islandora/object/uuid%3A1049e8a5-55e9-41b9-be9d-f84dd0fd80e5 (accessed August 25, 2021).
[201] J.F. Capsal, M. Lallart, J. Galineau, P.J. Cottinet, G. Sebald, D. Guyomar, Evaluation of macroscopic polarization and actuation abilities of electrostrictive dipolar polymers using the microscopic Debye/Langevin formalism, Journal of Physics D: Applied Physics. 45 (2012). https://doi.org/10.1088/0022-3727/45/20/205401.
[202] M. Akram, A. Javed, T.Z. Rizvi, Dielectric properties of industrial polymer composite materials, Turkish Journal of Physics. 29 (2005) 355–362. https://doi.org/10.22401/jnus.13.1.10.
[203] W.A. Hussain, A.A. Hussein, J.M. Khalaf, A.H. Al-Mowali, A.A. Sultan, Dielectric Properties and a.c. Conductivity of Epoxy/Alumina Silicate NGK Composites, Advances in Chemical Engineering and Science. 05 (2015) 282–289. https://doi.org/10.4236/aces.2015.53028.
[204] F. Pedroli, A. Marrani, M.-Q. Le, O. Sanseau, P.-J. Cottinet, J.-F. Capsal, Reducing leakage current and dielectric losses of electroactive polymers through electro-annealing for high-voltage actuation, RSC Adv. 9 (2019) 12823–12835. https://doi.org/10.1039/C9RA01469A.
[205] Das, Sourav, Synthesis, characterization and dielectric properties of nanocrystalline nickel, Indian Journal of Pure & Applied Physics (IJPAP). 52 (2015) 386–390.
[206] X. Zhang, M.-Q. Le, V.-C. Nguyen, J.-F. Mogniotte, J.-F. Capsal, D. Grinberg, P.-J. Cottinet, L. Petit, Characterization of micro-ZnO/PDMS Composite Structured via Dielectrophoresis – Toward medical application, Materials & Design. (2021) 109912. https://doi.org/10.1016/j.matdes.2021.109912.
[207] B.A. Aldar, R.K. Pinjari, N.M. Burange, Electric and Dielectric behavior of Ni-Co-Cd Ferrite, n.d.
[208] J.-F. Capsal, M. Lallart, J. Galineau, P.-J. Cottinet, G. Sebald, D. Guyomar, Evaluation of macroscopic polarization and actuation abilities of electrostrictive dipolar polymers using the microscopic Debye/Langevin formalism, J. Phys. D: Appl. Phys. 45 (2012) 205401. https://doi.org/10.1088/0022-3727/45/20/205401.
[209] C. Zhang, D. Wang, J. He, M. Liu, G.-H. Hu, Z.-M. Dang, Synthesis, nanostructures and dielectric properties of novel liquid crystalline block copolymers, Polym. Chem. 5 (2014) 2513–2520. https://doi.org/10.1039/C3PY01522J.

[210] G.L. Wang, Y.Y. Zhang, J. Zhang, K.H. Ding, Z.F. Wang, M. Zhang, Preparation and electrodeformation of silicone dielectric elastomers containing poly(propylene glycol diacetate) with different molecular weights, Journal of Applied Polymer Science. 134 (2017) 45329. https://doi.org/10.1002/app.45329.

[211] X. Huang, H. Zhang, Y. Lai, J. Li, The lowered dielectric loss tangent and grain boundary effects in fluorine-doped calcium copper titanate ceramics, Appl. Phys. A. 123 (2017) 317. https://doi.org/10.1007/s00339-017-0947-9.

[212] G. D'Ambrogio, O. Zahhaf, Y. Hebrard, M.Q. Le, P.-J. Cottinet, J.-F. Capsal, Micro-Structuration of Piezoelectric Composites Using Dielectrophoresis: Toward Application in Condition Monitoring of Bearings, Advanced Engineering Materials. 23 (2021) 2000773. https://doi.org/10.1002/adem.202000773.

[213] D. Kotnarowska, Influence of Ageing with UV Radiation on Physicochemical Properties of Acrylic-Polyurethane Coatings, Journal of Surface Engineered Materials and Advanced Technology. 8 (2018) 95–109. https://doi.org/10.4236/jsemat.2018.84009.

[214] M.H. Malakooti, H.A. Sodano, Toughening response of a crack-tip surrounded by a local elastic gradient, Smart Mater. Struct. 23 (2014) 035009. https://doi.org/10.1088/0964-1726/23/3/035009.

[215] T.S. Wilson, J.P. Bearinger, J.L. Herberg, J.E. Marion, W.J. Wright, C.L. Evans, D.J. Maitland, Shape memory polymers based on uniform aliphatic urethane networks, Journal of Applied Polymer Science. 106 (2007) 540–551. https://doi.org/10.1002/app.26593.

[216] J.-F. Capsal, E. Dantras, J. Dandurand, C. Lacabanne, Dielectric relaxations and ferroelectric behaviour of even–odd polyamide PA 6,9, Polymer. 51 (2010) 4606–4610. https://doi.org/10.1016/j.polymer.2010.07.040.

[217] T.-T. Fang, H.-L. Hsieh, F.-S. Shiau, Effects of Pore Morphology and Grain Size on the Dielectric Properties and Tetragonal–Cubic Phase Transition of High-Purity Barium Titanate, Journal of the American Ceramic Society. 76 (1993) 1205–1211. https://doi.org/10.1111/j.1151-2916.1993.tb03742.x.

[218] Z. Zhao, V. Buscaglia, M. Viviani, M.T. Buscaglia, L. Mitoseriu, A. Testino, M. Nygren, M. Johnsson, P. Nanni, Grain-size effects on the ferroelectric behavior of dense nanocrystalline BaTiO3 ceramics, Phys. Rev. B. 70 (2004) 024107. https://doi.org/10.1103/PhysRevB.70.024107.

[219] R. Köferstein, L. Jäger, M. Zenkner, S.G. Ebbinghaus, Phase transition and dielectric properties of BaTiO3 ceramics containing 10mol% BaGeO3, Materials Chemistry and Physics. 119 (2010) 118–122. https://doi.org/10.1016/j.matchemphys.2009.08.026.

[220] C.R. Farrar, K. Worden, An introduction to structural health monitoring, Philosophical Transactions of the Royal Society A: Mathematical, Physical and Engineering Sciences. 365 (2007) 303–315. https://doi.org/10.1098/rsta.2006.1928.

[221] P. Phillips, D. Diston, A knowledge driven approach to aerospace condition monitoring, Knowledge-Based Systems. 24 (2011) 915–927. https://doi.org/10.1016/j.knosys.2011.04.008.

[222] P. Zielbauer, Sikorsky Supplier Settles Case Arising From Helicopter Crash, The New York Times. (2001). https://www.nytimes.com/2001/04/11/nyregion/sikorsky-supplier-settles-case-arising-from-helicopter-crash.html (accessed August 9, 2021).

[223] T.R. Lin, K. Yu, J. Tan, Condition Monitoring and Fault Diagnosis of Roller Element Bearing, IntechOpen, 2017. https://doi.org/10.5772/67143.

[224] G. Byrne, D. Dornfeld, I. Inasaki, G. Ketteler, W. König, R. Teti, Tool Condition Monitoring (TCM) — The Status of Research and Industrial Application, CIRP Annals. 44 (1995) 541–567. https://doi.org/10.1016/S0007-8506(07)60503-4.

[225] J.-D. Kim, I.-H. Choi, Development of a tool failure detection system using multi-sensors, International Journal of Machine Tools and Manufacture. 36 (1996) 861–870. https://doi.org/10.1016/0890-6955(96)00115-0.

[226] R.G. Harker, J.S. Hansen, Rolling Element Bearing Monitoring Using High Gain Eddy Current Transducers, Journal of Engineering for Gas Turbines and Power. 107 (1985) 160–164. https://doi.org/10.1115/1.3239677.

[227] J.A. Henao-Sepulveda, M. Toledo-Quinones, Y. Jia, Contactless Monitoring of Ball Bearing Temperature, in: 2005 IEEE Instrumentationand Measurement Technology Conference Proceedings, 2005: pp. 1571–1573. https://doi.org/10.1109/IMTC.2005.1604416.

[228] R.B.W. Heng, M.J.M. Nor, Statistical analysis of sound and vibration signals for monitoring rolling element bearing condition, Applied Acoustics. 53 (1998) 211–226. https://doi.org/10.1016/S0003-682X(97)00018-2.

[229] B.T. Holm-Hansen, R.X. Gao, Vibration Analysis of a Sensor-Integrated Ball Bearing, Journal of Vibration and Acoustics. 122 (2000) 384–392. https://doi.org/10.1115/1.1285943.

[230] G. D'Ambrogio, O. Zahhaf, M. Bordet, M.Q. Le, N. Schiava, R. Liang, P.-J. Cottinet, J.-F. Capsal, Structuring BaTiO3 /PDMS Nanocomposite via Dielectrophoresis for Fractional Flow Reserve Measurement, Advanced Engineering Materials. (2021) 2100341. https://doi.org/10.1002/ADEM.202100341.

[231] M. Keetels, J. Vroomen, Perception of Synchrony between the Senses, in: M.M. Murray, M.T. Wallace (Eds.), The Neural Bases of Multisensory Processes, CRC Press/Taylor & Francis, Boca Raton (FL), 2012. http://www.ncbi.nlm.nih.gov/books/NBK92837/ (accessed May 3, 2023).

[232] C. Lenay, S. Canu, P. Villon, Technology and perception: the contribution of sensory substitutionsystems, in: 1997: pp. 44–53. https://doi.org/10.1109/CT.1997.617681.

[233] Y. Hamilakis, Archaeology and the Senses: Human Experience, Memory, and Affect, Cambridge University Press, 2014.

[234] M. Obrist, C. Velasco, C. Vi, N. Ranasinghe, A. Israr, A. Cheok, C. Spence, P. Gopalakrishnakone, Sensing the future of HCI: Touch, taste, and smell user interfaces, Interactions. 23 (2016) 40–44. https://doi.org/10.1145/2973568.

[235] What is Haptic Feedback? Types, devices and use | Teslasuit Blog, Teslasuit. (2022). https://teslasuit.io/blog/haptic_feedback/ (accessed May 3, 2023).

[236] The Purpose of Haptic Feedback in Cell Phone Devices, Boréas Technologies. (2022). https://www.boreas.ca/blogs/piezo-haptics/the-purpose-of-haptic-feedback-in-cell-phone-devices (accessed May 3, 2023).

[237] A.L. Guinan, N.A. Caswell, F.A. Drews, W.R. Provancher, A video game controller with skin stretch haptic feedback, in: 2013 IEEE International Conference on Consumer Electronics (ICCE), 2013: pp. 456–457. https://doi.org/10.1109/ICCE.2013.6486973.

[238] A. Flores Ramones, M.S. del-Rio-Guerra, Recent Developments in Haptic Devices Designed for Hearing-Impaired People: A Literature Review, Sensors. 23 (2023) 2968. https://doi.org/10.3390/s23062968.

[239] I. Shazhaev, D. Mihaylov, A. Shafeeg, A Review of Haptic Technology Applications in Healthcare, Open Journal of Applied Sciences. 13 (2023) 163–174. https://doi.org/10.4236/ojapps.2023.132013.

[240] Haptic Feedback: Feeling the Dance You Cannot See, AMT Lab @ CMU. (2022). https://amt-lab.org/blog/2022/4/haptic-feedback-feeling-the-dance-you-cannot-see (accessed May 3, 2023).

[241] M. Sreelakshmi, T.D. Subash, Haptic Technology: A comprehensive review on its applications and future prospects, Materials Today: Proceedings. 4 (2017) 4182–4187. https://doi.org/10.1016/j.matpr.2017.02.120.

[242] What is Force Feedback and Why is it so Important?, (2022). https://irisdynamics.com/what-is-force-feedback/ (accessed May 3, 2023).

[243] H. Team, What is Haptics? Part 3: Thermal Feedback, HaptX. (2016). https://haptx.com/what-is-haptics-really-part-3-thermal-feedback/ (accessed May 3, 2023).

[244] P. Kourtesis, F. Argelaguet, S. Vizcay, M. Marchal, C. Pacchierotti, Electrotactile Feedback Applications for Hand and Arm Interactions: A Systematic Review, Meta-Analysis, and Future Directions, IEEE Trans Haptics. 15 (2022) 479–496. https://doi.org/10.1109/TOH.2022.3189866.

[245] T. Carter, S.A. Seah, B. Long, B. Drinkwater, S. Subramanian, UltraHaptics: multi-point mid-air haptic feedback for touch surfaces, in: Proceedings of the 26th Annual ACM Symposium on User Interface Software and Technology, Association for Computing Machinery, New York, NY, USA, 2013: pp. 505–514. https://doi.org/10.1145/2501988.2502018.

[246] P. Kvandal, S.A. Landsverk, A. Bernjak, A. Stefanovska, H.D. Kvernmo, K.A. Kirkebøen, Low-frequency oscillations of the laser Doppler perfusion signal in human skin, Microvascular Research. 72 (2006) 120–127. https://doi.org/10.1016/j.mvr.2006.05.006.

[247] Edbhok, edbhok: Biological Basics of Haptic Perception, Edbhok. (2010). http://edbhok.blogspot.com/2010/03/biological-basics-of-haptic-perception.html (accessed May 3, 2023).

[248] Sense of Touch, Skin Receptors, Skin Sensations, Somatosensory System, Home Science Tools Resource Center. (2017). https://learning-center.homesciencetools.com/article/skin-touch/ (accessed May 3, 2023).

[249] Cutaneous Receptor - an overview | ScienceDirect Topics, (n.d.). https://www.sciencedirect.com/topics/neuroscience/cutaneous-receptor (accessed May 3, 2023).

[250] Absolute threshold, Wikipedia. (2023). https://en.wikipedia.org/w/index.php?title=Absolute_threshold&oldid=1150906436 (accessed May 18, 2023).

[251] R.F. Schmidt, H.-G. Schaible, Neuro- und Sinnesphysiologie, Springer-Verlag, 2006.

[252] Stiffness — an unknown world of mechanical science?, Injury. 31 (2000) 14–84. https://doi.org/10.1016/S0020-1383(00)80040-6.

[253] https://www.facebook.com/thoughtcodotcom, How Young's Modulus Defines the Relationship Between Stress and Strain, ThoughtCo. (n.d.). https://www.thoughtco.com/youngs-modulus-4176297 (accessed May 3, 2023).

[254] C. Nam, D. Shin, Force-touch measurement methodology based on user experience, International Journal of Distributed Sensor Networks. 14 (2018) 1550147718767794. https://doi.org/10.1177/1550147718767794.

[255] S. Priya, H.-C. Song, Y. Zhou, R. Varghese, A. Chopra, S.-G. Kim, I. Kanno, L. Wu, D.S. Ha, J. Ryu, R.G. Polcawich, A Review on Piezoelectric Energy Harvesting: Materials, Methods, and Circuits, Energy Harvesting and Systems. 4 (2017) 3–39. https://doi.org/10.1515/ehs-2016-0028.

[256] P. Poncet, F. Casset, A. Latour, F. Domingues Dos Santos, S. Pawlak, R. Gwoziecki, A. Devos, P. Emery, S. Fanget, Static and Dynamic Studies of Electro-Active Polymer Actuators and Integration in a Demonstrator, Actuators. 6 (2017) 18. https://doi.org/10.3390/act6020018.

[257] Y. Shouji, T. Sekine, K. Ito, N. Ito, T. Yasuda, Y.-F. Wang, Y. Takeda, D. Kumaki, F.D.D. Santos, A. Miyabo, S. Tokito, Fast Response, High-Power Tunable Ultrathin Soft Actuator by Functional Piezoelectric Material Composite for Haptic Device Application, Advanced Electronic Materials. n/a (n.d.) 2201040. https://doi.org/10.1002/aelm.202201040.

[258] J. Chen, E.H.T. Teo, K. Yao, Electromechanical Actuators for Haptic Feedback with Fingertip Contact, Actuators. 12 (2023) 104. https://doi.org/10.3390/act12030104.

[259] S.D. Mahapatra, P.C. Mohapatra, A.I. Aria, G. Christie, Y.K. Mishra, S. Hofmann, V.K. Thakur, Piezoelectric Materials for Energy Harvesting and Sensing Applications: Roadmap for Future Smart Materials, Advanced Science. 8 (2021) 2100864. https://doi.org/10.1002/advs.202100864.

[260] Harmonic Response Analysis in Ansys Mechanical, ANSYS Innovation Courses. (n.d.). https://courses.ansys.com/index.php/courses/harmonic-response-analysis-in-ansys-mechanical/ (accessed May 3, 2023).

[261] Materials and Stacking Technology, STRONG. FAST. TRUE. (n.d.). http://www.piezotechnics.com/piezo-technology/piezoelement/ (accessed May 3, 2023).

[262] Digilent Analog Discovery 2 | Farnell France, (n.d.). https://fr.farnell.com/digilent-analog-discovery-2 (accessed May 3, 2023).

[263] Common PCB Problems & Circuit Board Issues, Mcl. (n.d.). https://www.mclpcb.com/pcb-guide/ (accessed May 3, 2023).

[264] Diode Transil, Wikipédia. (2023). https://fr.wikipedia.org/w/index.php?title=Diode_Transil&oldid=200509275 (accessed May 3, 2023).

[265] T. Agarwal, Static Relay : Working, Types, Differences & Its Applications, ElProCus - Electronic Projects for Engineering Students. (2022). https://www.elprocus.com/static-relay/ (accessed May 3, 2023).

[266] What is a GUI (Graphical User Interface)?, (n.d.). https://www.computerhope.com/jargon/g/gui.htm (accessed May 3, 2023).
[267] Altium Designer – logiciel de conception de circuits imprimés, (n.d.). https://www.altium.com/fr/altium-designer (accessed May 3, 2023).
[268] Getting Started with WaveForms SDK - Digilent Reference, (n.d.). https://digilent.com/reference/test-and-measurement/guides/waveforms-sdk-getting-started (accessed May 3, 2023).
[269] Visual Studio, Wikipedia. (2023). https://en.wikipedia.org/w/index.php?title=Visual_Studio&oldid=1152264013 (accessed May 3, 2023).
[270] R.K. Mobley, An Introduction to Predictive Maintenance, Elsevier, 2002.
[271] Z. Cui, Printed Electronics: Materials, Technologies and Applications, John Wiley & Sons, 2016.
[272] M. Alberto, D. Micaela, S. Sarbjeet, Applications and Challenges of Maintenance and Safety Engineering in Industry 4.0, IGI Global, 2020.
[273] R. Morales, F.J. Badesa, N. Garcia-Aracil, J.M. Sabater, L. Zollo, Soft Robotic Manipulation of Onions and Artichokes in the Food Industry, Advances in Mechanical Engineering. 6 (2014) 345291. https://doi.org/10.1155/2014/345291.
[274] B. Bahr, Y. Li, M. Najafi, Design and suction cup analysis of a wall climbing robot, Computers & Electrical Engineering. 22 (1996) 193–209. https://doi.org/10.1016/0045-7906(95)00039-9.
[275] S.-M. Kirsch, F. Welsch, M. Schmidt, P. Motzki, S. Seelecke, Bistable SMA Vacuum Suction Cup, in: ACTUATOR 2018; 16th International Conference on New Actuators, 2018: pp. 1–4.
[276] A. Hehr, M. Norfolk, J. Wenning, J. Sheridan, P. Leser, P. Leser, J.A. Newman, Integrating Fiber Optic Strain Sensors into Metal Using Ultrasonic Additive Manufacturing, JOM. 70 (2018) 315–320. https://doi.org/10.1007/s11837-017-2709-8.
[277] S. Namuduri, B.N. Narayanan, V.S.P. Davuluru, L. Burton, S. Bhansali, Review—Deep Learning Methods for Sensor Based Predictive Maintenance and Future Perspectives for Electrochemical Sensors, J. Electrochem. Soc. 167 (2020) 037552. https://doi.org/10.1149/1945-7111/ab67a8.
[278] M. Hologne-Carpentier, J.-F. Mogniotte, M.-Q. Le, B. Allard, G. Clerc, P.-J. Cottinet, A multi-physics approach to condition monitoring of SiC power module, Microelectronic Engineering. 250 (2021) 111633. https://doi.org/10.1016/j.mee.2021.111633.
[279] K. Suganuma, Introduction to Printed Electronics, Springer Science & Business Media, 2014.
[280] S.M.F. Cruz, L.A. Rocha, J.C. Viana, Printing Technologies on Flexible Substrates for Printed Electronics, IntechOpen, 2018. https://doi.org/10.5772/intechopen.76161.
[281] Y.D. Kim, J. Hone, Screen printing of 2D semiconductors, Nature. 544 (2017) 167–168. https://doi.org/10.1038/nature21908.
[282] E.B. Secor, Principles of aerosol jet printing, Flex. Print. Electron. 3 (2018) 035002. https://doi.org/10.1088/2058-8585/aace28.
[283] H. Zhou, W. Qin, Q. Yu, H. Cheng, X. Yu, H. Wu, Transfer Printing and its Applications in Flexible Electronic Devices, Nanomaterials. 9 (2019) 283. https://doi.org/10.3390/nano9020283.
[284] Direct Patterning of Carbon Nanotube via Stamp Contact Printing Process for Stretchable and Sensitive Sensing Devices | SpringerLink, (n.d.). https://link.springer.com/article/10.1007/s40820-019-0323-8 (accessed March 9, 2022).
[285] H. El Maanaoui, C. Egelkamp, J. Meier, Influence of the tensile static preload dependency on the dynamic lifetime prediction for an HNBR elastomer, Journal of the Mechanical Behavior of Biomedical Materials. 119 (2021) 104502. https://doi.org/10.1016/j.jmbbm.2021.104502.
[286] D. Zymelka, T. Yamashita, X. Sun, T. Kobayashi, Printed Strain Sensors Based on an Intermittent Conductive Pattern Filled with Resistive Ink Droplets, Sensors. 20 (2020) 4181. https://doi.org/10.3390/s20154181.

[287] PCB Track Width and Track Resistance – Importance, Calculation, and Design Tips, (n.d.). https://pcbdesignworld.com/article/pcb-track-width-and-track-resistance-importance-calculation-and-design-tips (accessed July 27, 2022).

[288] P. Izak, J. Mastalska-Poplawska, J. Lis, A. Stempkowska, Modification of the rheological properties of screen printing ceramic paints containing gold, J. Phys.: Conf. Ser. 790 (2017) 012011. https://doi.org/10.1088/1742-6596/790/1/012011.

[289] V.-C. Nguyen, M.-Q. Le, A. Fimbel, S. Bernadet, Y. Hebrard, J.-F. Mogniotte, J.-F. Capsal, P.-J. Cottinet, Evaluation of electromechanical characteristics for screen printed piezoelectric sensor-based Pu/PZT composite, in: Electroactive Polymer Actuators and Devices (EAPAD) XXIV, SPIE, 2022: pp. 326–334. https://doi.org/10.1117/12.2609769.

[290] S. Nasrazadani, S. Hassani, Chapter 2 - Modern analytical techniques in failure analysis of aerospace, chemical, and oil and gas industries, in: A.S.H. Makhlouf, M. Aliofkhazraei (Eds.), Handbook of Materials Failure Analysis with Case Studies from the Oil and Gas Industry, Butterworth-Heinemann, 2016: pp. 39–54. https://doi.org/10.1016/B978-0-08-100117-2.00010-8.

[291] Resistance and Resistivity, (n.d.). http://hyperphysics.phy-astr.gsu.edu/hbase/electric/resis.html (accessed March 9, 2022).

[292] A.S. Khan, M. Baig, S. Hamid, H. Zhang, Thermo-mechanical large deformation responses of Hydrogenated Nitrile Butadiene Rubber (HNBR): Experimental results, International Journal of Solids and Structures. 47 (2010) 2653–2659. https://doi.org/10.1016/j.ijsolstr.2010.05.012.

[293] M. Kumar, A. Sharma, S. Hait, S. Wießner, G. Heinrich, I. Arief, K. Naskar, K.W. Stöckelhuber, A. Das, Effect of Prestrain on the Actuation Characteristics of Dielectric Elastomers, Polymers. 12 (2020) 2694. https://doi.org/10.3390/polym12112694.

[294] I.P. Nurprasetio, B.A. Budiman, A.A. Afwan, P.N. Halimah, S.T. Utami, M. Aziz, Nonlinear Piezoresistive Behavior of Plain-Woven Carbon Fiber Reinforced Polymer Composite Subjected to Tensile Loading, Applied Sciences. 10 (2020) 1366. https://doi.org/10.3390/app10041366.

[295] Y. Chang, D.-Y. Wang, Y.-L. Tai, Z.-G. Yang, Preparation, characterization and reaction mechanism of a novel silver-organic conductive ink, J. Mater. Chem. 22 (2012) 25296–25301. https://doi.org/10.1039/C2JM34569B.

[296] S. Wang, D.D.L. Chung, Negative piezoresistivity in continuous carbon fiber epoxy-matrix composite, J Mater Sci. 42 (2007) 4987–4995. https://doi.org/10.1007/s10853-006-0580-z.

[297] Z. Mei, V.H. Guerrero, D.P. Kowalik, D.D.L. Chung, Mechanical damage and strain in carbon fiber thermoplastic-matrix composite, sensed by electrical resistivity measurement, Polymer Composites. 23 (2002) 425–432. https://doi.org/10.1002/pc.10444.

[298] A. Todoroki, J. Yoshida, Electrical Resistance Change of Unidirectional CFRP Due to Applied Load, JSME International Journal Series A Solid Mechanics and Material Engineering. 47 (2004) 357–364. https://doi.org/10.1299/jsmea.47.357.

[299] E.-B. Jeon, T. Fujimura, K. Takahashi, H.-S. Kim, An investigation of contact resistance between carbon fiber/epoxy composite laminate and printed silver electrode for damage monitoring, Composites Part A: Applied Science and Manufacturing. 66 (2014) 193–200. https://doi.org/10.1016/j.compositesa.2014.08.002.

[300] M. Nowicki, Anhysteretic Magnetization Measurement Methods for Soft Magnetic Materials, Materials. 11 (2018) 2021. https://doi.org/10.3390/ma11102021.

List of Figures

List of tables

List of publications

Peer-reviewed publications:

1. Van-Cuong Nguyen; Minh-Quyen Le; Sophie Bernadet; Yoann Hebrard; Jean-François Mogniotte; Jean-Fabien Capsal; Pierre-Jean Cottinet. Design Rules of Bidirectional Smart Sensor Coating for Condition Monitoring of Bearings. Polymers 2023, 15, 826.

2. Van-Cuong Nguyen, Minh-Quyen Le, Amaury Fimbel, Sophie Bernadet, Yoann Hebrard, Jean François Mogniotte, Jean-Fabien Capsal, Pierre-Jean Cottinet. Printing smart coating of piezoelectric composite for application in condition monitoring of bearings. Materials & Design, Volume 215,2022, 110529.

3. Van-Cuong Nguyen; Minh-Quyen Le; Jean-François Mogniotte; Jean-Fabien Capsal; Pierre-Jean Cottinet. Extrusion-Based 3D Printing of Stretchable Electronic Coating for Condition Monitoring of Suction Cups. Micromachines 2022, 13, 1606.

4. Xiang, Z., Nguyen, V.-C., Ducharne, B., Della Schiava, N., Capsal, J.-F., Cottinet, P.-J. and Le, M.-Q. (2021), 3D Printing of Flexible Composites via Magnetophoresis: Toward Medical Application Based on Low-Frequency Induction Heating Effect. Macromol. Mater. Eng., 306: 2100211.

5. X. Zhang, M.Q. Le, V.C. Nguyen, J.F. Mogniotte, J.F. Capsal, D. Grinberg, P.J. Cottinet, L. Petit, “Characterization of micro-ZnO/PDMS composite structured via dielectrophoresis – Toward medical application,” *Mater. Des.*, vol. 208, p. 109912, Oct. 2021.
    1.
6. Rebecca Damamme, Laurence Seveyrat, Ana Borta-Boyon, Van-Cuong Nguyen, Minh-Quyen Le, Pierre-Jean Cottinet. 3D printing of doped barium-titanate using robocasting - Toward new generation lead-free piezoceramic transducers. Journal of the European Ceramic Society, Volume 43, Issue 8, 2023, Pages 3297-3306,ISSN 0955-2219.

Conference publications:

7. Van-Cuong Nguyen, Minh-Quyen Le, Amaury Fimbel, Sophie Bernadet, Yoann Hebrard, Jean-François Mogniotte, Jean-Fabien Capsal, and Pierre-Jean Cottinet "Evaluation of electromechanical characteristics for screen printed piezoelectric sensor-based Pu/PZT composite", Proc. SPIE 12042, Electroactive Polymer Actuators and Devices (EAPAD) XXIV, 120420X (20 April 2022).

Conferences participation:

SPIE Smart Structures + Nondestructive Evaluation, Online, March 2022.

Annex

The following work was carried out during my six-month master and the first six-month of my thesis. This research proposes an innovative method for condition monitoring of suction cups coated with stretchable printed electronics based on piezoresistive effect. The printing method here relies on the extrusion of conductive inks (developed in the lab), which is different to the one used in the thesis that is dedicated to screen printing performed by industrial process. However, this work is somehow related to the one of my thesis, particularly in the area of condition monitoring based on printed electronics via multifunctional materials.

Extrusion-based 3D printing of stretchable electronic coating for condition monitoring of suction cups

Abstract: Suction cups (SCs) are used extensively by the industrial sectors, particularly for a wide variety of automated material handling applications. To enhance productivity and reduce maintenance costs, an online supervising system is essential to check the status of SCs. This paper thus proposes an innovative method for condition monitoring of SCs coated with printed electronics whose electrical resistance is supposed to be correlate to the mechanical strain. Simulation model is first examined to observe the deformation of SCs under vacuum compression, which is needed for the development of sensor coating thanks to 3D printing process. The proposed design involves in three circle-shaped sensors, two opted for the top and bottom bellows (whose mechanical strain are revealed to be the most significant), and one for the lip (small strain but important stress that might provoke wear and tear in a long term). For a sake of simplicity, practical measurement is performed on 2D samples coated with two different conductive inks subjected to unidirectional tensile loading. Graphical representations together with analytical model of both linear and non-linear piezoresistive responses allows for the characterization of the inks' behavior under several conditions of displacement and speed inputs. After a comparison of the two inks, the most appropriate is selected as a consequence of its excellent adhesion and stretchability, which are essential criteria to meet the target field. Room temperature extrusion-based 3D printing is then investigated using a motorized 3D Hyrel printer with a syringe extrusion modular system. Design optimizations is finally carried out to enhance the surface detection of sensitive elements while minimizing the effect of electrodes. Although several issues still need to be further considered to match specifications imposed by our Industrial Partner, the achievement of this work is meaningful and could pave the way for a new generation of SC integrated with smart sensing device. Actually, 3D print of conductive ink directly on the cup's curving surface is a true challenge, which is demonstrated, for the first time, to be technically feasible throughout additive manufacturing (AM) process.

Keywords: design optimization, conductive coating, 3D printing additive manufacturing, printed electronics, condition monitoring, piezoresistive sensor, ink characterization.

1. Introduction

Today, manufacturers are looking to develop their products more added value and think about integrating functions to make the products "intelligent". The idea of having an intelligent predictive organ was born from the need for predictive maintenance and the evolution of printed electronics [270,271]. In the industrial context, it is important to have the highest possible productivity to remain competitive, which implies that the machines used must be in operation as long as possible. However, their maintenance is crucial: an undetected anomaly can, to some extent, lead to unexpected shutdown of the tools and even production stoppage, with sometimes considerable damage to those not affected by the initial failure [78,212,272].

Among strategic tools, suction cups (SCs) are one of the most widely used in industrial sectors such as packaging, plastics, food, sheet metal, robots, machine, or any other kind of automated process [273–275]. They are mostly exploited to handle or move fragile items, sometimes with huge amounts of weight. In its mode of action, the SC is subjected to vacuum that sucks out all of the air from the inside, and then is released after interruption of the vacuum. These actions are usually fast and repetitive in several cycles, resulting in drastically mechanical strain and stress to the SCs. Therefore, online condition monitoring of SCs is essential for a reduction of maintenance's cost, allowing for failure detection and spare parts order effectuated in time. Predictive maintenance can be achieved in several ways, either by integrating sensors directly into the structure or coating them on its surface [41,48,276–278]. The first solution leads to more accurate measurement as the sensor is usually mounted on the position where it needs to be sensed. However, this method is not applicable to any system because of its complicated integration and cumbersome issue. The second solution is thus chosen using printed electronics coating whose resistance variation is supposed to correlate to mechanical strain of the structure, making early failure detection of SC possible. This approach is defined as direct printing of electronic components on monitored substrates through the combination of 3D printing processes and conductive/dielectric inks with more functionalities (e.g., piezoelectric, piezoresistive, etc.) [46,47,49,145,147,279]. Additive manufacturing (AM) based 3D printing gives the ability to customize shapes, in addition, it can automate the printing process to save time and feed materials on-demand to minimize waste. Numerous printing technologies including screen printing, aerosol printing, transfer printing, and inkjet printing have been intensively investigated in literatures [280–284], but sometimes they are expensive and not suitable to high-viscosity materials. Hence, this study orients to extrusion printing technique with further advantages of easy process and reasonable cost.

It is obvious that sensor-based printed electronics open new opportunities for next-generation smart monitoring devices. Nonetheless, one of the limitations that are currently preventing wider adaption of AM technology is the lack of understanding of how ink properties affect the AM process and quality of the printed object. Therefore, selection of conductive inks suitable to the target application is of primary importance. In this work, two brands of carbon-based composite ink are chosen and compared in terms of morphological, electrical, and piezoresistive properties. For a sake of simplicity, experimental characterizations are conducted on 2D rectangular substrates made of the same material as 3D suction cups. The purpose here is to select the most adequate ink for the development of SC's coating via extrusion-based printing AM. Design optimization are then thoroughly investigated to enhance the detection area of the sensor coating as well as to minimize the electrode effect. To date, such investigations have rarely reported

in literatures, according to the best of our knowledges. Accordingly, the findings of this research could pave the new way for a development of electronic printing method in the context of SC's predictive mainteance.

The paper is organized as follows. After the introduction, Section 2 describes the design strategy of a SC with sensor coating using printing AM. Method of ink's characterizations for 2D and 3D samples are drawn in Sections 3, followed by results and discussions of the sensor-coating performance investigated in Section 4. Section 5 presents preliminary exploration for an improvement in the printing process thanks to an addition of a controllable robot arm with high degree freedom (DoF). Finally, Section 6 resumes the major findings of this paper and provides recommendations for future investigations.

2. Design strategy and printing process

2.1. Design of sensor coating

The suction cup (SC) involved in this study belongs to VSA series whose bellows combine the advantages of flat SCs with increased deflection, flexibility, and precision; ideal to handle uneven and rough surfaces. Table 2 shows the features of a Ø78 suction cup made of *hydrogenated nitrile butadiene rubber (*HNBR) with light weight of 42 g, i.e., provided by our Industrial Partner (*name will not be disclosed for the confidential purpose*).

Table 2. Dimension and force characteristics of a Ø78 suction cup.

Lip diameter (ØA)	78 mm
SCstroke (f)	14 mm
Depth of housing fitting (B)	20 mm
Height (H)	46.8 mm
External neck diameter (Ø D)	25 mm
Internal neck diameter (Ød)	12 mm
Internal volume (V_i)	76 cm^3
Top bellow diameter (Øa)	83 mm
Bottom bellow diameter (Øb)	43.7 mm
Tensile force (F_t)	110 N
Slipping force (F_g)	55 N

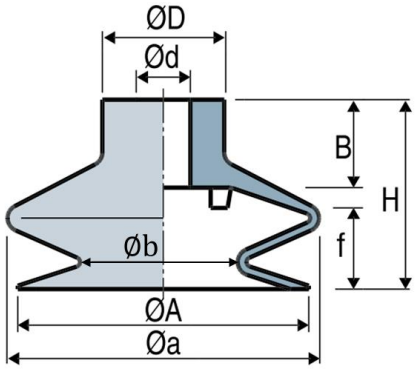

For an easier sensor design, the SC is decomposed into three principal zones: top bellows, bottom bellows, and lip (Figure 24a). To obtain the ranges of deformations seen by these structure areas, a finite element (FE) modeling was carried out using ANSYS software (previously developed by the Industrial Partner). As indicated in Figure 24b, the mechanical deformations are mainly located on the bellows of the structure (zones 1 and 2), particularly in the case of the concave surfaces where the curvatures is the most important. Since the sensors are intended to be printed on the outer surface of the SC, the deformation sensed by the coating will be smaller in the top bellows (~ 5 – 8 % on convex side) compared to the bottom below (~ 12 – 14 % on concave side). It is thus essential that the printed sensors are capable withstanding such

mechanical strains under static and dynamic regimes. As expected, the lip (zone 3) does not undergo any deformation as this part is always fix even though the SC is in movement. However, it could be subjected to important stresses pushed by atmospheric pressure on a small seal-contact area. Being the only one interfaced with an object, the lip is considered as a strategic part that can suffer from wear and tear. Since atmospheric pressure will always try to equalize itself, air naturally fills in any missing gaps. This pressure pushes against the air outside of the SC and forces the lip. If the lip is deteriorated, air can work under the edges of the SC, making the "seal" break and the SC fall off. Consequently, finding a good indicator to assess the lip's properties in a long-run perspective is mandatory for prevention and maintenance. That is the reason why a circle sensor is also coated on the lip, although this study takes a more focus on the bellows' monitoring. Eventually, the functional coating must adhere well to the HNBR material, and be able to operate for several million cycles without deterioration [285]. Piezoresistive technology can meet the application's needs based on conductive ink [286].

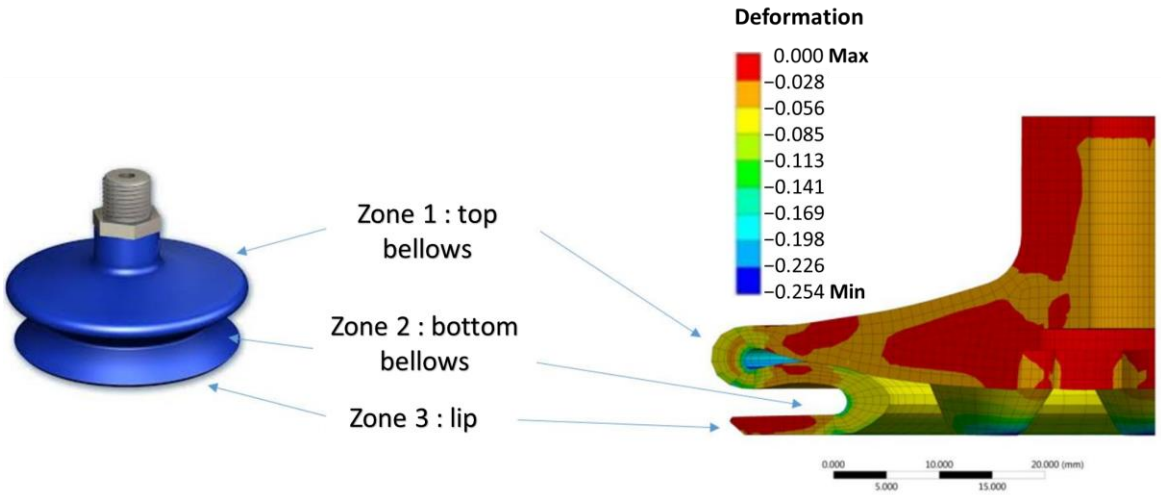

a) b)

Figure 24. Decomposition of three zones that need to be monitored: a) A SC provided by the Industrial Partner; and b) Mechanical deformation of SC based on FEM.

As shown in Figure 25a, the sensor network architecture consists of three circle resistors coated on the critical areas (two bellows and lip) identified above. Vertical lines are designed as electrodes attached to the head of the cup to facilitate the interconnection with electrical spring contacts. The whole sensor network can be modeled as a simple equivalent electrical circuit (Figure 25b), in which each resistive sensor is accompanied by 2 electrodes. To enhance accuracy measurement of the bellows' deformation, the resistance variations of the sensors must be much greater than those of the electrodes (e.g., a factor of 10). In other words, it is necessary to guarantee that

$$2\,\Delta R_{i\_electrode} \ll \Delta R_{i_{sensor}} \tag{3}$$

where ΔR denotes the resistance variation; the subscript *i* describes the location of the sensor corresponding to *l* (lip), *t* (top), and *b* (bottom). It can be deduced from the scheme of Figure 25b that $\Delta R_{i_{global}}$ is the sum of resistance variation by considering the presence of the electrodes. When the condition of Eq. (1) is met, $\Delta R_{i_{global}}$ value, which can be obtained by experiment, is expected to be close to the resistance variation of

the sensor (i.e., $\Delta R_{i_{sensor}} \approx \Delta R_{i_{global}}$). Therefore, it is believed that measuring $\Delta R_{i_{global}}$ leads to an estimation of the deformation of the structure on which was attached the printed coating.

For a given length, the resistance value of the sensors strongly depends on their thickness and width. A compromise should be taken into account to achieve high sensing performance with large resistance variation. On a one hand, the thickness of the printed lines should be as thin as possible to ensure good adhesion between ink and the SC surface. On the other hand, too thin layer could be fragile and broken under mechanical solicitation, provoking discontinuities in the patterns. Regarding the width of the sensor, it should be small enough to capably detecting the deformation at a precise location, and large enough to keep the resistance value under the limit imposed by the conditioning electronics. Indeed, to avoid any problem of parasitic resistance and to ensure good piezoresistive sensitivity, the resistances value of each sensor must not exceed 300 kΩ. Based on these best trade-offs, the patterns are designed with 1mm width and 20-50 µm thickness. In a practical point of view, 1 mm width is also compatible to the design of 6-electrode lines, which is not a trivial matter. Actually, to prevent capacitance parasite, the distance between two adjacent lines should be three-time larger than their own width [287]. Furthermore, the dimension of the 6-electrode line terminal must fit with the electrical connector provided by our Industrial Partner.

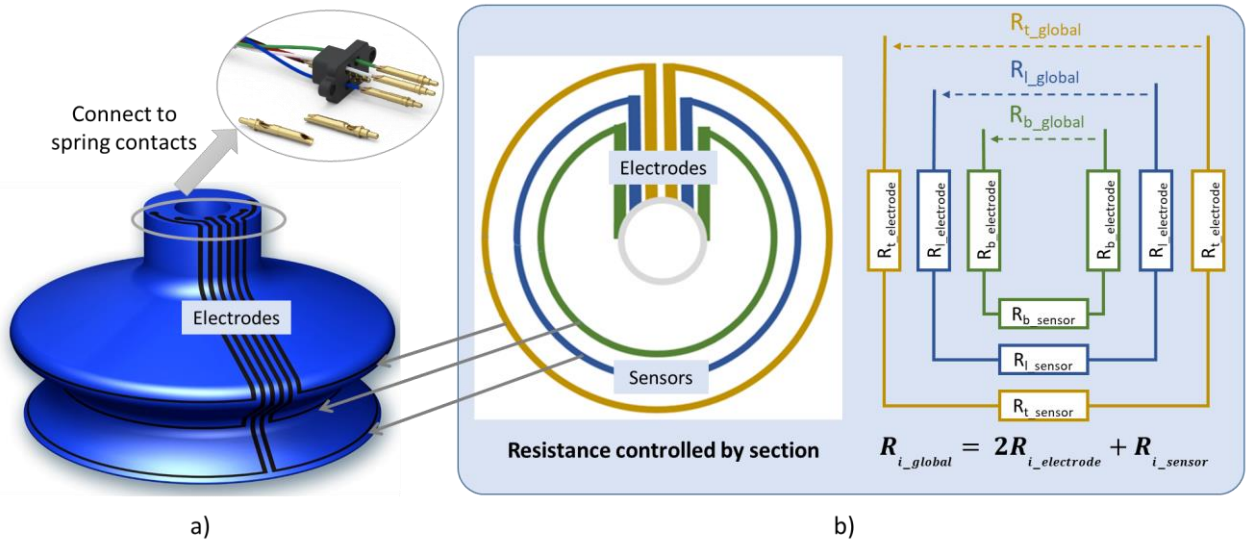

Figure 25. Design of sensor coating: a) Prototype consisting of 3 printed circle-shaped sensors coated on the lip, top and bottom bellows; b) Equivalent resistance defined by different zones.

2.2. Ink selection

Various conductive inks are now commercially available but only few of them adhere to HNBR and are sufficiently high mechanical resistant to withstand a huge deformation. To reach the target application, the selected inks must fulfill the following criteria:

- good adhesion to the SC's materials (HNBR), particularly for the curved-surface bellows;
- excellent stretchability to resist high deformation (~ 20%) under static and dynamic conditions;
- adequate electrical conductivity to counterbalance the electrode effect;

- high viscosity to achieve shape fidelity (as no thermal treatment is performed throughout printing process);
- stable electrical behavior under aging test.

After having tested several conductive inks, only two products met the first criterion where the sensor coatings adhere to the SC surface after printing process. The first one, supplied by Creative Materials (CM, 128-07 product), possesses lower viscosity but shape fidelity and adherence to the HNBR material are also attained. The second one exhibits very high viscosity (~ 57 000 cps) compared to those used in classical screen printing [39,288,289]. For a confidential purpose, the name of the second ink's supplier was not shown. Both inks were made of polymer-based carbon particles whose chemical composition is analyzed later using microscopy equipment (Subsection 4.1). Table 3 resumes essential properties of the two inks that are necessary for the printing and curing process.

Table 3. Properties of the conductive inks

	first ink	second ink
Viscosity (cps)	30000 – 35000	57000
Useful temperature range (°C)	–55 to 120	–50 to 100
Curing temperature range (°C)	50 – 180	50 – 120

For a sake of simplicity, characterization tests of the printed coating comprising morphological analyses, electrical conductivity, and piezoresistive behavior are conducted on 2D samples (dimension 120 x 20 mm). These samples, provided by the Industrial Partner, are made of HNBR material, i.e., identical to the one of the 3D suction cups.

2.3. Printing process

Figure 2.9 illustrates the printing setup conducted on a 2D sample using Hyrel 3D System (Ref. 30M), which consists of a glass platform and a modular head extruder (cold flow at room temperature) capable of translating in 3 directions. To efficiently extrude high-viscosity ink, a powerful printhead extruder (VOL-25) was chosen, together with an adequate stainless-steel nozzle tip whose inner diameter equals 1 mm. The syringe pump extruder has a standard ink reservoir of 25 ml containing fluids that were expected to be printed in desired patterns and shapes. The relationship between the 3D printer settings as well as the extrusion process variables and extrusion rate (driven by the stepper motor speed), was obtained by investigating the machine command (G-code). Repetrel plug-in controlling software is used to run most of the Hyrel equipment, enabling the generation of G-code from various 3D designs (e.g., .stl or .obj file, text file, etc.) and other system control functions. For instance, the desired shapes and size of the conductive tracks could be built by Computer Assistant Design (CAD) software. The models are then fed into Slice 3r that creates the 3D models into G-code. To perform the desired printing trajectories, relevant parameters affecting the printing quality such as layer height, ink flowrate, line density, pressure control, etc. are carefully tuned in the Slic3r software. After several adjustments, the flow rate and pressure control were respectively set at 300 pulse/µl and 0.8 (1 is the default). Finally, a simple printed-line resistor was coated on a 2D substrate using either the first or the second ink (see Figure 2.9). At each extremity of the resistor, a squared coating was designed to be used as electrical connection necessary for practical characterizations.

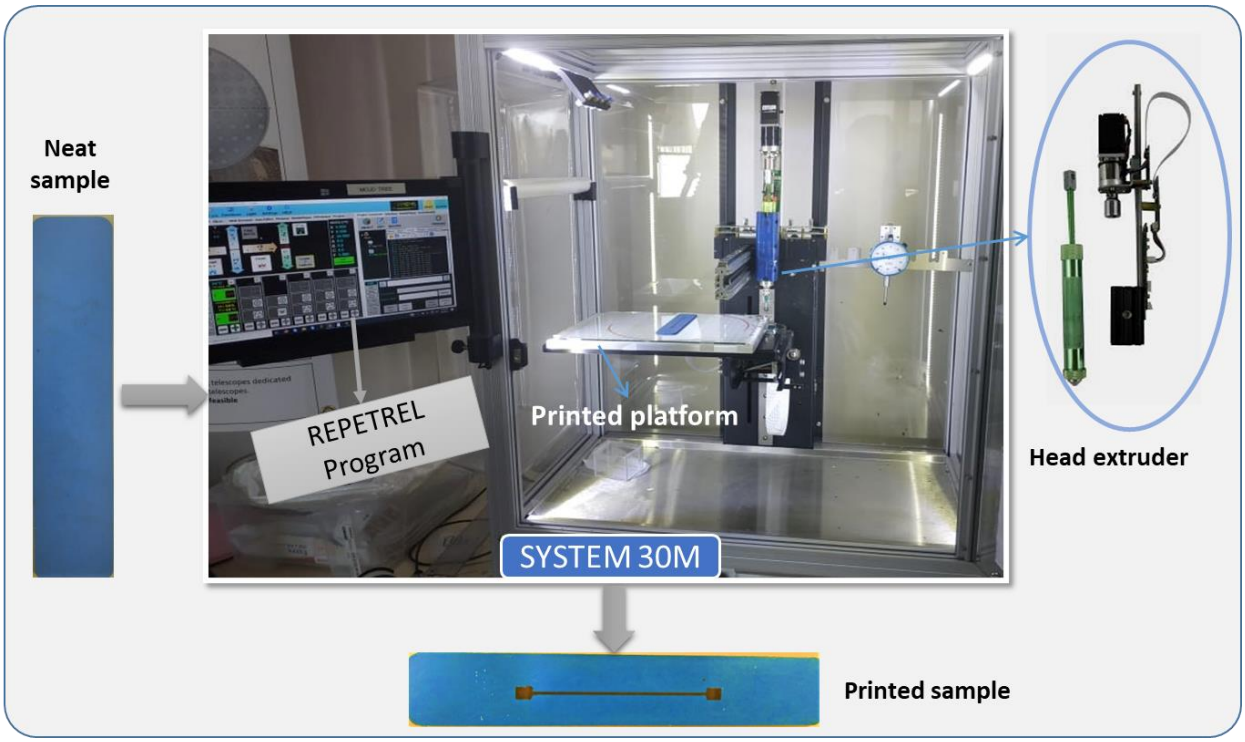

Figure 26. The printing process used to make a one printed-line coating on a 2D sample.

It is obvious that printing a straight-line resistor on a 2D substrate is not the same task as printing three circle-shaped lines on a 3D cup, which is a complex shape with the curved bellows. As a matter of fact, another 3D printer model (Hydra 16A), comprising a larger workspace platform with an addition of a motorized support, was getting involved to make the task feasible. As depicted in Figure 27, the sample's support can be rotated in a full range (0-360°) around Y-axis through the transmission of shaft B, and 0-180° around X-axis thanks to the shaft A. Based on this device, the coordinates of the SC in the X- and Y-axes can be adjusted by setting the rotation of these two shafts (with precision of 0.1°). The control of the motors is given by the Repetrel program where the CAD model is imported and converted into the Gcode language. The choice of the printhead, nozzle tip, and syringe pump extruder are the same as for the 2D-sample protocol. Also, the extruder system has a 3 degree-of-freedom (3-DoF) translation. Perfect synchronization between the support movement (2 DoF in rotation) and the extruder movement (3 DoF in translation) is undoubtedly a key issue of fabrication success.

To achieve the desired patterns of the SC and to improve the ink adhesion, the quantity of the output ink (adjusted by extrusion speed) and the distance between the nozzle needle tip and the substrate surface during the operation are of primary importance. This distance should be as small as possible, about 0.2–0.3 mm so that ink is injected with sufficient force to be quickly adhered on the substrate. Accordingly, the 3D printing process requires high precision of the SC position, the distance between the needle tip and the coating, as well as the synchronization between the motors' speed and the amount of the output ink. To some extent, these parameters substantially affect the pattern's shape fidelity, and thus the print quality.

Once the printing process is complete, the 2D and 3D samples are placed into an oven (Memmert V0 400 drying oven) under an adequate thermal condition to obtain cross-linking polymerization of the inks.

Regarding the recommendations given by the ink's suppliers, the coated samples are cured at 120 °C during 30 min for the second ink, and 175 °C during 10 min for the first ink.

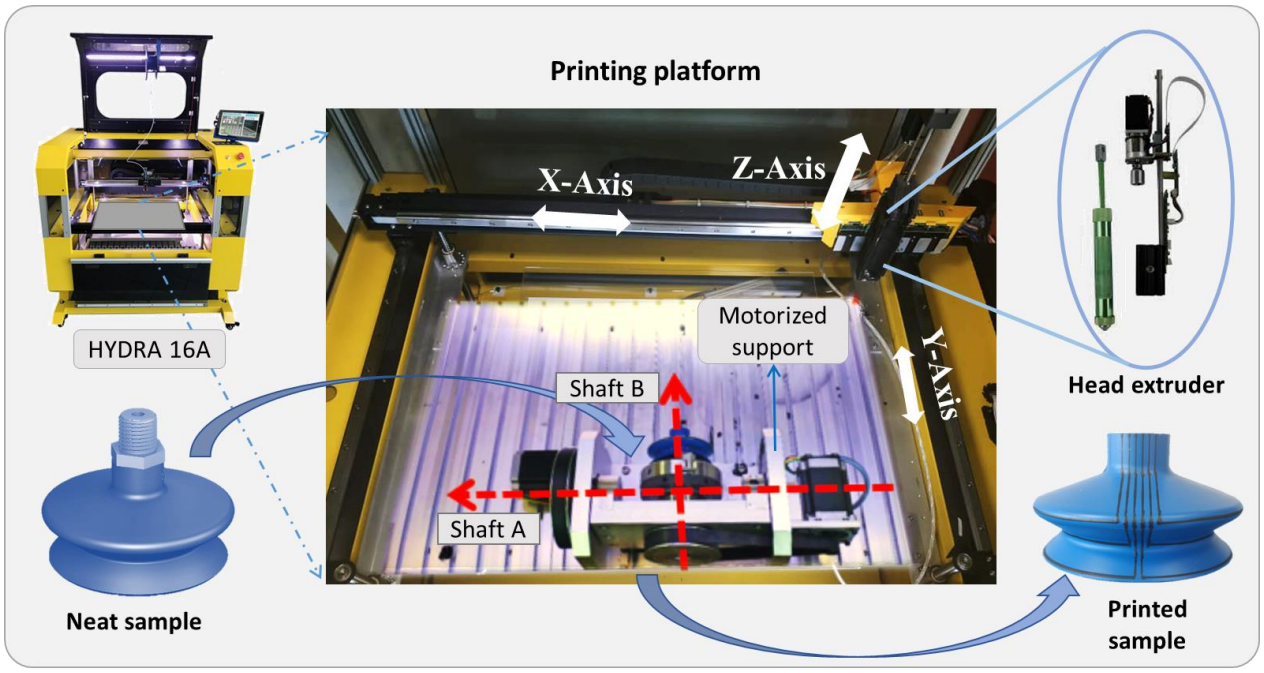

Figure 27. The printing process used to coat 3 resistive sensors on a 3D suction cup

3. *Characterization methods*

3.1. Morphological characterization

To visualize the surface state of the sensor coatings, morphological characterization via Scanning Electron Microscopy (SEM) was performed. Observation tests were conducted on the top surface of 2D samples using a compact SEM equipment (FlexSEM 1000II, Hitachi High-tech). The instrumentation is also equipped with an EDS system (Energy Dispersive Spectroscopy), allowing for the chemical analysis of inks' features being observed in SEM monitor. Eventually, signals produced in the SEM/EDS system includes secondary and backscattered electrons that are used in image forming for morphological analysis, together with X-rays that are used for identification and quantification of chemicals present at detectable concentrations. In general, EDS can detect major elements with concentrations higher than 10 wt% (major), and minor concentrations between 1 and 10 wt%. The detection limit for bulk materials is 0.1 wt%, therefore EDS cannot detect trace elements below 0.1 wt%. It has been well known that the detection limit in EDS depends on sample surface conditions: the smoother the surface the lower the detection limit [290]. In practice, the coating surface is considered to be smooth enough to make EDS experiment reliable, in which surface treatment of the printed coating is not necessary. To verify accuracy of the chemical composition analyses, EDS test was performed on several selected micro areas of the sample's surface.

3.2. *Electrical characterization*

The electrical characterization of the composite inks is carried out based on the determination of their resistance (denoted R). This allows for estimation of the material's conductivity (denoted σ) thanks to the following expression [291]:

$$\sigma = \frac{l}{R \times S} \tag{4}$$

where S and l respectively denotes the surface and the length of the printed coating. S is determined as $S = e \times w$ where e and w are correspondingly the thickness and the width of the coating (see Figure 28a).

There are many methods for determining the resistivity of a material, but the technique may vary depending upon the type of material, magnitude of the resistance, shape, and thickness of the material. One of the most common ways of measuring the resistivity of thin, flat materials like semiconductor or conductive coatings is to use a two-point probe method. Such a technique involves bringing two probes in contact with a material of unknown resistance. A DC current is applied between these two probes, and a voltmeter measures the voltage difference between them. The resistivity is computed from geometric factors, the source current, and the voltage measurement. For making a direct resistance measurement, the Ohm-meter (RM_804) used for this test includes a DC current source, a sensitive voltmeter, and two alligator-clip probes clamped on the two ends of printed coating (see Figure 28b).

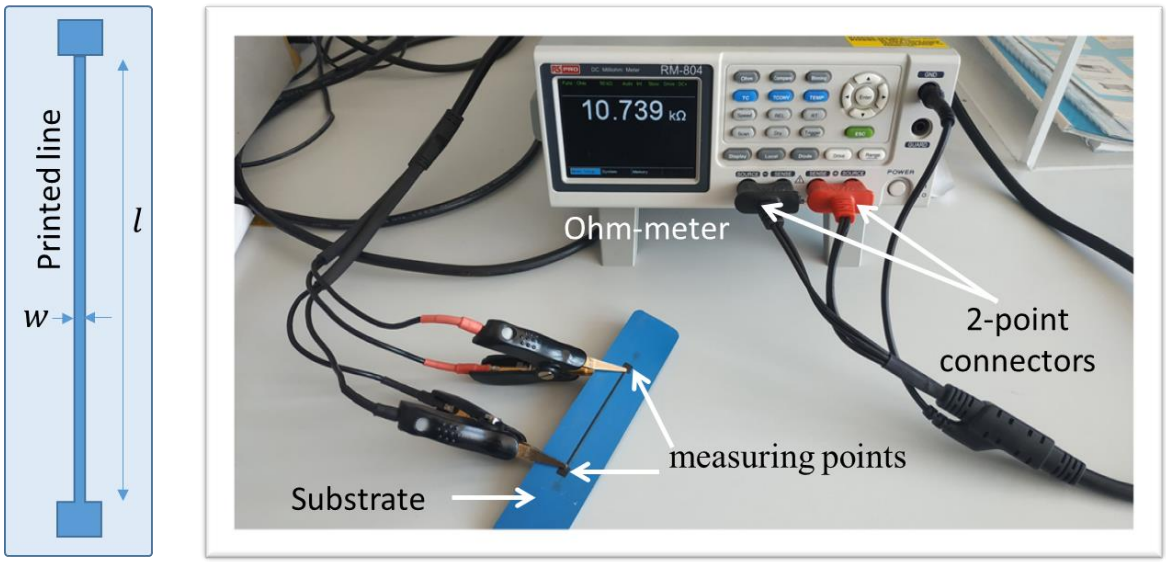

a) b)

Figure 28. a) Conductive coating printed on a 2D substrate; b) Experimental setup used for measurement of electrical resistance.

3.3. *Piezoresistive characterization*

3.3.1. 2D rectangular-shaped sample

Experimental monotonic tensile testing is applied to assess the piezoresistive properties of the printed sensors coated on the HNBR elastic substrate. Figure 29 shows the typical tensile configuration using a

SHIMADZU (AGS-X model) machine where the 2D specimen is firmly clamped by two pneumatic-actuated grips: The top grip can be freely moved in translation (via a controlled motor) while the bottom grip is fixed. By controlling the distance between the two grips, it is possible to impose a desired displacement (so the deformation) to the sample. The resistance variation of the printed sensor is thus evaluated as a function of the amplitude and the rate (i.e., speed) of the applied displacement, which is designed as a periodic triangle or trapezoidal waveform. Finally, the output resistance and the input displacement signals are simultaneously acquired and recorded in real-time through a Sirius 8XSGT card interfaced with the DEWE software. Post-data treatment was performed with MATLAB and Excel.

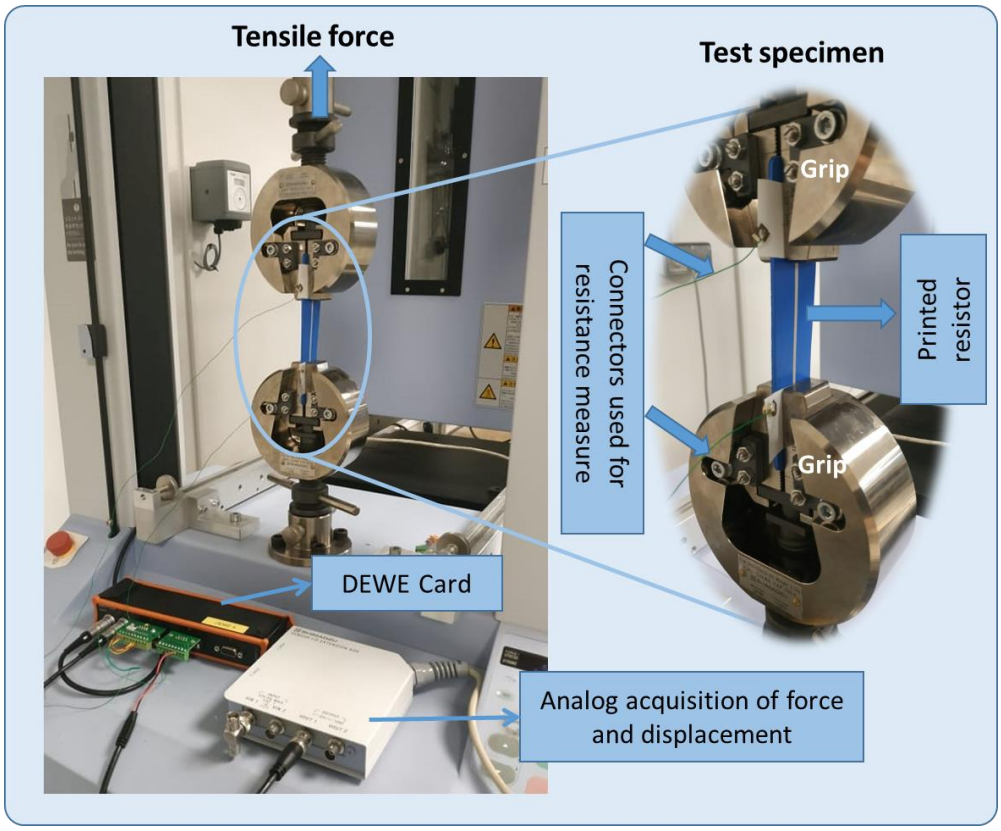

Figure 29. Experimental setup used for a piezoresistive characterization of 2D coated samples.

3.3.2. 3D suction cup

Figure 30a illustrates a specific test bench developed by our Industrial Partner, which allows for the characterization of printed sensors in a real condition. Thanks to an automatically controlled vacuum pump system, it is possible to actuate the suction cup (SC) under two operating modes: 1) compression : the SC is subjected to vacuum when being pressed against a tested surface; 2) release: the vacuum is interrupted, making the SC return to its original shape. To some extents, variation in the SC's shape leads to change in the resistance of the printed sensors. For a purpose comparison, the experimental setup enables testing two SCs simultaneously: one of them is performed on a standard flat surface while a specific configuration (i.e., incline, angle, or sphere surface) is used for the other (see Figure 30b). As a matter of fact, the SC is intentionally designed to be used on several types of object with different surfaces. The test bench is powered by a 24V DC generator. The resistance measurement is acquired by an acquisition card interfaced with a home-made software, allowing for monitoring and recording the signals in real-time. The multi-

channel box, also connected to acquisition card and computer via another home-made software, is used to generate an input waveform to drive the vacuum pump system. Parameters relating to the number and duration of the input cycles can be modified on-line from the computer.

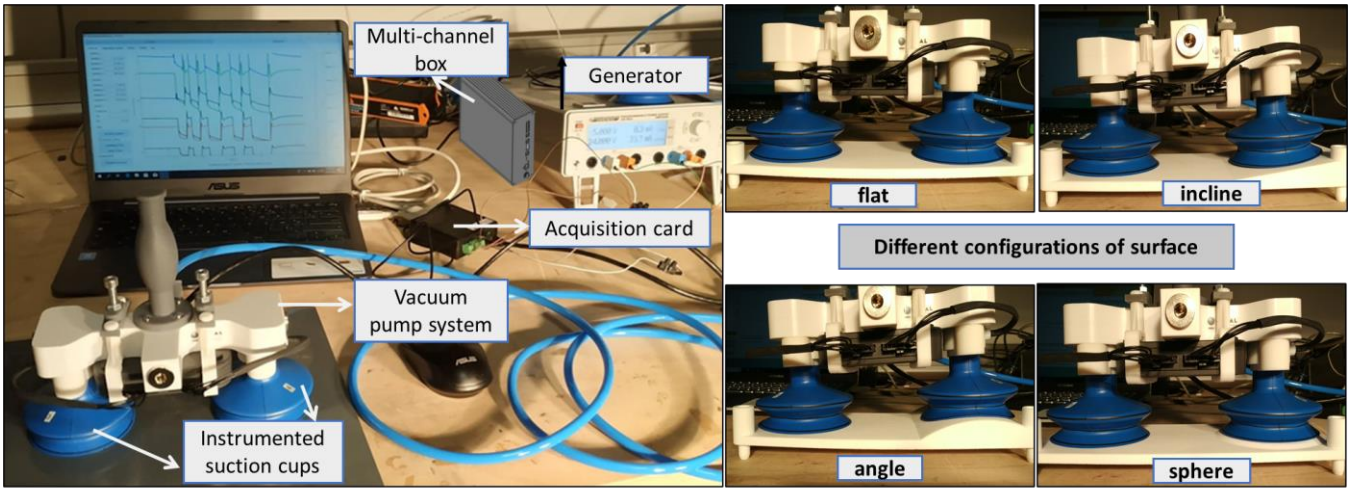

Figure 30. Experimental setup used for a piezoresistive characterization of 3D coated suction cups : a) specific test bench with acquisition system; and b) four configurations with flat, inclined, angular and spherical surfaces.

4. Results and discussions

4.1. Morphological properties

Figure 31 illustrates the SEM images of the first ink (a-b-c) and the second ink (d-e-f) made with 3 different magnifications (x75, x1000, and x2000, respectively). As observed, both of them lead to homogeneous printed surface, despite some tiny defects appearing on the coating layer. The second ink somehow exhibits smoother micro surface than its counterpart (Figure 31 e-f versus b-c), which is possibly originated from difference in the chemical compositions and the particles' size of these two inks. The EDS analysis showed in Figure 32 allows to partially confirm this hypothesis. The percentage range of the elements in the composite mass, visualized in the adequate accelerating voltage range and counted in seconds per electron-volt (cps/eV). It has been pointed out that both inks are made of major element like Carbon with high concentration (> 80 wt%), but other minor elements are not the same (e.g., 9.3 wt% of Cl for the first ink against 11.5 wt% of O for the second ink, and so on), confirming their dissimilarity in the chemical formulation.

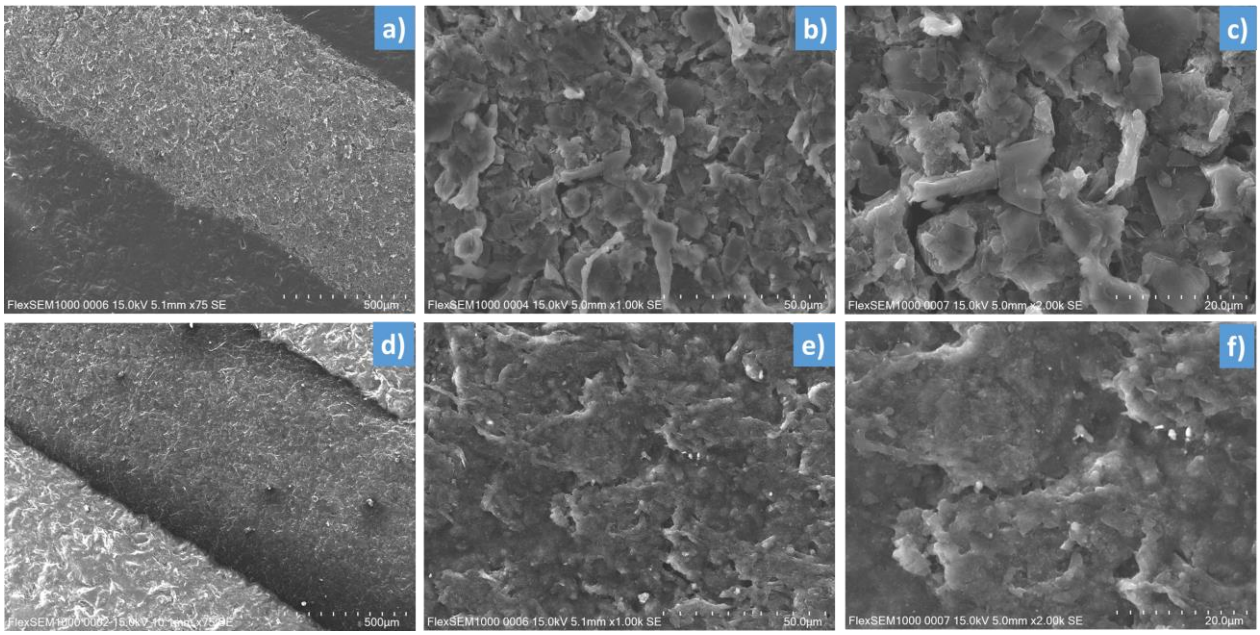

Figure 31. SEM image of 2D samples made of a-b-c) the first ink (a-b-c), and d-e-f) the second ink, correspondingly with different magnification of x75, x1000, and x2000 (from the left-hand side to the right-hand side).

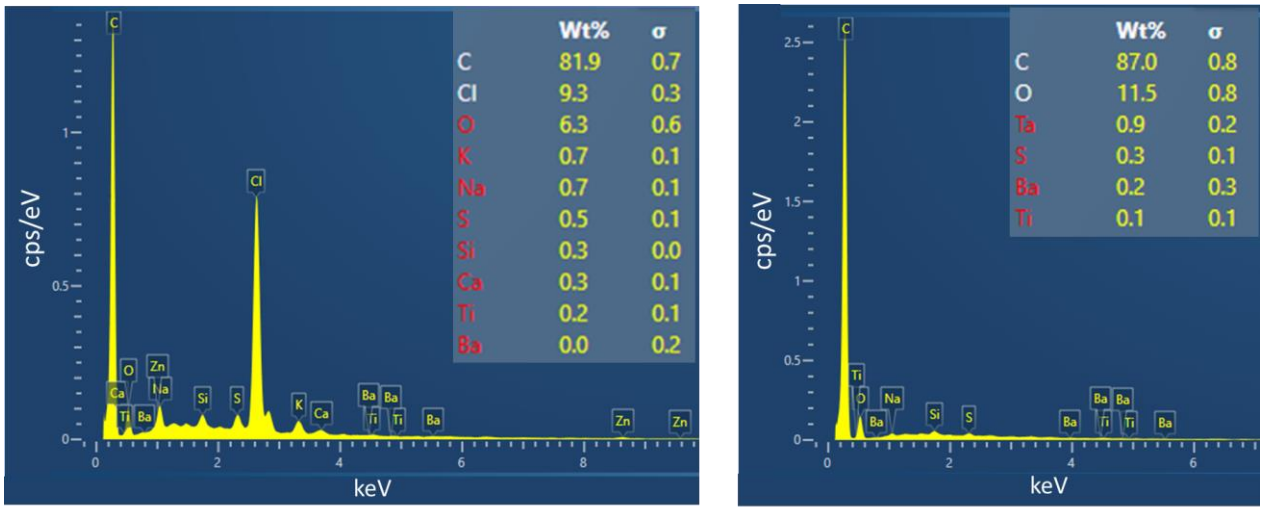

a) b)

Figure 32. Elemental distribution maps based on SEM-EDS spectrum analysis for a) the first ink, and b) the second ink.

4.2. Electrical properties

Based on the measurement of the resistance and the dimension of the printed lines made of the two selected inks (Table 4) on a 2D substrate (Figure 28a), it is possible to infer their electrical conductivity (σ) that equals 90 S/m and 140 S/m, respectively. These values are somehow smaller than those given in the inks' datasheet. It is worth noting that the measure uncertainties strongly depend on the uniformity of the coating's thickness as well as the surface contact between the probes and the sample. Although the two inks exhibits low value of σ, their electrical properties are revealed to be fit with our target application. Indeed,

the resistance value of each sensor coating printed on a 3D suction cup must not exceed 300 kΩ (either in static or dynamic regime), which is the limited value imposed by the acquisition software.

Table 4. Dimension and electrical measurements of the conductive inks

	first ink	second ink
Width *d* (mm)	1.18	0.9
Length *L* (mm)	60	60
Thickness *e* (µm)	36	22
Electrical resistance (kΩ)	10	34

4.3. Piezoresistive properties

4.3.1. 2D rectangular-shaped sample

a) First ink

Tensile tests were conducted on a 2D specimen coated with the first ink, i.e., subjected to a maximum deformation (or strain) of 10%. As demonstrated in Figure 33a, the resistance and the applied input strain are perfectly in phase, reflecting good correlation between the electrical and mechanical properties of the ink. Interestingly, when the strain is falling from the maximum (10%) to the minimum (initial state at 0%), the resistance is held in a few seconds. Indeed, HNBR material is an elastomer type that tends to shrink when being deformed [292]. This shrinkage needs time to return to its initial state [293]. A period of 20 s applied in this test is probably too fast for the shrinkage, which causes the non-linearity of the resistance signal from 2% down to 0%. For the rising phase of the strain from 0% to 10%, the resistance exhibits a small overshoot in a transient regime and then gradually decreases to attain the steady state.

Figure 33b confirms a linear relationship between the electrical resistance (*R*) and the mechanical strain, i.e., accompanied by somewhat hysteresis behavior linked to relaxation behavior of the elastomer. The linearity can be explained according to Eq. (1) where the specimen's length affected by the tensile strength is proportional to *R* and so is the deformation. Assuming that the section of the printed line is unchanged and variation in the resistance is mainly due to variation in length. During the rising and falling phases of the deformation (ε), the ink exhibits the same piezoresistive coefficient of around $\Delta R/\varepsilon = 8.6\ k\Omega/\%$, leading to a determination of the gauge factor (GF) according to the following expression:

$$GF = \frac{\Delta R}{R_0 \times \varepsilon} \tag{5}$$

where *R* and is the resistance of the undeformed gauge (~ 50 kΩ) ; and Δ*R* is the change in resistance caused by strain ε. The GF is then deduced equal to approximately 17.3, which is consistent to the value found in literature for plain-woven carbon fiber reinforced polymer (CFRP) [294]. Noted that most of standard commercial has positive piezoresistivity with gauge factor in a range between 2 to 4.

Besides the deformation, the tensile rate (or speed) is also a relevant factor that can influence the resistance change (ΔR). Indeed, the geometry of the fillers within the polymer matrix decides the reaction rate of the ink under a given deformation [295]. As displayed in Figure 33c, ΔR is somehow stable for different speeds from 0 to 4 mm/s, where discrepancy is less than 8%. Considering uncertainties of

measurements, it is reasonably to discard this discrepancy and consider that ΔR is unchanged as a function of the tensile rate. In conclusion, the sensor printed with the first ink exhibits excellent piezoresistive response with good stability, high sensitivity and linearity.

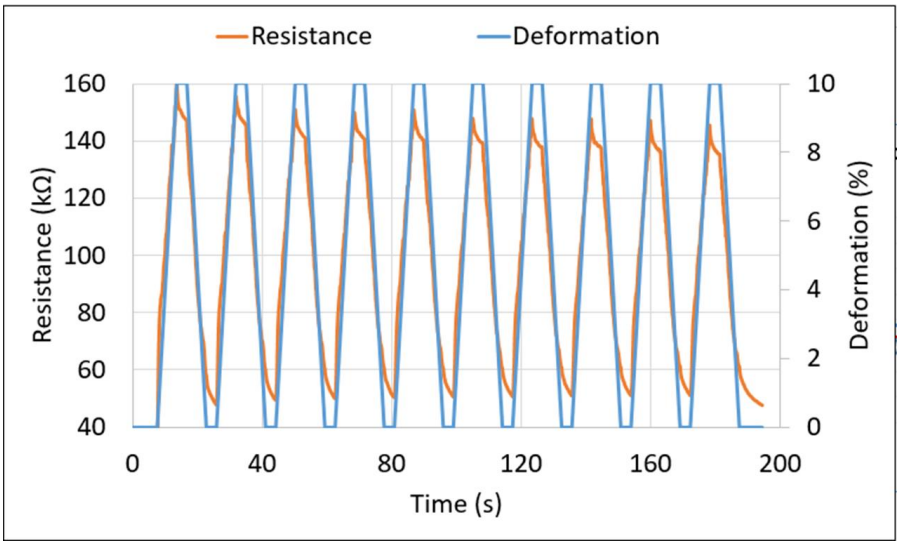

a)

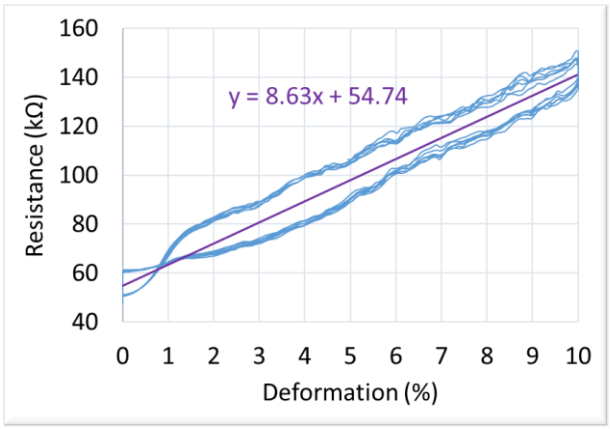

b)

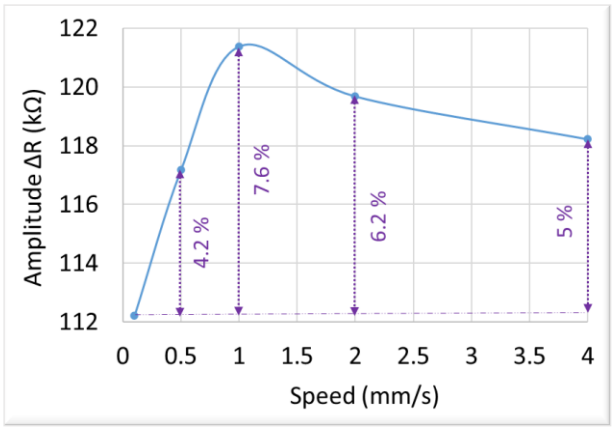

c)

Figure 33. Behavior of the first ink based on tensile tests: a) time evolution of resistance (red) and deformation (blue); b) resistance versus deformation; c) resistance variation (ΔR) versus speed at a 10% deformation.

b) Second ink

First of all, the tensile test conducted on a 2D specimen coated with the second ink is subjected to a constant speed (i.e., 1 mm/s) and varied strain. Figure 34a and b illustrate the resistance versus the displacement with different amplitude of respectively 4 mm and 10 mm (i.e., equivalent to a strain of ~7 % and 17). As it can be seen from the blue curve, the resistance (R) is not linear regarding the displacement (denoted x). Furthermore, the hysteresis behavior allows to infer that R does not only depend on x but also on its derivation dx/dt (so-called speed). An analytical model of the electrical resistance can be given by:

$$R(x) = R_0(x) + f(x)\frac{dx}{dt} \tag{6}$$

where R_0 is the 5th-order polynomial model dedicated to the resistance trend (the red curve displayed in Figure 34a-b), determined by the curve fitting tool of MATLAB. $f(x)$ denotes the speed factor, which was estimated based on the discrete interpolation of $R(x)$ function regarding the displacement. This method involves in the construction of data points for the $f(x)$ function so that the interpolated signal (yellow curve) built from Eq. (4) is fairly close to the original one (blue curve). Figure 34d shows the results of the speed factor estimated with different displacement's magnitude (denoted A) from 4 mm to 10 mm. It has been highlighted that under a constant speed, the $f(x)$ factor is almost similar whatever the value of A, meaning that the variation of A only leads to the change in the resistance trend (R_0) but not in the hysteresis behavior (second term of Eq. (4)). Interestingly, the hysteresis is maximum at the two extremities of the displacement (equal to 0 and A), and minimum at the displacement near to $A/2$ (Figure 34d). This observation is somehow related to the nonlinearity of the resistance, which is accentuated at the extremities and almost linear around the center of the displacement's interval.

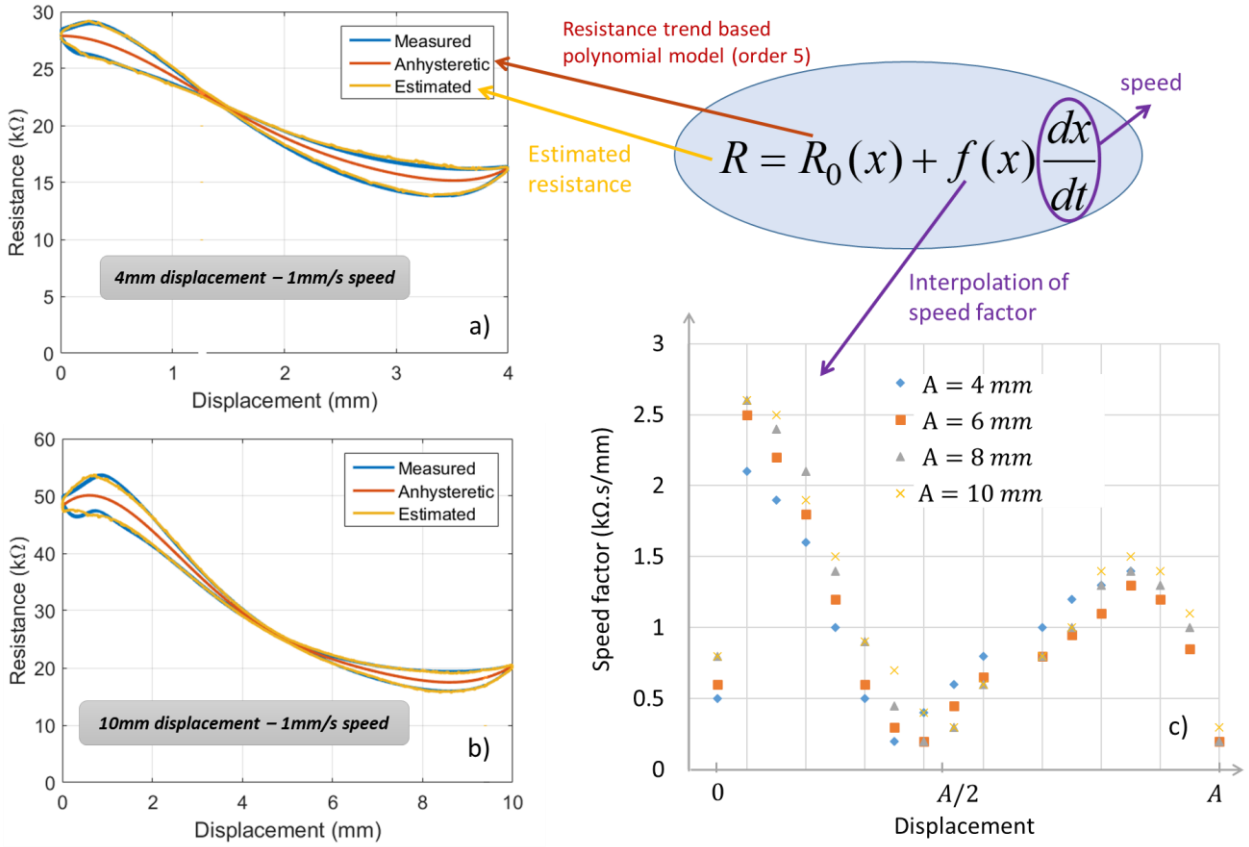

Figure 34. Behavior of the second ink subjected to different mechanical displacements (with speed constant of 1 mm/s) : a-b) resistance versus displacement with amplitude of 4 mm and 10 mm coresponndingly; c) formula of the estimated resistance ; d) interpolation of the speed factor.

Unlike to the fist ink that has positive piezoresistivity in which electrical resistance increases proportionally with the increased mechanical strain, the second ink exhibits a negative behavior ($R_0 < 0$). Similar results have been reported on the works of Wang *et al.* [296] and Mei *et al.* [297] for the CFRP using either two or four probe-wires method. Both argued that the positive piezoresistivity that was previously reported by many researches was caused by increased electrical resistance in electrodes, not from the changes in electrical resistance of CFRP. Todoroki and Yoshida conducted tests with similar techniques to [296,297] and produced negative piezoresistivity [298]. However, they contested that the negative piezoresistivity occurred due to poor surface treatment prior to the electrode attachment, which is contrary to fine surface treatment. The latest study was conducted by Jeon *et al.* to find out the effect of contact resistance between CFRP and electrodes to the piezoresistive behavior [299]. They also reported that the roughness of the composite surface attached to the electrodes affects the test results. Thus, these factors need to be considered in future testing and application.

Another test is set with a constant displacement of 6mm (i.e., corresponding to 10% strain) and varied speed with amplitude of 0.5 mm/s and 2 mm/s as shown in Figure 35a-b. To some extent, the resistance change (ΔR) somewhat increases with the speed value. Figure 35c represents the time evolution of the resistance and the displacement, in which these two signals are completely out of phase (i.e., the phase shift equals 180°). This confirms the negative piezoresistive response as described above, suggesting that the geometric factor gives a fundamental impact on the resistance value. Based on the nonlinear model of Eq. (4), it is possible to estimate the $f(x)$ speed factor in such a way that the estimated resistance (yellow curve in Figure 35a-b) perfectly fits with the measured one (blue curve). It is clearly pointed out in Figure 35d that $f(x)$ factor is velocity dependent and tends to decrease with an increase in the speed's amplitude. Exceptionally, very high speed makes $f(x)$ tend to 0 and the resistance becomes anhysteretic, whatever the applied displacement [300].

Accordingly, regarding the above characterization, it is clearly that the first ink is more suitable to be involved in the development of sensor thanks to its linear and positive piezoresistive response. The second ink, despite of its nonlinear and negative piezoresistivity that would make calibration and analyses complicated, exhibit better adhesion to HNBR material after a long-time mechanical solicitation. Since adhesion is a critical issue in additive manufacturing (AM), especially for the curved surface (e.g., bellows), the second ink is finally chosen to be coated on a 3D suction cup.

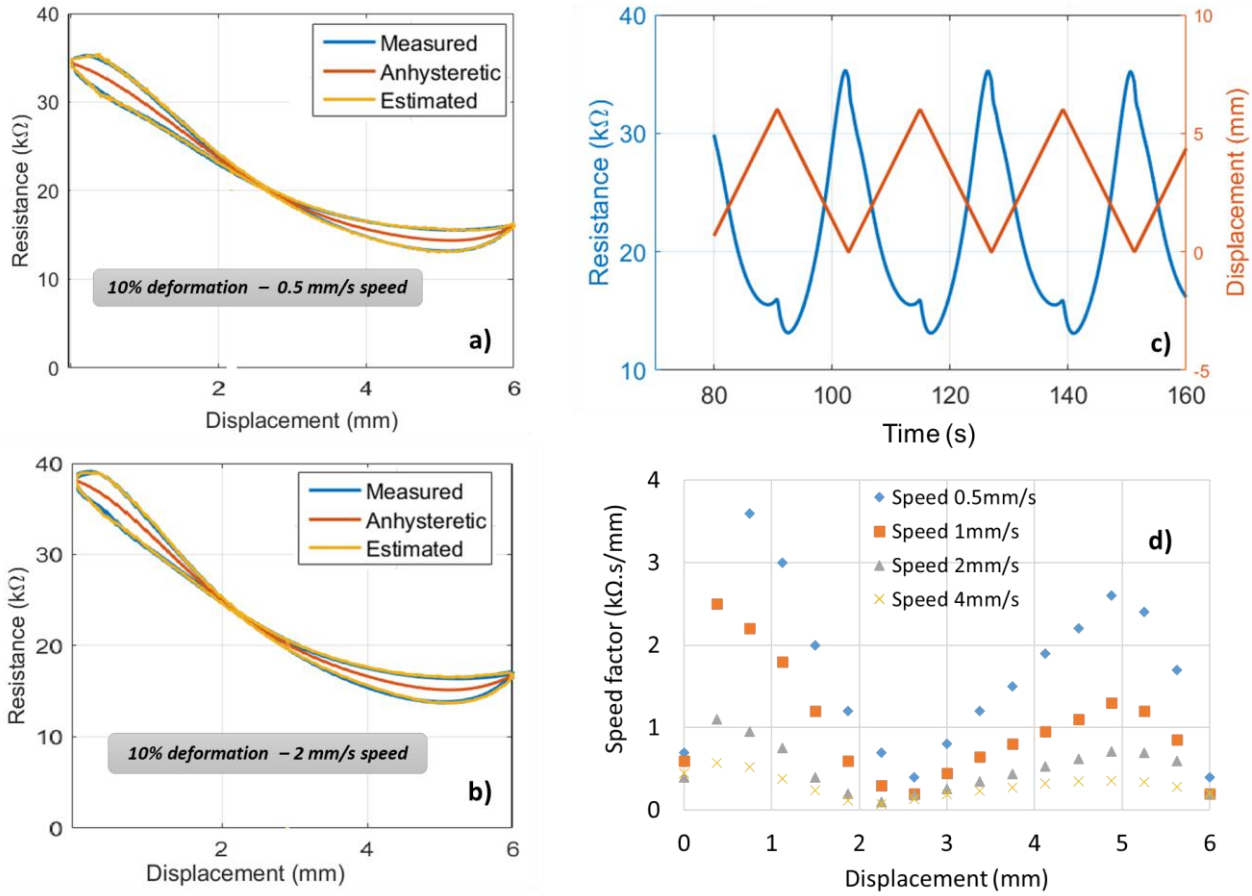

Figure 35. Second ink behavior subjected to a 10% deformation with different dynamics (speeds): a-b) resistance versus displacement under a speed of 0.5mm/s and 2mm/s corespondingly; c) time evolution of resistance and displacement; d) interpolation of the peed factor.

4.3.2. 3D suction cup

Figure 3.8a illustrates the experimental setup described in Subsection 3.3.2 that allows for an assessment of the resistance evolution of two suction cups (called SC1 and SC2) simultaneously, one tested on a flat surface while the other on the surface with different configurations (flat, incline, sphere, and angle). Both SCs were printed with three circle-shaped sensors using the second ink (Figure 3.8b), but observations were mainly focused on the top and the bottom bellows where the deformation was supposed to be important, and so was the resistance change.

Figure 3.8c displays FFT (Fast Fourier Transform) analysis of both SCs' resistance measured on the two bellows' sensors for different surface configurations. As expected, the resistance magnitude of the concave bottom bellows is higher than that of the convex top bellows, which agrees to the strain distribution shown on the finite element (FE) modeling (Figure 24b). Investigation performed on the 2D substrate coated with a printed-line sensor showed a resistance change of approximately 25 kΩ under a 10% deformation (Figure 35c). To simplify the estimation of the SC's strain, a quasi-linear relationship is considered. As demonstrated on Figure 35d, hysteresis behavior (i.e., image of the speed factor) could be negligible under a fast dynamic control of the vacuum pump system. In the case of SC1 tested on the flat surface, the resistance variation of the top and the bottom sensors respectively equals 43 kΩ and 17 kΩ, leading to a

strain prediction of 18% and 7%. For the SC2, these value are smaller, i.e., 15 % and 4% correspondingly. To some extent, these findings somehow corelate to the simulation result shown in Figure 24b, even though we used the hypothesis based on a linear model, which is somehow far from the reality.

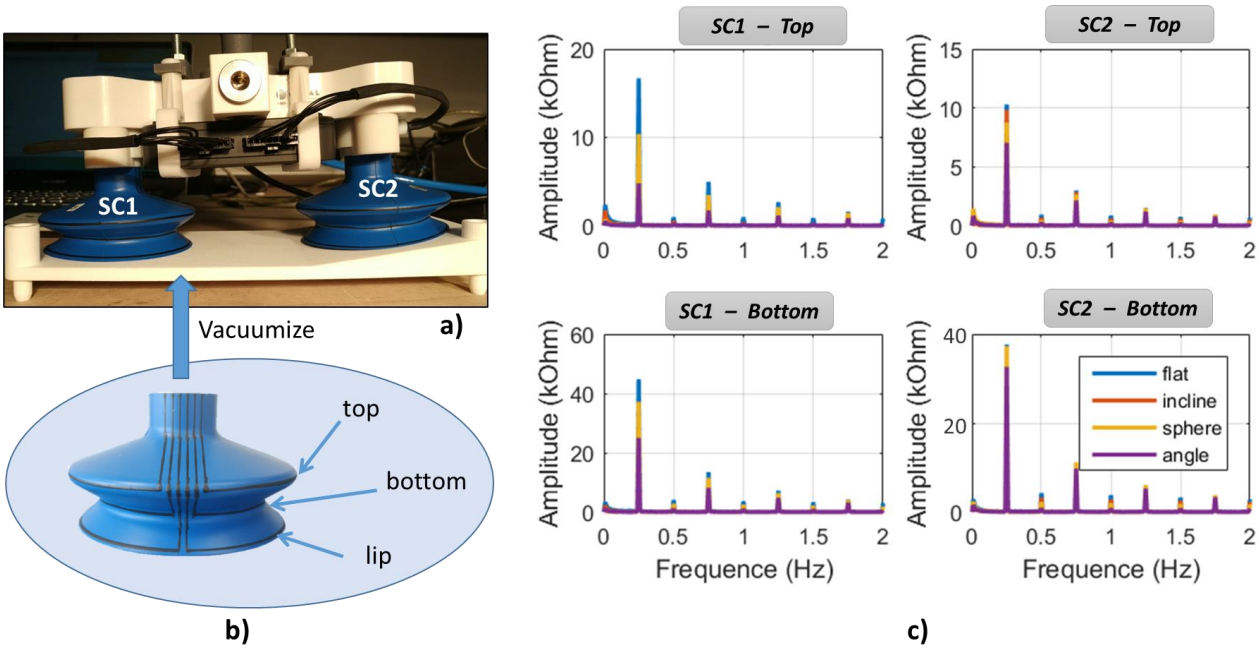

Figure 36. Resistance variation mesured on different configurations: a) setup of 2 suction cups (SC1 et SC2); b) three sensors coated on the samples; c) Resistance variation of the top and bottom bellows mesured on different surfaces for SC1 et SC2.

Among different surface configurations (cf. Figure 3.8c), the flat surface leads to the highest resistance value, followed by the spherical and inclined surfaces, while the angled surface makes the lowest contribution. On a one hand, the applied compression force is perpendicular to the flat surface, giving raise to maximum deformation that is symmetrical with respect to the central axis. On the other hand, the force is no longer perpendicular to the other types of surface, resulting in smaller deformation of the SCs. Particularly for the angled and spherical surfaces, the inner vacuum of the SC is somewhat filled by air through tiny gaps between the lip and the curved surface, provoking lower vacuum pressure and thus smaller resistance change.

Aging test was carried out to verify whether or not the adhesion between the carbon-based-composite ink and the SC surface can endure a long-time mechanical solicitation. Figure 37 displays the resistance measurement of the top and bottom sensors coated on two SCs' bellows during almost 1h. For all cases, the resistance slowly decreases during the transient regime occurring for the first 500 seconds, which relates to the mechanical relaxation of the HNBR's material. After around 100 cycles, the resistance magnitude becomes stable and reach the steady regime. Throughout 1h testing, the measured value remains unchanged, confirming high reliability of the developed sensing device based on additive manufacturing (AM) technique. Inset graphs reveals a square wave form of the resistance evolution in time domain, which is in agreement with the FFT spectrum of Figure 3.8c in frequency domain. Indeed, a square wave consists of a fundamental sine wave (of the same frequency as the square wave), and odd harmonics of the fundamental

whose amplitude decreases and proportional to $1/N$ (N denotes the harmonic, $N = 1, 3, 5 \ldots$). The fundamental frequency was found equal to 0.25 Hz, corresponding to the input waveform rate used to control the vacuum pump system. During a period of 4 s, compression and release phases are getting involved: First, the SC is pressed against a surface to create vacuum inside that sucks the bellows, making the strain increase (in absolute value) and so do the resistance variation. Second, the atmospheric air is filled into the released SC that tends to its initial shape, thus reducing the resistance value.

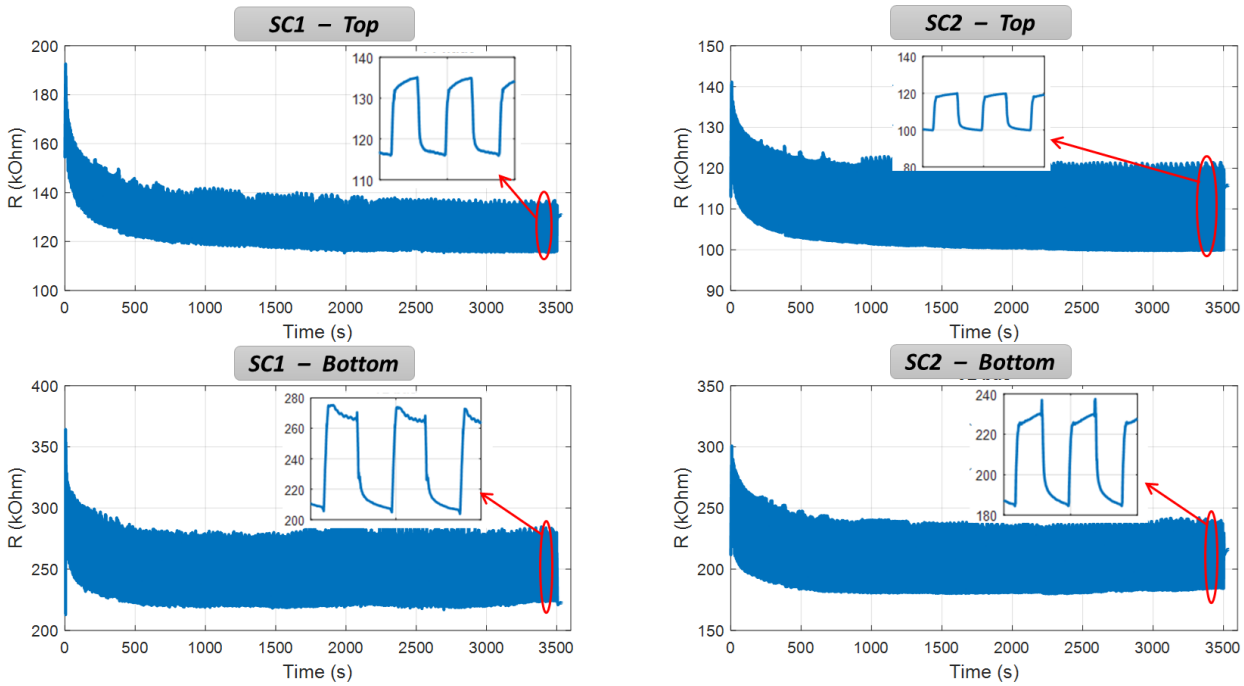

Figure 37. Aging test based on resistance measurement of the top and bottom coatings for SC1 et SC2. Inset graphs zoom in on the last portion of the curve for a short duration.

To assess the impact of the electrodes, two samples were conducted, one consisted of full sensor coating while the other was made with electrode lines only (cf. Figure 38a). A comparison of these samples was performed via analysis on the FFT peak value (i.e., deduced from the fundamental harmonic) with the four surface configurations (cf. Figure 38b). Surprising result was found at the lip's measurement, where the resistance change of the electrode coating was a little bit superior to the one of the full coating, regardless of which configuration was chosen. This maybe come from inevitable measurement uncertainties due to printing quality, homogenous ink, unperfect setup, and so on. More thorough analysis dedicated to the lip's wear monitoring will be involved in our future investigation. Regarding the top and the bottom bellows (see Figure 38b), the full sensor coating exhibits clearly higher FFT peak value (around factor 2) than the electrodes coating, whatever the surface configuration. These results clearly confirms the influence of the electrodes that would be minimized in the design optimization so as to improve accuracy of the resistance measurement.

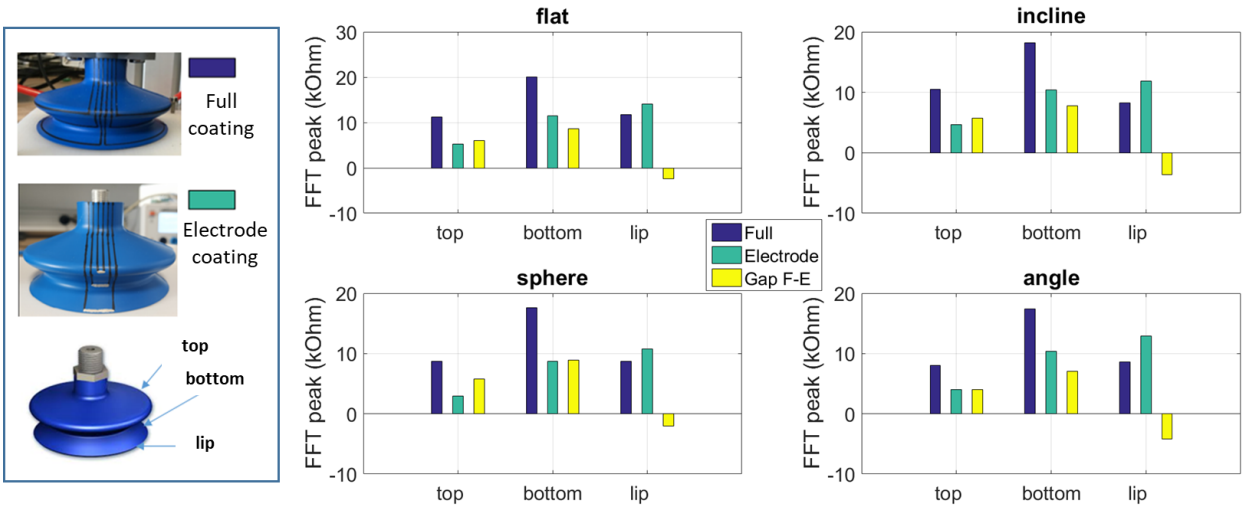

Figure 38. Influence of electrodes: a) Two SCs with full coating and electrode coating; b) FFT peak value (fundamental harmonic) using four surface configurations.

Therefore, an alternative solution was considered as illustrated in Figure 39a: the SC was designed with hybrid coatings where the electrodes were printed by another silver ink (Creative Material, ref. 127.07), while no change for the circle-shaped sensors. The selected silver ink has advantage of excellent electrical conductivity, making its resistance negligible compared to the one of the printed sensor. As expected in Figure 39b, the hybrid SC leads to substantially smaller resistance value with respect to the full coating printed with the second carbon ink. Regarding the resistance change, the FFT peak value displayed on Figure 39c is reduced for both sensors, particularily in the case of the top bellows. Such results are very encouraging, confirming high benefit of the hybrid design in which the influence of the electrodes could be ignored. Unfortunately, the hybrid prototype in reality is not robust enough to go through the aging test under a great deal of stress, because of poor adhesion property of the silver ink.

The last design involved in using only the second carbon ink, but increasing the length of the two sensors so as their resistance variation is sufficiently superior to the electrodes' one. As illustrated in Figure 40a-b, each bellows were printed with three circle-shaped resistors, which can be connected either in series or in parallel. The serial-connection sample was first fabricated, then was transformed to the parallel counterpart by adding short printed lines (illustrated as red lines for an easier visualization). Such a design allowed to enhance the detection area of the sensitive elements, with the aim of monitoring the global state of the bellows. Actually in the former sensor design based on a one-circle resistor, the printed lines had a 1mm narrow width located at the center of the bellows. To some extent, this position did not cover all relevant area of the bellows where the deformation was supposed to be meaningful. As a result, a new design involving in a three-circle resistor seemed to be a good alternative for an enhancement of the detection area.

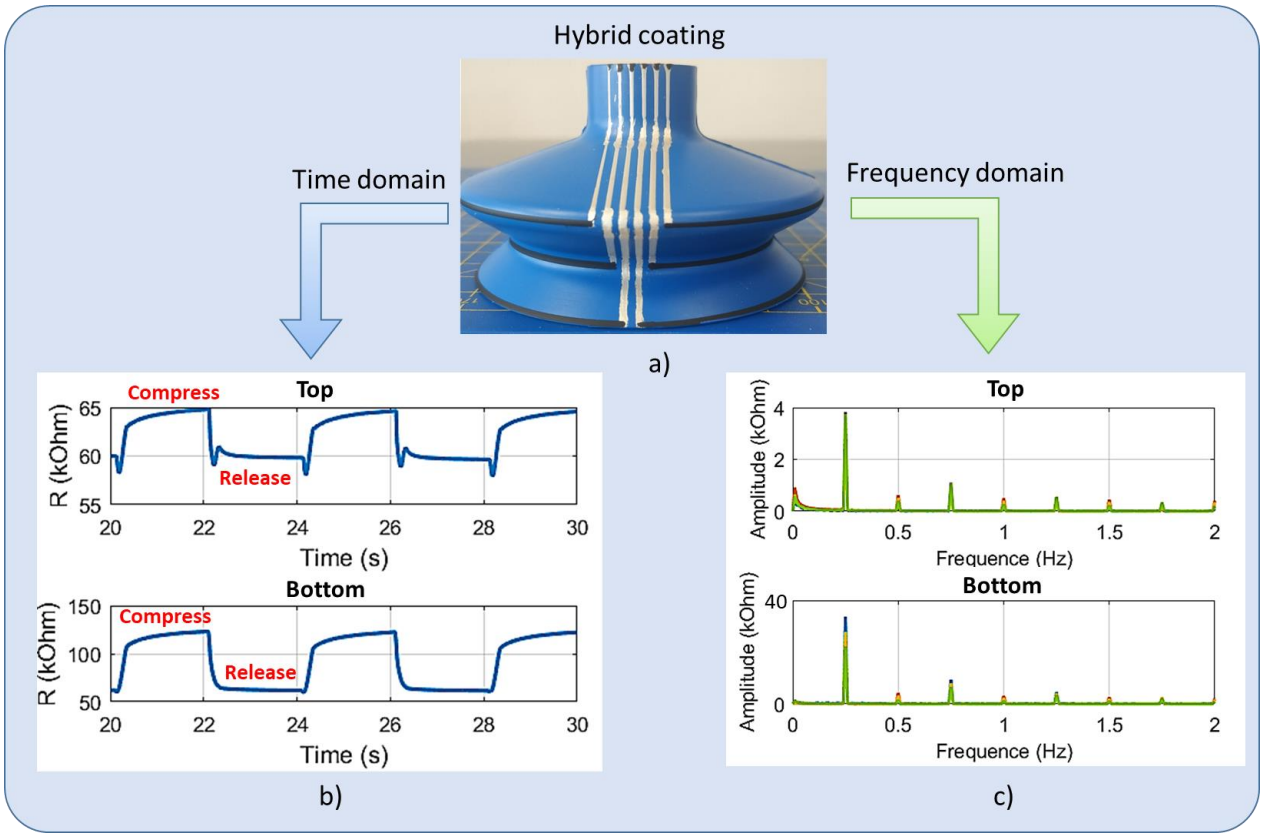

Figure 39. Time and frequency domain analyses of the top and bottom resistances for the hydride-coating suction cup.

Table 5 shows the absolute resistance variation (ΔR, where $\Delta R = R_{max} - R_{min}$) of the three SCs shown on Figure 39 and Figure 40. Logically, the one coated with three-circle serial resistors gives raise to the highest value of ΔR, whereas the parallel counterpart results in the smallest value. Whatever the coating's design, ΔR of the top bellows is significantly small compared to that of the bottom bellows, which agrees to the simulation and empirical results investigated above. To further highlight the comparison of the three designs, another indicator as the relative resistance variation (Δ_m) is given as following:

$$\Delta_m = \frac{R_{\max} - R_{\min}}{R_{\max} + R_{\min}} = \frac{\Delta R}{R_m} \times 100\% \quad (7)$$

where R_m denotes the mean resistance that is computed by $R_m = R_{max} + R_{min}$.

Regarding the results shown on Table 5, the one-circle hybrid coating gives raise to the maximum value of Δ_m performed on the bottom bellows. The three-circle parallel coating, on the contrary, induces to the minimum value. It can be therefore suggested that the center of the bottom bellows is the most deformed area, thus adding printed circles allows for an increase in the detection area but does not enhance the relative resistance variation (Δ_m). Concerning the top bellows, however, all designs exhibit moderate Δ_m value because of its smaller strain detection. Interestingly, the parallel coating give raise to somewhat higher variation with respect to the other (i.e., 7% versus 5%). Finally, the three-circle serial coating exhibits comparable performance to the one-circle hybrid coating. Although three-circle patterns is more complex,

this design make a possibility to employ only one type of ink. Inversely, the hybrid coating a supplementary silver ink whose adhesion and stretchability are still critical issues in 3D printing AM.

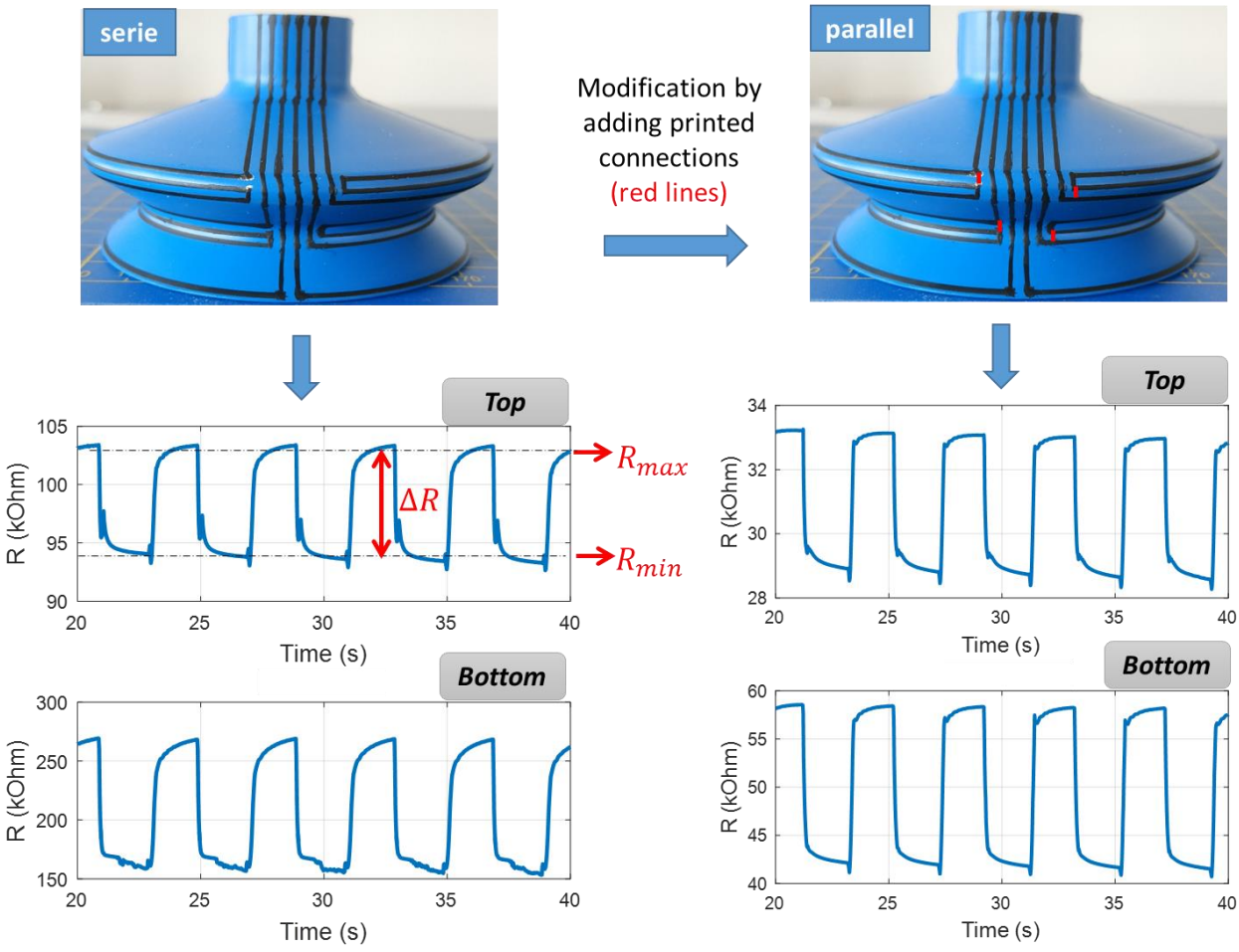

Figure 40. Time evolution of the three-circle resistances in a) serial connection or b) parallel connection coated on a 3D suction cup.

Table 5. Comparison of the absolute and relative resistance variation of three SC's coating designs.

	Type of suction cup		
	1-circle hybrid coating	**3-circle serial coating**	**3-circle parallel coating**
Top bellows	ΔR = 7 kΩ	ΔR = 10 kΩ	ΔR = 4.5 kΩ
	Δ_m = 5%	Δ_m = 5.1%	Δ_m = 7.3%
Bottom bellows	ΔR = 60 kΩ	ΔR = 110 kΩ	ΔR = 16 kΩ
	Δ_m = 35.2%	Δ_m = 26.2%	Δ_m = 16%

5. *Future development for printing-process enhancement*

To better improve the sensor sensitivity as well as the detection are, an innovative design using crenelated patterns coated on the two bellows is intended to be investigated on future work (see Figure 41). Each printed crenelation should be built in such a way that its resistance does not exceed 300 kΩ so not to alter the sensitivity of the sensor (relating to strain gage factor). Unfortunately, the limitation of our current printer does not allow to achieve such a complex design. Development involved in the robot control together with enhancement of ink stretchability is under exploration to fit with these complex patterns, especially when the substrates are extremely curved as in the case of the concave and convex bellows.

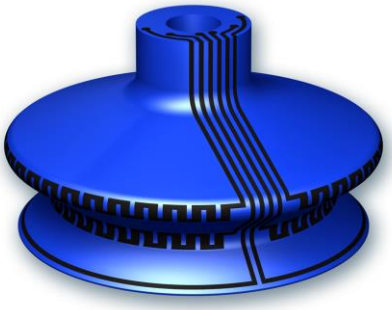

Figure 41. Design of SC with crenelated patterns

To completely automate the printing process, a 6-axis robot arm control (TX2-60, Stäubli Controller: CS9) developed by another company (name is not disclosed) was initially investigated as shown in Figure 42. The 30M Hyrel extruder drives the printhead nozzle that is kept fixed, while the robot arm carries the SC and performs movements in 6 DoFs. Including an automatically controlled robot arm into AM makes the printing stages more manageable and less time consuming, as the robot could perform more complex and precise trajectories than the printhead itself. Our preliminary results have demonstrated the feasibility of this approach, which have given out a real breakthrough in the field of sensor coating based 3D printing technology.

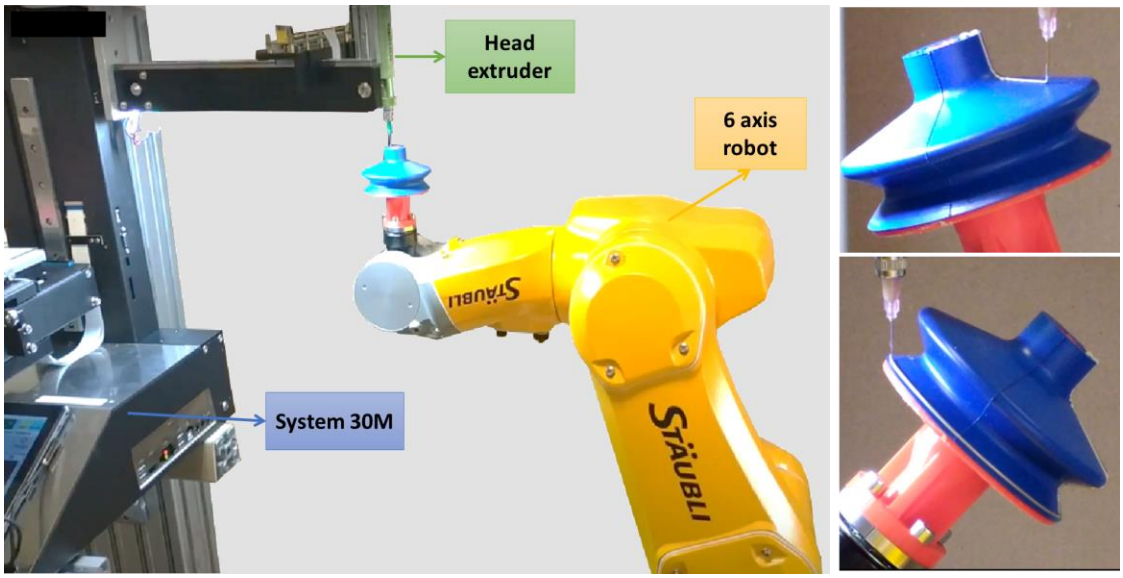

Figure 42. Advances on 3D printing process using a 6-DOF robotic arm.

6. Conclusion

In this study, we proposed an innovative method for condition monitoring a suction cup (SC) based on the resistance measurement of the printed conductive coatings. Particularly, we took a focus on the piezoresistive behavior of the two circle-shaped sensors coated on the SC's bellows where deformation was revealed to be considerable during vacuum operation, regarding the simulation result. On the other hand, deformation of the SC's lip was demonstrated to be negligible, thus not being considered in this work. However, a sensor coating was still printed on the lip's surface for future work purpose related to mechanical failure monitoring in a long term. Indeed, the lip is not subjected to high strain variation during the cup's action, but is exposed to important static pressure as being the only part that has a contact with the subject. Success of the printed sensor coatings are essential impacted by the properties of conductive ink, which must ensure good adhesion to the HNBR material and capable of undergoing an important deformation (~ 20%) throughout several compression/release cycles.

Although conductive inks have been intensively explored in 3D printing technology, their piezoresistive behavior still needs to be further clarified. For a sake of simplicity, experimental characterizations were first conducted on 2D substrates based HNBR material. A tensile unidirectional method was performed to figure out the relationship between electrical resistance and mechanical strains, through which the piezoresistive behavior of the two carbon-based-composite inks was clarified. The first ink exhibited a perfect linear characteristics but poor adhesion to the HNBR substrate under high dynamic solicitation. The second ink better fitted to the target field because of its excellent adhesion and stretchability, despite its nonlinear and negative piezoresistivity. Therefore, only the second ink was selected to be printed on 3D SCs conducted on different surface configurations (flat, incline, sphere, angle). Initial design consisted of one-circle-shaped sensors coated on the two bellows and the lip, demonstrating a reliability of the selected ink (i.e., the only "survivor" after the aging test). With the aim of enhancing the surface detection of sensitive elements as well as minimizing the effect of electrodes, design optimizations involved in the development of hybrid coatings and three-circle sensors connected in series or parallel. To achieve more complex and higher performance designs, our study oriented to automatic 3D printing using a controllable 6-axis robot arm. Preliminary results was encouraging for upcoming exploration in the failure detection and predictive maintenance of SC. Another aspect of this research focusses on investigating new conductive inks with improved features in terms of viscosity, linear piezoresistive response, high stretchability and adhesion. The relationship of such parameters needs to be revealed for the future implementation and development of condition monitoring technology.

FOLIO ADMINISTRATIF

THESE DE L'UNIVERSITE DE LYON OPEREE AU SEIN DE L'INSA LYON

NOM : NGUYEN DATE de SOUTENANCE : 07 /Juillet/ 2023

Prénom : Van Cuong

TITRE: Printing smart sensor and actuator coatings using piezoelectric composites

NATURE : Doctorat Numéro d'ordre : 2023ISAL0047

Ecole doctorale : MEGA.

Spécialité : MÉCANIQUE, ÉNERGÉTIQUE, GÉNIE CIVIL, ACOUSTIQUE

RESUME : Les matériaux piézoélectriques jouent un rôle crucial dans le développement des matériaux intelligents et des processus de fabrication additive. Ils sont utilisés comme matériaux fonctionnels dans diverses applications, notamment la détection, l'actionnement, la récupération d'énergie et la rétroaction haptique. Les composites piézoélectriques, en particulier, ont été largement étudiés en raison de leur potentiel à améliorer les performances des matériaux piézoélectriques. Avec l'avancée des techniques de fabrication additive, les matériaux piézoélectriques peuvent être imprimés en 3D dans des géométries complexes et intégrés à des composants électroniques pour créer des structures intelligentes. La combinaison de matériaux piézoélectriques et de la technologie d'impression 3D a conduit au développement de divers dispositifs, notamment des capteurs, des actionneurs et des systèmes de rétroaction haptique, qui peuvent être personnalisés et fabriqués rapidement.

Les travaux de cette thèse se sont focalisés sur deux applications, à savoir la réalisation de capteurs pour le développement de roulements instrumentés et le développement de réseaux de transducteurs pour les interfaces haptiques. Les deux applications sont basées sur le matériau piézoélectrique composite, qui joue un rôle principal dans le fonctionnement des capteurs ou actionneurs. Des études préliminaires sur les caractéristiques des composites piézoélectriques ont été menées afin d'optimiser les propriétés du matériau et sa compatibilité avec l'impression 3D.

Première application concerne à la réalisation de capteurs pour la surveillance de roulement à bille. Le composite piézoélectrique à base de polymère est directement sérigraphié sur la surface de la structure hôte, qui est assimilée à un substrat en acier instrumenté. Par conséquent, la méthode développée ici permet d'extraire de manière fiable le comportement piézoélectrique efficace du composite mince grâce à une méthode de flexion à 4 points (4PB). Des caractérisations complètes des propriétés diélectriques et mécaniques, ainsi que des mesures de détection directe par couplage électromécanique sont étudiées sur la conception de la structure faite maison. Des modèles analytiques et éléments finis sont développés pour prédire les propriétés mécaniques du substrat testé ainsi que la sensibilité du capteur sous différentes charges appliquées. Des expériences sont menées sur un montage 4PB, permettant de valider les solutions analytiques et numériques. Un bon accord entre les sorties de capteur prédites par le modèle et les mesures empiriques a été atteint, confirmant la grande fiabilité de l'approche proposée. Tous les résultats ont démontré que le capteur développé est capable de fournir une mesure directe de déformation/contrainte au lieu d'un capteur de jauge de contrainte traditionnel par interpolation, et offre ainsi une méthode efficace pour la surveillance en ligne et in situ des roulements.

La deuxième application consiste à fabriquer un retour haptique en utilisant un matériau piézoélectrique composite. Des simulations ont été effectuées avec ANSYS pour optimiser le choix du matériau et les dimensions du design. Les expérimentations ont montré la capacité de ce matériau à générer des vibrations pour un retour haptique. Enfin, un démonstrateur de retour haptique a été fabriqué pour permettre aux utilisateurs de ressentir ces sensations. Un circuit électronique a été conçu pour répondre aux spécifications du démonstrateur, et une application Python a été développée pour tester facilement différents types de formes d'onde.

Directeur de thèse: COTTINET Pierre-Jean

Co-directrice de thèse : LE Minh Quyen

Président de jury :

Composition du jury : DEMOLY Frédéric (rapporteur de thèse), BROITMAN Esteban (rapporteur de thèse), GUIFFARD Benoit (examinateur), BERNARD Yves (examinateur), COTTINET Pierre-Jean (directeur de thèse), LE Minh Quyen (co-directrice de thèse).